Studies of crystal growth using atomic force microscopy and interferometry

McLoughlin, Martin J.

Award date:
2002

Awarding institution:
University of Bath

STUDIES OF CRYSTAL GROWTH USING ATOMIC FORCE MICROSCOPY AND INTERFEROMETRY

Submitted by Martin J. McLoughlin
for the degree of
Doctor of Philosophy
of the University of Bath
2002

ProQuest LLC
789 East Eisenhower Parkway
P.O. Box 1346
Ann Arbor, MI 48106-1346

Abstract

Laser interferometry and atomic force microscopy (AFM) have been used together for the first time to study the growth of crystals from solution. Using potassium hydrogen phthalate (KAP) as a model crystal, *in-situ* measurements of normal growth rates of KAP {010} were made using a purpose built interferometer system, which allowed the controlled removal of crystals from the growth cell for subsequent AFM imaging. Computer software was developed to allow the retrieval of pixel intensity data from the interferometry video signal, allowing the simultaneous measurement of normal growth rates at multiple locations on the crystal surface. Using these data, (R,σ) curves were constructed for various solution saturation temperatures. These data were fitted with the growth rate model for spiral growth due to Burton, Cabrera and Frank. In agreement with similar measurements reported by previous workers, considerable scatter was found in the (R,σ) data. In contrast to earlier work however, *ex-situ* AFM imaging of the responsible growth sources allowed the (R,σ) data to be directly interpreted in terms of the structure of the responsible source, such as the number of co-operating dislocations. In this way, the (R,σ) data were rationalised in terms of source structure. *Ex-situ* AFM observations revealed a wide range of source strengths and structures, from single dislocations to multiple co-operating spirals and sources formed at inclusions. In the case of simple sources, where quantitative analysis was possible, the AFM and interferometry data were found to be consistent. Several other postulated features of crystal growth faces were also observed by AFM; including macrosteps, kinematic waves, step shock-waves, hollow dislocation cores and two-dimensional islands. The role of dislocation slip during the crystal growth process was also illustrated by the study. *Ex-situ* AFM was supported by *in-situ* AFM studies. From the AFM observations, a new hypothesis for the shape of polygonal growth spirals and two-dimensional islands on KAP {010}, which invokes the consequences of the point group symmetry of the crystal for the configurational entropy of surface steps, has been advanced.

Acknowledgements

The author would like to express his thanks to the following people and organisations. The academic staff of the former Department of Materials Engineering at Brunel University for introducing him to the fascinating field of crystal growth; Drs Peter Halfpenny and Graham Clark for providing the opportunity to work in this field; Dr Robert Price for his enormous energy, enthusiasm and friendship; Dr Tim Mays for his patience, interest and continuous support; and Brendan Donohoe, Ed Fahey and Mike Maxwell for their friendship throughout. Thanks are also due to the staff and students of the former Department of Materials Science at the University of Bath; the director and staff of the Centre for Electron Optical Studies at the University of Bath for the provision of instruments and facilities; the Department of Chemical Engineering at the University of Bath for the the provision of an instrument and technical assistance for the measurement of solution refractive indices; the Director and staff of CLRC Daresbury Laboratory for the provision of funds and equipment; the Engineering and Physical Sciences Research Council for the provision of a CASE award. Travel grants were generously awarded by the Institute of Materials, the Worshipful Company of Armourers and Brasiers, the British Association for Crystal Growth and the American Association for Crystal Growth.

I would especially like to thank my parents and family for their enormous support and encouragement. Finally, I am indebted to my wife Claire whose support, understanding and patience have been limitless.

Contents

List of Figures

List of Tables

Part I

Introduction

Chapter 1

Introduction and Scope

1.1 Introduction to the Field of Crystal Growth

It seems to be almost essential that any treatment of the subject of crystals should begin with a statement about mankinds' fascination with this particular state of matter from the earliest times. The simple fact is that crystals are fascinating objects on many levels. It is easy to understand how even the most primitive people could prize the best specimens of single crystals so highly, to the extent of elevating them to a mystical status and imbuing them with magical properties - anachronistic ideas that still persist into the present day. Claims of the supernatural aside, good quality single crystals are still highly prized as gemstones which can fetch enormous sums simply for their decorative value and are often found as museum exhibits. Aesthetics aside, crystals are also fascinating objects for scientific enquiry by virtue of the enormous variety of forms and properties, many of which are unique to the crystalline state, which they exhibit. Consequently, the study of the crystalline state forms a central part of much modern science. What is often unappreciated is the ubiquity of crystals - almost all solid matter is crystalline - at least to some extent. Non crystalline solids are very much the exception rather than the rule. The formal science of crystals is crystallography, however due to the abundance of crystals in nature, many branches of science which go by a variety of names have the study of crystals as a central theme. These include solid state physics and chemistry, materials science, mineralogy and even structural biology.

Arguably one of the most fascinating features of crystals is their formation from the fluid phase - the phenomenon of crystal growth. The fluid phase in question can be the vapour, a solution or a melt. In the field of crystal growth the fluid phase from which the crystal forms is termed the mother phase. This terminology for the fluid phase suggests that it 'gives birth' to the crystals which grow from it and implies an element of mystery in the process of crystal growth. In fact, as will be shown, the problem of explaining the rates of growth of real crystals remained an intractable problem for many years.

One of the most fascinating features of the growth of crystals is their myriad shapes, from the very simple to the incredibly complex, that spontaneously appear from a disordered mother phase - from perfectly facetted polyhedra to intricately patterned snowflakes. A central theme in science is the explanation of the patterns which occur in nature. The patterns formed in crystal growth are some of the most striking and beautiful to attempt to explain - hence the current study.

1.2 The Economic Importance of Crystal Growth

Leaving aside the scientific curiosity viewpoint for a moment, crystal growth also has major implications for industry, though at a first glance this is not always apparent. This is in large part a consequence once again of the ubiquity of crystals. Up until the mid nineteenth century crystals were mainly curiosities or - in the case of diamonds and rubies - gemstones. Perhaps the first non-aesthetic applications of single crystals were in scientific instruments, especially in microscopy and spectrometers, for example, with the invention of optical devices such as the Wollaston and Nicol prisms, based on single crystals of Iceland Spar (calcite).

Broadly speaking, the use of crystalline materials in modern industry falls into two categories. The first includes bulk commodities which are supplied in particulate form such as chemical feedstocks, fertilisers, sugar and salt. In keeping with the assertion from the previous section, usually such bulk particulates are substantially crystalline. Often, these materials have been subjected to several recrystallisation processes as purification stages. In terms of volume, these materials are by far the most important industrially. The majority of chemicals are supplied in crystalline particulate form. In many cases, the properties of the individual crystals in bulk particulate materials

has profound significance to the performance of the materials. For such materials, bulk properties such as particle size distribution, particle shapeand bulk density are of the utmost importance and are usually greatly affected by the crystallisation process used. Often, such properties only affect the bulk handling of the material. Nonetheless, when the scale of worldwide production of materials such as fertilisers is taken into account, the enormous economic significance of inefficient bulk handling is readily apparent. In some applications, the particulate form of bulk materials also has great significance to the end use. For example, the surface area of a catalyst is largely dependent on the particle size, and the performance of pigments is greatly influenced by the particle form. Pharmaceutical materials must necessarily be extremely pure and this is often achieved by at least one recrystallisation process. Also, their solubility and hence bio-availability and efficacy is greatly dependent on their particle size and perfection. In many cases, the final particulate form is currently achieved through milling or comminution operations. However, these processes are difficult to control and much work is being conducted in several industries currently to replace comminution processes with crystallisation processes, which promise better control of the final product. Much activity to further the understanding of crystallisation is currently underway in the pharmaceutical industry in particular [1]. The study of the crystallisation of bulk materials is typically referred to as industrial mass crystallisation and is a major branch of chemical engineering. The mechanisms of crystal growth play a role of central importance to the study of mass crystallisation processes. For example, in many cases a narrow particle size distribution is desirable. An understanding of the mechanisms of crystal growth can be applied in such cases to improve the understanding of the process and afford greater control over the particle size distribution. Attempts to "engineer" particle size distributions often reveal the complexity of crystallisation processes through the occurrence of phenomena such as growth rate dispersion in which individual crystals grow at different rates despite experiencing the same nominal conditions.

The electronics industry is perhaps the best example of the second category of industrial applications of crystal growth technology - the more specialist applications of large single crystals. The best known example of the growth of single crystals for technological applications is undoubtedly the growth of large, dislocation free crystals of silicon for the manufacture of integrated circuits and microprocessors. This is an example of an application in which a single crystal is not only desirable but imperative, for integrated circuits and microprocessors simply could not work unless made from dislocation free single crystals. It is quite reasonable to say that todays micro-

processor and computer industry simply could not exist without this breakthrough in crystal growth. Another less celebrated but nonetheless essential material for modern electronics is single crystal quartz for oscillators. Almost every modern electronic device will have a single crystal quartz oscillator at its heart. The demand for high perfection single quartz crystals for electronics is far too great to be met from natural sources and so quartz crystals are today also grown synthetically in hydrothermal autoclaves for use in electronic devices. Numerous other materials are also grown in single crystal form in large quantities for applications in electronics. The growth of such crystals is by now routine in the modern electronics industry. However there continues to be enormous effort in crystallisation research in new materials. For example, high temperature superconductors, the superconducting properties of which are sensitively dependent on the defect structure produced during crystal growth. Molecular beam epitaxy is an active field of research for new devices based on thin films and electronic heterostructures. For example, to produce quantum dots and wires.

Optoelectronic and non-linear optical (NLO) materials is another very active field of research which promises a whole new range of devices for optical data transmission. By exploitation of effects such as second harmonic generation, and the electro-optic effect, it will eventually be possible to replace much electronic data transmission with optical data transmission and exploit the benefits of faster transmission and higher bandwidths. This goal will require the creation of integrated optical circuits, which are the photonic equivalents of silicon based integrated circuits for electrons. Analogously, these devices require high perfection single crystals. Such crystals based on materials such as lithium niobate are now routinely produced. There is also great potential here for new organic materials with non-linear optical properties. Once synthesised, these materials must be formed into single crystal form before their NLO properties can be evaluated [2]. A particularly notable and unique example of the production and application of large single crystals for NLO applications is the well publicised example of the growth of potassium dihydrogen phosphate (KDP) crystals of the order of 50 cm in length by Zaitseva *et al.* [3] for the United States National Ignition Facility at Lawrence Livermore National laboratory. The role of these crystals in this device, which is used in laser fusion research, is to double the frequency of radiation from a carbon dioxide laser from the infra-red to the ultra-violet - a particularly striking example of non-linear optical properties.

Another noteworthy example for industrial application is the growth of single crystals of nickel super-alloy turbine blades for gas turbine engines. Due to the extreme op-

erating temperatures and stresses of these components, polycrystalline turbine blades are prone to creep deformation caused by the movement of grain boundaries. This limits their useful lifetime. By filling a turbine blade shaped mould with molten alloy and seeding it with an appropriately oriented single crystal of the alloy, a single crystal turbine blade is formed. Because grain boundaries are absent from such a crystal the creep problem is eliminated. Such turbine blades are now routinely produced.

To summarise this section, only a small number of the applications of crystals which demand careful crystal growth have been mentioned. To list them all in detail would no doubt require several volumes. Hopefully however, this section has served to illustrate the significance of crystal growth in modern science and industry - a significance that touches almost every industry in some form and is not always appreciated from outside the often narrowly regarded field of crystal growth research.

1.3 Scope of Thesis

The present study is concerned with extensive experimental studies of crystal growth rates and the nature of the solid-liquid interface during crystal growth. The rationale, objective and scope of the work contained within this study are perhaps best illustrated by way of passages from the literature on crystal growth which highlight the lack of direct experimental evidence for theoretical predictions at their time of writing. The following passages were all written in the context of the fact that theory had reached a level of development for which existing experimental techniques did not have the resolution to discriminate one theoretical prediction from another. The period over which this state of affairs persisted is notable.

In 1952, Frank [4] wrote the following with reference to the pitfalls encountered in the interpretation of measured crystal growth rates in terms of the dislocation theory.

> "Only when techniques are available that make mono-molecular steps in the crystal surface visible are we in a position to count all the screw dislocations emergent."

On a similar theme, in 1973 Ohara and Reid [5] wrote as follows.

> "We can only hope that the next quantum jump in surface controlled crystal growth theories can be induced by employing new and sophisticated instrumentation which may be more capable of probing the secrets of the molecular behaviour on a crystal surface."

Both passages anticipate new instruments that would one day make direct observation of crystal surfaces beyond the resolution limit of existing instruments a reality. As theorists, none of these authors went on to speculate about what such instruments would look like, what physical principles they would be based upon or when they would appear. However they were unanimous about the impact which these as yet un-invented instruments would have on their science. The instrument of which they prophesised became commercially available in the early 1990s and is of course the atomic force microscope (AFM). This instrument was a revelation in the field of crystal growth and rapidly provided what these authors had wished for - a means to study crystal surfaces at a level of resolution unachievable with conventional techniques, such that fundamental features of surfaces such as steps and dislocation outcrops could be directly observed.

In 1974 Bennema [6] wrote the following with respect to the various interrelated, and to some extent, competing theories of crystal growth.

> "The best way to check the network of theories is to use a network of experiments in which (R,σ) curves are measured under very well defined conditions of supersaturation, purity or planned impurity, hydrodynamics, together with observation of step patterns during and after growth and a study of dislocations. This ideal may be difficult to achieve."

This latter passage essentially represents what the current study set out to achieve, at least in part. Despite Bennema's warning of difficulty, this work represents an attempt to measure crystal growth rates under carefully controlled conditions by means of optical interferometric techniques, and to relate those results to the structure of the crystal surfaces by way of atomic force microscopy.

1.4 Structure of Thesis

The remainder of the present thesis is organised as follows. Part II deals with the background necessary for the present study. Chapter 2 discusses the theory of crystal growth. Chapter 3 describes experimental studies of crystal growth, experimental techniques used in the study of crystal growth and presents a case study of previous results obtained with a crystal which features prominently in the present study. In part III the experimental techniques employed in the present study are discussed in some detail. Chapter 4 deals with the development and operation of a laser interferometer for growth rate measurement and dynamic observation of crystal growth. Chapter 5 describes the techniques employed for the atomic force microscopy of crystals in the present study. Part IV presents the results and discussion of the present study. Chapter 6 presents the results and limited discussion of combined interferometry and *ex-situ* atomic force microscopy experiments in which measured growth rates are interpreted in terms of the structure of the sources responsible. Chapter 7 presents and discusses *in-situ* atomic force microscopy studies of crystals growing from impure solutions. Chapter 8 presents a general discussion of the results in terms of theories of crystal growth and experimental studies by other workers. Part V presents conclusions from the present study and suggests future experimental studies prompted by the results of the present study. Finally, part VI presents appendices of experiments and computer program listings in support of the main study.

Part II

Background

Chapter 2

The Theory of Crystal Growth

2.1 Introduction

In the field of crystal growth, theoretical ideas have always held a position of central importance. Even before the modern era man has speculated about the nature and formation of crystals. Scheel [7] has discussed the history and origins of the subject in considerable depth. This history is interesting in its own right, however this chapter is necessarily restricted to a more focussed description. The chapter is informally divided into three parts. The first considers the thermodynamic and crystallographic background which is basic to crystal growth. The second considers the development of the modern theory of crystal growth up to and including the theory of Burton, Cabrera and Frank, which marked a turning point for the subject. The final section discusses developments from that time to the present.

2.2 Chemical Thermodynamics

The growth of crystals from a mother phase is an example of a phase transition and as such is subject to the laws of chemical thermodynamics. The discipline of chemical thermodynamics is, as the name suggests, the study of the application of the laws of thermodynamics to chemical systems. The power of thermodynamics lies in its generality. The four laws of thermodynamics are axiomatic, therefore results formally

derived from them may be regarded as truths. A caveat of this statement is that they generally hold strictly true only under very precisely defined conditions. Usually this means at equilibrium. Thermodynamics itself is therefore divided into equilibrium thermodynamics and non-equilibrium thermodynamics. The latter is a highly specialised and somewhat esoteric field and will not be considered further here, though it does have specific applications in crystal growth, see for example van der Eerden [8]. Equilibrium chemical thermodynamics on the other hand is basic to the study of crystal growth, hence its discussion at this stage. Numerous texts dealing specifically with the equilibrium thermodynamics of crystal growth systems are available [9–11]; a brief review of key results is presented here.

In essence equilibrium chemical thermodynamics comprises a set of relationships between functions of the state of a system, which are derived from the laws of thermodynamics applied to the system at equilibrium. Familiar examples of the functions of state of particular relevance to crystal growth are the temperature, T, the pressure, P, the internal energy, U, the enthalpy, H and the entropy, S. The first two functions are examples of intensive functions of state, which depend only on the state of the system and not its size. The remainder are all extensive functions of state because they are dependent on the size of the system.

This generality and the absence of assumptions means that thermodynamics can provide insights about the bulk properties or behaviour of a system without the need for a detailed atomic model of the system under consideration (which is the realm of statistical mechanics). The significance of this fact to the history of the study of crystal growth is that important progress was possible in the understanding of crystal growth phenomena even in the absence of a coherent atomic theory and decades before a true understanding of the structure of crystals was available through pioneering work in x-ray crystallography. Much of the detail of chemical thermodynamics was worked out by one man, J W Gibbs, who is now regarded as the father of the subject. Between 1875 and 1876 Gibbs published a series of seminal papers entitled *"On the Equilibrium of Heterogeneous Substances"*, which have been collected together [12]. Amongst the numerous ideas promulgated in this work, perhaps the most important from the point of view of crystal growth were the concept of the chemical potential, the phase rule (or Gibbs phase rule) and the insights into the role of interfaces and the process of nucleation.

2.2.1 Gibbs Free Energy and Chemical Potential

Of the thermodynamic functions of state, one of the most important from the perspective of crystal growth is the Gibbs free energy[1] or Gibbs function, G, which is defined as

$$G = H - TS \tag{2.1}$$

where H is the enthalpy, T is the absolute temperature and S is the entropy.

The Gibbs free energy is an example of a thermodynamic potential function. It is a property of the Gibbs function that when a system at constant temperature and pressure is at equilibrium, the Gibbs function is at a minimum. A frequently cited mechanical analogy is the location of a ball in a cup, or similar. At mechanical equilibrium the ball will come to rest at the bottom of the cup. In this case the potential is gravitational, in chemical systems a thermodynamic potential such as the Gibbs function applies. In differential form the condition for equilibrium can be expressed as,

$$dG = 0. \tag{2.2}$$

From this condition it follows that at constant temperature and pressure, any chemical change which results in a reduction of the Gibbs function will occur spontaneously as it will occur in the direction of the equilibrium condition. Such a process can be represented by changes in the Gibbs function. If the Gibbs function of the initial state of a system is $G_i = H_i - TS_i$ and the final state is $G_f = H_f - TS_f$, then the change in the Gibbs function ΔG on going from the initial to the final state is $G_f - G_i = (H_f - H_i) - T(S_f - S_i)$ hence

$$\Delta G = \Delta H - T\Delta S \quad (\text{constant } T). \tag{2.3}$$

When ΔG is negative, then the change will occur spontaneously, since it serves to lower the Gibbs free energy. If then, the Gibbs free energy of a crystal at constant temperature and pressure is G_c and that of the fluid phase (i.e. solution, melt or vapour) is G_f then the Gibbs free energy of crystallisation will be $G_f - G_c = \Delta G_{cryst}$. If $\Delta G_{cryst} > 0$ then the crystal will be unstable with respect to the fluid phase and will evaporate, melt or dissolve. If $\Delta G_{cryst} < 0$ then the crystal will be stable and grow. Another thermodynamic function which plays an important role in the description of crystal

[1] So called because it represents the maximum available work available from a system at constant temperature and pressure.

growth is the chemical potential. The chemical potential is a unifying concept for the description of chemical equilibrium in heterogeneous systems. For a system at constant temperature and pressure, it is defined as the change in the Gibbs free energy of a phase due to the addition or subtraction of an infinitesimal amount of a component[2] to that phase. Hence the chemical potential μ_i of the ith component within a phase is defined as

$$\left(\frac{\partial G}{\partial n_i}\right)_{T,P,n_j} = \mu_i \tag{2.4}$$

where G is the Gibbs free energy of the phase and n_i the number of moles of component i. It should be noted that the chemical potential is equivalent to the partial molar Gibbs function. Gibbs showed that, when a system was in a state of thermodynamic equilibrium, the chemical potential was equal in every phase. He subsequently used this concept to formulate the phase rule which describes the relationship between the number of separate components of a system, the number of phases and the variance[3]. Though the phase rule plays a fundamental role in many crystal growth systems, particularly multicomponent systems, for growth from solution its implications are usually obvious and it will not be considered further here.

2.2.2 Supersaturation

Since the equilibrium condition for a chemical system is that the chemical potential of each component is the same in every phase, then the driving force for change is a difference in chemical potential. The difference in the chemical potential of a component between phases is termed the *absolute supersaturation*, $\Delta\mu$:

$$\Delta\mu = \mu_i - \mu_j \tag{2.5}$$

where μ_i and μ_j are the chemical potentials of the component in the ith and jth phases respectively. Thus a crystal will be in equilibrium with its vapour or solution when $\mu_f = \mu_c$ and hence $\Delta\mu = 0$. For $\mu_f \neq \mu_c$ growth or evaporation/dissolution will occur. Because the chemical potential is a somewhat abstract concept and not an easily measured quantity, the absolute supersaturation is not a practical measure of the potential

[2]The term component as used here implies a chemical entity such as an element or compound which cannot be separated without chemical reaction

[3]A phase is defined as an intimate and completely homogeneous mixture of components. The variance is the total number of intensive state variables which can be adjusted without producing a change in the equilibrium number of phases

for change. As a result, other more practical measures have been established to describe the driving force for change. With suitable assumptions, such as ideal gas or solution behaviour, these measures can be related to the chemical potential difference. One of the most important definitions for the study of crystal growth from solutions is the *relative supersaturation* based on the solubility of a solute in a solution. The relative supersaturation of a solution, σ, is defined as the following dimensionless ratio[4],

$$\sigma = \frac{C_T - C_0}{C_0} \tag{2.6}$$

where C_T is the actual concentration of solute in solution at temperature T and C_0 is the equilibrium concentration of solute at temperature T. The ratio C_T/C_0 in equation 2.6 is called the saturation ratio α. Thus equation 2.6 can be written as

$$\sigma = \alpha - 1. \tag{2.7}$$

It must be stressed that equilibrium thermodynamics alone can say nothing of the rate at which a process such as a phase transition will occur. Time is not a variable in any thermodynamic relation. Thermodynamics can only state under what conditions a change can occur in terms of state variables. In fact, equilibrium thermodynamics is strictly limited to so called reversible processes. A reversible process is one which occurs infinitely slowly and never deviates from equilibrium. Clearly these conditions are never actually met in practice and must therefore always be regarded as limiting cases. The explanation of the rates of processes is the subject of chemical kinetics. Equilibrium thermodynamics does nonetheless play a role in determining the kinetics of a process as will be discussed in the next section.

2.2.3 Finite Phases and Nucleation

Another major contribution by Gibbs to the chemical thermodynamics of heterogeneous systems was his realisation that the thermodynamics of finite phases are complicated by the presence of an interface. The term finite phases implies phases whose dimensions ensure that a significant amount of the matter of the phase is in the vicinity of the phase boundaries. Obviously the smaller the dimensions of a phase, the more of it will be in the vicinity of the phase boundary. The concept of a *surface tension* had

[4]It should be noted that the definition of relative supersaturation varies depending on the nature of the system. For example, in the vapour phase it is defined in terms of the actual and equilibrium pressures. In melts, typically the supercooling ΔT is used.

been first introduced by Young and Laplace to explain the shapes adopted by liquid droplets, bubbles and liquids in capillaries. Gibbs formalised the concept and introduced the concept of a specific surface or interfacial free energy which is equivalent to the reversible work required to create unit area of surface. The specific surface free energy is then the excess free energy associated with a phase due to the presence of unit area of surface. Gibbs used purely thermodynamic arguments to arrive at the concept of the surface free energy, however its origin is often qualitatively explained in molecular terms. The equilibrium state of a molecule in a bulk phase assumes it to be completely buried within the phase and to be completely surrounded by an equilibrium number of neighbours (the *coordination number*). At the interface however, molecules have fewer than their equilibrium number of neighbours. Consequently their chemical potential differs from that of the molecules within the bulk of the phase. This is the origin of the excess chemical potential that is the surface free energy. The quasi-chemical argument given here is often referred to as the "dangling bond" model.

The interface between different phases always has an associated interfacial free energy. Gibbs realised that when a new phase forms in an existing phase that work must be done to create the interface. Consider the case where a new phase forms spontaneously in an existing phase as a consequence of its having a lower free energy than the parent phase. Initially the new phase must be very small and therefore the surface area to volume ratio would initially be large[5]. If the positive work of formation of the surface of the new phase exceeds the negative free energy change due to the formation of the bulk of the new phase, then the net free energy change will be positive and in accordance with equation 2.3 the change will be thermodynamically unfavourable. Thus, the work required to create the interface acts as a barrier to the formation of the new phase. The new phase will only become stable when it grows beyond a certain size after which the negative free energy change due to the formation of the bulk of the new phase exceeds the positive free energy change due to the surface. That is, the contribution to the total free energy from the surface becomes negligible. In order to illustrate these concepts more formally, consider the following simplified analysis.

For the sake of simplicity consider the case of the formation of a spherical liquid droplet from a vapour. If n_v is the number of moles of vapour with chemical potential μ_v (which is a function of the temperature, T and pressure, P) then the Gibbs free

[5]An exception to this assertion occurs for the case of formation of a new phase by spinodal decomposition.

energy of the initial state of the system at constant T and P will be given by,

$$G_i = n_v \mu_v \tag{2.8}$$

If now a liquid droplet with bulk chemical potential μ_l forms from n_l moles of the vapour then the new expression for the state of the system will read

$$G_f = (n_v - n_l)\mu_v + n_l \mu_l + 4\pi r^2 \gamma \tag{2.9}$$

where γ is the surface free energy of the liquid surface[6]. That is, in addition to the free energy of the bulk phases, there is an additional contribution from the surface.

Subtracting equation 2.9 from equation 2.8 and making the substitution $n_l = 4\pi r^3/3v_l$, where v_l is the volume per molecule in the liquid, then we obtain the following expression for the free energy change of the system due to the formation of a spherical droplet of radius r,

$$\Delta G(r) = -\frac{4}{3}\frac{\pi r^3 \Delta\mu}{v_l} + 4\pi r^2 \gamma \tag{2.10}$$

where $\Delta\mu = \mu_v - \mu_l$.

Equation 2.10 possesses a term for the bulk phases and a term for the interface or surface between phases. A maximum in this function occurs at a specific radius r^* which may be obtained by differentiation. Doing so yields the following formula for r^*,

$$r^* = \frac{2\gamma v_l}{\Delta\mu}. \tag{2.11}$$

Equation 2.11 is a form of the Gibbs-Thomson equation and gives the condition for equilibrium of the droplet or nucleus with the vapour phase. It effectively states the excess chemical potential due to the size and curvature of the droplet. The equilibrium of the nucleus with the vapour is unstable however. Removal of molecules from it will reduce the Gibbs free energy of the system giving it a tendency to evaporate. Addition of molecules will similarly reduce the Gibbs free energy and so there is a thermodynamic tendency for the nucleus to grow. This is equivalent to saying that the vapour pressure of the droplet is greater than that of the bulk liquid phase. Nuclei of radius r^* are called critical nuclei and r^* is termed the critical radius. Unstable nuclei with $r < r^*$ are commonly referred to as embryos. The maximum value for $\Delta G(r)$ can

[6]Strictly, the surface energy will exhibit a dependence on the droplet size and curvature. These effects are usually neglected in elementary treatments.

be obtained by substitution of 2.11 into 2.10 giving

$$\Delta G^* = \frac{16\pi\gamma^3 v_l^2}{3\Delta\mu^2}. \tag{2.12}$$

Equation 2.12 represents the free energy barrier which must be surmounted for condensation from a vapour to occur and it is this barrier which allows a parent phase to become supersaturated without formation of the new phase. This is the origin of the so called *metastable zone*. The metastable zone is a region of the phase diagram of a system in which, despite being supersaturated, nucleation of the equilibrium phase does not occur. An interpretation of this effect is that the equilibrium phase diagram applies to an infinite phase and does not consider the work of formation of the interface. Put another way, the excess energy required to surmount the free energy barrier to condensation is provided by the supersaturation. The supersaturation represents the chemical potential energy available to do work of interface formation. The greater the supersaturation then the greater the chemical potential energy available for interface formation and hence nucleation. More detailed treatments of nucleation go on to consider the equilibrium population of critical nuclei in a phase at a given supersaturation. In general it is found that above some threshold of supersaturation the population of critical nuclei in the system increases rapidly.

The foregoing discussion has been restricted to the case of homogeneous nucleation. In the case of heterogeneous nucleation, the nucleus uses a foreign phase as a substrate on which to form. This may result in a reduced free energy barrier to nucleation if the interfacial energy between the new phase and the substrate is less than that between the new phase and its parent phase. The relative importance of homogeneous and heterogeneous nucleation is the subject of much discussion. For the sake of simplicity condensation of a liquid droplet from the vapour phase has been considered however similar arguments apply for nucleation of solids from melts, solutions and other solids. The key complications are the possibility of anisotropy in surface energy and the existence of lattice strain at the interface. Further discussion of the former will be given in section 2.4.1. In such cases, analogues of the equations in the preceding argument exist. In particular the Gibbs-Thomson equation also applies in solutions however in this case it relates the size of the nucleus to its solubility rather than its vapour pressure.

The field of nucleation is substantial and active in its own right and only the most elementary of descriptions has been given here. For the purposes of crystal growth theories nucleation is often taken as given. According to this rationale, crystallisation

can be considered the result of two sequential processes, nucleation and growth. In attempting to explain the rates of growth and the morphology of crystals very much larger than a critical nucleus, the assumption is valid. For more detailed discussion of nucleation consult Chernov [9], Strickland-Constable [10] or Markov [13]. It should be stressed that at high supersaturations and in other cases where the size of the critical nucleus is very small, the macroscopic thermodynamic concepts such as surface energy are no longer applicable as they become ill-defined when the dimensions of the phase approach the order of magnitude of molecules. In these cases, the atomistic approach, avoiding the use of bulk thermodynamic properties becomes more appropriate. An elementary introduction of atomistic nucleation theory has been given by Markov [13].

2.3 Crystallography and Crystal Defects

2.3.1 Crystallography

The study of crystal growth is intimately linked to the science of crystallography and crystal defects. Clearly it is not possible to understand the formation of crystals without a knowledge of the structure of the resulting crystals. Crystallography, the formal science of crystals, originated from mineralogical descriptions of habit and form of natural mineral specimens [7]. In the early days it was largely taxonomical, however gradually a scientific understanding developed. This included the concept of the unit cell as a conceptual building block from which the entire crystal could be built and the description of crystal faces and edges by a system of indices, the Miller indices. Also the recognition of the 14 fundamental space lattices (the Bravais lattices) and their relationship to the unit cell; the different symmetry classes and their mathematical description by point groups and space groups and their division between 7 crystal systems; all contributed to the framework of formal crystallography. It is worthy of note that many of these developments occurred long before the general acceptance of the atomic theory.

The real breakthrough for crystallography came with the discovery of x-ray diffraction which is now virtually synonymous with crystallography. With this development the unit cell was formalised as the smallest subdivision of a crystal which retains all of

the symmetry characteristics of the bulk crystal. The Miller indices were generalised to describe crystal planes in terms of the unit cell and to the x-ray reflections from a specific set of planes. The historical development of x-ray crystallography has been discussed in many books including one by W L Bragg, a founder of the discipline [14], in which the concepts mentioned here are introduced in a personal and highly entertaining account.

2.3.2 Crystal Defects

As will be shown, the growth of crystals is perhaps even more intimately linked to crystal defects than to formal crystallography itself. The defects present in crystals are typically divided into three groups, defined by their spatial dimensions. These are the point, line and planar defects respectively. The point defects include vacancies, interstitials, Schottky and Frenkel defects. The presence of these defects in crystals serve to increase the configurational entropy of the crystal. By reference to equation 2.3, this results in a reduction of the free energy of the crystal and so at equilibrium there will be an equilibrium concentration of point defects. That is, at temperatures greater than zero Kelvin, crystals always contain point defects.

The planar defects include free surfaces, grain boundaries, stacking faults and twin planes. Clearly all finite crystals must have a surface. However crystals without the other types of defect can be obtained since these always raise the free energy of the crystal and consequently cannot exist in equilibrium with the crystal. The surface is of course where growth occurs and so it holds a special position with respect to crystal growth. Surfaces can differ significantly in their structure from the bulk underlying solid as a result of phenomena such as relaxation and reconstruction, in addition to adsorption of other species from the surroundings. Relaxation is the phenomenon in which the interatomic spacing of crystal lattice planes near the surface differ from those in the bulk. Reconstruction is the phenomenon where the actual atomic positions of the structure at the surface differ from those in the bulk. Reconstructions are considered to be actual phase transitions of the surface and have associated transition temperatures. These phenomena are driven by the tendency to reduce the surface free energy because the molecular arrangement which minimises free energy in the bulk may not be that which minimises it at the surface. In this sense they are related to the quasichemical dangling bond model of section 2.2.3. According to this model, reconstruction occurs in an attempt to minimise dangling bonds.

The line defects or dislocations also hold a special position in crystal growth though at first sight this is less obvious than for the surface and so a little more detail is warranted. Before proceeding it should be noted that all classes of defect apply to all types of crystal from simple metals and ionic solids, through molecular crystals to macromolecular crystals of proteins, for example. Their relative importances may vary however.

In the early days of x-ray crystallography, the measured intensities and linewidths of diffracted x-ray beams were found to be much more intense and wider respectively than predicted by theory. Darwin [14] reasoned that this may be due to slight misalignments of regions of the crystal and he introduced the concept of the mosaic crystal to explain this. The mosaic crystal was very successful in explaining the intensity and linewidth of diffracted x-rays, however Darwin did not offer a theory for the occurrence of the misorientations. Contemporary with the development of X-ray diffraction in the early decades of the 20th century, there was increasing realisation that existing theories of the solid state were inadequate to explain the mechanical properties of crystals. An increasing number of physicists and metallurgists were attempting to explain the strength and plasticity of crystals - particularly metal crystals. In particular it was found experimentally that the yield stresses of real crystals were several orders of magnitude lower than that predicted by theory, based on the work required to break the bonds between crystal layers [15].

This lead to the concept of the dislocation, introduced independently by Taylor, Orowan and Polanyi [16], as a model for explaining this observation. It is notable that this was introduced as a theoretical construct with no experimental basis. Taylor [17] suggested that if an incomplete plane of atoms were present within a crystal lattice, that a stress applied to the crystal could cause the relative movement of this half-plane of atoms through the crystal, hence leading to a plastic deformation by the successive breaking and reforming of the bonds at the end of the half plane only. Thus, the number of bonds required to be broken for plastic deformation to occur was dramatically cut, thus reducing the necessary work required and hence the yield stress. The success of the dislocation model of plastic deformation stimulated much new research in this area. Subsequently, it was realised by the Dutch physicist Burger [17] that the dislocation described by Taylor [17] was only one example of a family of defects which could be characterised abstractly as one-dimensional or "line defects". In the case of Taylor's original dislocation formed by a half-plane inserted in the crystal, the line defect is considered as the edge of the half plane for this is where the crystal structure is dis-

torted. Hence this type of dislocation is known as an edge dislocation. Burger [17] realised that other types of dislocations could exist. He introduced a vector defined as the closure failure of a circuit around lattice points in a dislocated crystal, encompassing the dislocation line, compared to the same circuit in a region of perfect crystal. The circuit is known as a Burgers circuit, the vector is the Burgers vector, **b** of the dislocation.

Dislocations are characterised by the orientation of the Burgers vector with respect to the dislocation line direction. In Taylor's edge dislocation the direction of deformation is normal to the dislocation line direction. The plane within which both vectors lie is called the slip plane. At the other extreme from the edge dislocation, Burgers [17] conceived a dislocation in which his vector is parallel to the line direction vector. Geometrically, such a dislocation can be represented as creating a shear deformation along the axis of the dislocation line, resulting in a helical distortion of the crystal structure centred on the dislocation line. For this reason, such dislocations are referred to as "screw" dislocations.

Burgers [17] went on to show that, conceptually at least, dislocations of arbitrary orientation could exist in which the Burgers vector could be represented as the vector sum of edge and screw dislocations and moreover that the character of a dislocation could change along its length. Such a dislocation is a "mixed" dislocation. As a vector, the Burgers vector has an orientation which implies that dislocations of opposite sign may exist. For example, if a screw dislocation with Burgers vector **b** forms a right handed screw, then a dislocation with Burgers vector $-\mathbf{b}$ will form a left handed screw. Referring to figure 2.2, the dislocation of opposite sign will be the mirror image of this, that is, the right hand side of the crystal will be higher than the left. A similar argument holds for edge, or indeed, mixed dislocations. It should be obvious that if two dislocations of equal magnitude but opposite sign meet, that they will annihilate each other, leaving a region of perfect crystal.

A large body of knowledge now exists about the genesis and mechanics of dislocations and their reactions and interactions with each other and other types of defect. Some of the more important results from the point of view of crystal growth are summarised here. A fundamental feature of dislocations in crystals is that the Burgers vector is always conserved. That this is necessarily true is easily shown by the fact that the dislocation line cannot simply cease to exist within the crystal. In the example of the edge dislocation formed by the extra half plane of atoms, the extra half plane and its

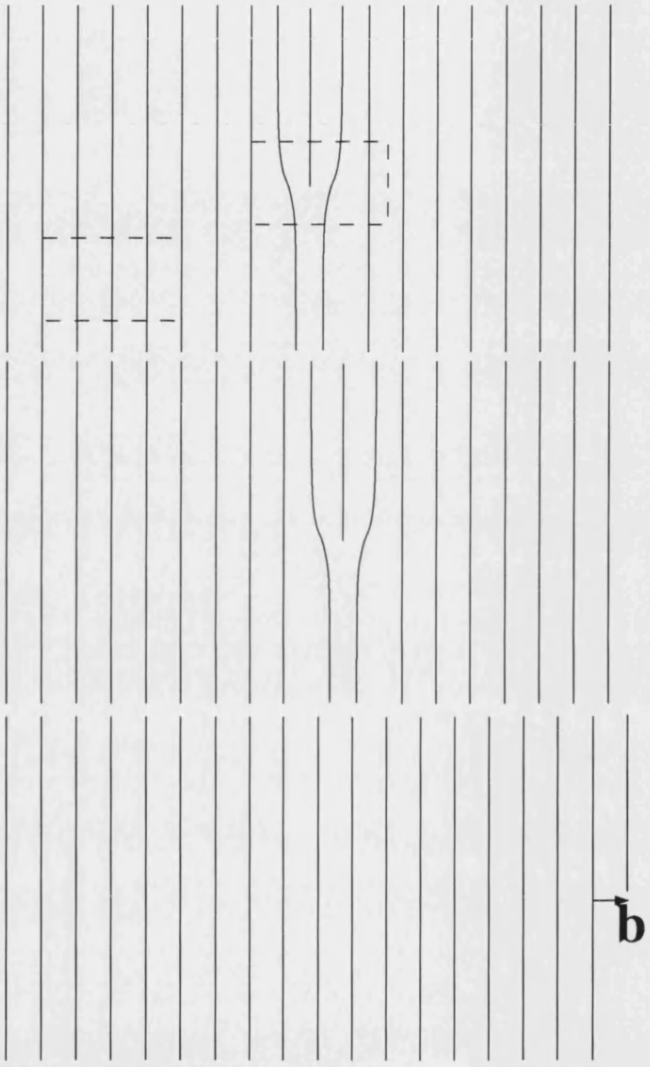

Figure 2.1: Schematic of a crystal with an edge dislocation formed by the insertion of an extra half-plane. The sequence illustrates the glide motion of the dislocation resulting in a deformation of magnitude $|\mathbf{b}|$, where $\mathbf{b}$ is the Burgers vector. In the first image a schematic Burgers circuit through perfect and dislocated crystal is shown.

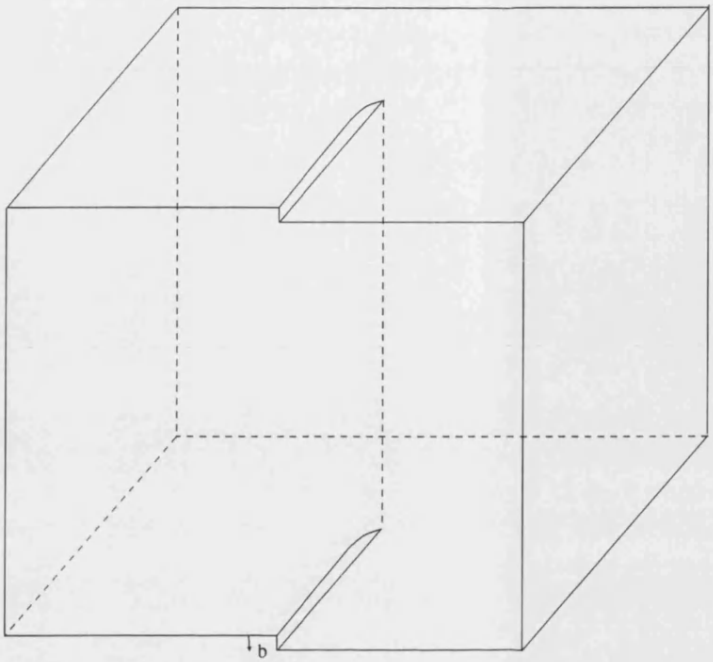

Figure 2.2: Schematic of a crystal with a screw dislocation.

edge, the dislocation line, is either present or not. The edge of the half plane can only cease to exist at a free surface of the crystal or it must form a junction with other dislocations or a closed loop with itself. If the Burgers vector is equivalent to a lattice translation vector then it is a *perfect dislocation* because passage of the dislocation through a region of perfect crystal results in no net change to that region of crystal, i.e. it remains perfect. When this condition is not met, passage of such a dislocation results in a change to the packing of the original perfect crystal. This type of dislocation is referred to as a partial dislocation because its Burgers vector is some fraction of a lattice translation vector. The region of distorted crystal left in the wake of a partial dislocation is called a stacking fault. It should be recognised at this point in the discussion that the lattice planes of a crystal containing a single perfect screw dislocation will form a single helicoidal lattice plane; that is, a single spiral ramp.

The distortions of the crystal structure at the dislocation line are effective strains and are therefore necessarily accompanied by a stress field and the dislocation will have an associated elastic strain energy, which is found to be proportional to the square of the magnitude of the Burgers vector, $|\mathbf{b}|^2$. The magnitude of the stress at the core of a dislocation is dependent on the details of the crystal structure and is directly related to the elastic constants of the particular crystal. Because of the strain energy, work must be done on a crystal to create a dislocation. This work can be regarded as a dis-

location line energy or "line tension" by analogy with surface tension. It follows that the free energy of a dislocated crystal will differ from that of a perfect crystal by an excess free energy which is the line tension. Because of the line tension, a dislocation within a crystal will strive to minimise its length, and at equilibrium should disappear altogether as was discussed previously.

The mechanism of plastic deformation requires the motion of dislocations. There are two mechanisms by which a dislocation can move. The first is variously called slip, glide or conservative motion and occurs when the dislocation line moves through the crystal structure under the application of an applied stress in the manner described above for Taylor's edge dislocation. The second mechanism is climb and results from the interaction of the dislocation with vacancies within the crystal. The diffusion of vacancies to the dislocation line results in a vacancy in the dislocation line called a jog. Consider the edge dislocation. If vacancies diffused to the edge of the half plane along its length, the half plane would move upwards by one lattice position. This is an important mechanism in the annealing out of dislocations in crystal structures.

From the preceding discussion it should be clear that the various classes of crystal defect do not exist in isolation, they are all capable of interaction in some way. For example, dislocation arrays can form grain boundaries and sub-grain boundaries, partial dislocations can form stacking faults, vacancies can form jogs in dislocation lines *etc*, the list is long. Finally, it should be remarked that the concept of dislocations provided a microscopic explanation of the mosaic blocks invoked by Darwin [14] to explain the intensity and linewidth discrepancy in the x-ray diffraction patterns from single crystals. The mosaic blocks would now be interpreted as relatively perfect blocks of crystal separated one from another by a narrow region of dislocated crystal. The presence of the dislocations is sufficient to provide the small angular distortions between the mosaic blocks which give rise to the mosaic spread.

2.4 Morphology of Crystals

Attempts at an explanation of the morphology or shape of crystals has a long history and goes back to the early mineralogical investigations. The problem is essentially one of a successful synthesis of the ideas of the foregoing sections on crystallography and thermodynamics with the forthcoming sections on growth kinetics. The developments

however have not always occurred in a strict chronological order. A succinct review, emphasising the synthesis aspect has recently been given by Chernov [18]. Early efforts at explaining the morphology of crystals considered only the equilibrium form and perfect crystals. Later developments have accounted for the importance of kinetic factors and defects in the formation of crystals. There is a certain nomenclature for the description of the morphology of crystals. A *form* is the collection of faces, expressed by their Miller indices which are present on a crystal specimen. The *habit* of a crystal is its shape defined by the relative sizes of faces of the form. Thus, two crystals may have the same form but a different habit if the relative sizes of individual faces differ. The relative sizes of different faces on a crystal form what is known as the order of *morphological importance.*

2.4.1 The Gibbs - Wulff - Curie Theorem

Gibbs' work on the properties of surfaces and interfaces in heterogeneous systems as discussed in section 2.2 led him to consider the equilibrium shape of finite solid phases [12] by extension to the rules for liquid phases. The basic problem is the same as that for liquid phases - to find the shape of the solid which will minimise the free energy of the system. For isotropic solids, i.e. solids in which the surface energy is equal in all directions, the problem is equivalent to that for a liquid. In this case the shape that minimises the surface free energy is a sphere, as this is the shape with the lowest surface area to volume ratio in three dimensions. Gibbs [12] realised however that crystals may have an anisotropic surface free energy and that this would give rise to a non-spherical equilibrium shape. The equilibrium shape itself is given then by that shape which for a given amount of matter minimises the surface free energy. Gibbs [12] also realised that crystal faces coincident with lattice planes will be close packed and have very much lower surface free energies than neighbouring orientations and that these would consequently be most prominent on crystal forms. Wulff [13, 19] introduced the concept of a polar free energy diagram (often referred to as a γ-plot) to represent the anisotropy of surface free energy and a theorem which bears his name which essentially states that the equilibrium shape of a crystal can be obtained from a construction based on the polar surface free energy diagram. Because of the close packed orientations, the polar diagram is considered to contain cusps or singularities coincident with these orientations. Application of Wulff's theorem (also known as the Gibbs-Wulff-Curie theorem) to a cusped polar diagram results in faceted crystal forms of *singular* faces, so called as they are associated with singularities in the γ-plot.

Apparently simple though these concepts appear, this is deceiving and they hide a considerable amount of mathematical complexity which is a subject in its own right. Key areas of which have included seeking proofs of Wulff's theorem and using the concepts in the statistical mechanical description of crystal surfaces. For a more complete description consult Pimpinelli and Villain [19]. Amongst these developments, Herring [20, 21] published lengthy extensions to the earlier work. Notable amongst his findings was that in some circumstances the equilibrium form could contain non-singular faces which may be curved on the equilibrium form.

2.4.2 The Law of Reticular Densities

Because of the special role played by close packed or singular faces in determining the equilibrium crystal shape, it was expected that the shapes of crystals, dictated by the order of morphological importance, could be predicted from the order of close packed crystallographic planes. That is, the crystal planes with the highest planar density of atoms (the highest reticular density) would have the highest morphological importance. As a general rule this corresponds to the lattice planes of greatest separation, d_{hkl}, and so the predicted crystal form could be constructed simply from known plane spacings. This law, known as the Bravais-Friedel law [22], was found to be quite successful in predicting the shapes of some mineral crystals, though there were notable failings also. Following extensions by Donnay and Harker and Donnay and Donnay [22], in which consideration of the symmetry elements of the crystal structure was shown to account for some of the noted discrepancies, these laws are now variously known collectively as the geometrical law, the law of reticular densities or the Bravais-Friedel-Donnay-Harker (BFDH) law. An obvious limitation is that no account is taken of the process of formation of the crystal or the medium from which it forms. It simply relates the shape to the internal structure of the crystal. That the internal structure of a crystal plays a role in dictating its shape was quite apparent from many observations, however the counter-examples were sufficiently numerous to imply that this was not the sole factor.

There is also a kinetic interpretation of the law of reticular densities, which is that the faces of highest reticular density are those which are slowest growing because they are formed of more molecules than other faces and therefore take longer to construct. From simple geometric considerations of the rate of advance of a face away from the growth centre, it is obvious that the slowest growing faces on a crystal will become

the largest. The fastest growing faces will be eliminated altogether from the crystal form by a process called "wedging out". This argument indicates that there are kinetic factors in determining crystal habit and form in addition to equilibrium factors.

2.4.3 The Morphological Theory of Hartman and Perdok

In an attempt to rectify the inadequacies of the purely geometrical basis of the law of reticular densities, Hartman and Perdok [22–25] presented an analysis of the relationship between crystal structure and crystal morphology based on the energies of the bonds formed during crystallisation. They introduced the concept of attachment energy defined as the bond energy released when a single building unit is integrated into the crystal. They postulated that the time required for the formation of a bond decreases with increasing bond energy. Therefore the displacement of a face will be proportional to the attachment energy. Though they could not provide a formal justification of the method, they found in practice that it gave rather good agreement with the observed morphology of several minerals.

In order to estimate the attachment energies they devised the concept of the periodic bond chain (PBC). A periodic bond chain is an uninterrupted chain of strong bonds which runs through the crystal structure and which are formed during the crystallisation process. Hartman and Perdok stressed the latter caveat. Only the bonds which form during crystallisation are significant. They devised a classification scheme for crystal faces based on the number of PBCs which lie parallel to them. Citing an analogy with Burton and Cabrera [26] for the terminology, Hartman and Perdok classified faces as flat, stepped or kinked. Kinked, or K-faces have no PBCs parallel to them. Stepped or S-faces, lie parallel to one PBC. Flat or F-faces lie parallel to at least two PBCs. According to Hartman and Perdok, the attachment energy for the respective classes of face increases in the order F,S,K. Therefore, from their original postulate they state that the advance velocities of crystal faces will increase in the same order. Therefore by classifying the faces of a crystal through the number of PBCs parallel to them, the growth rates and hence morphology of the crystal could be found. They argue on this basis that only the F-faces are significant on crystal forms and that, although under some circumstances the S-faces may appear with minor importance, K-faces are rapidly eliminated by wedging out and consequently never appear on a crystal form.

2.5 Classical Theories of Crystal Growth

The equilibrium shape of a crystal is almost never observed in practice, except in the case of very small crystals [27]. As Frank has pointed out [28], once a crystal exceeds a certain size the excess free energy associated with a deviation from the equilibrium shape becomes negligible compared to the supersaturation. Its shape will then be dictated by its kinetics of formation. The first "scientific" description of the kinetics and mechanism of the growth of crystals is attributed to Gibbs [12] who anticipated the later development of the theory. This description, although lucid, formed only a footnote in the work of Gibbs [12]. Gibbs' principle concern was thermodynamics and equilibrium. Since mechanism and kinetics is not the concern of thermodynamics it is unsurprising that Gibbs did not pursue the argument. Aside from contributions from Wulff and Curie [13], the theory of the kinetics of growth of crystals mainly developed during the first half of the twentieth century and is largely associated with the names Kossel, Stranski, Kaishew, Volmer, Frenkel, Becker and Döring. In the following discussion for the sake of brevity the findings of this group of authors will mainly be referred to collectively. A more comprehensive history of the development of the early classical theories is available in older textbooks, for example Strickland-Constable [10]. Also, a succinct and lucid account of the salient features of these ideas has been given by Frank [4]. The early theories were intimately related to general theories of nucleation and growth of phases such as the nucleation and growth of liquid droplets from supersaturated vapours. Given the thermodynamic formalism of Gibbs, these authors considered questions about the equilibrium population of nuclei of a second phase in a parent phase under given conditions as outlined in section 2.2.3. These authors also collectively considered the rates of growth of a new phase. In particular Becker and Döring [10] developed a formal "molecular" theory of nucleation in which nuclei were considered to be molecules in their own right and the addition of true molecules to the nuclei was a chemical reaction characterised by conventional reaction rates and equilibrium constants. For an introductory description of the theory see, Strickland-Constable [10], Markov [13] or Frank [29] . This theory proved to be a great success in predicting the nucleation of liquid droplets from supersaturated vapours. Having dealt with the formation of stable nuclei, the theories of growth of droplets, based on the accretion of molecules by collision with the nucleus, was similarly successful. For these models the kinetic theory was drawn upon for the collision frequency of vapour molecules with liquid droplets and the rate of growth was completely explained by mass transport to the growing nucleus.

2.5.1 The Kossel Crystal

The classical theory was less successful in predicting the rates of growth of crystals from the vapour phase however. Kossel in particular recognised that this could be explained if collision with the nucleus was not a sufficient condition for integration into the solid. To better illustrate the point, consider the collision of a vapour phase molecule with a liquid droplet. Due to the disordered structure of the liquid it is isotropic and homogeneous. Therefore the probability of a colliding molecule "sticking" to the droplet is effectively unity since no particular locations in the droplet are special. The growth rate is then simply obtained by calculating the number of collisions. Crystals however have an ordered structure which implies that some ordering of the incumbent molecules is necessary before they may be considered integrated into the crystal. In the case of a crystal then the "sticking" probability may be significantly less than unity. To assist in the description of such ideas Kossel [10] introduced the model crystal which bears his name. The Kossel crystal is a simple cubic lattice of cubic "molecules" which interact through nearest and second nearest neighbour bonds only. The nearest neighbour bonds are formed between molecules which share a cube face and second nearest neighbour bonds are formed between those which have an edge in common. The coordination number for molecules in a perfect Kossel crystal is 6 for nearest neighbour bonds and 12 for second nearest neighbour bonds. If the bond energy is ϕ_1 between nearest neighbour bonds and ϕ_2 between second nearest neighbour bonds then each molecule in the bulk has a bond energy of $6\phi_1 + 12\phi_2$. Note that according to this model the crystal binding energy, the work required to separate the molecules to infinity, is $(6\phi_1 + 12\phi_2)/2 = 3\phi_1 + 6\phi_2$; the factor 2 arising since each bond is shared between two molecules. This is actually none other than the enthalpy of sublimation of the crystal.

Kossel [10] identified several energetically unique sites on the surface of such a crystal, characterised by the number of unsaturated bonds for a molecule at these sites. These are shown in the illustration of an incomplete {001} face on a Kossel crystal, illustrated in figure 2.3. By counting the number of unsaturated first and second nearest neighbour bonds of each type the distinction between these sites is made clear. It should be noted that these unsaturated bonds are equivalent to the dangling bonds referred to in the discussion of the surface free energy and should be considered the origin of the macroscopic surface energy. It is possible to identify the following energetically unique sites:

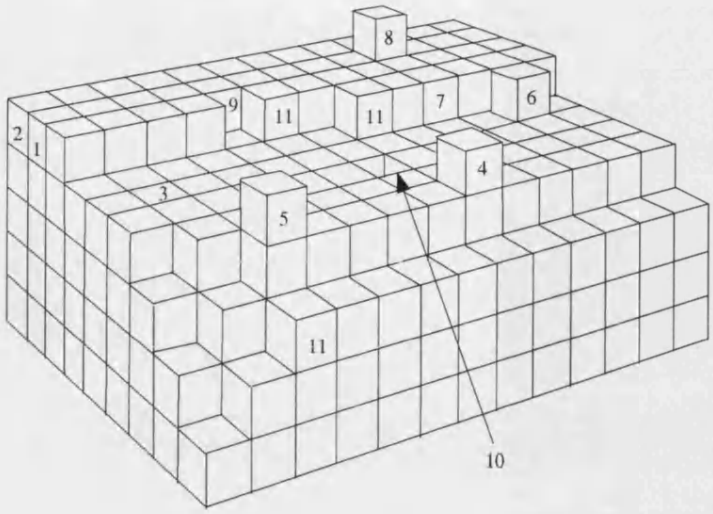

Figure 2.3: The Kossel crystal (Reproduced from Lewis [30])

1. completed edge,
2. completed corner,
3. completed surface,
4. incomplete edge,
5. incomplete corner,
6. step edge,
7. completed step,
8. adsorbed atom,
9. edge vacancy,
10. face vacancy,
11. half crystal position or kink.

Of the various sites shown in figure 2.3 the most important from the point of view of crystal growth are those labelled 11. Consideration of the number of unsaturated bonds at this type of site reveals that it has energy $3\phi_1 + 6\phi_2$, which is equal to the mean bond energy per molecule in the bulk. As a consequence this site is called the half crystal position, or by reference to its geometry on the surface, a kink site or kink. A consequence of the unsaturated bonds at a kink is that addition of a molecule to the site

does not lead to an increase in the number of unsaturated bonds at the surface. From a macroscopic viewpoint this is equivalent to having no increase in the surface free energy. As a consequence there is no energetic barrier to the addition of a molecule to a kink. Geometrically it can be seen that no new unsaturated bonds are created by addition at a kink site since the kink merely moves one position along on the step. It may also be readily seen that formation of any of the other labelled sites leads to a change in the number of unsaturated bonds. According to this model, molecules incorporated at a kink site become a part of the crystal proper since they then have the same mean bond energy as molecules in the crystal interior.

From the above discussion it may therefore be expected that the kink sites will play a crucial role in the growth process since this is the main point of entry of a molecule into the crystal. Molecules may also become incorporated at edge or face vacancy positions however due to the work of formation of such sites their concentration at the surface is expected to be much lower than that of kinks for which the work of formation is small. Consequently these sites play only a very minor role in crystal growth compared to kinks. The growth of a Kossel crystal then may be considered to be the process of addition of molecules to kink sites. The kinks then are the special sites which molecules must reach before they may join the crystal and their concentration is related to the sticking coefficient described above. Clearly, for a crystal with different faces with different kink concentrations, the growth rates of those faces will differ. Faces with high kink densities will be rapidly eliminated from the crystal form by "wedging out". For example the {111} faces of Kossel crystals are populated entirely by kink sites and will therefore be expected to be the fastest growing. During growth they will therefore rapidly disappear leaving {100} faces only on the crystal form. In the growth of macroscopic crystals then it is expected that the faces of lowest kink density and hence slowest growing will dominate the growth process. There are clear parallels here between this model of growth and the theory of Hartman and Perdok [22–25] discussed earlier. If only first nearest neighbours are considered, then the PBC directions are those which are shared between cube faces of the molecules. Only directions which contain exclusively cube faces are PBC directions. Directions in which some molecules are only joined by edges are not PBC directions. According to Hartman and Perdok [22–25], the {111} face, of which a portion is shown on the nearest corner of figure 2.3, is a kinked or K-face. The top and side faces of this crystal, the {100} family of faces, are F-faces. Any face misoriented to one of these faces but parallel to the others will be an S-face as it will contain steps. Note that when complete, the F-faces are singular, or close packed, in the Gibbs-Wulff-Curie sense.

Another feature of note is that the existence of kinks relies on the existence of surface steps. For a {100} surface of the Kossel crystal it can be seen that once a step is completed that a kink must form on the completed step before the next step layer can propagate. It is, however, reasonable to expect that a step will have an equilibrium concentration of kinks for entropic reasons and therefore that the propagation of the next step layer is not impeded. This point shall be returned to in a later section. However, once the surface layer is complete no step and hence kink remains for further growth and growth must cease until a new kink site becomes available. Gibbs [12] himself recognised that once a face was completed its surface free energy would become singular. The entropic formation of an entire step on a singular face is improbable and is unlikely to result in the formation of new steps.

2.5.2 Two-Dimensional Nucleation

The foregoing conclusion leads to an apparent paradox. If growth leads to the completion of the face and hence to the elimination of all kinks and steps, how can further growth proceed? The early workers considered that the only conceivable mechanism by which growth could continue would be if a small island of a new layer formed on top of the completed layer by a process of nucleation analogous to the process described for nucleation of a bulk phase in section 2.2.3. The analysis is similar to that for bulk nucleation with the dimensionality of the problem reduced. Therefore the surface free energy is replaced by the step free energy and the process is called two-dimensional nucleation. By analogy with the bulk case it is found that there exists a critical dimension for the equilibrium nucleus at a given supersaturation and that nuclei of size less than this dimension will tend to evaporate whilst those larger are stable and will tend to grow. Therefore, the formation of a new layer relies on the formation of a two-dimensional nucleus of critical size. Since this process is far slower than the growth of the layer itself it is rate determining for crystal growth. Calculations of the growth rate of crystals based on this model by Becker and Döring [10] suggested that crystals could not grow at an observable rate unless the supersaturation was of the order of 50%. This was contrary to the frequent observation that real crystals may grow at observable rates at supersaturations of the order of 1%. In particular, Volmer and Schultze [4] had measured the growth rates of iodine crystals from the vapour and had found a more or less linear relationship between growth rate and supersaturation down to supersaturations of approximately 1%.

The discrepancy between theory and experiment was, therefore, very large indeed. Burton, Cabrera and Frank [31] have shown that the observed growth rate actually exceeds that predicted by the model by a factor of e^{3600}. Burton [32] has remarked that this must be one of the largest recorded discrepancies between experiment and the best prevailing theory ever recorded in science and that a crystal growing at the rate predicted by two-dimensional nucleation would not change perceptibly over a length of time of the order of the known age of the universe! Clearly then, the two-dimensional nucleation model was inadequate and had to be revised. Burton, Cabrera and Frank [31] re-examined the assumptions about the shape of the two-dimensional nucleus in Becker and Döring's model and found a new expression for the equilibrium shape of the two-dimensional nucleus by considering the configurational entropy contribution due to kinks. However this correction was insufficient to reduce the error by any more than a few per-cent at best. A completely new idea was required to break the impasse. The problem was how could a repeatable step form and persist on a crystal surface without being eliminated by growth?

2.6 The Crystal Growth Model of Burton, Cabrera and Frank

The theoretical breakthrough that was required to break the impasse produced by the discrepancy between the experiments of Volmer and Schultze and the classical nucleation models came in 1949 with Frank's realisation that the growth of real crystals is intimately related to their defects. The earlier models described in section 2.5 were all models of the growth of perfect crystals. Frank realised that the problem of generating a repeatable step would be circumvented if the crystal contained a dislocation with a screw component terminating at a free surface. Frank realised that a screw dislocation would produce a step in the crystal surface which would not be eliminated by the completion of a layer because the dislocation would distort the entire crystal lattice into a single helicoidal layer. Such a step is illustrated in figure 2.2. This idea first found its way into print in the transactions of the 1949 meeting of the Faraday Society in Bristol [33] which was devoted to the study of crystal growth.

According to Frank's postulate, such a step contains kinks along its length and that

as a result of incorporation of molecules the step will advance with constant linear velocity. However, since it is regarded as immobile at the dislocation itself, the steps' advance here is impeded and the result is that the step winds up into a helicoidal spiral centred on the dislocation outcrop. Frank realised that the winding up of the spiral would be limited by the maximum step curvature allowed by the Gibbs-Thomson effect and that this would depend on the applied supersaturation. The maximum step curvature is greatest at the centre of the spiral and is related to the radius of a critical nucleus from the classical models. With these ideas the main obstacle to the explanation of the measured growth rates of crystals - the need to nucleate new layers on completed singular surfaces - was eliminated.

In 1951 Burton, Cabrera and Frank published their seminal paper [34] in which they developed the theory of crystal growth to take into account the role of screw dislocations. The importance of this paper to the science of crystal growth was enormous. The theory contained in this paper has come to be known as the BCF theory and it now occupies a central position in the theory of crystal growth. The BCF theory has been the subject of numerous in depth reviews [4, 5, 10, 35], however its importance warrants some discussion. In the following the general development of the theory will be outlined with the focus on the most important assumptions and results. The full mathematical theory is left out for the sake of brevity.

2.6.1 BCF Part 1: Movement of Steps on a Crystal Surface

In discussing the BCF theory it is important to note first that it is essentially a theory of growth from the vapour, though brief consideration of growth from solutions is given. The BCF paper itself is divided into four parts. The first part, attributed to Burton and Cabrera, deals with the rates of growth of crystals from the vapour. The objective is to obtain an analytical expression for the crystal growth rate normal to the surface, which is equivalent to the experimentally measured rate of advance of a face. The immediate presupposition is made that after a very short period of growth only close packed faces (F-faces in the Hartman-Perdok sense) will remain on the crystal and that the problem of growth is to obtain an expression for the rate of growth of these faces in terms of surface steps, which must be present on the surface if kinks are to be present. The first stage is to consider the rate of advance of a single isolated step due to exposure to a supersaturated vapour. Using the Kossel crystal model presented before, it is assumed that molecules adsorb on the surface from the vapour and that they are mobile on the

surface, i.e. that surface diffusion occurs. The molecules are considered to have a mean lifetime on the surface before they desorb and return to the vapour and that as a consequence they have a mean displacement, x_s. Also an estimate of the concentration of kinks along a step is obtained which a yields a value, x_0, for the mean kink separation. From reasonable assumptions and estimates, it is found that $x_s \gg x_0$. This result is significant to the theory because it allows the step to be regarded as a continuous line sink for molecules. As a corollary it also implies that the rate of step advance will be independent of the orientation because there will be very many more kinks than growth units so that no particular step orientation will be retarded due to a low kink concentration. Thus, the surface has circular symmetry with respect to the advance velocity of steps.

Having obtained this result, a classical diffusion equation is set up for diffusion into the step edge. The boundary conditions of which assume that molecules approaching the step from both sides (i.e. either the upper or lower terraces) have equal probability of entering the crystal. It is assumed that the number of adsorbed molecules increases with increasing supersaturation and hence that the surface is supersaturated with adatoms. It is also assumed that the relaxation time for entry into the kink is very short compared to the mean adsorption lifetime, however a retardation factor, β, is introduced at this stage to accommodate the possibility that the relaxation time may be longer due to steric, conformational and orientation considerations. It is also pointed out here that if $x_0 \gg x_s$ the model will still hold if diffusion along the step edge is permitted. With these assumptions the diffusion equation is solved and an expression for the rate of advance of the step is obtained. Using this result, the rate of advance of an equidistant parallel train of steps with separation y_0 is next obtained. The significant result here is that when the diffusion fields of the steps overlap, adjacent steps must compete for growth units and so the advance velocity of the steps of the group is less than that for an isolated step. Clearly, the amount of overlap and hence competition is a function of the ratio of y_0/x_s.

The next stage in obtaining the normal rate of growth is to consider the rate of growth of small closed step loops. At this point the results of the earlier theory of growth of perfect crystals is introduced [31], in particular the concept of the critical nucleus. It is pointed out here that the shape of the critical nucleus is exactly defined and that its step will have the same kink concentration at the same orientation as an infinite step. However, it is pointed out that if the nucleus exceeds the critical size then it will grow and that its shape will then be dictated by the relative velocities of different orientations,

rather than thermodynamic considerations. When the condition $x_s \gg x_0$ is met then, as discussed earlier, no particular orientation is favoured and the advance velocity of the step will be independent of orientation. Notable results here are that the critical nucleus will have a corresponding critical radius, ρ_c, which is given by,

$$\rho_c = \frac{\gamma_s a}{kT \ln \alpha} \tag{2.13}$$

where γ_s is the free energy of a molecule in the step, a is the linear dimension of the molecule, k is Boltzmann's constant, T is the absolute temperature and α is the supersaturation ratio[7], p/p_0. Equation 2.13 is a form of the Gibbs-Thomson equation for a two-dimensional island and is obtained by a similar argument to that of equation 2.11. With suitable assumptions about the diffusion length with respect to the critical radius the following expression for the dependence of the advance velocity, v, on the radius, ρ, of a closed step is obtained,

$$v(\rho) = v_\infty(1 - \rho_c/\rho) \tag{2.14}$$

where v_∞ is the velocity of an infinite straight step. Following this an expression is obtained for the rate of advance of a sequence of concentric circular step loops by solution of the appropriate diffusion equation.

2.6.2 BCF Part 2: Rates of Growth of a Crystal Surface

Having obtained expressions for the rate of advance of single steps, parallel trains of steps and concentric step loops without a consideration of their origin, attention is turned to the problem of the growth rate of a crystal surface as a whole. Inevitably this leads to the problem of the origin of the steps. The next section of BCF is attributed to Frank, who pursues the quantitative analysis of the earlier qualitative discussion of a step formed by a screw dislocation winding up into a spiral in light of the analytical results of the preceding section. BCF stresses that the term screw dislocation is used as a matter of convenience to mean any dislocation which possesses a screw component normal to the surface[8].The key to the description is equation 2.14, from which it can be seen that when the radius of curvature of the step reaches ρ_c, then it will cease

[7]This is analogous to the supersaturation ratio of equation 2.7 however it is defined in terms of the equilibrium (p_0) and actual (p) partial pressures of the vapour.

[8]In fact subsequent developments have shown that even dislocations with no screw component normal to the surface in question can nonetheless initiate growth in some circumstances.

advancing. When this curvature is reached at the spiral centre then the spiral will cease winding up and will rotate with a constant angular velocity, ω, and a stationary shape. Due to the circular symmetry of the advance velocity of steps when the condition $x_s \gg x_0$ is met then this shape will be circular. A differential equation for the spiral shape was obtained and solved by approximating the spiral as an Archimedean spiral. Only approximate solutions were given, however this served to illustrate the essential idea. This analysis leads to the concept of a spiral *activity* which is defined as the number of spiral turns per second, $\omega/2\pi$. From this it is obvious that the normal growth rate R of the growth pyramid or *hillock* formed by the spiral will be,

$$R = \frac{\omega a}{2\pi} = \frac{n_0 \Omega v_\infty}{4\pi \rho_c} \tag{2.15}$$

where $a = n_0\Omega$ is the height of the step, n_0 being the number of molecules per unit area of surface, Ω the volume occupied by a molecule. The following result is also obtained,

$$y_0 = 4\pi\rho_c. \tag{2.16}$$

That is, the width of the terraces of the spiral are proportional to the radius of a critical nucleus. Before arriving at the final expression for the growth rate BCF digress to consider the interactions of groups of dislocations and their concomitant growth spirals from a topological viewpoint. Some of the key results are stated here briefly. If two dislocations of opposite sign co-exist on the surface then a step will form between them. If the separation of their emergent points is less than $2\rho_c$ then the step will not grow freely because its advance will cease when its curvature reaches that of the critical nucleus. If the step separation exceeds $2\rho_c$ however then closed step loops will form before the critical radius is reached, hence the dislocation pair will emit closed loops of steps. It should be noted that the activity of such a pair is dependent on the supersaturation. If the supersaturation should increase then ρ_c will become smaller and an inactive pair may become active. Note also how the activity of an active pair is approximately equal to that of a single dislocation.

The *strength*, s, of a growth source is defined as the excess of screw dislocations of one sign over screw dislocations of opposite sign in a *cooperating* group[9]. In the above example, the strength is zero since there is no excess of either type of dislocation. A single isolated dislocation of either sign clearly has a strength of unity. In the case of dislocation groups of like sign the situation becomes more complex.

[9]This is not the same as the vector sum of the Burgers vectors.

If a pair of dislocations of like sign co-exist on a surface then the strength, and hence the activity, of the pair will be dependent on the separation of their emergency points. If the separation exceeds $2\pi\rho_c$ (i.e. half the separation between successive spiral turns, y_0 from equation 2.16) then the steps emitted from the respective sources will merge together and the activity will be essentially the same as that of a single source. In which case the dislocations act independently as separate sources of strength 1 and they are said to be *non-cooperating*. If however their separation is less than $2\pi\rho_c$ then the dislocations will cooperate to form a double spiral. Because this source will emit more steps per unit of time, the activity will be correspondingly higher than that of a single source. In this case, since the two dislocations are cooperating and there is an excess of two dislocations of one sign then the source strength is 2. The concept is readily extended to groups of more than two dislocations. Figure 2.4 shows a single, double and triple spiral respectively. If there is a separation L between the dislocations of like sign in a multiple source then it is readily seen that the this adds an additional time to the rotation of the spiral due to the extra time required for the steps to execute a circuit around the group. Expressions for this are given by BCF but are not reproduced here because they have been subsequently modified in view of later developments [36] and extended [37]. In general however, the activity of a group of dislocations will be ε times that of a single dislocation depending on the strength and separation of the source and this may be many times that of a single dislocation. It should also be noted that the strength of a dislocation group is a discontinuous function of supersaturation since the condition for spirals to cooperate is defined by ρ_c, which is itself an inverse function of the natural logarithm of the supersaturation ratio (equation 2.13). Therefore dislocation groups which are cooperating at low supersaturation may abruptly cease cooperating if the supersaturation increases because of the reduction in size of the critical nucleus, causing the dislocation separation to exceed the condition for cooperation. Hence, during crystal growth the strength and consequently activity of sources may be expected to change abruptly. As a corollary to this, since dislocations are themselves mobile, motion of dislocations may cause their separations to change sufficiently to modify source strength and activity which will similarly result in abrupt changes in growth rate. The motion of dislocations was however disregarded by BCF.

Having considered the nature of the sources and obtained expressions for the rate of advance of a spiral step, BCF then substitutes the relevant expressions into a single expression for the rate of normal growth, R, from the vapour. Though the original theory gives the full expression in terms of the molecular parameters, including the molecular dimensions which define the height of a step, the more common parameterised version

Figure 2.4: Schematic growth spirals formed by screw dislocations. Left, a spiral formed by a single unit dislocation. Middle, a double spiral formed by a dislocation of strength 2. Right, a triple spiral formed by co-operation between a double and a single dislocation.

is given here for brevity and clarity of discussion. In any case, in anticipation of the later development of the theory, a similar though generalised expression encompassing the case of growth from solution is presented in a subsequent section in which the full molecular parameters are detailed.

$$R = C\frac{\sigma^2}{\sigma_1}\tanh\frac{\sigma_1}{\sigma} \tag{2.17}$$

where σ is the relative supersaturation defined in 2.6, C is a rate constant and σ_1 is a critical supersaturation. Inspection of 2.17 reveals that the critical supersaturation indicates a transition between two kinds of growth dependence. For $\sigma \ll \sigma_1$, the growth rate has a parabolic dependence on σ, i.e. $R = C'\sigma^2$, where $C' = C/\sigma_1$. For $\sigma \gg \sigma_1$ the dependence is linear, $R = C\sigma$. The interpretation of this transition is that, at low supersaturation, the step separation y_0 is very much larger than x_s and therefore not every adatom can reach a step and hence a kink, before returning to the vapour. As the supersaturation increases the inter-step separation y_0 decreases and the adatom concentration increases resulting in the parabolic dependence. At higher supersaturations when the steps become closer than $2x_s$, their diffusion fields now overlap and so they compete for growth units. Also, now all adatoms can reach a step before desorption and the growth rate becomes insensitive to increases in step density as a result so the dependence becomes linear. There are a number of corollaries to this law to accommodate different situations such as the source strength, the condition $x_0 \gg x_s$ and a large retardation factor for entry to the kink; however these factors all simply lead to different values for the parameters C and σ_1, the basic functional relationship is unchanged. The relationship between the slope of the spiral p, the step spacing y_0 and the angle θ is

$$p = \tan\theta = h/y_0, \tag{2.18}$$

where h is the step height. This relationship is depicted in figure 2.5 along with the relationship between the normal growth rate R and the advance velocity of the step v

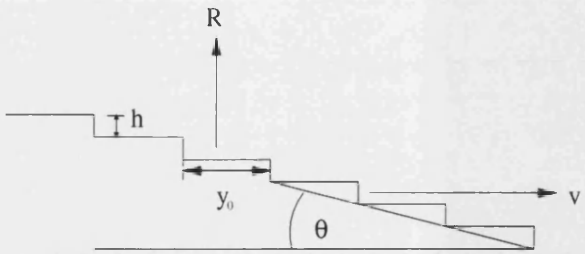

Figure 2.5: Relationship between the parameters for a step train on a growth hillock (reproduced from Markov [13])

for which it should be readily apparent that the following relationship holds.

$$R = pv. \tag{2.19}$$

Subsequent comparison of this model with a number of experimental measurements gave good agreement, indicating that the model was successful in predicting the rates of growth of real (i.e. defective) crystals from the vapour.

At this point growth from solution was briefly considered. BCF assumed that the model presented above for growth from the vapour was essentially unchanged for growth from solution. The main difference was considered to be that the diffusion rates to the kinks, whether through the solution, over the surface or in the edge of the step; were very much smaller than on the free surface of the crystal and their relative importances were less clearly defined. In order to simplify the analysis BCF considered only the diffusion flux direct to the kinks from the solution. The diffusion equation which they set up for this situation was of a hemispherical diffusion field centred on the step within an un-stirred boundary layer of thickness δ in contact with the bulk stirred solution with supersaturation σ. Without entering into excessive detail, a similar functional dependence as that of equation 2.17 is obtained, however some of the values which make up the parameters are now different; for example the definition of σ_1 now contains δ as a factor. In particular however both parabolic and linear growth laws result with a critical supersaturation for the transition. The BCF solution model is generally referred to as BCF volume diffusion and has been considered at some length [5]. The sentiment expressed by BCF with respect to the solution case is distinctly less certain of some of the assumptions than the case of growth from the vapour.

2.6.3 BCF Parts 3 and 4: Development

Having obtained expressions for the growth rate in terms of a pyramid or hillock formed by a dislocation, BCF went on to re-examine some of the presuppositions and assumptions of the earlier sections through the study of the equilibrium structure of the crystal surface. These arguments are statistical mechanical in character and produced several new results in the statistical mechanics of surfaces themselves. BCF is in fact seminal for these sections alone. As this would imply, the arguments are detailed and so only the results which are key to the present study are summarised here. A presupposition (based on earlier work by Burton and Cabrera [26]) of the earlier sections was that steps would always possess kinks at any finite temperature. This was re-examined and the free energy of a step was also obtained. The conclusion was found to hold true, that is at $T > 0$ a step always contains a high concentration of kinks due to their low work of formation (since few bonds need be broken to form them) and the resulting contribution to the configurational entropy of the step. This result is of great significance to the earlier section because it means that if a step is present on the surface, then there will be kinks in thermal equilibrium at which molecules may join the crystal. This means that a step is never smooth and can never become singular in the way that a face can. Otherwise on completion of a step, a "one-dimensional" nucleation energy barrier would have to be surmounted. In other words, a step is always rough. The problem of crystal growth then was one of explaining the existence, and persistence, of steps. Frank had already shown that a screw dislocation could do this. The question was, is the screw dislocation actually essential to the argument[10]?

In earlier work Frenkel [38] had extended the concept of thermal roughening to the formation of steps in a singular surface to explain the persistence of steps, though Burton and Cabrera [26] had shown this conclusion to only be true at temperatures near the melting point. This was re-examined in BCF and it was found by the application of statistical mechanical methods that below a certain temperature, steps could not be created thermally in a singular surface. However it was found that there exists a critical temperature, T_c, above which the surface becomes rough; that is, steps are formed spontaneously by thermal fluctuations and the surface becomes non-singular. This is actually a phase transition of the surface and T_c is the transition temperature. Because of the change in character of the surface it is called a roughening transition and the phenomenon is termed surface roughening. It was found in general that for a free surface

[10]It should be borne in mind that the understanding of dislocations themselves was in its infancy at this time. The success of BCF was actually instrumental in their full acceptance.

in equilibrium with the vapour, that T_c was close to the melting point or even higher. The roughening transition is an example of a critical phenomenon. At T_c the free energy of the step vanishes and steps may therefore be created without restriction. This is analogous to the disappearance of the vapour-liquid phase boundary at the critical point of a pure substance where the distinction between liquid and vapour disappears. BCF concluded therefore that for growth below T_c, at low supersaturations and low temperatures with respect to the melting point, that the growth of crystals could only be explained by assuming that they were not perfect and, in particular, that they must contain screw dislocations. On the other hand, if growth occurs at $T > T_c$, then their is no restriction on growth. The growth rate may therefore reach a limiting value based on the collision frequency. This is called the Wilson-Frenkel maximum growth law [39]. Because singularities in the surface free energy disappear above T_c, facetted surfaces are not necessarily favoured and un-facetted shapes may develop. For the case of a crystal growing from its melt, the surface is more likely to be rough, hence un-facetted growth is more likely to occur. Such un-facetted growth leads to the formation of cellular interfaces and dendrites, where matters of mass and heat transport dominate the crystal morphology.

2.7 Developments Since BCF

The breakthrough in the understanding of crystal growth provided by the BCF theory led to a subsequent explosion of interest in the subject by theorists and experimentalists alike. The experimentalists set out to find new evidence of spiral patterns on real crystal surfaces and to reinterpret old observations of such. They also sought more accurate measurements of crystal growth rates with which to test the predictions of BCF. These experimental developments will be discussed further in the following chapter. For the theorists, taking the BCF theory as a starting point and extending the results became the priority. Like the BCF paper itself much of this effort divided itself along the lines of the kinetic aspects of step dynamics and the statistical mechanical aspects of crystal surfaces. Many of the later developments have been the result of questioning the assumptions and presuppositions of the BCF model, particularly those of the mode of mass transport. In short, the BCF theory is not the final word in crystal growth, it was more of a beginning.

2.7.1 Two-Dimensional Nucleation Revisited

Despite the success of BCF in demonstrating the importance of dislocations for crystal growth, the earlier two-dimensional nucleation models did not disappear. They were after all accepted as valid for growth at high supersaturations. These models continue to be of importance, particularly for growth from melts, and theoretical work has continued on these models. There are now three distinct variations on the two-dimensional nucleation theme. These are the mononuclear, polynuclear and multi-level models. In the first model, which is essentially the original model due to Becker and Döring [10], it is considered that the formation of a critical nucleus is much slower than the propagation of a step. Therefore, immediately that a single nucleus reaches critical size, it rapidly grows to cover the entire surface, leaving a singular surface once more, ready for the cycle to repeat. If, however, formation of a critical nucleus can occur on the timescale that it takes an island to grow to fill the surface then several critical nuclei may form on the surface at one time, in which case all will grow until their growth fronts merge and they cover the face. This is the polynuclear model. Finally, if the timescale of formation of a critical nucleus is less than the time to cover the face then new nuclei may form on existing islands before they have filled the face. This is the multi-level or "birth and spread" model developed by Ohara and Reid [5]. As a final note on two-dimensional nucleation, if the critical dimension of a nucleus becomes of the order of a small cluster of molecules then a very large population of critical nuclei may form on a singular surface. The surface becomes rough, analogous to a surface above T_c, though for kinetic rather than thermodynamic reasons. For this reason the phenomenon is known as *kinetic roughening* and is important in molecular beam epitaxial (MBE) growth (see Markov [13]).

2.7.2 Spiral Shape

In the section on the BCF analysis of the growth spiral it was stated that the solution of the differential equation for the steady state spiral was only obtained approximately as an Archimedean spiral. Subsequently, Cabrera and Levine [36] obtained a numerical solution to the equation. This resulted in a modification of the dependence of the spiral spacing, y_0, on the radius of the critical nucleus, approximated in BCF by equation 2.16. The new expression was,

$$y_0 = 19\rho_c. \tag{2.20}$$

Consequently, any of the relationships from BCF derived from the original expression (equation 2.16) may be modified to account for this development. For example the threshold separation of dislocations for the cooperation of growth spirals, $2\pi\rho_c$, becomes $19\rho_c/2$. Frank [40] had shown previously that the core of a dislocation may be hollow if the elastic strain energy at the dislocation core exceeded the surface free energy of the extra surface required to create the hollow core. At equilibrium the elastic strain energy due to the core is balanced by the surface free energy of the core surface. Cabrera and Levine also accommodated the elastic strain energy into their model of the spiral shape and used this in an analysis of etch pit formation.

Further analysis of the spiral shape as a function of supersaturation by Cabrera and Coleman [41] revealed the existence of a so-called *back stress effect.* The back stress effect arises due to the lower supersaturation experienced at the centre of the spiral due to the diffusion field of the first turn of the spiral. The step acts as a sink for growth units and depletes the surface of growth units in the immediate vicinity, effectively decreasing local supersaturation. Because the curvature at the centre of the spiral dictates the curvature of the rest of the spiral, the back stress effect can result in a deviation from equation 2.20. Furthermore, as the bulk supersaturation is increased the spiral becomes more tightly wound still, and the back stress effect becomes increasingly significant. Thus, there is an inherent feedback effect opposing the tendency of the spiral to wind up (hence "back stress"). One significance of the back stress effect is that it ultimately restricts how tightly a spiral can wind and hence how steep a vicinal hillock can become. Also, the effect may lead to a more gradual transition between the parabolic growth law regime and the linear growth law regime and so may be significant when interpreting (R,σ) curves. These and similar effects on (R,σ) curves have been considered in detail by Gilmer and Bennema [35].

Subsequently attempts have been made to extend the theory of the steady state growth spiral to the more general case of the anisotropic or polygonised growth spiral. An anisotropic growth spiral forms when the step velocity is anisotropic. This may arise because of anisotropy in the step free energy, the retardation factor β, or because of an orientation dependence in the kink density, x_0, such that at certain orientations the condition $x_s \gg x_0$ is not met. In such circumstances then the steps will tend to follow the underlying crystallographic orientations. These effects are dependent on the underlying crystal structure. Budevski *et al.* [42] considered the case of the polygonised spiral. They considered that the spiral is formed by intersecting straight step sections forming a polygonal spiral. In their model, step sections are considered sessile until their length

exceeds $2\rho_c$ after which they propagate with the velocity of an infinite step, independent of orientation. Solutions of the resulting differential equation showed that with these considerations, a shape preserving steady-state spiral developed. Furthermore, the relationship of equation 2.20 was also found to hold approximately true for the polygonal case also. In subsequent work on the mathematics of steady state spirals, Müller-Krumbhaar *et al.* [43] reported that their work disagreed with this result and made some suggestions for the discrepancy. Theoretical and experimental developments in the shapes of growth spirals have been reviewed by Sunagawa and Bennema [44]. In such analyses the relative roles of volume, surface and edge diffusion are often prominent in the assumptions. In general, the spiral treated by BCF and solved by Cabrera and Levine [36] is only one of a family of steady-state shape preserving solutions of the differential equation. The problem of finding such solutions has attracted theoreticians and mathematicians and has become something of a subject in its own right [8, 45, 46].

2.7.3 Kinematic Theories of Crystal Growth

The so called kinematic models of crystal growth developed from theoretical interest in transient effects, stability of step trains and attempts to explain the presence of macroscopically visible spiral steps on crystal surfaces. The latter had been reported by numerous workers and further discussion of these experimental observations will be made in section 3.2. Such steps were termed macrosteps and most workers accepted them at the time as evidence of the validity of the spiral growth model of BCF [47]. However others dismissed them as mere experimental artefacts because the growth spirals described by BCF should be invisible optically since the monomolecular step heights are well below the resolution of the optical microscope. A good account of the points and counter points made by supporters of each argument can be found in Gomer and Smith [48].

The BCF spiral growth theory deals only with the steady state of a crystal growing at constant rate under the action of a growth spiral rotating with constant angular velocity. The transient effects due to fluctuations in supersaturation, for example, were not considered. The later work of Cabrera and Levine [36] cited above also dealt entirely with the steady state growth spiral. The question of the stability of this steady state naturally arises [49]. In other words, how stable is the steady state with respect to a small perturbation? For example, if for some reason, an individual step in a step

train is impeded or accelerates, is there an effective force restoring the steady state or does a new state develop? In this case the separation of this step from one of its neighbours will decrease. If the two steps become sufficiently close that their diffusion fields overlap then both steps will compete for the same growth units and the pair will move more slowly than fundamental steps. The limiting case is for both steps to join together to form a single step of height $2h$ moving with velocity $v/2$. Because of the slowing of the step pair, other steps will now catch up with the pair and since they cannot overtake the pair, they may join up to form a step of height $3h$ and so on. This is a simple description of the formation of a macroscopic step or macrostep. Note that the vertical leading face of the macrostep may be a singular crystallographic face itself and that consequently dislocations may emerge on this face or two-dimensional nucleation may occur. Cabrera [48] has suggested that this may indicate a mechanism for the formation of stacking faults in crystals. This mechanism for the formation of macrosteps helps to explain the existence and origin of optically observable steps.

The kinematic theory of crystal growth introduced simultaneously by Frank [50] and Cabrera and Vermilyea [51], was the first to deal with the question of transients. The treatments of these respective authors is sufficiently similar to regard their models as the same. The model is kinematic because the details of the source and individual steps are neglected. Instead, to model transient behaviour the crystal surface is considered to be continuous and its elevation z above a singular reference plane to be a function $z = z(x,y,t)$, where x and y are the coordinates of the reference plane and t is the time. From this equation, its derivatives and suitable assumptions and conditions; a differential equation was formulated, the solution of which gives the spatio-temporal dependence of the surface profile. The assumptions are that the source strength is a function of time only and that the growth rate away from the source is a function of the local slope only. The condition is that steps are always conserved. The solutions illustrate the possibility of the existence of so called kinematic waves. Kinematic waves are regions of constant surface profile which migrate along the surface as a function of time. Frank pointed out that a kinematic wave does not always consist of the same steps nor does it move with the same velocity as the steps themselves. Frank [50] and Cabrera-Vermilyea [51] analysed the motion of the fundamental steps forming kinematic waves by analogy of the bunching of cars on a highway by application of the "traffic flow theory". This analogy is applicable to the situation of steps on a crystal surface because the problem is effectively one-dimensional. Since steps cannot overtake one another, the situation is analogous to cars which are forbidden from overtaking. The description of step motion in kinematic waves is as follows.

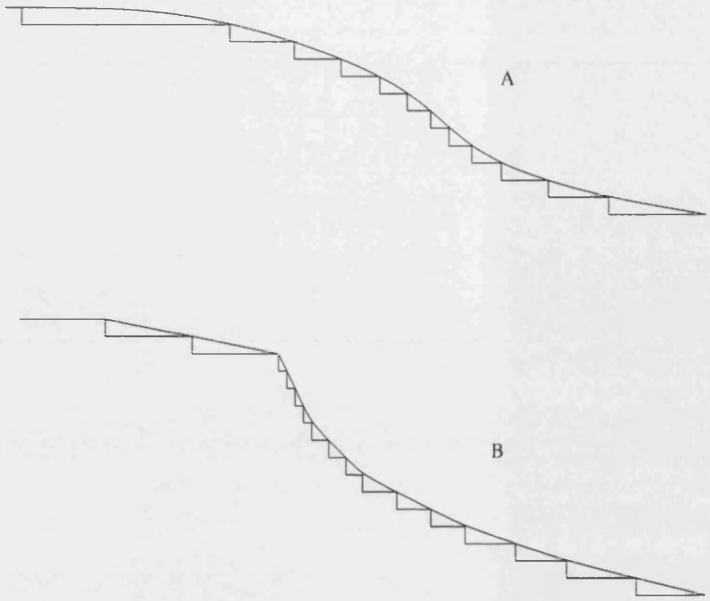

Figure 2.6: Schematic of A) a step kinematic wave and B) a step shockwave (reproduced from Markov [13])

If in some locality of a step train on a crystal surface, a bunch of steps occurs which results in a steeper local slope and narrower terraces than the average, then these steps will compete for growth units and the bunch will consequently move more slowly than equidistant steps. Consequently steps catching up from behind will be impeded by the step bunch and will become part of the bunch. However the steps at the front of the bunch will be less impeded and will therefore accelerate away, leaving the bunch behind. A steady state can therefore develop in which the rate of steps leaving the bunch from the front is equal to the rate of steps joining the bunch from the back and a wave of constant surface profile will propagate along the surface, without the formation of a true macrostep. If large enough these kinematic waves may also be observable optically and thus offer an alternative explanation of visible steps. It is also possible that a discontinuity may develop in the profile of the kinematic wave, resulting in a step shockwave. Frank showed that the formation of shockwaves may be regarded as the result of collisions between kinematic waves.

According to Cabrera and Coleman [41], the significance of the kinematic theory of crystal growth is that most experimental measurements of crystal growth take place under transient conditions since the time required for a genuine steady state to develop is long. A similar sentiment was expressed by Cabrera and Vermilyea [51] themselves, who argued that many of the peculiarities of crystal growth would only be explained

by the kinematic theory.

2.7.4 Impurities

Since all real systems are impure, the role of impurities in crystal growth is clearly relevant. Many empirical observations prior to the publication of BCF had shown that often very small quantities of an impurity could play a very significant role during the crystallisation, in some cases effecting profound habit modification. A comprehensive survey of observations prior to and contemporary with BCF has been made by Buckley [48]. Impurities in crystal growth environments may produce significant modifications to the thermodynamic state of the system itself. Familiar examples of colligative (concentration dependent) effects in bulk thermodynamics are depression of the freezing point and elevation of the boiling point. In solutions, impurities can significantly alter the structure of the solution, for example through the formation of complexes with solute molecules. The thermodynamics of an impurity species on the surfaces and in the bulk of the crystal is also of great importance in this regard. For this reason a rigorous description requires the consideration of adsorption equilibria and distribution coefficients. For example, in ionic crystals, charge conservation must be maintained which may result in the formation of compensating vacancies in the bulk solid. A lattice mismatched impurity may also impart considerable strain energy to the crystal with consequences for crystal growth through interactions with dislocations for example. The body of knowledge pertaining to the role of impurities in crystal growth is very large and only a short introduction is possible here. For further discussion and examples see Chernov [9]. Usually however, in discussions of the role of impurities on crystal growth, only their effects on the kinetics of growth in the context of the BCF model and its extensions are considered. The remainder of the discussion of impurities will focus on these general mechanisms.

The role of impurities was omitted from the BCF theory. However its authors did acknowledge their role and the formalism of BCF gave a basis for the development of theories of impurities. There are a number of ways in which impurities can conceivably affect the growth of low index crystal faces in the context of BCF. Perhaps the most obvious mechanism is their potential for adsorption at kink sites, blocking the integration of further molecules. Clearly, due to the central importance of kink sites for crystal growth, if rendered non-viable by impurities then the crystal growth rate must necessarily be affected. In effect the inter-kink spacing, x_s, along the step

is increased. This will typically lead to increased polygonisation of the growth spiral. Perhaps more subtle is the effect on the step free energy due to the adsorption of impurities. This reduction arises because of the configurational entropy associated with the adsorption of a second species at the step. In any of the aforementioned processes in which the step free energy plays a role, for example two-dimensional nucleation, the presence of impurities may cause substantial changes; even to the extent of completely changing the character of a face altogether. For example, if the step free energy is reduced significantly, the energy barrier to two-dimensional nucleation may become sufficiently small that kinetic roughening of the surface occurs. For spiral growth, the effect of such an impurity will be to increase the slope of the vicinal hillock due to the dependency of step spacing on the radius of the critical nucleus which will be reduced. In both of these cases the role of the impurity is to increase the rate of growth.

Another mechanism for the action of impurities is their adsorption on the terraces between steps, introduced by Cabrera and Vermilyea [51]. If impurity molecules are adsorbed on the terraces between steps then it is likely that the approaching step will be pinned back when it encounters an adsorbed impurity molecule, thus retarding its progress. Unimpeded segments of step between the pinned back points will continue to propagate forward, however they will develop a curvature as they bow out around the impurity pinned points[11].

Ultimately the maximum possible radius of curvature, ρ_c, will be reached as prescribed by the Gibbs-Thomson effect and the step's advance will be arrested. If the separation of impurities in the adsorbed "fence" is less than $2\rho_c$ then the step will be completely arrested. Clearly due to the supersaturation dependence on the maximum curvature, this effect is most severe at low supersaturations, where even wide spacings of impurities may be sufficient to completely arrest growth. Thus, the effects of impurities in inhibiting growth are greater at low supersaturation. This leads to the formation of a *dead zone*, which is a finite range of supersaturation within which the crystal will not grow at all, despite immersion in a supersaturated medium. In order to breach the impurity fence the impurity adatoms must either desorb into the mother phase, be incorporated into the crystal or be displaced, either forwards onto the same terrace or upwards onto the upper terrace. Cabrera and Vermilyea [51] used this concept in their formulation of the kinematic theory. They considered an impurity which forms an adsorbed layer on the terraces between the steps of a crystal surface growing layer-wise.

[11]This is conceptually similar to Orowans' [15] mechanism of impedance of dislocation glide within the bulk of the crystal

They considered that a certain amount of time was necessary for the impurity adatoms to reach their equilibrium concentration on the terrace. Clearly, the period allowed for adatom adsorption is related to the velocity and the separation of the steps since these define the period of time for which a given area of terrace is exposed to the vapour or solution. For the same step spacing, if steps are moving quickly then less time is permitted for the adatoms to reach equilibrium concentration before they are either buried or displaced than is the case for slow moving steps. If now, the impurity adatoms pin back the steps as described above then the step will move more slowly still, in turn allowing even more time for the adatom concentration to increase and so on. So it may be seen that a positive feedback mechanism comes into play in which slow moving steps are impeded more than fast ones. For steps moving with the same velocity, wide step spacings will allow more time for adsorption and hence will be more impeded than narrow step spacings.

Returning now to the traffic flow model of kinematic waves, it is seen that if a region of surface has greater local slope and hence, narrower terraces than the average; then the steps of this region will be less impeded and will move with higher velocity than the steps with wide terraces. The result is a kinematic wave the velocity of which exceeds the mean velocity of the steps themselves. Phenomenologically, steps in front of the wave will be caught up by the faster moving steps of the wave, steps behind the wave will be left behind. Steps therefore briefly become a part of the wave before being left behind.

More recently, Kubota and Mullin [52] have proposed a new kinetic model for crystal growth in the presence of impurities which relates step velocities to the adsorption isotherm of the impurities explicitly. An impurity effectiveness factor is introduced and the Cabrera-Vermilyea model is invoked to explain the supersaturation dependence. The model and extensions have recently been successfully applied to the interpretation of experimental data [53].

2.7.5 Crystal Growth from Solutions

The BCF theory of crystal growth is principally a theory of crystal growth from the vapour phase in which it is found that surface diffusion plays an essential role. The treatment of growth from solution in BCF, described briefly in section 2.6.2, is comparatively cursory. Several variants of the volume diffusion model have been published.

The various models have been critically reviewed by Ohara and Reid [5].

Surface Diffusion and Solution Growth

Perhaps unfortunately, the results of the BCF surface diffusion model and the volume diffusion models predict similar (R,σ) dependencies. This made it impossible to distinguish one growth mechanism from another on the basis of measured (R,σ) curves since any of these models could be made to fit the data by selection of suitable numerical values for the parameters. For a discussion of this point see Bennema [54, 55]. Bennema [56], having measured growth rates of a number of compounds from aqueous solution, subsequently argued that surface diffusion had to be invoked in order to explain the measured (R,σ) dependencies. In order to introduce the concept of surface diffusion for crystal growth from solution, Bennema introduced concepts from Eyring's formalism of chemical kinetics to the case of crystal growth. In particular, Bennema gave an explicit description of the steps involved in the integration of a molecule into the crystal from the solution. In Bennema's model, for a growth unit to be incorporated into a crystal (i.e. be adsorbed at a kink site) it must first become partially desolvated, it may then either integrate directly into a likewise desolvated kink site by volume diffusion through the stagnant layer or may adsorb onto the terraces, remaining partially solvated. When adsorbed on the surface it may make surface diffusional jumps on the terrace. If the growth unit reaches a desolvated kink site then it may fully desolvate and become incorporated into the crystal. Alternatively further partial desolvation steps may occur if the molecule becomes adsorbed at the step edge, where diffusion in the step edge may occur. Bennema attributed an activation free energy and a corresponding relaxation time to each of these processes in common with Eyring. Bennema's model is in fact a generalised model because by selection of the activation free energy barriers for each of the processes involved, the volume diffusion model is included as a special case. On this basis Bennema [56] argued that the surface diffusion model was the most general, the volume diffusion models being special cases with $x_s = 0$. When surface adsorption and diffusion are admitted, desolvation of the growth unit can occur in steps with individual activation energy barriers which are small in comparison to the single activation energy barrier which must be surmounted in the volume diffusion models. Bennema therefore concluded that growth by surface diffusion is energetically favourable and hence that surface diffusion must be an important mass transport mechanism for growth from solution as well as from the vapour. He cites kinetic data and polygonisation of spirals in support of this. In spite of these developments there

is still much debate over the relative importance of each mass transport mechanism. Bennema's modified expression for the normal growth rate is,

$$R = \beta c_0 \Omega \left[\frac{kT}{h} \Lambda N_0 \exp\left(\frac{-\Delta G_{deh}}{kT}\right)\right] \frac{\sigma^2}{\sigma_1} \tanh\frac{\sigma_1}{\sigma} \tag{2.21}$$

where β is the retardation factor, c_0 is the equilibrium solution concentration, h is Planck's constant, Λ is the thickness of the adsorption layer, N_0 is the number of growth units in solution per unit volume, ΔG_{deh} is the activation free energy for entering the adsorption layer. Comparison of equation 2.21 with 2.17 reveals how the rate constant C in the former equation is interpreted by Bennema. The critical supersaturation, σ_1, is given by,

$$\sigma_1 = \frac{9.5}{s} \frac{\gamma_s}{kT} \frac{a}{x_s} \tag{2.22}$$

where, as previously defined, s is the source strength (i.e. the number of cooperating spirals), γ_s is again the free energy of a molecule in the step and x_s is the surface diffusion distance. In this model, the surface diffusion distance, x_s, is given by,

$$x_s = a \exp\left(\frac{\Delta G_{deads} - \Delta G_{sdiff}}{kT}\right) \tag{2.23}$$

in which ΔG_{deads} is the activation free energy for desorption and ΔG_{sdiff} is the activation free energy for a surface diffusive jump. The retardation factor β is defined by Bennema as,

$$\beta = \left[1 + 2c_0 \exp\left(\frac{-\Delta G_{deads} - \Delta G_{sdiff} + 2\Delta G_{kink}}{2kT}\right) \tanh\frac{\sigma_1}{\sigma}\right]^{-1} \tag{2.24}$$

where ΔG_{kink} is the activation free energy of dehydration for entry into a kink. Bennema's generalisation of growth from solution has been considered in greater detail by Gilmer and Bennema [35] who have also shown the existence of so called "second" linear and parabolic laws which may occur under certain circumstances.

With respect to questions of mass transport, BCF made the presupposition that the incorporation of growth units into a step was isotropic. That is, molecules enter the step from both sides with equal probability. Schwoebel [57, 58] introduced the idea that descent of a step from the upper terrace may be unfavourable due to the potential barrier resulting from the number of bonds which have to be broken for a molecule to descend a step. To illustrate the origin of the potential barrier, using a simple cubic

Kossel model of a step on a low index surface it can easily be seen that to descend a step to the lower terrace, bonds must be broken simply due to the co-ordination number of a molecule at the step edge. If integration of a molecule into a kink is similarly impeded then an asymmetry in mass transport will result. Molecules within x_s of the step on the lower terrace will be able to integrate into the crystal. Molecules within x_s on the upper terrace will be ineffectual. The implications of a Schwoebel barrier for crystal growth have been considered by Pimpinelli and Villain [19] and Gilmer and Bennema [35]. The latter reference is a general review of crystal growth kinetics and describes a number of other modifications to the theory as a result of different mass transport conditions.

Another presupposition of BCF is that the condition $x_s \gg x_0$ is always met in the case of growth from the vapour, resulting in circular symmetry of step advance and hence, circular spirals. The status of this assumption is less clear in the case of growth from the vapour and numerous experimental observations have revealed the presence of polygonal spirals suggesting that this condition is not met.

Kinetic Coefficients and Conformation

Although BCF introduced the step retardation factor, the molecular origin of this factor was only briefly considered. As discussed in section 2.6.1 this factor arises due to conformational, steric and orientation considerations. Specifically, mere arrival at a kink site is not necessarily a sufficient condition to ensure integration into the crystal, if the molecule does not arrive in the specific orientation necessary for integration then it may not enter the crystal. The Schwoebel effect is an extreme case of this. Clearly these factors are likely to be more important in the case of complex molecules. These steric effects may be encompassed by the model of Bennema for growth from solution, equations 2.21 and 2.24, through suitable selection of the various activation free energies. More recently, Liu *et al.* [59] have considered the role of steric factors in dictating growth rates and hence, morphology. Related to the retardation factor, the kinetic coefficient of a step, β_s, is essentially a constant of proportionality between the supersaturation at the step and its velocity. Orientational anisotropy of this parameter may result in polygonisation of growth spirals. A distinction between different modes of growth results from the rate limiting process during crystal growth. When the rate of advance of a step is determined by mass transport from the solution then the growth is said to be in a *diffusion regime*. When the rate limiting process for growth is the

incorporation of molecules into kinks, as characterised by β_s, then the growth is said to be in a *kinetic regime.* This has important experimental implications since it is important to know whether an experiment is conducted in a kinetic or diffusive regime in order for correct interpretation of results. Practically, where a kinetic regime is desirable, this is ensured by adequate stirring and supply of supersaturated solution.

2.7.6 Surface Roughening and Morphological Prediction

Although mostly outside the scope of this thesis, some of the theoretical developments in surface roughening since BCF are noteworthy. The BCF paper caused a growth of interest in statistical mechanics of surfaces, particularly roughening transitions. Work based on the foundations laid by BCF now occupies a central position in the theory of crystal growth and the structure of surfaces and has been reviewed by Bennema [39]. More specifically, Bennema [35, 60–62] has formulated a synthesis of the morphological theory of Hartman-Perdok [22–25] with the statistical mechanical theory of roughening and spiral growth. Liu and Bennema [63] have included the fluid phase in the analysis. Other developments in this field have included attempts [64, 65] at the *ab initio* determination of PBCs and consequently of the crystal morphology therefrom.

It is normally tacitly assumed in models of crystal growth that the structure of the surface is essentially that of the bulk. However it is actually well known that surfaces may be relaxed or reconstructed. The overwhelming amount of information about relaxation and reconstruction at the present time is for semiconductor and metal surfaces in vacuum, however the possibility that all crystals may exhibit these phenomena should not be ruled out and if it does occur on a given crystal then it may significantly affect the resulting morphology. The likelihood of occurrence will depend on the details of the bond strength and directionality. Furthermore, it is probable that the surface structure will be influenced by the medium; that is, immersion in solution may change the surface structure from that in, say, a vacuum. The role of relaxation and reconstruction has been considered by Rohl and Gay [66] and by Vlieg [67].

2.8 Computer Simulation

Before considering experimental methods in crystal growth in the next chapter, a brief consideration of the role of computer simulation in the development of crystal growth theory is warranted. Arguably, computer simulation has played a role intermediate of theory and experiment. Computer simulation has been used to formulate and perform idealised "experiments" in order to test the predictions of the theories. In some cases, this has often been the only way in which the predictions of the theories could be directly explored. With new experimental techniques this state of affairs is changing however the importance of computer simulation in confirming significant results should not be overlooked. Most aspects of the theory of crystal growth have at some time been the subject of computer simulations. Part of the attraction of such methods is that, within the constraints imposed by computation time, the "experimenter" can exercise more or less arbitrary control over the details of the system. Also, where analytical solutions are unavailable, simulations may be the only way of obtaining solutions. The statistical mechanics of surfaces and the roughening transition have been particularly fertile areas in this regard. Most simulation studies to date have used the Monte Carlo method, however molecular dynamics and other techniques have been used. Several reviews of work in this field have been published, for example van der Eerden *et al.* [68] have reviewed the earliest work on Monte Carlo simulations.

Chapter 3

Experimental Studies of Crystal Growth

3.1 Introduction

In addition to theory, the literature of crystal growth contains a vast amount of experimental data. This applies even in the various sub-fields such as growth from solution, with which the present study is concerned. No single discussion can assimilate all of this information and consequently no attempt to do so shall be made here. Instead, the purpose of this chapter is to describe general experimental techniques used and to cite some specific examples of each. In addition, a widely studied model crystal, which will play a central role in the remainder of the present study, is considered at the end of the chapter. Significant results from several other studies will be considered in the discussion chapter with the results of the present study and are not duplicated here.

3.2 Early Observations

The role of observations in establishing the laws of crystallography have been described at length by numerous authors. In particular, the role of measurement of interfacial angles on mineral specimens served to establish the law of constancy of

interfacial angles, or the law of rational indices as it is nowadays known. The history of these developments has been discussed by Scheel [7]. In the early years of the twentieth century, whilst making precision measurements of interfacial angles, Miers [69, 70] noted that there was often a small angular discrepancy between the measured interfacial angles and the law of rational indices on some crystals, amounting to no more than a few minutes of arc. He attributed these to growth and called them growth pyramids. Since this observation apparently contradicted the law of rational indices, it came to be known as Miers' paradox. Subsequently, in the development of their theory discussed in the preceding chapter, Burton, Cabrera and Frank [34] recognised that Miers' growth pyramids could provide evidence of the shallow growth pyramids or *hillocks* which their theory predicted. At the 1949 discussion of the Faraday Society in Bristol at which Frank [33] promulgated the dislocation theory of crystal growth, Griffin [71] described his results on the microscopic examination of the faces of natural beryl crystals on which he had observed layered spiral patterns. These results were unpublished at that time though they provoked great interest. In particular, Mott [72], in a letter to the journal *Nature* on the theory of crystal growth, included a photograph of a beryl surface obtained by Griffin and commented on his results. Griffin's images were eventually published [73] and were accompanied with a commentary by Frank [47] in which he examined the images in terms of the spiral growth theory. Subsequently Griffin [74] published further work on beryl crystals using multiple beam interference methods developed by Tolansky [75], in addition to bright field, oblique dark field and phase contrast microscopy.

Shortly after Griffin's original observations, a plethora of examples of growth spirals on a variety of different crystals, studied by a variety of methods, were published. Verma [76, 77], using phase contrast microscopy and multiple beam interference techniques due to Tolansky [75], made extensive observations of growth spirals on the surfaces of carborundum (silicon carbide) crystals. Notable in these images were the apparent pits at the spiral centre which prompted Frank [40] to perform his analysis of hollow dislocation cores. Amelinckx [78] also published images of growth spirals on carborudum and subsequently used phase contrast microscopy to observe growth spirals on the surfaces of crystals of long chain organic compounds [79]. Forty [80], a contemporary of Griffin and Verma, using bright field reflection and reflection phase contrast microscopy, observed growth spirals on cadmium iodide crystals. Later, Forty [81] published a sequence of images showing the growth of cadmium iodide crystals by a spiral growth mechanism. There are numerous other examples of observations of growth spirals on crystal faces contemporary with those described above, including

transmission electron microscopy of replicas of crystal surfaces. Frank has reviewed these early observations [4] and the original references may be found therein. The extensive investigations of crystal surfaces by Tolansky [75] and co-workers using multiple beam interference techniques have been collected in a monograph. Microscopic techniques, in particular interference methods such as phase contrast and differential interference contrast, continue to be used for crystal growth studies, both *in-situ* and *ex-situ*, in the present day. Their use *in-situ* allows the velocities of steps on surfaces to be measured directly, though resolving fundamental steps is difficult and depends on the crystal in question. More recently this technique has been automated by combination with video signal processing techniques [82].

To conclude this section it should be remarked that, as discussed in the last chapter (section 2.7.3), not everyone was convinced of the validity of the spiral growth mechanism despite the many and varied observations of spiral step patterns on a variety of crystals. For the skeptics, these were insufficient evidence of the general validity of the spiral growth mechanism [48]. For them, further evidence was required, preferably quantitative.

3.3 Growth Rate Measurements

Striking though the observations described above were, BCF is primarily a theory of growth rates and so its confirmation relied on the quantitative agreement with measured crystal growth rates. BCF was successful in explaining the growth rate data of Volmer and Schultze [4] and the numerous observations of spirals on surfaces had provided supporting evidence of the model. However within BCF is a plea for more kinetic data with which to test the theory since measurements of the growth rates of crystals at the time was generally sparse. Furthermore, there was of course particular interest in measuring growth rates from solution as well as vapour. The earliest measurements of this kind were made by studying the displacement of a crystal edge or face with a travelling microscope. Several such studies are discussed by Gilmer and Bennema [35]. The technique continues to be used in the present day [83].

In response to the requirement for more experimental data on the rates of growth of real crystals, particularly at very low supersaturations, Bennema [84] developed a crystal weighing technique which allowed the accurate measurement of the crystal growth

rate as a function of supersaturation by monitoring the increase in mass of a crystal suspended in solution from the arm of an analytical balance. The entire apparatus was enclosed in a thermostat. The growth rates of individual faces were obtained by measuring their areas before and after growth. The overall (R,σ) dependencies were calculated by a computer model which took account of the depletion of solute, the change in mass and the change in surface area of the faces. The model assumed that the geometry of the crystals did not change during the growth experiment. Using this technique Bennema [85] measured (R,σ) curves for crystals of potassium aluminium alum and sodium chlorate at relative supersaturations from 0 to 1.25% and 0 to 0.175% respectively. For potassium aluminium alum at relative supersaturations below 1% a linear dependence of R on σ was measured. For $\sigma > 1\%$, (R,σ) points lying above the line for $\sigma < 1\%$ were obtained with considerable scatter. For sodium chlorate, a parabolic (R,σ) dependence was observed for $\sigma < 0.05\%$ and a linear dependence was obtained for $\sigma > 0.05\%$. For sodium chlorate, the theoretical BCF (R,σ) dependence was found to fit the data satisfactorily. The general technique suffers from a number of limitations. The assumption that the crystal geometry does not change during growth is not always met. Also, the method can only give the mean growth rate of a face. As will be shown in the present study, in general the growth rate undergoes both spatial and temporal fluctuations which are not resolved by the weighing technique. The same criticism also applies to the edge and face displacement studies.

The development of low cost high powered lasers lead to their use for interferometric investigations of crystal growth rate *in-situ* by Michelson interferometry. In this technique, the crystal face for study becomes one of the reflecting surfaces of the interferometer. The rate of advance of the face may then be measured by counting the passage of interference fringes which move as the optical path length changes due to growth of the crystal. The number of fringes passing a point on the crystal surface in unit time is therefore a measure of the growth rate normal to the surface. The change in height, d, from consecutive fringes is given by the relationship

$$d = \frac{\lambda}{2n}, \tag{3.1}$$

where λ is the wavelength of the light used and n is the refractive index of the medium. The factor 2 arises in the denominator since the change in optical path length is the distance traversed by both incident and reflected beams. In this way the normal growth rate, R, of an individual growth hillock may be measured directly by counting the number of fringes passing a point on the crystal surface in unit time (i.e. the fringe

frequency) and multiplying by the change in height per fringe d, that is,

$$R = df = \frac{f\lambda}{2n}, \tag{3.2}$$

where f is the fringe frequency. This allows the direct measurement of (R,σ) curves. The technique has been successfully applied to the aqueous solution growth of a variety of crystals including ammonium dihydrogen phosphate (ADP) [86–88], potassium dihydrogen phosphate (KDP) [88, 89], barium nitrate [90], potash alum [91] and the protein lysozyme [92]. An advantage of the technique is that it also provides an image of the surface in which the surface relief is revealed by concentric interference fringes. In this way both the slope of a growth hillock and its normal growth rate may be measured from which the step velocity may be obtained, allowing (v,σ) dependencies to be plotted. Anomalies are often reported in these studies where the dependence of the growth rate does not reflect anticipated trends. Often these are attributed to impurity effects, see for example Onuma [91]. By means of video equipment, movies of the crystal growth may also be made.

The interferometry technique has also been used to study the concentration of solution around a growing crystal, making use of the refractive index change as a function of solution concentration [88, 93, 94]. In the study by Tsukamoto [94], the technique was applied in microgravity during space flight where crystal growth could be studied in the absence of convection due to density gradients in the solution. One of the main obstacles to successful interferometry in the past has been the reliable counting of the passage of interference fringes. Various techniques have been used in the publications cited, in particular the attachment of a photodiode to the video display has been used. With the development of digital video image capture *etc.* more sophisticated signal processing techniques have become available. Vekilov *et al.* [92] developed an interferometer and cell for a conventional optical microscope from which they obtain a video signal. By signal processing techniques they were able to digitise the intensities of the pixels in the video display and, by means of the fast Fourier transform (FFT) algorithm, they obtained a frequency spectrum of the interference fringe time series from which the fringe period and hence, normal growth rate could be obtained. The technique was applied to microcrystals of the protein lysozyme. Recently, heterodyne lasers in which the Zeeman effect is exploited have been applied to the study of protein crystal growth [95].

3.4 The Study of Crystal Surfaces

There are two overlapping aspects to the experimental study of crystal growth. It is a dynamic phenomenon and so growth rates must be measured and have been done so by the methods described in the preceding section. Also, the step patterns which occur on the surfaces as a result of growth can yield an enormous amount of information about the crystal growth process and are therefore essential for a complete study. In particular, observation of step patterns can reveal the structure of growth sources. Methods of observation of step patterns on surfaces were discussed before but include optical microscopy including interference microscopy such as phase contrast and differential interference contrast techniques. Also multiple beam interferometry and electron microscopy have been used. Unfortunately, all of these techniques can only resolve fundamental surface steps (that is, the smallest step which occurs on a surface rather than bunches or multiples thereof) in the most idealised circumstances. The attention to detail for sample preparation required to achieve this ideal is great. Regarding *in-situ* studies of crystals during growth, the situation is even more difficult with respect to these methods and in the case of the electron microscopic techniques is simply not possible since a vacuum is required. Ultimately, the resolution of optical and electron techniques is fundamentally limited by the wavelength of light or electrons used. The fundamental molecular processes involved in crystal growth occur beyond the resolution limit of most optical or electronic instruments. This restricts the direct observation of fundamental crystal growth phenomena and features by these instruments. Consequently, direct observation of the structure of growth sources on crystal surfaces has not been possible, until recently.

3.4.1 Scanning Probe Microscopy

With the invention of the scanning tunneling microscope (STM) by Binnig and Rohrer during the 1980s [96], it became possible for the first time to study surfaces directly with true atomic resolution. This immediately stimulated much research into the study of suitable surfaces such as metals, semiconductors and cleavage planes of graphite crystals. These researches resulted in many striking images of surface vacancies, islands, steps and reconstructions; and provided direct verification of several predictions and experimental findings from indirect methods such as electron diffraction [97]. However, because of the mode of operation of the STM, relying on a quantum me-

chanical tunneling current between the surface under study and an atomically fine tip, the instrument relied upon the surface of interest being an electronic conductor. For this reason, efforts were conducted to extend the scanning probe principle to new instruments which were not subject to the same limitations. This culminated with the development of the atomic force microscope (AFM) [98].

Atomic Force Microscopy Principles

The original principle of operation of the AFM is that an extremely fine stylus (the "tip" or "probe"), only a few atoms across at the finest point, mounted on the end of a fine cantilever beam; is brought into intimate contact with and scanned over the surface under study. The tip is scanned over the surface in a raster pattern by piezoelectric actuators controlled by the instrument control program running on a digital computer. The changes in surface topography encountered by the tip as it is scanned causes the cantilever beam to undergo deflections brought about by the "atomic forces" between the tip and the surface. A laser beam reflected from the upper surface of the cantilever onto a four quadrant photocell serves to amplify these deflections. The amplification of the cantilever deflections is achieved by the "optical lever" principle. The amplification achieved by the instrument depends on the reflection angle and the path length of the reflected beam to the photocell. When these parameters are optimised, very large amplifications of the cantilever deflections are possible. From the laser intensity falling onto each quadrant, the photocell converts the amplified deflections into an electronic signal which forms the input signal to a comparator circuit. The comparator circuit compares the actual signal with the reference signal generated when the cantilever beam is undeflected. The resulting error signal is used as the control signal for a piezoelectric actuator. In one embodiment of the AFM principle, the surface of interest is mounted on the piezoelectric actuator. A schematic of the operating principles of the AFM are shown in figure 3.1.

The actuator moves in response to the control signal in such a way as to restore the cantilever to the undeflected condition. The control signal as a function of position within the raster scan is therefore a representation of the relief of the surface. This signal is digitised and synchronised with the raster scan by the digital computer so that a digital image of the surface topography is generated. In addition, the deflection signal from the photodetector serves as another signal channel from which an image of the surface may be formed. The control signal image is that which contains the raw

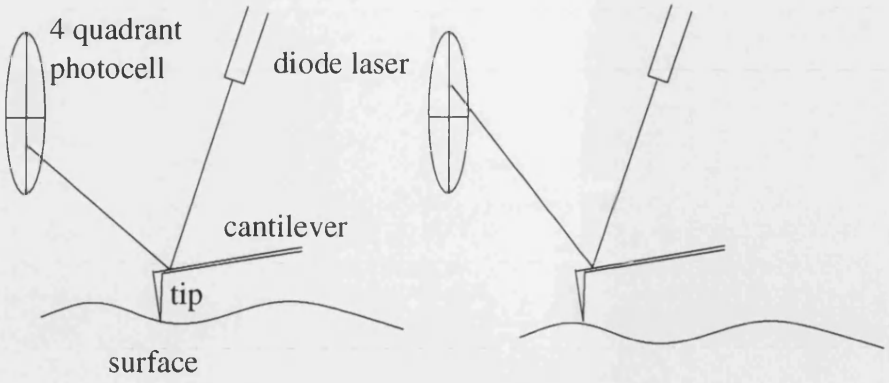

Figure 3.1: Schematic of the optical lever principle of atomic force microscopy.

data about the topography of the surface, however for display purposes the deflection signal is often preferred as it may represent the surface features more clearly. Having obtained digitised images of the surface, the full range of standard image analysis techniques are available to process the resulting images. Also, the actuator control signal image can be digitally processed to extract information about step heights, pit depths *etc.*

Clearly, the resolution of the instrument is crucially dependent on the fineness of tip used. AFM tips and cantilevers are integrally fabricated from silicon or silicon nitride by nanofabrication techniques similar to those used in microelectronics such as microlithography and vapour deposition. These techniques allow the fabrication of tips which approach atomic dimensions. Use of such fine tips allows atomic resolution to be approached. However, in contrast to STM, true atomic resolution is not routinely achieved by AFM. This is because many atoms in the stylus interact with many atoms in the surface, unlike STM in which single atoms in the surface interact with the terminal atom of the tip. Even at resolutions well below the achievable maximum there are resolution limits as a result of the mechanism of image formation used in the AFM. These limitations may produce artefacts which are prone to misinterpretation. The main source of such artefacts is the relationship of the tip to the sample. Despite being of microscopic dimensions, the tip is finite in size and can therefore not enter every fissure or feature of the surface. The image formed by an AFM is actually the convolution of the true surface with the profile of the tip used. The obvious example is that of undercuts on the surface which the tip cannot enter and so will not feature on the resulting image. Similarly, a pit or trench in the surface can only be imaged reliably if it is less deep than the height of the tip itself. If it exceeds the dimensions of the tip then it will not be possible to image its profile reliably because the tip will be unable to

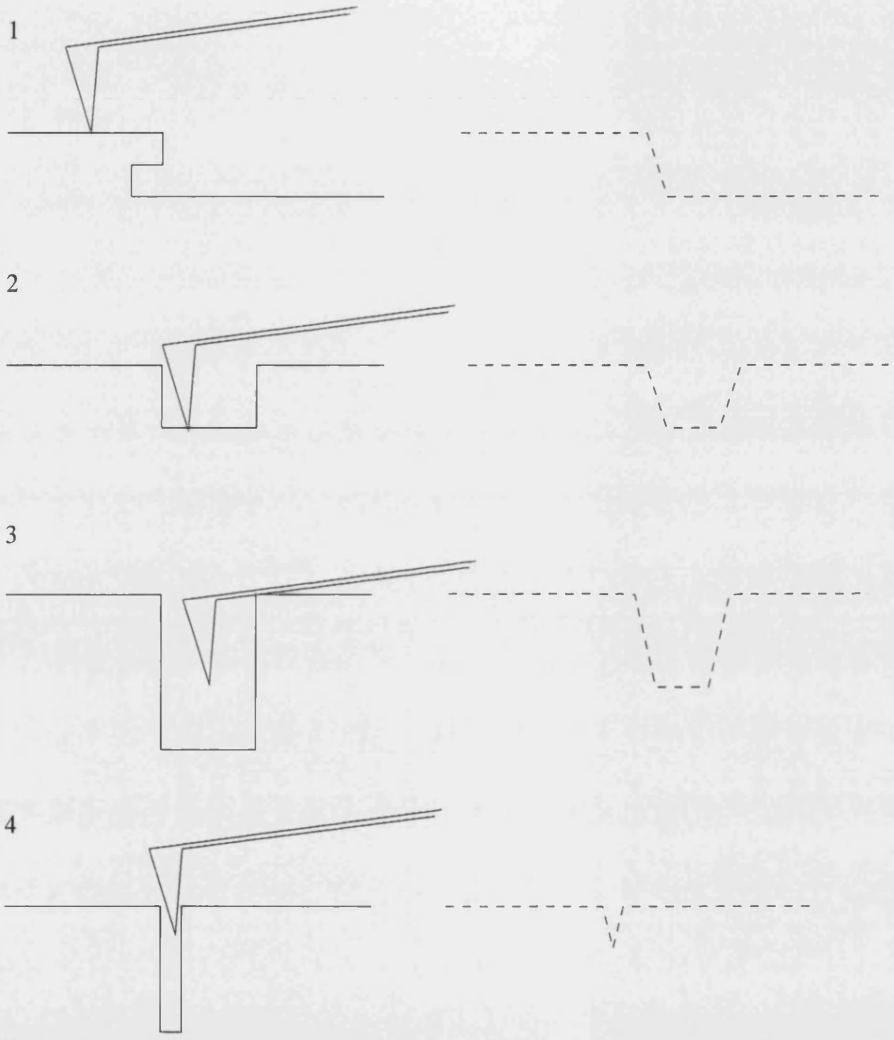

Figure 3.2: Typical AFM tip-surface convolution artefacts; 1. undercut, 2. shallow trench, 3. deep trench, 4. narrow fissure. The solid lines show the true surface profile, the dashed lines show the convolution of the tip and surface from which the final image is constructed.

penetrate to the bottom of the feature. The measurable depth of a surface pit or trench is therefore restricted by the height of the tip. Also, due to the finite tip width, vertical terraces may appear sloping in images. Illustrations of typical tip-surface convolution artefacts are shown in figure 3.2. For these reasons a range of tips such as high aspect ratio tips are available for most commercial AFM's. In AFM studies of crystal surfaces, tip-surface convolution artefacts are possible with features such as etch pits, hollow dislocation cores and macrosteps and care should be taken in their interpretation. Another source of image distortion which can occur is due to capillarity effects produced by adsorbed liquid layers on the surface of interest. In air, very thin films of liquid water can form on some surfaces which can significantly modify the behaviour of the tip through surface tension. This can lead to reduced resolution and so control of the ambient environment may be necessary in some cases.

The AFM and STM are related in the sense that both use the same comparator - piezoelectric actuator system to adjust the position of the crystal surface whilst piezoelectric actuators scan the probe across the sample. The techniques differ in the means by which the feedback signal itself is generated. For this reason the AFM and STM belong to a class of instruments called scanning probe microscopes which encompasses any instrument which forms images according to the scanning probe principle. The development of scanning probe microscopes is a very active field of research at present and new innovations are frequent. Most modern instruments are modular in design, having a standard piezoelecric scanning system with separate modules for the various modes of operation such as STM, AFM and developments thereof.

Amongst these innovations is the development of oscillating cantilever modes of operation[1]. The original mode of operation of the atomic force microscope described above is now typically referred to as contact mode AFM in which the tip is brought into intimate contact with the surface and the cantilever deflection remains constant until a change in surface relief is encountered. This can have the limitation that soft surfaces can appear poorly resolved or may even be damaged by the hard tip if it is driven too forcefully into the surface. In the oscillating cantilever mode the cantilever oscillations are driven at its natural resonant frequency by a small piezoelectric transducer. The oscillations of the cantilever bring the tip into intermittent contact with the surface. In this way the tip effectively "samples" the surface topography once per cycle. The reflection of the laser beam from the cantilever onto the four quadrant pho-

[1]In the Digital Instruments Nanoscope instruments, this mode is called "tapping mode", which is a trademark of Digital Instruments.

tocell produces an oscillating signal as the reflected spot oscillates with the cantilever from the upper to the lower half of the photocell. It is the amplitude of this oscillating signal which is used as the feedback signal in this mode. The amplitude signal is compared to a user defined setpoint amplitude and the piezoelectric actuator adjusts the surface position to restore the actual amplitude signal to the setpoint as the surface relief changes with the raster scan. The amplitude changes with surface relief because the gap between the surface and the mean position of the cantilever varies as the tip is scanned.

Similarly to contact mode AFM, the amplitude signal itself may be used as a second signal channel for image formation. The intermittent contact between the tip and the surface minimises the potential for tip induced surface damage and can often lead to better images. Also, because of the inertia of the cantilever as it oscillates, the tip is less prone to the resolution limiting capillarity effects than is the case for contact mode AFM. A disadvantage of the oscillating cantilever mode of operation is that it is restricted to low raster scanning rates compared to contact mode because of the requirement for the tip to sample the surface sufficiently frequently to reliably form an image of the surface topography. This restricts its use for dynamic imaging of surface processes such as crystal growth. In any case, in the case of crystal growth from solution, the presence of the solution damps the cantilever oscillations and therefore makes *in-situ* imaging unreliable. For these reasons this mode is usually restricted to the study of surfaces *ex-situ.*

Ex-Situ Versus *In-Situ* Atomic Force Microscopy

The *in-situ* and *ex-situ* modes of operation of atomic force microscopy each have their own inherent advantages and disadvantages. *In-situ* AFM allows surfaces to be imaged in their native environment. In the case of crystals, this can be the solution from which they are growing. The advantage of this technique is that because the crystal does not have to be separated from its solution there is no risk of introducing artefacts to the crystal surface as a result of separation. *Ex-situ* observations of crystal surfaces often show many artefacts due to separation from the mother liquor. This complicates the study because of the risk of misinterpreting artefacts as real features of the crystal growth. *In-situ* observations also allow the crystal to be grown or dissolved *in-situ* such that a "movie" of the process can be produced. This technique can however be plagued with difficulties, not least due to the difficulty of maintaining a stable temper-

ature and therefore supersaturation in the *in-situ* cell. In recent years, the development of heating/cooling stages based on the Peltier principle has been applied successfully to this problem [99]. These advances notwithstanding, the main limitation of *in-situ* observations is due to the mode of imaging of the AFM itself. Because the surface is scanned in a raster pattern the image is built line by line. High resolution imaging requires slow scanning. Because the velocities of surface steps during crystal growth can be very high with respect to the scanning rate, depending on the supersaturation, the surface can change greatly between the start and end of a scan. Indeed many new crystal layers can form in the time required to make a single medium resolution image - even at relatively low supersaturation. Therefore, the image obtained will always be a distortion of the real surface. In extreme cases the steps may be moving so fast that they cannot be imaged at all - effectively a blurred image is obtained.

Ex-situ AFM, despite the aforementioned problems of artefact creation due to the separation of crystal from solution, offers a number of advantages over the *in-situ* technique. Most importantly, undistorted images of crystal surfaces can be obtained at any practical supersaturation, provided that the crystal harvesting technique does not introduce artefacts. In this way, a representative snapshot of the surface can be obtained during growth by abstracting a growing crystal from its mother liquor. By doing so over a range of known supersaturations, a study of the crystal growth over a range of conditions unattainable by *in-situ* AFM can be conducted. If such studies are to be conducted, it is necessary that techniques are devised to minimise the production of artefacts due to removal of a crystal from its solution. When the solution is supersaturated and the crystal is growing, this becomes still more difficult. These techniques have to be devised on an empirical trial and error basis and often a degree of practice is required until sufficient skill is developed in the technique to be successful most of the time. It is true that even the best methods cannot work perfectly all of the time and some degree of artefacts have to be tolerated. Fortunately, these artefacts are often localised to small regions of the surface and with practice high quality images of sections of crystal surfaces free from artefacts can be obtained. To the trained eye, it is usually quite straightforward to distinguish most artefacts from real features of crystal growth. A study of removal induced artefacts on potassium hydrogen phthalate crystals has been published by Campbell *et al.* [100]. One further advantage of *ex-situ* observations are that they allow the AFM to be operated in non-contact mode which, as described above, can result in superior imaging with reduced risk of damaging the surface. Finally, it should be stated that neither technique, *in-situ* or *ex-situ*, is superior; only that they are complementary and are best used together and in conjunction

with other techniques to obtain the most detailed understanding possible.

Application of AFM to Solution Crystal Growth

In the field of solution crystal growth research, the majority of AFM studies to date have been performed at resolutions much less than the maximum. Typically a range of piezoelectric scanners of various resolutions are available to suit specific situations. Arguably, from the point of view of understanding the crystal growth process the resolution of fundamental surface steps over comparatively large areas of surface with respect to the height of the steps is ideal. In this way, the patterns formed by steps as the crystal grows can be clearly seen and it is such patterns which are most instructive in explaining the mechanism of growth. On this scale, the outcrop of screw dislocations at the surface is clearly disclosed by the abrupt termination of the associated surface step. Fortunately, modern instruments can comfortably resolve such step heights over the distances necessary to meet this ideal. As a drawback however, with present AFM technology, observations at this scale result in a loss of resolution at the molecular scale and as a result the molecular structure of surface steps, such as kink sites, cannot usually be resolved. Though more recently some studies have achieved near molecular resolution of terraces [101].

Since the earliest reported applications of AFM to the study of crystal growth from solution, a wide variety of crystals have been studied and have revealed dislocation outcrops, growth spirals, hollow dislocation cores, two-dimensional islands *etc.* The earliest studies revealed differences in growth behaviour, for example between calcite and fluorite [102]. Mineral crystals which, due to sparing solubility and consequently slow growth and dissolution, can be reliably imaged *in-situ* without the need for sophisticated temperature control, have therefore featured quite prominently in *in-situ* studies. There has been particular interest in studying biomineralisation processes and to this end several studies have measured step velocities on calcite crystals directly by AFM scanning [103, 104]. The effects of doping with biologically relevant compounds and studying their effects on the crystal growth has also been investigated in these studies. Another class of crystals which grow particularly slowly are biological macromolecules such as proteins and viruses. For this reason there has been great interest in studying the growth of these crystals *in-situ.* Another particular attraction is that, due to the very large lattice parameters of these crystals, in ideal cases individual kinks in steps can be resolved *in-situ* during growth. Another attraction of studying

such crystals is that the AFM can assist in obtaining crystallographic information for structure solution by x-ray diffraction studies. Some of these studies have been reviewed by Kuznetsov *et al.* [105].

The AFM study of simpler, more soluble compounds has been somewhat slower to develop due to the difficulties of reliable *in-situ* imaging and the problem of preserving sample surfaces during removal from solution. Nonetheless several studies have successfully overcome these difficulties and reliable imaging is now achieved [106–109]. The results of several of these studies will be covered in more depth in the subsequent discussion.

3.5 X-ray Techniques

X-ray diffraction is of course synonymous with crystallography, however there are a number of variations of the basic x-ray techniques which have specific applications in the field of crystal growth. Two of these of particular interest to the present study are outlined below.

3.5.1 X-ray Topography

The Bragg condition for x-ray diffraction, $2d_{hkl}\sin\theta = \lambda$, relates the diffraction angle, θ, from a set of crystallographic planes, hkl, to the lattice spacing d_{hkl}, for radiation of wavelength λ. In a normal x-ray diffraction experiment the beam is very narrow and a small region of the crystal is illuminated. If however an extended x-ray beam is used; that is, a beam which illuminates the whole crystal, then at the diffraction condition an image of the crystal will be formed which can be projected onto and captured by a photographic plate. If the crystal contains defects which strain the crystal lattice locally, then the diffraction condition will not be met in the strained region. As a result, no intensity will be diffracted from the strained region of the crystal and it will appear dark in the image of the crystal. Thus, contrast is achieved locally from strained portions of the crystal. In this way defects with associated strain fields including impurity striations, growth sector boundaries, dislocations, stacking faults, twin planes *etc.* can be resolved within the crystal. Generally speaking, the strain fields due to point defects

are not resolved. The defect structure of the crystal contains a history of its growth and the resulting images can be interpreted to establish details of how the crystal grew. This can include the genesis and movement of dislocations and the formation of inclusions. Also, by taking x-ray reflections from several sets of lattice planes, the Burgers vectors of dislocations can be obtained quantitatively if the invisibility criterion can be met[2]. The origins of the technique have been discussed by Lang [110]. A number of real time and *in-situ* x-ray topographic studies have been performed during growth by utilising the very high x-ray intensities available from synchrotron sources, see for example Chernov [18, 87]. X-ray topographic studies relevant to the present study will be considered later.

3.5.2 Surface X-ray Diffraction (SXRD)

X-ray diffraction from a bulk crystal is subject to the three Laue conditions, one for each dimension, as a result of the three dimensional periodicity of the crystal. Consequently, diffracted intensity is restricted to a point. If however x-rays can be diffracted from a surface, which is only periodic in two dimensions then one of the Laue conditions is relaxed and a "rod" of diffracted intensity is possible. This is an example of diffuse x-ray scattering, i.e. the scattering of x-rays where the Bragg condition is not met. In a normal x-ray diffraction experiment, the specularly reflected intensity from the Bragg condition is very much larger than that from the non-Bragg diffuse reflections due to the surface and other defects, which are insignificant and barely detectable. If however the diffraction geometry is arranged such that the angle of incidence with the surface is very small (grazing incidence) then due to the geometry the diffuse reflections from the surface will become stronger in proportion to the intensity at Bragg peaks. Effectively the Bragg peak becomes "smeared" out into a rod of intensity. Because the non-specular reflections come from the surface, they carry information about the surface layer. If the angle of incidence is sufficiently small that the condition for total external reflection is met then the diffraction signal will come entirely from the surface layer. The rods of intensity which result are called crystal truncation rods (CTRs). Thus by measuring the intensities along CTRs between Bragg peaks, structural information about the surface can be obtained. When the surface layer has the same periodicity as the bulk crystal then integer CTRs result in which two of the indices *hk* are as for the bulk crystal and the third index assumes fractional

[2]This is analogous to similar techniques in transmission electron microscopy.

positions between Bragg peaks at which finite intensities can be measured. If the surface is reconstructed then the surface net will have a different periodicity from that of the underlying crystal and so the CTRs may have non-integer indices in terms of the underlying structure. Thus by integrating the measured intensities along CTRs the structure of a surface may be obtained by methods analogous to those for conventional x-ray diffraction. This can yield information about the nature of the surface termination, surface domains and adsorbed monolayers *etc.* Also, by studying the linewidths of CTRs, information about the statistics of steps and kinks on the surface can be obtained in principle.

The technique is analogous to low energy electron diffraction (LEED) in principle though, since x-rays are weakly interacting with matter, many of the intensive computations required to interpret LEED patterns are not necessary. For the same reason, where LEED has to be conducted in high vacuum, this is not essential for SXRD. The intensities of CTRs are typically exceedingly small and for this reason very intense x-ray sources are required. For this reason the technique has been restricted to synchrotron wiggler and undulator sources and has been most successful on high intensity third generation synchrotron sources. With sufficient intensity it becomes possible to study "buried" interfaces, which include surfaces immersed in solution. Thus it becomes possible in principle to study crystal surface structure during growth. To date, only a small number of studies have been successful in this respect and most have been conducted with crystals in equilibrium with solution rather than during growth. Nonetheless some interesting results have been achieved [101, 111–114]. A recent review of results achieved to date and anticipated future developments has been given by Vlieg [67]. The techniques have been subject to a number of reviews [115, 116].

3.6 Case Study: Potassium Hydrogen Phthalate

In this section the results to date for the crystal growth of potassium hydrogen phthalate, a much studied model crystal will be reviewed. This crystal features prominently in the remainder of this study therefore a review of previous work is necessary in its own right, however it also serves to illustrate the application of some of the above described techniques.

3.6.1 Introduction

Potassium hydrogen phthalate (KAP)[3] has featured in numerous crystal growth studies because it possesses a number of properties which make it an ideal model crystal. These include:

- easily grown from low temperature aqueous solution,
- solubility data are available [117],
- a well defined platelet habit which exhibits well formed vicinal faces on its largest faces, (the {010}),
- the lattice parameter normal to the {010} faces is large, which facilitates atomic force microscopy imaging of surface features,
- the (010) planes are cleavage planes which facilitates sample preparation and interferometer alignment,
- exhibits both spiral growth at screw dislocations and growth by two-dimensional nucleation,
- growth is sensitive to impurities,
- it has been the subject of several previous studies of crystal growth.

3.6.2 Crystal Structure

As its name suggests, potassium hydrogen phthalate, $C_6H_4COOH.COOK$, is the potassium salt of the diacid phthalic acid. It is an acid salt because it is normally only partially dissociated, with one of the acid groups retaining its proton. Figure 3.3 shows the asymmetric unit of the KAP crystal. The asymmetric unit consists of a phthalic acid residue (partially ionised as a hydrogen phthalate ion) and a potassium counter-ion. This basic structural unit forms the KAP crystal.

[3]The acronym KAP arises from the alternative name potassium acid phthalate.

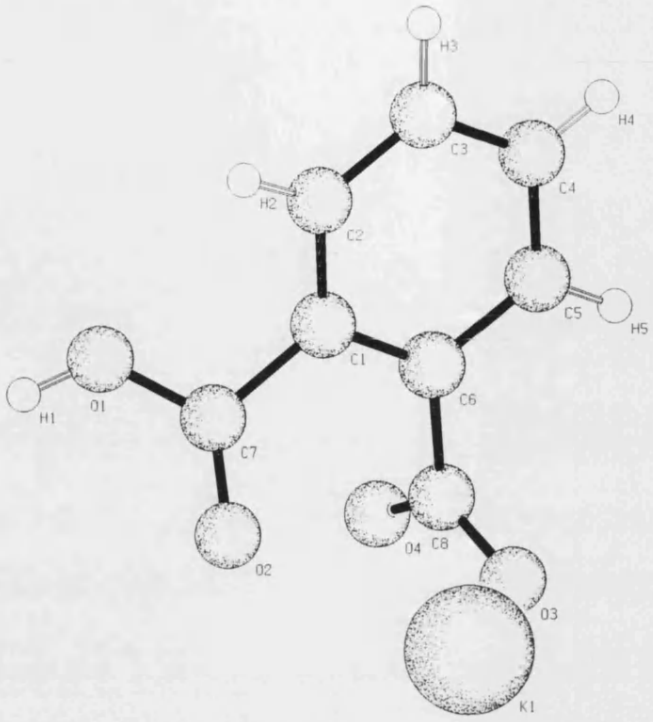

Figure 3.3: The asymmetric unit of the KAP crystal. The following symbols are used to label the atoms and ions: C, carbon; H, hydrogen; O, oxygen; K, potassium ion.

The crystal structure of KAP was determined by Okaya [118] who found that it crystallises in the orthorhombic system with lattice parameters[4] $a = 6.46_6$ Å, $b = 9.60_9$ Å, $c = 13.25_7$ Å and space group $P2_1ab$. Jetten [119] subsequently exchanged the axes to give the lattice parameters as $a = 9.60_9$ Å, $b = 13.25_7$ Å, $c = 6.46_6$ Å and space group $Pca2_1$. This notation has subsequently been used almost exclusively in the crystal growth literature for KAP and will continue to be used in the present study. As is most clearly illustrated by the projection of the KAP structure along the [001] direction shown in figure 3.6, the resulting crystal has a layer structure with alternate hydrogen phthalate and potassium layers along the [010] direction. KAP crystallises with a platelet habit [120] in which the order of morphological importance is typically {010}, {110}, {111}, {121}, {210}, {120} and {102}. The habit is shown in figure 3.7.

Solc *et al.* [117] measured the solubility of KAP in aqueous solution within the tem-

[4]The lattice parameters for KAP as reported in the original structure paper contained a typographical error. Despite an erratum in a later edition, the erroneous value has continued to be used in many later studies of KAP crystal growth. The value used here is the correct value taken from the erratum.

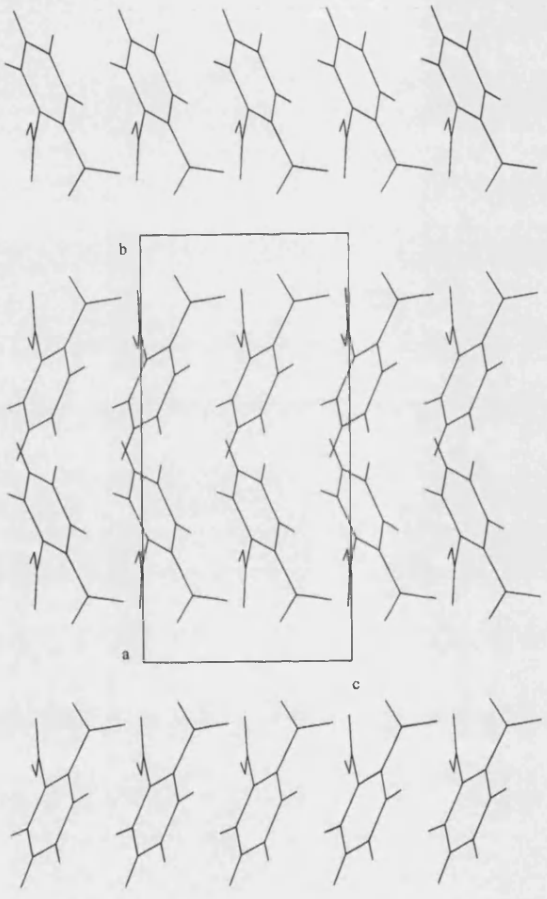

Figure 3.4: Projection of the KAP structure along [100]. The lattice parameters are indicated by a, b and c.

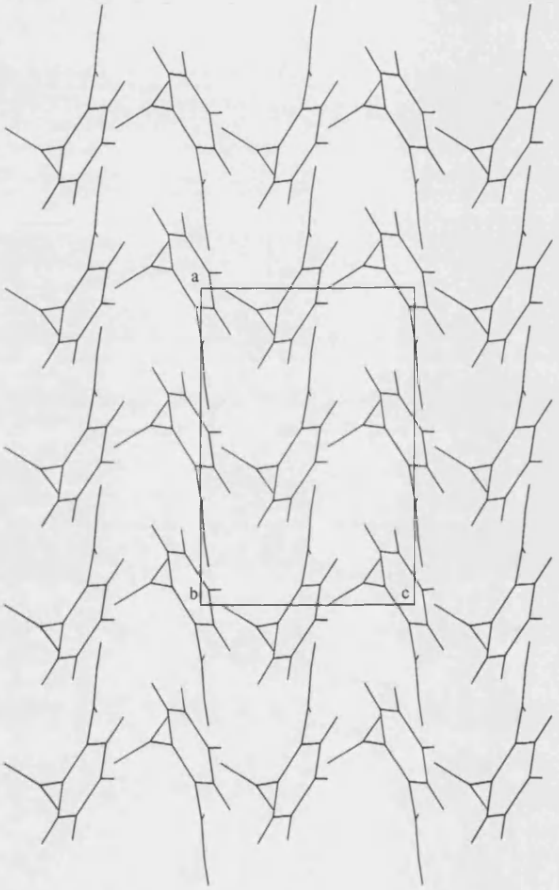

Figure 3.5: Projection of the KAP structure along [010]. The lattice parameters are indicated by a, b and c

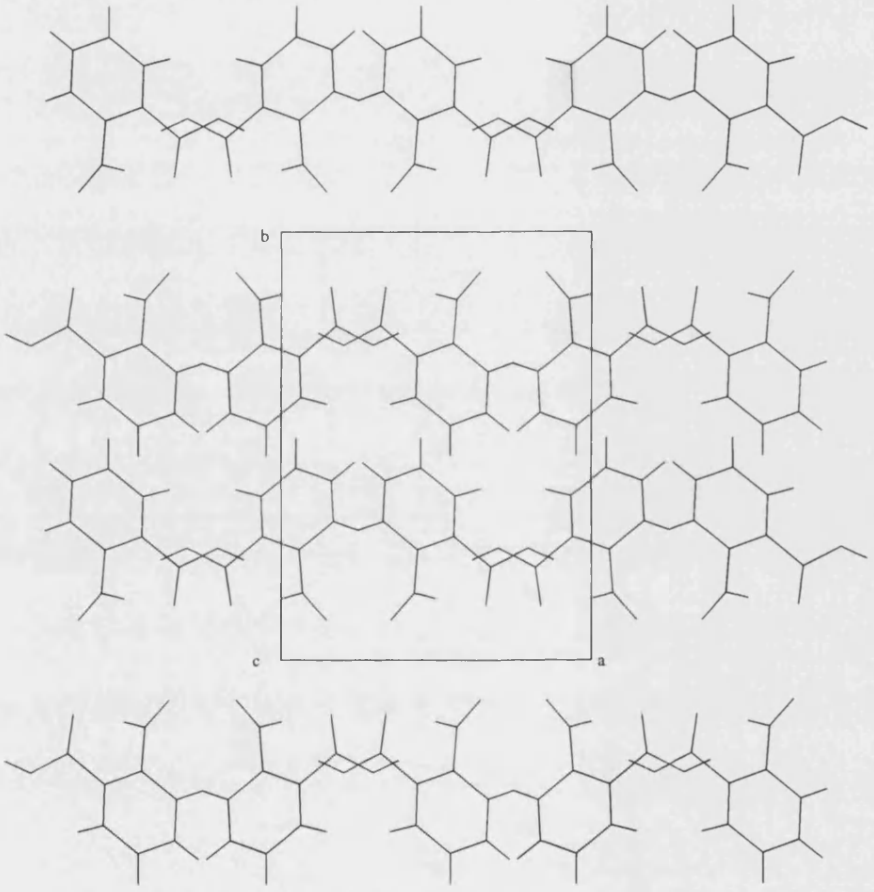

Figure 3.6: Projection of the KAP structure along [001]. The lattice parameters are indicated by a, b and c.

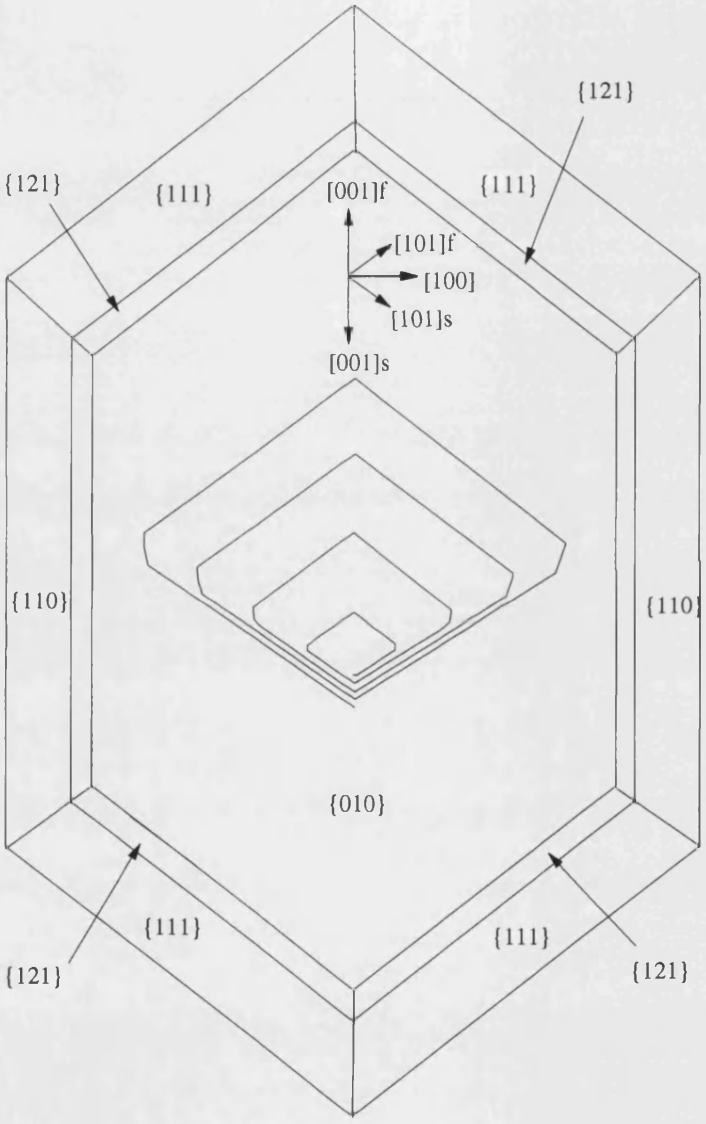

Figure 3.7: Schematic of the platelet habit of potassium hydrogen phthalate (KAP)

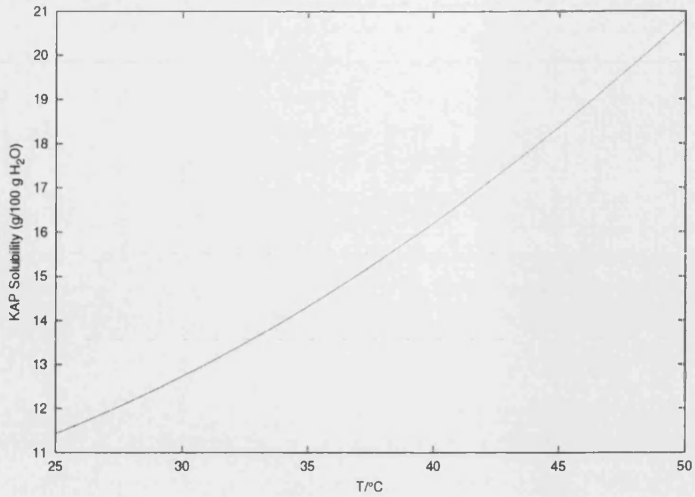

Figure 3.8: Solubility curve for potassium hydrogen phthalate (KAP) in water (data from Solc *et al.* [117])

perature range 25 - 50 °C and published the following relationship,

$$C_0 = 9.2837 - 0.0591T + 0.0058T^2 \tag{3.3}$$

where C_0 is the equilibrium concentration of KAP expressed as grams per 100g water and T is the temperature in degrees Celsius. The resulting solubility curve is shown in figure 3.8. Srinivasan *et al.* [121] have made solubility measurements in the temperature range 30 - 50 °C and have obtained good agreement with the results of Solc *et al.* [117]. The temperature - solubility relationship 3.3 has been employed [122–125] in crystal growth studies of KAP with saturation temperatures of 25 °C and growth temperatures as low as approximately 20 °C with no significant deviations from equation 3.3 reported.

3.6.3 Experimental Investigations

Following preliminary microscopic studies of the as grown surfaces of KAP crystals [119], several *in-situ* studies have been made using conventional reflected light microscopy and differential interference contrast microscopy (DICM) [126, 127]. Despite the limited resolution of the optical method, growth steps forming polygonised spirals, which in turn formed macroscopic growth hillocks, were clearly apparent on the surface and their motion was reported. The polygonised spirals were seen to have a

characteristic shape which is shown schematically in figure 3.7. Van Enckevort [127] lightly etched the surfaces of crystals and reported two types of hillock. Shallow hillocks were found to have only a limited number of etch pits at the spiral centre, indicating a small number of emergent dislocations. Steep hillocks, which often dominated the crystal surfaces, were found to exhibit a large number of etch pits, suggesting a large number of emergent dislocations.

The role of impurities on the crystal growth of KAP was studied extensively using DICM [122, 123, 128]. Also, measurements of the distribution coefficient of impurities in the crystal were made by spectroscopic techniques. These studies also included measurements of step velocity by DICM such that the growth retarding effects of the impurity could be observed. It was found that the impurities retarded the steps of the spiral anisotropically. A nomenclature for the step orientations of the characteristic growth spiral, as indicated on the schematic of the spiral in figure 3.7, was proposed. The slow moving and narrowly spaced <101> orientations were designated slow steps and indicated by a subscript s, $<101>_s$; the widely spaced fast moving <101> orientations were designated $<101>_f$. The steps intermediate of these orientations and close to <001> were found to have intermediate velocity and were labelled <001>. The <001> and $<101>_f$ were found to be most affected by the addition of impurity. The results of these studies have been discussed further [129, 130]. The results of some of these observations will subsequently be scrutinised further in light of the results of the present study. Subsequent studies of secondary nucleation by rod contacts with the {010} face of KAP have been performed [131, 132]. Also, further studies of the role of impurities [133] and microcrystal adhesion [83] in influencing the growth rate have been made by means of edge displacement measurements. The role of organic impurities on the growth of KAP has been studied by Kuznetsov *et al.* [134] who found a growth rate enhancing effect at low concentrations followed by growth inhibition at higher concentrations. Habit modification of KAP crystals by the addition of organic impurities and consequent effects on optical transmission have been reported by Murugakoothan *et al.* [135]. The modification of the nucleation characteristics by addition of a chelating agent has been reported by Srinivasan *et al.* [121].

Several x-ray topography studies of the defect structure of KAP have been performed [136–139]. In the most recent by Ester *et al.* [138, 139] the results were compared with AFM studies to obtain a more detailed understanding of the growth behaviour. These studies will be considered subsequently. Several AFM studies have been reported on the {010} face of KAP. AFM studies of removal induced formation of defects and the

development of a method for the preservation of surfaces during removal from solution [125] have been reported. Images of the fundamental steps of the characteristic growth spiral have been shown. A linear dependence between supersaturation and step spacing over a limited supersaturation range was reported. Another significant observation by AFM has been the observation of two-dimensional islands on the {010} faces of thin platelet crystals on which no screw dislocation is emergent [140].

3.6.4 Periodic Bond Chain Analyses and the KAP Growth Unit

Periodic bond chain (PBC) analysis of the KAP crystal structure has been invoked by several authors to explain experimental observations from crystal growth experiments with KAP (see for example Hottenhuis and Lucasius [128]). Three PBC analyses of the KAP crystal structure have been published. Jetten performed the first such analysis [119]. The work of Jetten was extended by Hottenhuis *et al.* [120] who performed extensive and comprehensive first order (i.e. neglecting second order bonds) PBC analyses of the KAP crystal structure and compared various morphological models with actual experimental results. Finally, Hottenhuis and Lucasius [124] performed a second order PBC analysis though this was confined to the {010} crystal slice. In all cases {010} was reliably found to be the most important face though the analyses were less successful in predicting the order of morphological importance of the lesser faces as observed in experiments.

Strom [141] has recently discussed the validity of PBC analyses for the prediction of crystal habit from solution in which she has stressed the appropriate choice of growth unit and crystal slice thickness. The choice of growth unit plays an important role in PBC analyses since only bonds formed during the growth process are significant. To date every observation of which the author is aware has shown the height of fundamental steps on KAP to be of unit cell height (see for example [125]). Consideration of the KAP unit cell shown in figures 3.4, 3.5 and 3.6 shows that the KAP unit cell comprises four KAP residues, stacked two high in the [010] direction (normal to the (010) plane). The fundamental step therefore must be two KAP residues high and this implies that this unit cell high step should represent the crystal slice in the PBC analysis. Reference to these figures also suggests that the slice may be coincident with the (010) planes of the unit cell indicated, or that it may be coincident with the (020) planes of this unit cell. In the absence of significant reconstruction of the surfaces, which appears unlikely with the highly directional bonding in this structure, this would imply a

potassium terminated surface or a hydrogen phthalate terminated surface respectively. In previous work it has been assumed that KAP grows by the arrival of potassium, K^+, and hydrogen phthalate, HP^-, ions at kink sites. According to Jetten [119] the rate determining step in the growth of KAP from aqueous solution is the incorporation of the K^+ ion because it has the highest hydration energy of the two ions. Before integration to the crystal the bonds with the solvent molecules must be broken. According to this hypothesis, the advance of a unit cell high step must proceed by the arrival and dehydration of two ions of each kind, resulting in the stacking of one KAP residue on top of another. This could conceivably occur sequentially rather than simultaneously, with the arrival of one ion pair forming a KAP residue at the step followed by a second which stacks on top of the first. From probabilistic and steric viewpoints the sequential route appears to be a more favourable proposition. There is, however, a third possibility which is that the actual growth unit is a dimer formed from two K^+ and two HP^- ions, which pre-exists in solution. Growth then would proceed simply by the integration of these dimers at the kink sites. The dimer as growth unit idea for KAP was promulgated by Barber and Petty [142] who argued that KAP would be expected to dimerise in solution and that this accounted more readily for the crystal habit of KAP than assuming separate ions as growth units.

One further piece of experimental evidence lends indirect support to the dimer hypothesis. In one of a series of studies of the effect of impurities on the crystal growth of KAP, Hottenhuis and Lucasius [123] concluded that although cations, particularly trivalent cations such as Cr^{3+}, had a profound effect; anions had no discernible effect on the growth of KAP {010}. This was confirmed through experiments with the chloride ion in advance of experiments with chloride salts of transition metals. Considering the Cabrera-Vermilyea terrace adsorption model, this requires that the adatoms are immobile and by implication that the bond between terrace and adatom is strong. This should imply that the {010} surface termination of KAP in solution is anionic. That is, the surface would be expected to be terminated by HP^- anions, since a cationic termination would not be expected to strongly interact with impurity cations. If the growth units are the individual ions and they join the step sequentially in the manner described above, then exposed or partially hydrated potassium cations must nonetheless exist briefly at the step. The simultaneous arrival, dehydration, orientation and integration of two ions of each kind must be regarded as energetically unfavourable and improbable. Neglecting steric hindrance then (since anions are typically larger than cations), it is to be expected that exposed potassium cations will occasionally interact with impurity anions and a discernible impurity effect due to anions would result. However,

in the KAP dimer described by Barber and Petty [142], the potassium cations would be effectively screened electrostatically and sterically from impurity anions, both in solution and in the step. The surface presented to the solution if growth proceeds by the KAP dimer would automatically be the hydrogen phthalate termination suggested by the role of impurities. Therefore, the dimer hypothesis deals with the relative effects of anions and cations whether terrace adsorption by a Cabrera-Vermilyea model, or step or kink adsorption is assumed. In contrast, the separate ions hypothesis requires that supposition about steric effects must apparently be invoked to account for the absence of an anion effect. In their own study Hottenhuis and Lucasius [124] have stated that the {010} face is terminated by potassium ions, however the theoretical or experimental basis for this conclusion is not made clear and seems contrary to their own experiments with cations and anions. If the growth units were separate ions then phenomena such as surface domains of different termination (for example caused by stacking faults), half unit cell height steps and other phenomena may be expected to occur. However, none of these effects have been reported, lending further circumstantial weight to the dimer hypothesis.

A similar debate has developed over the nature of surface terminations with another common model for crystal growth. In a synchrotron radiation surface x-ray diffraction study, de Vries *et al.* [112, 113, 143] have concluded that the pyramidal {101} faces of potassium dihydrogen phosphate (KDP) are potassium terminated and that this explains the ineffectiveness of cations in affecting growth on these surfaces due to the large adsorption energy barrier which must be overcome. Recently, Strom [141] has examined the claims of de Vries *et al.* in which she has also made an appeal for greater consideration of the step height and hence total growth layer rather than simply the outermost layer of the crystal.

In the PBC analysis of Hottenhuis *et al.* [120] the growth unit was assumed to be the K^+ and HP^- ions. The results of the PBC analysis did not exactly predict the observed habit of KAP. The authors concluded that despite considering Coulomb interactions, Van der Waals interactions and hydrogen bonding, that the analysis suffered from the consideration of only first nearest neighbour bonds; the computational complexity of including second nearest neighbour bonds being too great at that time. They also invoked relaxation and reconstruction of certain faces to account for the noted discrepancies. The role of relaxation and reconstruction on the habit of crystals has been discussed elsewhere [66, 144]. Unfortunately such conjectures are difficult to test experimentally at present however surface x-ray diffraction promises to resolve such

matters in the future. Another potential source of error was present in all of these PBC analyses because the erroneous lattice parameter for KAP mentioned in section 3.6 was used. Since some of the bond energies were based on pair separation potentials, an error in the positions of atoms within the unit cell could result in the assignment of erroneous bond energies. The error amounted to a 4.5% error in the *b* lattice parameter which may have been sufficient to invalidate the analysis. Despite this error however the PBCs predicted for the {010} slice appear consistent with observations which may be due to this slice lying normal to the erroneous lattice parameter, thereby minimising its effect. In any case, since a PBC analysis is concerned only with the actual bonds which form during the formation of the crystal, then the assumption of the growth unit is also of great significance. If the KAP growth unit is in fact the dimer then this analysis would be invalid because one of the stronger bonds of the first coordination sphere of the crystal would have formed in solution and played no role in the crystallisation process. Barber and Petty [142] have critically discussed the results of the PBC analysis of Hottenhuis *et al.*

Part III

Experimental Studies

Chapter 4

Interferometric Studies of KAP Crystal Growth from Aqueous Solution

4.1 Introduction

This chapter contains a description of experiments that were undertaken to accurately measure the growth rates of crystals from solution *in-situ*, as a function of supersaturation and temperature, using optical interferometry. For this work, a novel data acquisition system was developed which allowed the accurate measurement of the normal growth rate simultaneously at multiple points on the crystal surface. This technique has the advantage that correlation and dispersion of growth rates across the face can be studied. This ability is important in providing an experimental means to study the dispersion of growth rates due to step sources of different activities, local supersaturation variations, hydrodynamic effects and growth rate differences between different vicinal facets of the same hillock.

In addition to measuring the normal growth rate, by knowledge of the refractive index of the solution, the wavelength of the light employed and the gradient of the vicinal surfaces, the lateral velocity of surface steps could be calculated. By measuring crystal growth rates in this manner over a range of temperatures and supersaturations, growth rate vs supersaturation relationships can be established, the qualitative form of which

can assist in elucidation of the crystallisation kinetics obeyed during growth.

4.2 Apparatus

The instrument used for interferometric studies of crystal growth is perhaps best described as a system built from a number of subsystems. A schematic diagram of the complete system is shown in figure 4.1. The component subsystems are described in some detail below.

4.2.1 The Optical Subsystem

The equipment used in this study comprised of a two beam Michelson interferometer in which the crystal surface acted as the first reflecting surface and an optically flat mirror acted as the reference surface. Illumination was provided by a 20 mW Helium:Neon laser source providing a fixed wavelength of 632.8 nm (16 in figure 4.1). The light from the laser was first filtered by a set of neutral density filters (17) in order to reduce the intensity. It subsequently passed through a spatial filter assembly comprising a 10x microscope objective (18) which focused the beam to a point in the aperture of a pinhole (19). Diffracted by the pinhole, the light spreads out, forming the characteristic Airy diffraction pattern. The zero order beam was selected by means of an iris diaphragm (20). Higher order rings and noise due to scattering from atmospheric dust were therefore eliminated - providing a stable beam. The cone of light from the iris diaphragm was next focused into a parallel beam again by means of a lens (21) positioned such that it was exactly one focal length from the pinhole aperture. In this way a narrow, parallel "pencil" of light was produced, the diameter of which was a function of the focal length of the lens employed. It was possible to vary this to accommodate crystals of various sizes, however it should be noted that expanding the beam reduced the intensity and therefore adjustments to the amount of filtration had to be made. The narrow pencil of light was next separated into two beams at 90° to each other by means of a beam-splitter (22). The beam-splitter divided the amplitude of the beam evenly and therefore the intensity in each beam was equal.

One of the beams, hereafter referred to as the reference beam, fell onto the optically

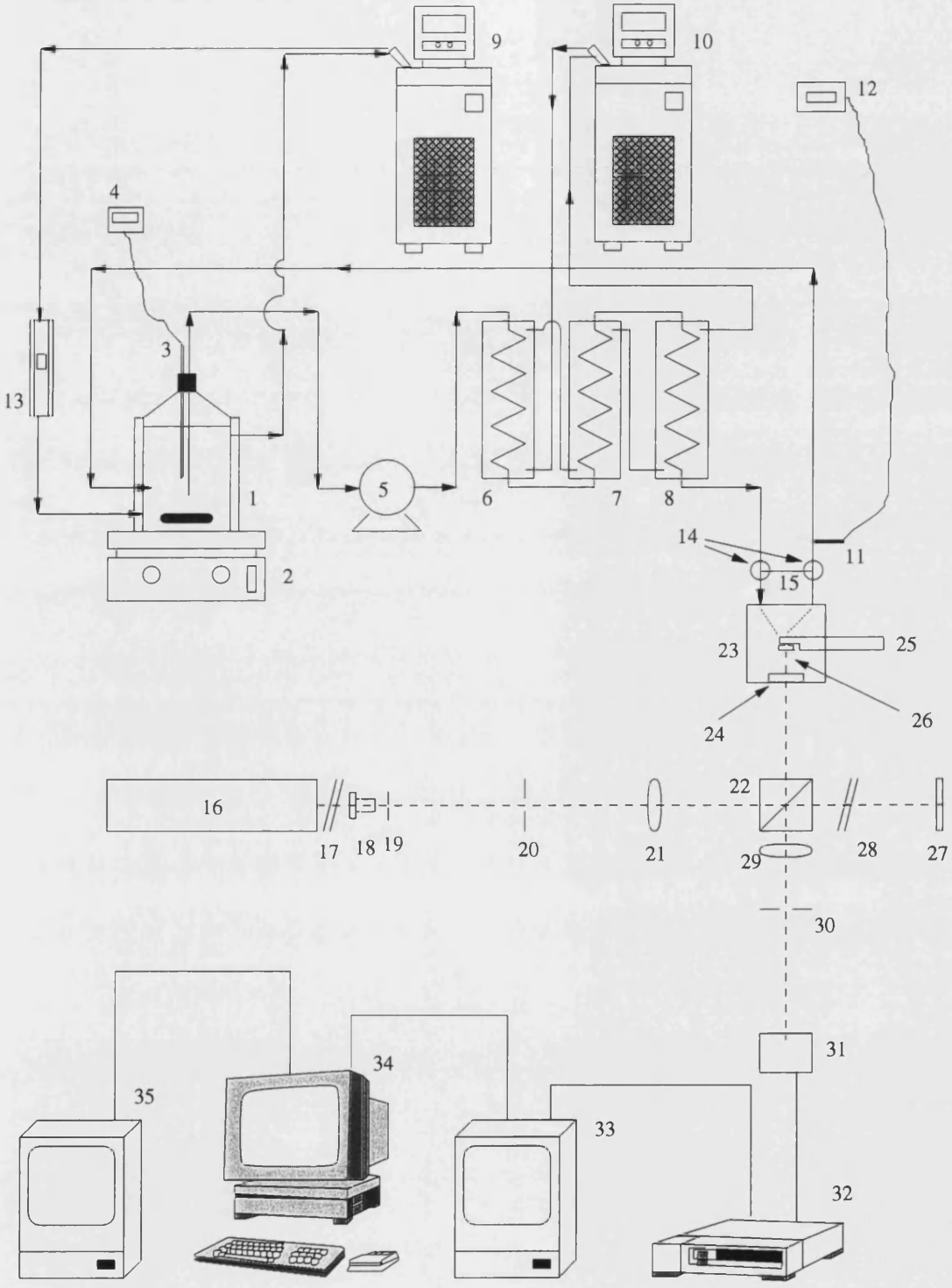

Figure 4.1: The interferometer system (see text for description of numbered components)

flat mirror (27), the other - the object beam - illuminated the crystal (26) which was located on a stub (25) in a growth cell (23) with an optical flat (24) for a window. It was important that the stray reflections from the cell window were not projected onto the camera (31). For this reason an iris diaphragm (30) was located in the back focal plane of the objective and the cell was tilted just sufficiently that the stray reflection was obscured by it. The slight difference in the optical path length across the crystal introduced by this measure was, in any case, corrected for by the crystal alignment procedure to be described later. The optical path lengths of the two beams were carefully adjusted to be equal to each other. Since the illumination source was a laser and therefore highly coherent, this was not as strict a condition for successful operation of an interferometer as would be the case with an incoherent source. Nonetheless, the best results were obtained when the optical path lengths were kept as similar as practically possible.

The reflected object and reference beams were recombined at the beam-splitter and collected by an objective lens (29) which formed a sharply focused image of the mirror and the crystal face on a precisely aligned charge coupled device (CCD) (31), from which a video signal was produced. A live display of the video signal was shown on the high resolution monitor (33). Since the reference mirror is optically flat it therefore formed a featureless and coherent image on the CCD which, when observed without the crystal image, was seen as a field of uniform intensity. If the crystal face was observed without the image of the mirror, then it was observed as a microscopic image of the crystal face. When the image of the crystal was simultaneously focused onto the CCD with that of the mirror however, the phase differences between the two beams caused by the differences in path length due to the surface relief of the crystal resulted in the formation of interference fringes superimposed on the image of the crystal face. Bright fringes were formed in regions of constructive interference, dark fringes in regions of destructive interference. Because the incident beams are of equal intensity and the reflectivity of the crystal surface is substantially less than that of the mirror, for maximum contrast in the interference pattern, it was necessary that the intensity of the reference beam was attenuated in order that it was of equal intensity after reflection as the reflected object beam. This was achieved by placing neutral density filters (28) in the reference beam. Obviously, the optical path length of the reference beam had to be corrected for this.

When correctly aligned such that the mirror was parallel to the net crystallographic plane of interest and the images of both mirror and crystal were correctly focused onto

the CCD, the interference pattern formed was effectively a contour map of the surface relief of the crystal. All points on a given fringe were at the same elevation above an arbitrarily chosen reference plane, normal to the direction of incidence of the object beam and parallel to the net crystallographic planes. Obviously, any changes to the surface relief of the crystal resulted in the motion of fringes as the optical path length differences responsible for the interference pattern changed. A rough surface would give rise to diffuse reflections which would result in a random interference pattern which would appear to be incoherent in the final image. A smooth[1] surface on the other hand would give rise to specular reflections which would produce interference fringes which are coherent over long distances in the final image. Clearly then, if crystal growth proceeds by a cooperative layer-wise mechanism, then the observed motion of the resulting fringes would also appear to be cooperative and orderly.

Clearly it was important for a system capable of measuring extremely small displacements that vibrations which could otherwise destroy the interference pattern, were kept to an absolute minimum. This was achieved by mounting the entire interferometer assembly on an air cushioned optical bench.

4.2.2 The Solution Flow Subsystem

The role of the solution flow system, also illustrated schematically in figure 4.1, was to supply solution at the correct composition, temperature, flow rate and supersaturation for the experiment in question. This required an accurate and stable temperature regulating system and adequate pumps. This was achieved using a circuit in which an undersaturated solution was pumped from a temperature regulated reservoir (1), through a battery of heat exchangers (6,7,8), before entering the growth cell. On exit from the cell the solution returned to the reservoir via a fluid flow meter (13). The reservoir was a custom glass vessel with dual walls for supply of heat exchange fluid. The solution within the vessel was stirred continuously with a magnetic stirrer (2) to eliminate temperature and composition gradients. Pumping was achieved by a magnetically coupled liquid pump (5). Medical grade silicone and glass capillary tubing was used to connect the circuit. The jacket of the reservoir and the heat exchangers were supplied with temperature regulated water from recirculating water baths (9

[1]The terms rough and smooth in this case do not apply to the concept of atomically rough and smooth surfaces as discussed in chapter 2. Rather they apply to surfaces which are rough or smooth on a scale of the order of the wavelength of the light used.

and 10 respectively), with a refrigeration facility[2] . All tubing was lagged with foam rubber insulation which provided sufficient insulation to variations in ambient temperature. The solution temperature was monitored within the reservoir and immediately after exit from the crystal growth cell by platinum resistance thermometers (3 and 11 respectively). The temperature of the water in the recirculating baths was also monitored. The temperature of the solution at the exit from the growth vessel was found to be stable to better than 0.02 °C.

Thus, by adjusting the temperature of the reservoir and heat exchanger recirculating circuits, the temperature of the solution supplied to the growing crystal could be accurately controlled. It should be noted that the solution temperature at the growth cell was under open loop control in as much as there was no feedback mechanism by which a desired setpoint temperature could be reached automatically. Some operator adjustment was necessary to achieve specific temperatures. With the exception of setting the saturation temperature of the solution, specific temperatures were not required exactly and so this was not a major limitation. The main limitation to the achievable supersaturation was the temperature difference between the reservoir and the heat exchanger. The maximum sustainable temperature difference was found to restrict the maximum achievable relative supersaturation to approximately 8%, depending on the saturation temperature of the solution. The systems' solution contact silicone tubing was periodically replaced to minimise the risk of solution contamination. Immediately following crystallisation experiments the crystal growth cell would be removed for cleaning and the circuit would be disconnected from the reservoir vessel and drained of solution by vacuum applied to the reservoir return line. Once drained, the circuit would be flushed several times with de-ionised distilled water to remove all traces of solute. The spent solution was captured in a trap and recrystallised a number of times to recover the solute. As described in section 4.2, the optical system was isolated on an air cushioned optical bench which eliminated most external vibrations. The major remaining source of vibrations was the solution supply pump. It was found however that these were effectively damped by the battery of heat exchangers and that the remaining vibrations could be minimised by suspending the solution supply hose above the bench on a laboratory clamp-stand.

[2]The refrigeration facility was important in ensuring that the ambient temperature did not affect the temperature stability or capability of the system

4.2.3 The Crystal Growth Cell

The growth cell (23) is the part of the system where the optical and solution flow subsystems meet and its importance warrants special consideration. The requirements for a growth cell were that it should allow for the accurate positioning and adjustment of the crystal face (including orientation of the crystal), allow for careful control of the solution flow over the crystal without stagnation or provision of easy nucleation sites, be free from leaks and finally, should provide an un-obstructed optical path for incident and reflected beams. The growth cell used in these experiments was machined from PTFE. PTFE is chemically inert which minimises the risk of contamination of the solution. In addition, PTFE is poorly wetted by aqueous solutions, making it unfavourable for heterogeneous nucleation and, therefore, reduces the risk of unwanted nucleation in the cell. The growth cell cavity was cylindrical in shape with an optical flat window (24) at one end of the cylinder. The optical flat was sealed with a rubber 'O' ring and secured in place with a stainless steel retaining ring.

The seed crystal was mounted on a cylindrical PTFE stub (25) the end of which was cut to accommodate the crystal such that the stub with crystal in place could be inserted into or removed from the cell. Crystals were mounted on the stub with a small amount of two-part epoxy resin. The amount of resin used was kept to a minimum to prevent excessive stresses being induced in the crystal as the resin hardened. The crystal on its stub was introduced into the growth cell through a cylindrical orifice in the wall of the cell, such that it was normal to the axis of the cavity cylinder and hence the incident sample beam. The stub was sealed in position by a rubber 'O' ring which allowed free rotation of the stub, and hence the crystal, with respect to the incident beam. This provided a valuable additional degree of freedom to the assembly which assisted in crystal alignment.

Solution was admitted into the cell through an inlet port on the underside of the cell and exited through a second port on the top of the cell. The location of the solution inlet port was such that solution impinged on the crystal parallel to the face under observation. The exterior of the cell provided integral fittings onto which the silicone tubing of the circuit could be directly connected. The entire cell assembly was mounted onto a precision positioning stage with multiple degrees of freedom, allowing the crystal to be more or less arbitrarily oriented with respect to the incident sample beam. The degrees of freedom provided by the cell assembly included: translation in all three dimensions, rotation in the optical plane and tilt through the optical plane. These were essential for

adjusting the crystal such that the net crystallographic planes of interest were correctly aligned. The solution circuit to the cell also included a bypass line (15) which was opened and closed by means of two three-way (two open, one closed) PTFE valves (14). This allowed the cell to be isolated and removed without stopping the flow of solution in the circuit altogether and risking nucleation in the stagnant solution. This greatly facilitated experiments by allowing rapid crystal changes, eased the start up of experiments and allowed growth to be arrested rapidly for atomic force microscope studies of the crystal face.

4.2.4 The Data Acquisition Subsystem

The purpose of the data acquisition system was to obtain normal growth rates from specific locations in the image of the crystal face using equations 3.1 and 3.2, from which lateral growth rates may be obtained through equation 2.19. In order to do this, some mechanism of counting the number of interference fringes passing a particular point per unit time was necessary. The system that was developed for this purpose is also illustrated in figure 4.1. The system exploited the video signal from the CCD camera. The system consisted of a video cassette recorder (32), a high resolution video monitor (33) and an IBM compatible personal computer (34) equipped with a high resolution video digitiser. The output signal from the video digitiser was displayed on a second high resolution video monitor (35).

Using the video digitiser[3], it was possible to digitise the frames of the video signal into 8 bit gray-scale images. The images generated by the digitiser were represented in memory as 512x512 matrices of pixels with gray-scale values ranging from 0 to 255 representing the brightness of each individual pixel. The software libraries supplied with the video digitiser provided functions for the retrieval of individual pixel gray-scale values and to draw lines and place text on the video display. Thus, it was possible to write software with which the user could select individual pixels within the video image and to sample the gray-scale values of those pixels as a function of time from which the fringe frequency could be obtained.

For this purpose, two separate computer programs were written. The first of these programs, `PIXSEL` (pixel-selector), was used to interactively select individual pixels

[3]The device used was a CX100 image capture board from Imagenation Corporation.

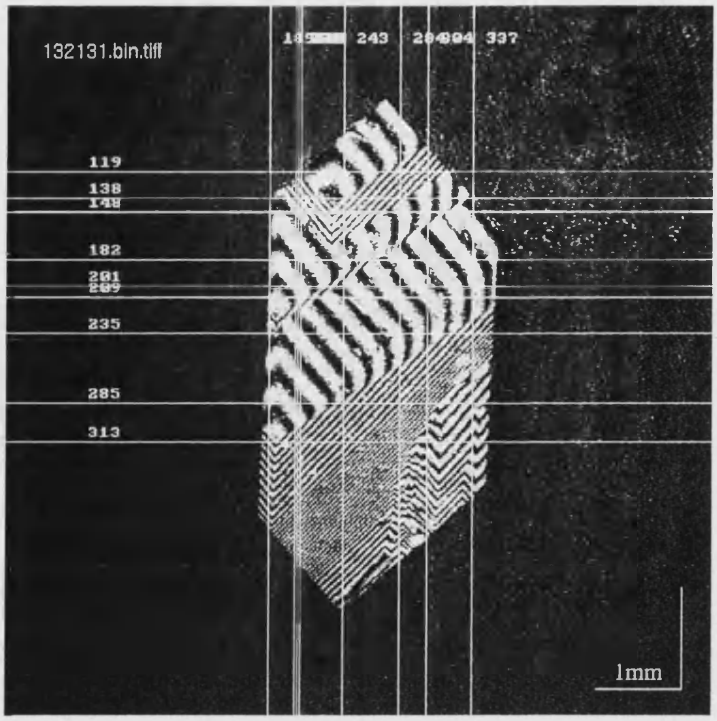

Figure 4.2: An interference image of a growing crystal

for analysis directly on the video monitor screen by presenting the user with a cursor which could be moved by the cursor keys. The selected pixel locations (identified by their display coordinates within the 512x512 pixel matrix) were automatically entered into a parameter file by PIXSEL. These pixel locations were subsequently read by the program ANALYSE which sampled the intensities of the selected pixels at an appropriate sampling rate. ANALYSE also grabbed whole frames at preset intervals onto which it overlaid a grid representing the selected pixels so that a record of the the pixel location with respect to the crystal surface was preserved. ANALYSE was designed in order that it could be run non-interactively from a control script (i.e. an MS-DOS batch file) by use of command line parameters. Figure 4.2 shows an example of an interference image of a growing crystal as captured by the program ANALYSE. The grid superimposed on the image field represents the coordinates of the pixels selected with PIXSEL.

The programs PIXSEL and ANALYSE were written in the C programming language and descriptions and program listings can be found in appendix C. This provided the basis of an interference fringe counting system from which accurate normal growth rates could be measured and from which lateral growth rates could be obtained. When a pixels' gray-scale value is plotted as a function of time, the passage of interference fringes past the represented point on the crystal surface is clearly evident in the peri-

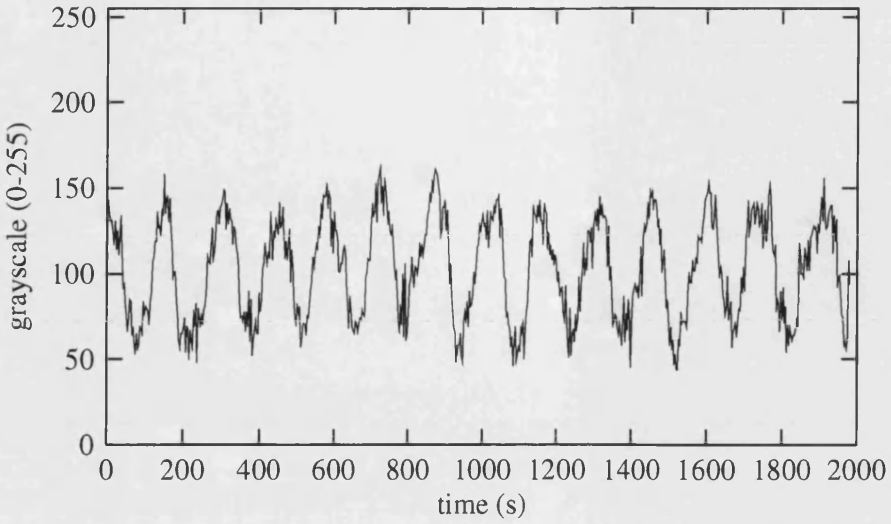

Figure 4.3: An example of a raw intensity time series

odicity of the resulting plot. Bright fringes are shown as high gray-scale values, dark fringes as low values. Figure 4.3 shows examples of raw time series data obtained by ANALYSE.

The number of fringes passing a point in a given time, the fringe frequency, can be measured simply by counting the number of fringes and dividing by the duration of the measurement to obtain the fringe period, the reciprocal of which is the fringe frequency. In figure 4.3 there are approximately 14 fringes in 1980 seconds which yields the approximate value of 141 seconds for the fringe period and 0.0071 Hz for the fringe frequency. However, this approach is only accurate if the time series contains an integer number of fringes which is seldom the case. A more accurate estimate of the fringe period would be obtained by taking a sub-series of fringes between the peaks or troughs of two fringes and dividing by their separation in time. However, a still more elegant approach exploits the fast Fourier transform (FFT) algorithm to perform a spectral analysis of the time series data. Spectral analysis of the time series also allows for additional trends in the raw data such as long wavelength modulations to be observed which are too subtle to be observed by manual fringe counting. For example, in certain cases, the growth rate of a crystal, and hence the fringe period, appears to vary periodically with time. Manual fringe counting methods simply give the average fringe period and this information is therefore lost. Such modulations are however shown as side bands in the frequency spectrum and so they may be quantitatively studied. Figure 4.4 shows the frequency spectrum, or periodogram, obtained by application of the FFT algorithm to the time series shown in figure 4.3. The strong

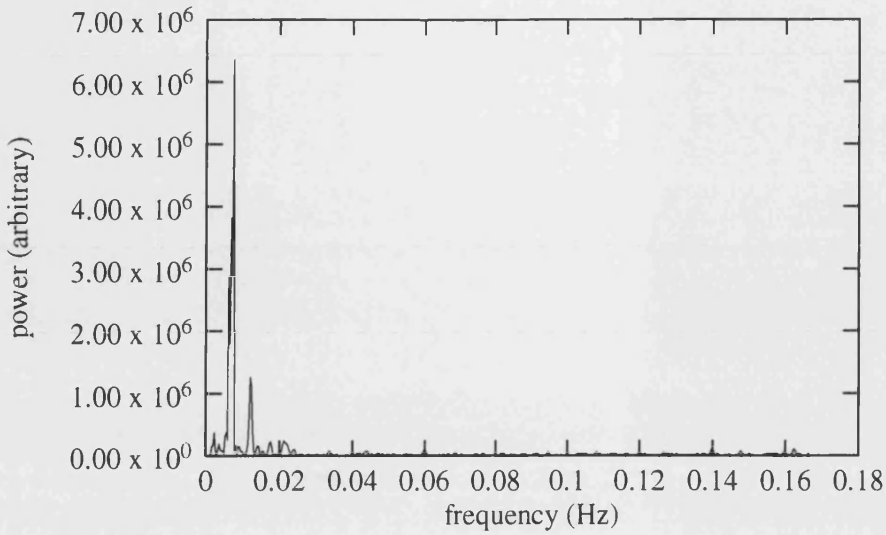

Figure 4.4: Frequency Spectrum of raw time series from figure 4.3

peak represents the fringe frequency of the time series, the peak value is at 0.0071 Hz corresponding to a fringe period of 141 seconds, in good agreement with the values obtained manually. The actual numerical values of the ordinate, power, are related to the image contrast, device gains and the overall sharpness of the spectrum estimate, i.e. the quality of the data.

A major advantage of the spectral analysis approach over the manual fringe counting method was that it was possible to automate the processing of a large number of fringe time series by means of a computer program. For this purpose, a Matlab program `TRANSPOSE` was written[4] which performed the FFT on a batch of fringe time series data-files, calculated the normal growth rate of each pixel studied by means of equations 3.1 and 3.2 and generated a graphical report.

Another advantage to using a digitiser to solve the fringe counting problem was that, because the whole video frame was digitised simultaneously, any number of pixels in the image of the crystal could be studied simultaneously. For practical reasons however, an upper limit of 13 individual pixels was chosen. The main reason for this limit was the memory requirement. The more pixels that were digitised, the greater the amount of data collected and hence the amount of memory required to store it. Additionally, the time series data for each individual pixel was most conveniently handled within an individual file. The MS-DOS operating system as used, placed an upper limit of 14 on the number of files that could be simultaneously open, thus with one

[4]See Appendix C

control script, this left 13 files available to receive data. As will be seen, in practice it was found that 13 pixels was sufficient to completely characterise the crystal growth in almost all cases.

Typically, 13 pixels allowed for some redundancy in that surplus pixels could be selected so that, in the event that crystallisation conditions rendered some pixels useless for analysis, enough data would be collected from other parts of the crystal that reanalysis was seldom necessary. In normal operation of the system, the data acquisition was performed offline in a batch-wise process by recording the CCD video signal onto videotape for subsequent processing. This approach was preferable to live analysis of fringe motion because the videotape could be replayed and the most appropriate pixels for analysis could be selected, with the advantage that the future behaviour of the surface was already known in advance. In addition, by storing a permanent record of the interferometry footage, the crystal growth could be reanalysed at will.

4.3 Data Processing and Analysis

4.3.1 Interpretation of Frequency Spectra

With good quality raw time series data, the fringe frequency obtained is an accurate and precise measurement of the fringe periodicity. However, in some cases, interpretation of the spectra obtained by application of FFT to the time series requires an element of caution. Good quality data means low noise, high amplitude time series with sufficient periods present to allow the FFT to produce a sharp spectrum. The latter is very important because the FFT effectively estimates the spectrum from the data with which it is supplied. The more periods which are present in a time series then the more precise this estimation can be and the sharper the spectrum. Therefore it is very important when performing such an experiment that the duration is sufficient to capture enough periods for accurate spectral estimation. Clearly, lower growth rates will result in lower fringe frequencies and will require a correspondingly longer data capture duration to sample sufficient periods. During an actual experiment, the duration required for sufficient fringes can only be estimated by reference to the fringe frequency observed live. With practice it becomes possible to estimate minimum durations quite accurately. As a general rule however, at least ten minutes of footage

was collected in most cases. The major source of noise in such time series was wobbling of the interference fringes as a result of vibrations. As described in section 4.2, measures were taken to minimise this noise; however some small vibrations, particularly from the pump, were inevitable. Provided that these vibrations were small then reliable time series could be obtained. Excessive noise, especially if periodic, could result in spurious peaks in the frequency spectrum and a less sharp spectrum generally. If noisy time-series resulted, it was possible to use orthodox signal processing techniques such as filtering, autocorrelation and smoothing, to extract a reliable signal. Though these techniques worked satisfactorily, with sufficient vibration reduction and the redundancy built in to the data acquisition system, it was almost never necessary to perform any signal processing.

Another possible source of spurious peaks in the spectrum was due to saturation of the CCD and video digitiser. These devices can only respond proportionally to changes in intensity within a finite range or bandwidth. There is an upper limit to the maximum intensity which the device can distinguish. Above this threshold the device is saturated and can only output a signal equal to the upper limit of the range. If a periodic signal exceeds the intensity threshold of the device then the peaks of the input signal are "clipped" or flattened off. Effectively, the input signal has been modulated or "windowed" by the intensity range of the device. Such clipping is unambiguous in the resulting raw time series output from the device and it does not affect the number of fringes which can be counted manually. However, when the FFT is applied to obtain the frequency spectrum, spurious peaks appear due to the device saturation. Without reference to the original time series, these peaks may be misinterpreted as real features of the input signal. Where only the fringe frequency is required and the true signal is strong such that its peak dominates the spectrum, then some clipping is tolerable. Nonetheless, experimental measures were taken to prevent saturation and the raw time series was always inspected for evidence of saturation. This check was facilitated by the graphical report produced by `TRANSPOSE` which placed the raw time series adjacent to the corresponding frequency spectrum so that they may be compared.

The simplest measure to eliminate saturation is to adjust the intensity of the light falling on the CCD by means of neutral density filters. Also, where possible the saturation threshold of the devices may be adjusted. If a clipped time series is obtained it is again possible to remove the spurious spectral peaks by signal processing techniques however this is seldom necessary if appropriate precautions are taken in the operation of the experiment. The approach taken throughout was to obtain the best quality raw data

possible through experimental adjustments to prevent reliance on signal processing.

The final possible source of spurious peaks in the frequency spectrum was due to the finite sampling rate. According to a theorem of Nyquist [145], there exists a fundamental upper limit to the highest frequency which may be reliably reconstructed from an input signal by discrete sampling of that signal. This frequency, the Nyquist frequency, is one half of the sampling frequency. For example, if a signal is sampled at 20 Hz, then the highest frequency which can be reliably obtained in the resulting frequency spectrum is 10 Hz. Conversely, the sampling frequency must be at least double the highest frequency in the signal if the signal is to be reproduced without loss of information. Any frequency which exceeds the Nyquist frequency will be aliased. Aliasing is the phenomenon in which a high frequency appears spuriously at some lower frequency below the Nyquist frequency as a result of being sampled after multiple periods. In the above example, a frequency at 15 Hz may be aliased to 7.5 Hz as a result of being sampled at every other cycle. In order to maximise the reliability of the sampling process then, the sampling rate should be maximised. In practice however, higher sampling rates increase the memory and storage requirements of the computer and demand more "mission critical" software. In this study the time series were typically obtained by sampling the video signal once every 3 seconds, giving a sampling frequency of 0.333 Hz and a Nyquist frequency of 0.1666 Hz. This was equivalent to a minimum fringe period of 6 seconds which could be reliably sampled at this frequency. In general only the very shortest fringe periods encountered in this study, at high saturation temperatures and high supersaturations, approached this limit. In these cases the sampling period was increased to 1 second corresponding to a sampling frequency of 1 Hz and a Nyquist frequency of 0.5 Hz which was sufficient for all fringe frequencies encountered in this study.

4.3.2 Vicinal Facet Inclination

For calculations of step velocity the vicinal hillock slope referred to the net crystallographic plane, in this case the (010) plane of KAP, had to be measured. This was also achieved by way of the interference fringes. For measurements of normal growth rates the intensity of a fixed point on the crystal surface was monitored as a function of time to give a temporal distribution of fringes. In the case of slope measurements, the spatial distribution of intensity normal to the interference fringes was measured along a line at a fixed instant in time. This was achieved by digitising frames from the video

footage and using image processing software which allowed the gray-scale intensity of a user selected line in an image to be retrieved. Because of the periodicity of the fringes along the line, the resulting intensity distribution along the line is also periodic. The result is a periodic function qualitatively similar to the time-series, however here the abscissa is replaced by distance rather than the time. Therefore the number of fringes per unit distance can be counted along the line and from this the surface slope, $p = \tan\theta = h/y_0$, can be obtained. The more closely spaced that the fringes are then the steeper is the surface. From the surface slope, the mean step separation can be obtained. In conjunction with the normal growth rate these data can then be used to obtain the mean surface step velocity, v, from the relationship $R = pv$. The step separations and velocities obtained by interferometry are at best only averages because only the aggregate behaviour of several hundred steps can be resolved. This limit is imposed by the resolution limit of the laser light used. Because the distribution of steps on the crystal surface cannot be resolved directly it is not possible to obtain a direct measurement of step velocities by interferometry. If however the step distribution on the surface can be observed by an alternative technique, then the step velocities obtained by the interferometry technique can be re-interpreted.

By direct analogy with the spectral analysis of the time series data, the spatial fringe data could be analysed by the FFT algorithm to produce a spatial frequency spectrum. In this case, the positions of peaks gave the separation of fringes in space rather than in time. All of the preceding arguments about the interpretation and processing of time frequency spectra apply equally to the spatial frequency spectrum.

4.4 Experimental Procedure

4.4.1 Seed Preparation

Seed crystals for crystallisation experiments were prepared by the evaporation method. An aqueous[5] potassium hydrogen phthalate (BDH "Analar", recrystallised once) solution, saturated at 35°C, was poured into crystallisation dishes and covered with PVDC film. A single pin hole was made in the film on each dish and the dishes were transferred to a laboratory incubator maintained at a constant 35 °C. Thus, the solution was

[5]De-ionised, distilled water water was used throughout.

initially maintained at its saturation temperature, providing no driving force for nucleation and crystal growth. However with the slow evaporation of solvent afforded by the pinhole, the solution became supersaturated very slowly. This resulted in a very low nucleation rate leading to the production of a small number of relatively large, relatively perfect crystals. The crystals were harvested from the solution when they had reached the optimum size for interferometry of approximately 5 mm in the longest dimension.

The harvesting step was particularly critical. It is the step in the process in which the seed crystal was removed from its solution. However the necessary disturbance to the crystal and solution could damage the crystal and also result in rapid nucleation which could cause new crystals to grow rapidly on existing crystals. This kind of uncontrolled growth had to be minimised. Therefore the seed crystals were removed from their solution as quickly and as gently as possible. Harvesting was performed by removing the film from the dishes and pouring hexane onto the solution. Care was required to ensure that disturbance of the solution was minimised during this step. Hexane was used because it forms an immiscible layer on top of the solution and KAP is insoluble in it. The seed crystals were gently lifted through the hexane layer on a softwood spatula, carved specifically for the purpose. The use of a softwood spatula minimised the risk of damaging the crystals and the capillary effect of the wooden grain assisted in removing excess solution from the crystals. Because of the immiscibility of the hexane and the aqueous solution, the solution is displaced from the crystals as they are pulled through the hexane layer. Immediately after removal from the crystallisation dish the crystals were rinsed with more hexane from a wash bottle to ensure that all traces of solution were displaced. The crystals were then dried on tissue paper before wrapping in tissue paper and storage in individual sample boxes.

4.4.2 Solution Preparation

Solutions were prepared for crystallisation experiments by filling the solution reservoir with de-ionised, distilled water and an excess of potassium hydrogen phthalate (BDH "Analar", recrystallised once). The reservoir was then sealed and stirred continuously whilst recirculating water through the vessel jacket at the desired saturation temperature for no less than 72 hours. This ensured complete saturation of the solution. The solution was subsequently filtered under vacuum into a preheated Buchner flask to remove any un-dissolved solid and nuclei before transfer into a preheated conical flask.

The conical flask was sealed with laboratory film and stirred for approximately 2 hours with gentle heating to re-dissolve any crystal nuclei which may have formed during the filtration stage and to remove dissolved gases which could otherwise accumulate in the circuit due to cavitation from the solution pump. Whilst the solution was stirred, the vessel was thoroughly cleaned and rinsed with de-ionised, distilled water to remove all traces of solid KAP. Finally, the solution was returned to the reservoir vessel. Once in place, the circuit was primed with solution by drawing it through the circuit under vacuum applied to the solution return line. The first 200 ml of solution drawn through the circuit was collected in a trap and discarded to prevent contamination from any residues left in the circuit from previous crystallisations. After ensuring that all air was removed from the circuit lines the circuit was closed and solution was pumped in the undersaturated condition for several hours to allow the system to stabilise before attempting any crystallisation. All glassware used in the preparation of solutions was thoroughly cleaned with a preparation of potassium permanganate in concentrated sulphuric acid followed by rinsing with de-ionised distilled water.

4.4.3 System Calibration

Certain parts of the system required periodic calibration. The platinum resistance thermometers were periodically calibrated by immersion in an ice-water temperature invariant bath and in boiling distilled water. The set temperature of the recirculating units was checked in turn with the calibrated thermometers and the appropriate temperature offsets were programmed into their controllers. The other crucial calibration was the magnification of the optical subsystem. In order to obtain useful quantitative data from the instrument, particularly with regard to lateral step velocities across the crystal surface where precise knowledge of the true dimensions was essential, accurate calibration of the instrument was required such that dimensions in the digitised images could be accurately measured. Magnification calibration was achieved by the use of a glass rectangle of known dimensions placed at the object plane of the objective lens. The glass rectangle, similar in dimensions to a typical crystal sample, was cut from a normal microscope slide[6]. The dimensions of the glass test-piece were accurately measured with a travelling microscope and the surface was scored in order that its orientation would be unambiguous. The rear surface of the test-piece was ground with emery paper to prevent it from specularly reflecting light which could otherwise be

[6]Microscope slides are sufficiently optically flat to serve as a cheap, readily available reference surface.

confused with reflection from the front surface. The test-piece was then permanently glued into place on a PTFE sample stub with two-part epoxy resin.

The instrument magnification was calibrated by placing the test-piece into the growth cell. During calibration, solution was pumped in the cell in order to keep the conditions the same as in a true crystallisation[7]. The test-piece was first adjusted such that it was in normal alignment to the CCD. This was achieved by first blocking the reference beam such that the image formed by the CCD was of the test-piece without a superimposed fringe pattern, followed by translation of the stage normally with respect to the CCD. By so doing, differences in focus across the sample could be observed in the image of the test-piece formed on the monitor. If one side of the sample is in sharp focus when the other side is blurred, the test-piece is not aligned with the CCD. The sample orientation was adjusted until the focus was even across the sample. Once the correct sample orientation with the CCD was established, the reference mirror was adjusted to give the correct orientation with the test-piece. This was achieved by obtaining a single fringe spanning across the entire test-piece. Once this condition was reached, a digital frame was grabbed from the live video display and the aforementioned pixel selection program `PIXSEL` was used to measure the number of pixels in the appropriate known dimensions of the test-piece. Thus, the length represented by a pixel in the display could be measured.

When subsequently performing a crystallisation experiment, the limited depth of focus of the image forming optics ensured that the crystal face was located at exactly the same position as the test-piece had been, and therefore that the relevant pixel magnification values could be reliably used. In addition to allowing the instrument magnification to be accurately established, the calibration test-piece of known dimensions allowed the system to be checked for aberrations and distortion caused by misalignment of optical components. This was performed by checking the aspect ratio of the image of the test-piece. By ensuring that the image aspect ratio matched the true test-piece aspect ratio, aberration and distortions could be eliminated. A useful test of the resulting images for distortions was to measure angles in the images of crystals. As will be shown, the angles formed between different vicinal facets by the interference fringes are unreliable, however the angles between face edges in the image are fixed by the crystal structure and may be reliably measured to check for distortion.

[7]Failure to do so would result in errors as a result of the change in optical path length produced by the refractive index change on filling the cell with solution.

For the purposes of accurate measurement of growth rate, it was also crucial that the refractive index of the solution was accurately known. Because the crystal was immersed in its solution, differences in surface relief across the crystal surface were observed as interference fringes due to differences in optical path length. The optical path length differences were, therefore, dependent on the refractive index of the solution. For this reason it was important that accurate measurements of the refractive index were made. To this end, a series of measurements of solution refractive index were made over a range of temperatures and concentrations by means of an Abbé refractometer. Details of these measurements can be found in appendix A.

Though not strictly a calibration, it was necessary to know if the crystallisation process in the growth cell was operating within a diffusion or a kinetic regime. Ideally, for a study of surface dynamics and growth kinetics such as this, the supply of solution should not be the rate determining step in the growth process. If this were the case, then volume diffusion effects would make the interpretation of growth rates in terms of elementary processes considerably more difficult if not impossible. Thus, a series of preliminary experiments was conducted in order to establish if the crystallisation was volume diffusion limited or otherwise. These experiments involved growing a crystal at constant supersaturation with a variable solution flow rate. These experiments revealed a flow rate threshold below which the growth rate dropped for a given supersaturation which was interpreted as a transition to the diffusion limited growth regime. For this reason, all experiments described here were performed at the maximum achievable flow rate of the system at which the growth rate was insensitive to flow rate. Details of these measurements may be found in appendix B.

4.4.4 System Operation

In order to perform a crystallisation experiment, initially the temperature regulating circuits were adjusted such that the solution temperature in the growth cell section of the circuit was equal to the nominal saturation temperature (the temperature at which the solution was originally saturated). This was achieved by adjusting the temperature regulating circuit of the heat exchanger whilst ensuring that the reservoir temperature remained 1-2 °C above the saturation temperature[8]. At this stage, the growth cell itself was bypassed and empty of solution. Once the nominal saturation temperature of the

[8]This is essential to ensure that nucleation does not occur in the reservoir.

solution was reached, a freshly cleaved crystal on a PTFE stub was introduced into the growth cell and adjusted to form a focused image on the video monitor. Solution was then admitted into the growth cell by switching the bypass valves so that all of the solution was flowing in the growth cell. The crystal was readjusted to compensate for the change in optical path length due to the solution and the illumination intensity was adjusted by means of neutral density filters to compensate for the reduced reflectivity of the crystal face in solution compared to air. Once a sharp image was obtained, the crystal was adjusted in order that the cleavage face was correctly aligned in the interferometer. This was done by adjusting the various positioning screws of the cell assembly until a single interference fringe covered the image of the face. When this condition is met, the optical path length is the same across the face. Once this condition is met it is necessary to ensure that the crystal remained in alignment during translation of the crystal forward, as will be the case during growth. In order to do this the crystal is translated forwards and lateral adjustments made iteratively until the single fringe remains during translation. If during translation the face rotates with respect to the interferometer then multiple fringes will appear. Once correctly aligned, the crystal was not adjusted further.

The crystal was next observed to establish if it was at equilibrium, growing or dissolving. Despite careful preparation of the solution, it is possible that its saturation temperature may change slightly due to evaporation of solvent during the filtering stage or due to residual rinsing water in the flow-system. For accurate measurements, it is essential that accurate determination of the saturation point is achieved. Extremely low growth or dissolution rates are difficult to observe so to make this possible, a frame was grabbed by the video digitiser and the still image was displayed on the video monitor. The live crystal image was then compared to the still image to observe changes with time. This could be achieved on the same monitor by switching between the live and the stored images. This technique allowed far greater sensitivity to subtle changes to be achieved. In the event that the crystal was growing or dissolving, the solution temperature was modified appropriately and the process of recording a frame and comparing with the live image began again. This iterative process was continued until the live and stored crystal images remained unchanged for at least 60 minutes. Once this condition was met, the actual solution saturation temperature was recorded. The problem of establishing the true saturation temperature is made more difficult by the possibility of a dead zone due to impurities. As a result, it is possible that the crystal may neither grow or dissolve, despite a significant supersaturation or undersaturation. This results in an uncertainty in the actual saturation temperature. This situation was remedied to

some extent by dissolving the crystal slightly until a small number of etch pits appear and then iteratively changing temperatures whilst studying the etch pits. The opening and closing of the etch pits is very sensitive to the supersaturation and by examining if they are growing larger or smaller the saturation temperature may be found with more certainty. Nonetheless some uncertainty will always remain in the absolute saturation temperature though by following these methods this may be minimised.

The growth experiment could now begin. Firstly, the solution temperature was increased and the crystal was dissolved substantially until the specular reflection from the crystal face disappeared altogether. The crystal was then re-facetted by adjusting the solution temperature to a moderate supersaturation between 3-4% and allowing it to grow until the face was recovered. This step of dissolving and re-facetting the crystal served to eliminate stresses and cracks etc induced in the crystal by harvesting and cleaving or to remove solvent occluded during the seed growth. Thus, a relatively perfect crystal surface for observation was obtained. Re-facetting was conducted at moderate supersaturations because growth at low supersaturation promoted the effects of solution borne impurities whereas high supersaturation growth promoted the occlusion of solvent, forming inclusions buried within the crystal.

It was particularly important to avoid the latter as they were aligned with the crystallographic plane of interest and were very strongly reflecting, preventing the observation of either the surface or interference fringes which, if sufficiently large, rendered the crystal useless for study. Once the crystal had re-facetted fully, after checking the crystal alignment and focus, video footage of the growing crystal was recorded for subsequent growth rate measurements. Video footage was collected at constant solution temperature for a period of time appropriate for the growth conditions. This meant ensuring that recording time was adequate for recording sufficient interference fringes to produce a well defined time series of pixel intensities with sufficient periods for accurate spectral analysis. The actual duration of each recording was dependent on the supersaturation and the temperature because these parameters affect the rate of crystal growth and hence the number of fringes passing a point in unit time. An upper limit to the duration of the recording was given by the necessity for the image of the crystal to remain in focus. The depth of focus of the instrument was limited and adjustments to focus could not be made during individual recordings as this would destroy the stable interference pattern. For this reason, the focus was checked and adjusted prior to each recording and recording durations were limited to periods within which no significant change of focus occurred (typically 10 to 30 minutes, depending on growth rate).

After recording growth at one temperature, the solution temperature was adjusted and the system was allowed to equilibriate for no less than 30 minutes before the next recording was made. Typically, having started recording at the re-facetting temperature, the temperature would be increased in steps (with recordings made at each step) toward the known saturation temperature and thus to increasingly lower supersaturations. The size of the temperature steps used depended on the supersaturation. At lower supersaturations, the temperature steps were necessarily smaller, as a given temperature step had a greater effect on the relative supersaturation than at higher supersaturations. Each crystal and videotape used was given a unique reference number. The crystal identity, solution temperature, saturation temperature *etc.* was conveniently recorded on a chart as appearing between specific times on the videotape. Thus each crystal and piece of footage had a unique identity and were easily traced. Video footage of crystallisation was always recorded for an integer number of minutes to simplify the subsequent analysis of the videotapes.

Having approached as close as practically possible to the saturation temperature, higher supersaturations would next be set by lowering the temperature beyond the re-facetting temperature. In some cases, especially where there appeared to be excessive impurity poisoning, the crystal would be re-facetted again to allow measurements to be conducted on a relatively perfect surface. In making recordings at higher supersaturations, the solution temperature was typically taken to its limit (i.e. the maximum sustainable temperature drop) to provide growth rate data over the widest possible range of supersaturations.

4.4.5 Data Analysis

Once the actual live footage was recorded then the data analysis was performed to produce digital time series data of the fringe motion. In practice this was performed by digitising an entire video tape in a single pass. Firstly, the videotape was reviewed with reference to the crystallisation record. For each individual segment of crystallisation footage on the videotape, `PIXSEL` was used to select up to 13 pixels for digitisation. Pixels for digitisation were selected by observation of the growth footage and seeking pixels representative of specific vicinal faces or pixels of particular interest for specific reasons such as the observation of growth rate fluctuations. Often, pixel pairs related by crystalline symmetry would be selected. This allowed observation of any asym-

metry in crystal growth behaviour which may be due to experimental limitations or possibly for phenomenological reasons. Subsequently, a script program was written to sequentially call the ANALYSE program with the appropriate command line parameters for each segment of crystallisation footage. For videotape segments with no data, a call to an additional program called WAIT was made. The function of WAIT was simply to do nothing for the number of minutes passed to it as an integer parameter on its command line. Because the duration of videotape footage for each segment was always an integer number of minutes, it was therefore possible to write a single control script which would reliably call the appropriate programs with the correct command line parameters at the correct moment. Once the control script and pixel parameter files were set up, it only remained to execute the control script and start the videotape replay simultaneously. This step was typically executed overnight and the individual pixel intensity data files and gray-scale image files were collected for further analysis and archiving the next day. Correct execution of the script was checked by studying the image files grabbed during the course of the analysis. Once recorded and checked, spectral analysis of the raw data and report generation was performed by the purpose written Matlab script program TRANSFORM. TRANSFORM analysed an entire directory of raw intensity time series files non-interactively. This greatly reduced the time required for data analysis.

Chapter 5

AFM Studies of the Growth of KAP Crystals

5.1 Introduction

The experiments described in this chapter were undertaken to study the step structure of the surfaces of potassium hydrogen phthalate crystals, both *in-situ* and *ex-situ*, by means of atomic force microscopy. In particular, most of the observations described here involved imaging the surfaces of crystals after interferometry observations had been made. As described in section 3.4 the atomic force microscope is a relatively recent innovation which allows surfaces to be imaged without the resolution constraint imposed on optical techniques by the wavelength of light. It is a relatively simple matter to obtain images of fundamental surface steps and dislocation outcrops with an AFM. Nonetheless, conducting AFM observations on crystal surfaces presents many unique problems which must be overcome for successful imaging of the surfaces, both with *ex-situ* and *in-situ* observations. However, once overcome, the AFM is an unsurpassed instrument for obtaining a huge amount of information about the crystal growth process at the scale of surface steps; which, from the standpoint of theories of crystal growth, is perhaps the most important length scale.

5.2 *Ex-Situ* Experiments

With the theme of complementary techniques in mind, this section describes experiments which were performed specifically to obtain structural information about the surfaces of crystals grown over a range of supersaturations and temperatures in the optical interferometer described in chapter 4. As was described in that section, the interferometer is an ideal technique for studying crystal growth on the macroscopic scale, allowing the accurate measurement of the normal growth rate and calculation of the step velocity as a function of the supersaturation and temperature through the measured hillock slopes. In addition to the quantitative growth rate data provided, the interference images and "movies" it produces provide considerable information about the motion of steps and dislocations on the whole crystal surface as it grows. However, the directly obtained information is limited to measurements and observations at the macroscopic scale and conclusions about the structure of the surface at finer scales can only be made by inference from the direct observations. This is ultimately a function of the resolution limit of an optical instrument. As the resolution limit of the AFM is much finer than that of optical instruments, further information about the crystal at finer scales can be obtained by removing the crystal from the interferometer growth cell in such a way that the surface is kept largely free from artefacts. If this is performed rapidly then the crystal growth can be abruptly arrested, leaving a snapshot of the crystal surface substantially as it was when growing. Once dry, the crystal surfaces are stable and can be stored for subsequent imaging by AFM. This is the essence of experiments described in this section.

5.2.1 Crystal Removal

As discussed in section 3.4.1, the main obstacle to reliable *ex-situ* AFM observations is the controlled removal of the growing crystals from their solution without the formation of artefacts. Thus, in order to perform such experiments a method had to be devised by which the crystal in the interferometer cell could be removed from its solution extremely rapidly such that artefacts could be minimised. The method adopted followed the argon jet method devised by Ester *et al.* [125] for small KAP crystals. This method was adapted to the large crystals (several millimetres in longest dimension) used in the interferometry experiments. An apparatus was devised which would allow the crystal to be removed on its PTFE stub from the interferometry cell and be

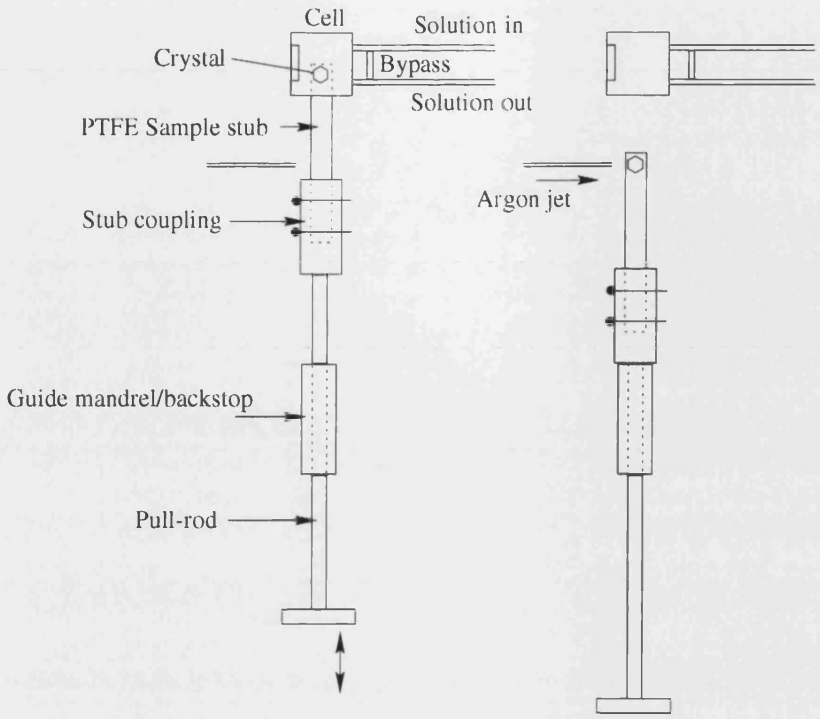

Figure 5.1: Schematic of the pull-rod assembly used for removal of crystals from the growth cell.

immediately subject to a jet of argon gas to remove the residual solution. The apparatus, illustrated in figure 5.1, consisted of an optical mount identical to that of the sample stage of the interferometer, mounted on a bench.

A reciprocating pull-rod assembly was designed to couple with the PTFE sample stub. The argon nozzle was set perpendicular to the pull-rod at the position at which the crystal would come to rest when the pull-rod reached a backstop which also served as a guide mandrel for the pull-rod. The distance and elevation from the crystal position was set to give optimum solution removal without artefact generation. To operate the system during an interferometry experiment, at the desired moment during the crystallisation, the growth cell was removed from its sample stage in the interferometer and transferred to the optical mount on the bench. Solution supply was maintained and uninterrupted during this procedure. The pull-rod was coupled to the PTFE sample stub before the solution supply was rapidly switched through to the cell bypass line and the sample stub simultaneously rotated through 90° and withdrawn from the cell with a smooth, swift action. At the instant at which the pull-rod reached the backstop, the argon jet was activated to remove all solution from the crystal surface. The entire procedure could be completed in less than 60 seconds. This meant that the final crystal surface as obtained for *ex-situ* imaging was essentially the same as that in the last

seconds of interferometry footage. The observations from the two techniques could, therefore, be compared directly.

It is inevitable in any such procedure that a thin layer of solution will remain strongly adsorbed to the crystal surface despite the forced removal of solution by the gas jet. The solute contained within this layer will precipitate onto the underlying surface once the remaining solvent is completely removed. The effective supersaturation in this very thin layer of solution is likely to be far in excess of that experienced during crystal growth in the interferometry cell due to rapid evaporation of solvent. It is, therefore, possible that this material will precipitate onto the surfaces of the crystal in small two-dimensional islands which might be erroneously interpreted as two-dimensional nucleation during the normal course of growth. However, the fact that the technique can produce large crystals with no evidence of two-dimensional nucleation suggests that the amount of adsorbed solvent is very small and does not normally have a substantial effect on the surface structure.

Once completely dry, the crystal surface is then stable and can be removed to an AFM sample stub for subsequent observation. This was achieved by removing the PTFE stub from the coupling and removing the crystal from the stub with a razor blade. This is facilitated by the weak bond between the PTFE and the resin, allowing the crystal to be lifted off onto the razor blade with very little force. Great care must be taken during this step to prevent damage to the crystal. It is crucial that the surface is not contacted at any stage. With the crystal on the razor blade, it can then be carefully deposited onto an AFM sample disk onto which a small amount of paraffin wax has been previously deposited and melted to form a thin film across the disk by the action of a soldering iron tip applied to the underside of the disk. Once the crystal is centrally located on the disk, the soldering iron tip is again brought into momentary contact with the edge of the disk. This is sufficient to melt the wax which wets the underside of the crystal, firmly bonding it in position. This crystal mounting technique has the advantage that very little force or heating is required and the risk of adhesive depositing accidentally onto the crystal face is eliminated. Furthermore, many adhesives and resins contract considerably on curing which could be sufficient to impose considerable stress on the crystal which may distort it and result in changes to the surface as a result.

Once the crystal was firmly bonded to the stub it was transferred to a small sample box in the bottom of which a small magnet was glued. The sample disk is held firmly in place by the magnet ensuring that it does not come into contact with the walls of

the box or any other solid surface which may destroy its as grown surfaces. Samples stored this way were stable and well protected for a considerable period. The face of the crystal whilst growing is in a non-equilibrium state. Once removed from solution there exists the possibility that the surface may relax towards equilibrium with time. The relaxation time for the surface would therefore limit the useful time over which the surface could be reliably interpreted as that due to the growth process. Such caution would be especially true if the material were hygroscopic. Experience has shown however that when stored in dry conditions at room temperature, the surfaces of KAP crystals remain unchanged for at least six months. A discussion of the stability of KAP crystal faces in air and hexane has been given by Ester *et al.* [125]. As a precaution however the crystals were always stored in an airtight dessicator over silica gel.

5.2.2 Crystal Imaging

All crystals obtained from the interferometer cell by the method described above were imaged by tapping mode AFM on a Digital Instruments Nanoscope III scanning probe microscope. A J type scanner, with full scale scan dimensions of 125 μm laterally and 5 μm vertically, was used due to its suitability for imaging at the scale of interest for crystal growth. Silicon tapping mode cantilevers of length 125 μm and nominal force constant of 42 N m^{-1} with square pyramidal tips were used throughout. The instrument was periodically calibrated by means of a semiconductor calibration reticle with a lithographically etched grid of rectangular pits of known dimensions. By obtaining AFM images of such a grid, software routines allow the scanner displacements to be calibrated. In this way dimensions in images could be accurately obtained. The instrument was fitted with an optical microscope with CCD video camera and monitor in order that the crystal and the AFM cantilever could be precisely positioned and located for AFM imaging. This made it possible in some cases to find the centres of vicinal hillocks at which a dislocation outcrop could be found. By working with an interferometry image or real time video playback of the late stages of growth for the corresponding crystal, the location of regions of interest on the crystal surface was greatly facilitated. This was most readily achieved by connecting a video recorder to the microscope video monitor and switching between interferometry playback and live video of the crystal on the AFM sample stage.

Imaging of the crystal was initially performed at low or medium resolution, corresponding to 128 x 128 and 256 x 256 pixel arrays respectively. Once a region of

interest had been found, high resolution imaging at 512 x 512 pixels was performed. Typically, a region of interest would be imaged several times with the image field being enlarged or decreased to show more or less of the surface. AFM requires a considerable amount of operator intervention to maintain image quality by adjusting the various instrument gains. Also, successful imaging is very much an iterative process, requiring decisions to be made based on the foregoing image. For example, if a vicinal hillock centre cannot be found by studying the video monitor, then the scan position must be adjusted by reference to the surface steps observed during imaging. With experience, it becomes possible to work out where the centre of a vicinal hillock must be from the direction of the steps. Finding the centre of a hillock is equivalent to finding a local maximum in the height of the surface, therefore the centre may be located by iteratively searching and moving "uphill". With practice vicinal hillock centres can be found in relatively short time and the dislocation outcrop can be imaged.

Dislocation outcrops at the centres of vicinal hillocks are of course not the only feature of interest on the surface. In this study, surfaces were studied systematically to provide a "survey" of all of the significant features of the crystal surface. This is actually a major undertaking. Given that the maximum image area of the J type scanner was 125 μm on a side and that the crystals used were approximately 5 mm in length, then a crude calculation shows that the maximum image area is of the order of a ten thousandth of the total area of the face. The whole surface therefore represents an enormous area to survey, even more so since the upper size limit of actual scans for reliable imaging were typically 70 μm on a side. Inevitably then the whole surface could not be imaged and some features of surface would be missed. However, by careful reference to the interferometry footage, areas of high activity during growth could be determined and imaged. Indeed, without the complementary interferometry data a detailed survey of the crystal would be considerably more difficult.

The first step in a survey of the surface was to image all of the dislocation outcrops on the crystal. Once this was accomplished, wide area scans of regions of interest suggested by the microscopic examination of the surface and interferometry footage would be scanned. If the area revealed interesting features, then the surface would be imaged more thoroughly with higher resolution and magnifications. Features of interest other than dislocation outcrops could include etch pits, macrosteps, kinematic waves, slip steps, impurity pinned steps, twin crystals and two-dimensional islands. Once the crystal had been thoroughly surveyed it was carefully replaced in its sample box for future study if required. In addition to the study of crystals removed from

the interferometer growth cell, additional miscellaneous observations of KAP crystals were undertaken. In particular this included the observation of freshly cleaved {010} faces to observe the defects introduced by cleaving. Such observations have the potential to help explain the early stages of crystal growth when a freshly exposed surface is first immersed in a supersaturated solution; such as the origin and location of growth spirals.

5.2.3 Post Imaging Analysis

Once the crystals had been surveyed, the images obtained could be analysed to provide quantitative information about the surfaces. For example, surface relief could be viewed by taking a digital section through the image along a line selected by the operator. In particular this allowed the heights of fundamental and macrosteps to be measured, the profile of kinematic waves and shock waves to be measured and the profile of etch pits and hollow dislocation cores to be examined. In lateral directions, step separations, dislocation separation, two-dimensional island size could all be measured. Chapters 2 and 3 have already described the importance and significance of such measurements. When interpreting the resulting images, the resolution limits and artefact and aberration causing mechanisms described in section 3.4.1 were considered.

5.3 *In-Situ* Experiments

This section describes the methods used to study the crystal growth of potassium hydrogen phthalate *in-situ* by AFM. As was described in section 3.4.1, *in-situ* AFM is restricted to the case of very low growth rates and therefore very low supersaturations and accurate temperature control is crucial. For this reason, methods developed by Donohoe *et al.* [146] for the study of protein crystal growth were applied to studies of KAP. In particular, Donohoe *et al.* [146] developed a temperature stage for the Nanoscope III AFM. This device comprised a thermoelectric heat pump based on the Peltier effect, a heat sink for the efficient convection away of heat during cooling and a thermocouple to provide an error signal for a PID controller specifically designed for Peltier thermoelectric devices (from Marlow Corporation). The device fitted within the AFM head without interfering with the *in-situ* cell, the scanner or the optical system.

This device worked with a standard glass *in-situ* AFM cell or with an electrochemistry cell adapted such that a thermocouple junction could be immersed in the growth solution. Donohoe *et al.* successfully used this device for the *in-situ* imaging of lysozyme crystals growing at finite supersaturations by contact mode AFM. For KAP however, despite the sensitive temperature control afforded by this device, it proved very difficult to hold the crystal in a condition of very slow or arrested growth as required for successful imaging of surface steps without excessive distortion. In part this was due to the great difficulty of maintaining a stable temperature in such a small volume of solution. Inevitably small temperature fluctuations arise which can have a large effect on the crystal growth. For protein crystals, this was easily tolerated by their low growth rates but was intolerable for KAP.

As is well known from the theory of crystal growth, the pinning back of steps by impurities can result in a threshold supersaturation below which the steps cannot advance and hence the crystal cannot grow - this is the *dead zone* described in section 2.7.4. For practical purposes, this amounts to a finite range of temperature over which the crystal can be imaged statically *in-situ*. For nominally pure solutions of KAP however, the fact that a static surface could not be achieved suggested that the temperature range over which the dead zone persisted was too narrow for practical imaging. In order to obtain very slow or static images of the surfaces *in-situ* the solution was therefore artificially doped with impurities known from interferometry experiments and previous studies by other workers [122, 123, 128] to slow the growth rate and extend the dead zone. By this method, practical *in-situ* imaging was made possible. Obviously the observations were limited to growth at very low supersaturations or within the dead zone, and in the presence of the impurity. Nonetheless valuable observations were made possible by this technique which provided a useful complement to previous *ex-situ* studies of the effects of impurities on KAP growth.

5.3.1 Crystal Preparation

The *in-situ* studies were performed on micro-crystals of KAP, of the order of 100 μm in length. The method of their production was essentially that described by Ester *et al.* [125]. KAP (BDH, Analar) solutions were prepared from de-ionised, distilled water[1]. Microscopic crystal seeds were nucleated on a stainless steel AFM sample disk

[1]The solution from which the seeds were grown was not doped with impurity

by placing a droplet of KAP solution on the disk and leaving it for several minutes. The excess solution was then removed by a jet of dry argon; leaving small, dry crystal seeds. The disk was then subsequently examined under a low powered microscope to establish that the crystals were suitable in size, number and distribution. If so then they were accepted for *in-situ* observations. The size, number and distribution are functions of the nucleation and growth rate. Excessively large supersaturation gives rise to a high nucleation rate which can result in crystals nucleating on top of each other, uncontrolled growth and consequently poorly defined crystals unsuitable for AFM. The supersaturation could be controlled by controlling the size of the droplet and the saturation temperature of the solution. The extent of growth could be controlled by the residence time of the droplet on the disk.

Once suitable crystals were obtained they were mounted onto the Peltier temperature stage which was in position on the AFM scanner. The AFM head and cell was then assembled around the sample. Doped solution was next introduced into the cell. The doped solution was produced from the same solution from which the seed crystals were grown so that the saturation temperature would be the same. To a fixed amount of this solution the dopant solution was dispensed with a micro-pippette (Eppendorf, 0.1 μl graduations, 10 μl tips) in order to give the desired impurity concentration. This solution was maintained at slightly above the saturation temperature. To fill the cell with this solution, a small quantity was withdrawn by a syringe through narrow bore medical grade silicone tubing and an in-line syringe filter. The syringe was then connected to the input tubing of the *in-situ* cell and solution was gently pumped into the cell, avoiding the entrainment of air. This is essential because air bubbles trapped in the cell prevent imaging by multiple refraction of the laser beam. The outlet port of the cell was also connected to silicone tubing and was left open during filling so that solution could be flushed right through the cell. Once the cell was filled the tubing on the inlet and outlet ports was clamped to isolate the solution in the cell. During the filling process, the temperature controller of the Peltier stage was switched off to avoid excessive control responses resulting in oscillations. Once isolated, the controller was switched on and the temperature reached its setpoint. Provided that during the filling process and early stages of experiment the temperature of the solution was close to its saturation point then the seed crystals were little affected. Once the temperature had stabilised the AFM laser and photocell were adjusted to maximise the signal strength. This step must be performed with solution in the cell because of the changes to the optical path of the laser beam due to the change in refractive index on filling the cell. Once a strong signal was obtained, imaging could commence.

5.3.2 *In-situ* Imaging

The crystal was imaged in contact mode using the J type scanner and silicon square pyramidal tips, 450 μm in length with a nominal force constant of 0.2 N m^{-1}. The scanning conditions were regularly changed to reflect the nature of the scan. The scanning frequency was always set to the maximum allowable for good imaging in order to minimise the distortion due to the finite scanning rate. In practice this was of the order of 10 Hz. Large area scans were avoided where possible due to the potential for even greater distortion.

A significant point about the operation of the Digital Instruments Nanoscope is that the scan direction reverses after each scan. That is, immediately that the end of a scan is reached in the "down" direction the instrument starts to scan the same region in reverse, that is from the "bottom" up. In this way the scanner does not have to make large vertical jumps and imaging reliability is improved since scanner hysteresis effects and so forth are minimised. The complication is that the up and down scans are interleaved in time and therefore the time elapsed between consecutive scans of the same line depends on its location in the raster. The time elapsed between the top and bottom lines between frames is zero, the same scan being used in both frames. The time between scans of the central lines is equal to the scan duration however. For static imaging *ex-situ* this is of little concern, however for dynamic *in-situ* imaging the time elapsed between consecutive scans of the same line is of considerable importance when interpreting images. It is often desirable that the time elapsed between successive scans of the same line in an image sequence is the same for each line. For this condition to be met, either alternate up or down scans must be used, the interleaved scan of opposite direction being left out. Of course this results in the penalty that a period of two complete scans must elapse between successive scans of the same line. However, provided that the dynamics of the surface under observation are sufficiently slow on the time-scale of the scan then no great penalty is incurred.

Crystals were imaged whilst growth was completely arrested and during very slow growth at supersaturations just above that of the dead zone. The upper limit to the obtainable supersaturation was fixed by the extent of distortion and blurring encountered. The effect of blurring due to high growth rates is illustrated in figure 5.2 and the effect of distortion as a result of imaging a large area is illustrated in figure 5.3. For *in-situ* studies, hydrated chromium (iii) chloride was used as the dopant. The solution preparation and concentrations will be given in the relevant results chapter.

Figure 5.2: Blurred AFM image of high velocity steps. KAP {010} growing from nominally pure solution. Scan size 15 μm

Figure 5.3: Distorted AFM of low velocity steps over a large area. KAP {010} growing in chromium (iii) chloride doped solution. Scan size 40 μm

Part IV

Results & Discussion

Chapter 6

Growth Rates and Surface Structure of KAP Crystals

6.1 Introduction

This chapter presents the results of interferometric studies of crystal growth of KAP and the normal growth rates and step velocities obtained therefrom, combined with *ex-situ* AFM of the resulting surfaces where available. The experiments were conducted according to the methods described in chapters 4 and 5. The subsequent discussion seeks to compare the experimental observations with the theoretical models discussed in chapter 2 and, where relevant, with the results of other experimental studies. Due to the large number of figures which must necessarily be presented in a study dominated by imaging techniques, some discussion of the salient features of the figures are presented with the results so that the text may remain close to the figures for ease of reference. A general discussion of the results is nonetheless given in chapter 8.

6.2 Cleaved KAP {010} Faces

Before proceeding to results and discussion of growing crystals it is useful to consider first the structure of the freshly cleaved {010} surfaces of KAP crystals, as revealed

by AFM. Figure 6.1 shows an AFM image of a macroscopically visible cleavage step on an {010} face of a KAP crystal. Several notable features are present in this image. Most notably, the outcrops of two screw dislocations, labelled 1 and 2 for clarity, are visible on the right hand side of the image. As postulated by Frank [33], elementary steps are produced by the screw dislocations. The interpretation of these features as screw dislocation outcrops is quite unambiguous as it is the only crystallographic feature which can explain the termination of the surface steps. It is impossible to tell from this image if the screw dislocations were present prior to the cleavage or if they were generated by the stress of the cleavage. X-ray topography of KAP [139] has shown that screw dislocations are present in as grown crystals and that dislocations may be mechanically generated through cleavage. Regardless of the origin of these specific dislocations, the image is clear evidence for the initial presence of screw dislocations on the surfaces of the seed crystals used in this study, some of which will almost certainly act as growth centres as soon as the crystal is immersed in a supersaturated solution. Other features notable in this image are the large number of elementary steps which combine to form the macroscopic cleavage step. In the lower half of the image, where the elementary steps are more widely separated it can be seen that the crystal appears to have cleaved along clearly defined directions due to the straight edges of the steps and the consistent angles formed between them, which were measured as 90°. This is consistent with the orthorhombic unit cell of KAP. Digital image analysis of the heights of the elementary steps in this image has shown them to be in the range of 1.2-1.4 nm in height which roughly corresponds to the height of the unit cell of KAP in the [010] direction (normal to the image plane).

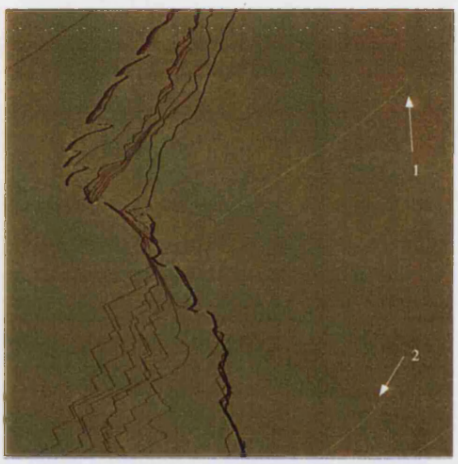

Figure 6.1: Freshly cleaved KAP {010} crystal face. Scan size 25 μm.

Figure 6.2: Close up of cleavage step shown in fig 6.1. Scan size 10 μm.

6.3 Normal Growth Rates of KAP {010}

Having dealt with the origin and occurrence of steps due to screw dislocations on the cleavage surface, this section considers the normal growth rates of such faces. Before presenting and discussing the data itself a comment on its representation is necessary.

6.3.1 Representation of Growth Rate Data

The results presented in this section are a composite overview of crystal growth rates of KAP {010} made on a range of crystals at a range of supersaturations and saturation temperatures. The data presented here have all been obtained by digitising the intensities of individual pixels in the images of growing crystals as described in sections 4.2.4 and 4.4.4. In every case multiple pixels have been simultaneously studied. Typically, the faces of the crystals studied have had multiple sources responsible for their overall growth rate, which is evident from the presence of multiple hillocks. Ideally, the growth rates of individual hillocks are measured at multiple points which, due to the anisotropic nature of KAP growth hillocks, should include measurements on each vicinal facet of the hillock. Often, the various sources on a crystal face have different activities and hence growth rates. This can present some difficulties for the interpretation and representation of the growth rate data. For example it is not valid to simply take some average measure of all of the measured growth rates on the crystal surface. The growth rates measured at different locations on the same growth hillock are correlated due to the fact that they are all produced by the same source and should therefore be identical, assuming that the growth spiral has achieved a steady state. If the latter condition is unmet then the hillock profile will change with time. In the present study, with few exceptions the growth rates of individual facets of vicinal hillocks were found to be the same. However, there is not necessarily any such correlation between the growth rates of individual hillocks as the growth rate of each hillock is due to the structure and supersaturation of the source alone. It is, therefore, possible to measure a distinct and independent growth rate for each hillock.

Occasionally it happens that the growth rates of all of the individual hillocks are the same. When this is the case it may be supposed that the sources all have the same simple structure such as a single dislocation and are all experiencing the same supersaturation. The overall growth rate of the crystal face is that due to the most active

hillock, which will normally come to dominate the crystal face, given sufficient time. This is the growth rate which would be measured with a less discriminating technique such as measurement of the rate of advance of the face. An unambiguous way to represent the growth rate of a crystal at a specific supersaturation would be to report the highest measured growth rate due to the most active source. Valid though this is, it has the disadvantage of making the study of growth rates as a function of supersaturation difficult. This is because from one crystal to another, or even on the same crystal at different times, the activity of the dominant hillock will differ. To establish relationships between growth rate and supersaturation requires comparison of the growth rates of hillocks of *equal activity* at different supersaturations. Since the most active hillocks are likely to be the most complex and therefore effectively unique, this condition seldom holds true and satisfactory relationships cannot be obtained. For low activity sources, the condition of equal activity is much more easily met because the sources are simpler and will tend to have a small number of dislocations. For example, if a source comprised of a single dislocation can always be found on the crystal at any supersaturation then a clear relationship between growth rate and supersaturation is possible because the activity is the same for each source. Unfortunately, this situation is also rare because of the tendency for the sources of highest activity to dominate the growth of the crystal by engulfing the low activity hillocks, causing them to effectively disappear from the crystal face. Due to the chance nature of the occurrence of sources on a crystal face, the activity of the sources present is beyond control. For this reason caution and judgement are required in interpreting crystal growth rate data.

These limitations notwithstanding, in the following pages measured growth rate data in the form of (R,σ) curves are presented. As will be shown, questions about these data arise which demand closer scrutiny of the crystal surfaces. This closer examination will be given in a subsequent section. In the charts which follow the data are presented in such a way as to make the relationships between the growth rate and the supersaturation as clear and unambiguous as possible. Due to the potential for ambiguities to arise as a result of the differences in source activity described in the foregoing discussion, individual representative growth rates measured at a given supersaturation will be presented, no statistical manipulation of the data has been used.

6.3.2 (R,σ) Curves

Figure 6.3 illustrates the composite chart of all of the (R,σ) curves reported in this section. Each curve corresponds to growth rate measurements performed with the same growth solution, the saturation point of which having been determined as described in section 4.4. Each data set has been fitted with a non-linear best fit BCF curve of the form given by equation 2.17[1]. The best fit parameters from the curve fitting are shown in table 6.1 along with standard error estimates of the fitted parameters expressed as both error bounds and as a percentage standard error s_e. Figure 6.3 and table 6.1 allow the trends in growth rate as a function of saturation temperature to be seen, however the individual curves shown in figures 6.4 to 6.9 illustrate the individual data sets more clearly and are discussed individually below. Supersaturation, σ, was adjusted by adjusting the crystal growth temperature as described in section 4.4. The corresponding values for supersaturation were obtained by substitution of the saturation and growth temperatures in equations 3.3 and 2.6. The actual growth temperatures and supersaturations are tabulated in tables 6.2 to 6.7. The error bounds for supersaturation in figures 6.4 to 6.9, and tables 6.2 to 6.7, are due to the potential ± 0.02 °C error in both saturation and growth temperatures, described in chapter 4; and an assumed 5% error in the solubility obtained from equation 3.3. The ordinate error bounds for the growth rate, R, in figures 6.4 to 6.9 account for the error due to the variability of the solution refractive index (see appendix A) and an estimate of the reliability of the FFT procedure for obtaining growth rates. Throughout the remainder of the text, where growth or saturation temperatures are quoted without error bounds, it is to be understood that this means the stated temperature ± 0.02 °C. It is also to be understood that, throughout the following discussion, the actual crystal growth temperature is different for each value of supersaturation for the same solution. The implications of this in terms of thermal effects will be considered subsequently. For convenience, in the following discussion, individual curves are referred to by the saturation temperature of the solution from which they were obtained.

$\mathbf{T}_{sat} = 25.56$ °C

Figure 6.4 shows the normal growth rate data for KAP {010} as a function of relative supersaturation for the solution saturated at 25.56 °C. Two sets of data are shown. The

[1]Curve fitting was performed using the non-linear least squares algorithm of the program GNUplot which utilises the Marquardt-Levenberg algorithm [147].

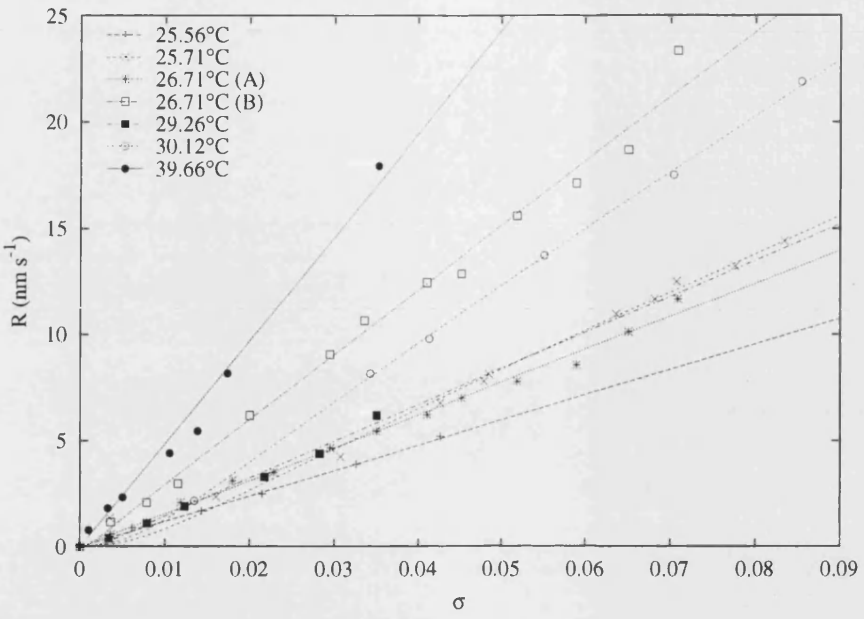

Figure 6.3: Normal growth rate vs supersaturation at several saturation temperatures. The points show measured growth rates, the curves are the corresponding best fit BCF curves according to the key.

T_{sat} (°C)	C ($nm\ s^{-1}$)	s_e (%)	σ_1	s_e (%)
25.56	119.46 ± 2.21	1.85	$1.94 \times 10^{-6} \pm 4.58$	2.36×10^{8}
25.71	176.24 ± 4.76	2.72	0.0203 ± 0.00653	32.09
26.71 (A)	155.17 ± 2.16	1.39	$4.24 \times 10^{-6} \pm 2.22$	5.22×10^{7}
26.71 (B)	303.2 ± 5.80	1.91	0.0032 ± 0.0058	179.4
29.26	169.23 ± 7.11	4.20	0.0071 ± 0.0037	52.05
30.12	258.52 ± 2.15	0.83	0.0194 ± 0.00187	9.63
39.66	485.79 ± 18.05	3.72	$3.93 \times 10^{-7} \pm 5.71$	1.45×10^{9}

Table 6.1: Adjustable parameters obtained from BCF curve fit to experimental (R,σ) curves. s_e is the standard error in the respective fitted parameters expressed as a percentage.

T/°C	σ
25.26 ± 0.02	0.0062 ± 0.0008
24.86 ± 0.02	0.0143 ± 0.0008
24.51 ± 0.02	0.0215 ± 0.0008
23.96 ± 0.02	0.0326 ± 0.0008
23.46 ± 0.02	0.0427 ± 0.0008
23.10 ± 0.02	0.0499 ± 0.0008

Table 6.2: Growth temperatures and relative supersaturation for solution saturated at 25.56 ± 0.02 °C

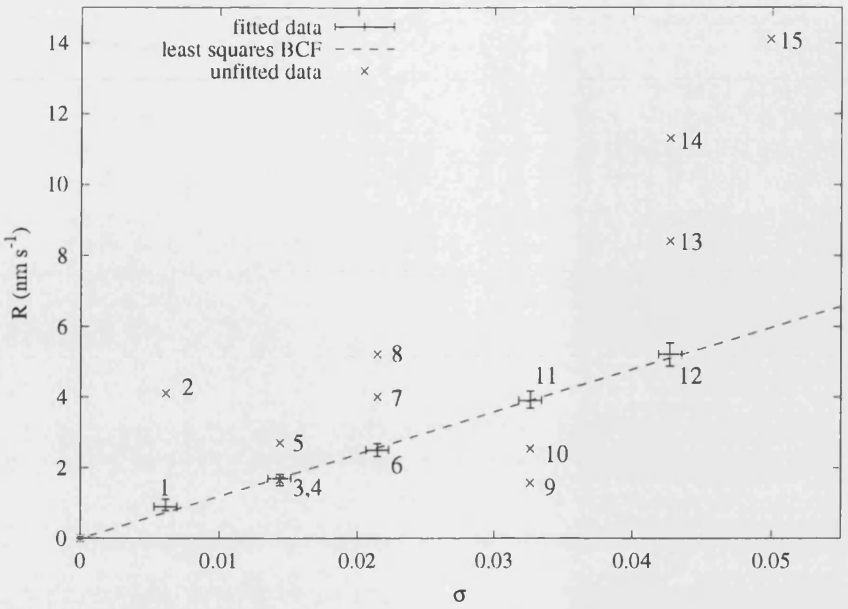

Figure 6.4: Normal growth rate vs supersaturation for KAP, $T_{sat} = 25.56$ °C, with best fit BCF curve.

first set exhibits a linear dependence of normal growth rate on supersaturation and is fitted with a best fit BCF curve. The second set of data exhibits considerably more scatter and no attempt to fit a model relationship has been made. The numeric labels on the individual data points correspond to interferometry and AFM measurements and observations and will be dealt with in the following section. The values for C and σ_1 obtained from the BCF curve are given in table 6.1. The fitted value of the critical supersaturation σ_1 is very small with comparatively very large error bounds. This has resulted in an enormous value for s_e, the percentage standard error. This effectively means that σ_1 is statistically insignificant from zero. This is a consequence of insufficient data at low supersaturation which would be required for a reasonable estimate of σ_1. For the value of the growth rate constant C, the standard error is small suggesting good agreement of the linear segment of the BCF curve with the data.

$\mathbf{T_{sat} = 25.71\ °C}$

Figure 6.5 shows two sets of data. Once again, one data set is substantially linear and a BCF curve has been fitted. The second data set shows considerably more scatter and has not been fitted with a BCF curve. It is notable in this case that the critical supersaturation, σ_1, obtained from the best fit curve is the largest of those obtained and is at least an order of magnitude larger than that obtained for the other data sets with one excep-

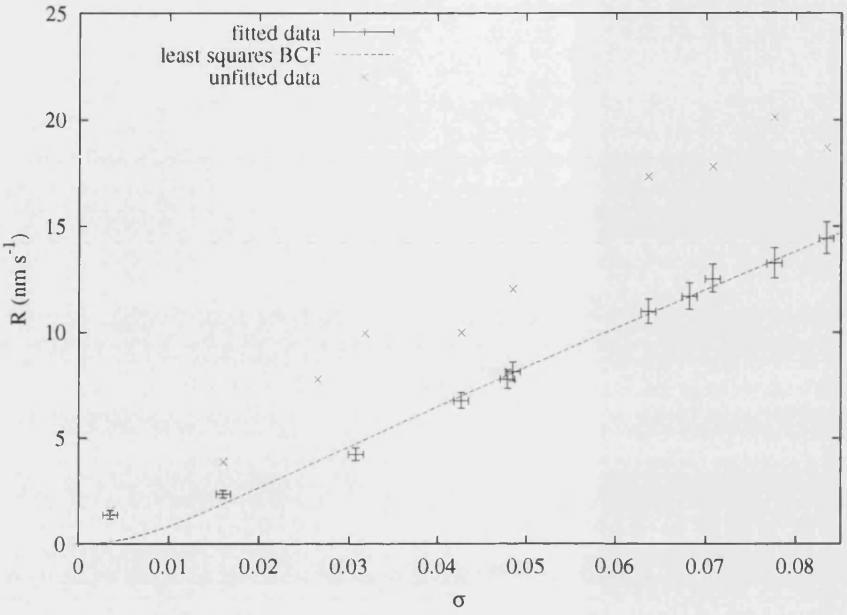

Figure 6.5: Normal growth rate vs supersaturation for KAP {010}, $T_{sat} = 25.71$ °C, with best fit BCF curve.

T/°C	σ
25.54 ± 0.02	0.0035 ± 0.0008
24.93 ± 0.02	0.0160 ± 0.0008
24.42 ± 0.02	0.0265 ± 0.0008
24.21 ± 0.02	0.0307 ± 0.0008
24.16 ± 0.02	0.0317 ± 0.0008
23.62 ± 0.02	0.0427 ± 0.0008
23.36 ± 0.02	0.0479 ± 0.0008
23.33 ± 0.02	0.0485 ± 0.0008
22.57 ± 0.02	0.0636 ± 0.0008
22.34 ± 0.02	0.0682 ± 0.0008
22.21 ± 0.02	0.0707 ± 0.0008
21.86 ± 0.02	0.0776 ± 0.0008
21.56 ± 0.02	0.0834 ± 0.0008

Table 6.3: Growth temperatures and relative supersaturation for solution saturated at 25.71 ± 0.02 °C

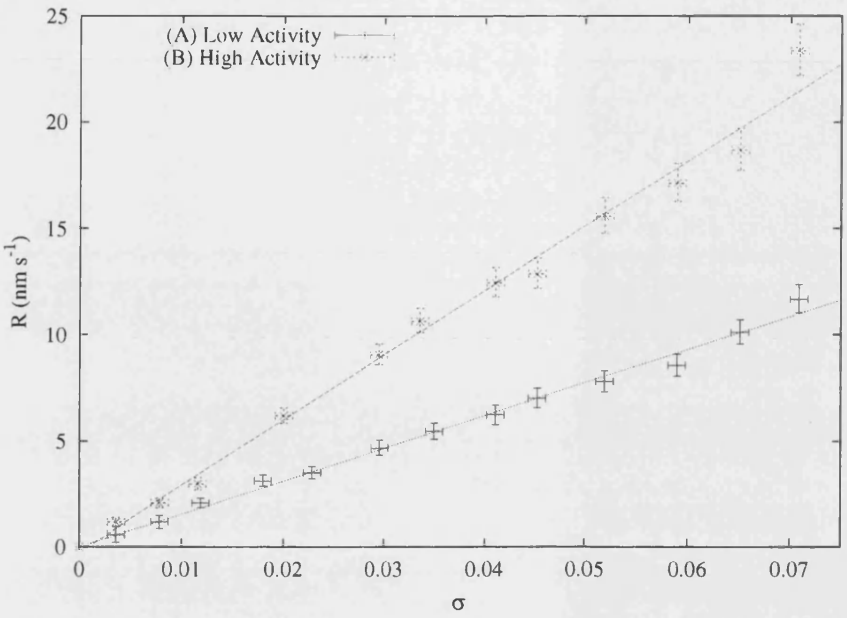

Figure 6.6: Normal growth rate vs supersaturation for KAP {010}, $T_{sat} = 26.71$ °C, with best fit BCF curves.

tion. Consequently a significant parabolic growth regime is observed at low supersaturation. However, despite being very much smaller than that for $T_{sat} = 25.56$ °C, the standard error estimate is nonetheless larger than is acceptable for a reliable estimate. Once again, sufficient data at low supersaturations is absent and the best fit curve is effectively extrapolated from the data at high supersaturation in this case. This makes it difficult to draw firm conclusions about the nature of the (R,σ) dependence at low supersaturation, though it seems reasonable from the size of the standard error that their is a finite parabolic growth regime in this case. However, the standard error in C is again small. Figure 6.3 and table 6.1 indicate that this data set is slightly anomalous with respect to the data obtained at other saturation temperatures in that it has a steeper dependence on supersaturation than is consistent with the other data sets. It would be expected to have a rate constant, C, smaller than that at higher temperatures. It is seen then that this curve is qualitatively and quantitatively different in character from the majority. It is possible that the noted anomalies in this data may be a result of unintentional impurities in the growth solution.

T/°C	σ
26.54 ± 0.02	0.0036 ± 0.0008
26.34 ± 0.02	0.0078 ± 0.0009
26.16 ± 0.02	0.0116 ± 0.0009
26.15 ± 0.02	0.0118 ± 0.0009
25.86 ± 0.02	0.0180 ± 0.0009
25.76 ± 0.02	0.0201 ± 0.0009
25.63 ± 0.02	0.0228 ± 0.0009
25.31 ± 0.02	0.0295 ± 0.0009
25.05 ± 0.02	0.0350 ± 0.0009
25.12 ± 0.02	0.0335 ± 0.0009
24.76 ± 0.02	0.0411 ± 0.0009
24.56 ± 0.02	0.0452 ± 0.0009
24.24 ± 0.02	0.0519 ± 0.0009
23.90 ± 0.02	0.0589 ± 0.0009
23.60 ± 0.02	0.0651 ± 0.0009
23.32 ± 0.02	0.0708 ± 0.0009

Table 6.4: Growth temperatures and relative supersaturation for solution saturated at 26.71 ± 0.02 °C

$\mathbf{T}_{sat} = 26.71$ °C

Figure 6.6 shows the most complete data set obtained from this study, provided by a solution saturated at 26.71 °C. The data reveal two distinct data sets (labelled A and B in figure 6.6), both of which have been fitted with BCF curves. This implies that two distinct types of source of different activity consistently appeared on the crystals studied. Moreover, from the discussion of section 6.3.1 it may be conjectured that the sources responsible for the data were particularly simple because of the consistency of the data. Complex sources would be expected to demonstrate greater variability in growth rate. The values for the critical supersaturation σ_1 in table 6.1 are small with very large error bounds making the estimate of σ_1 statistically insignificant from zero. Thus both data sets are substantially linear. The standard errors in C are small indicating a reliable fit. The position with respect to the other data sets for the shallowest curve (A) appears to be consistent. The steepest curve (B) indicates a greater growth rate dependence on supersaturation than obtained at higher solution saturation temperatures. This is consistent with growth due to dislocation sources of higher strength than those measured at the other saturation temperatures. Another notable feature of the values obtained for C from these data sets is that they differ by approximately a factor of two, being 155 and 303 nm s^{-1} respectively, indicating that the sources of 26.71 (B) have twice the activity of those of 26.71 (A).

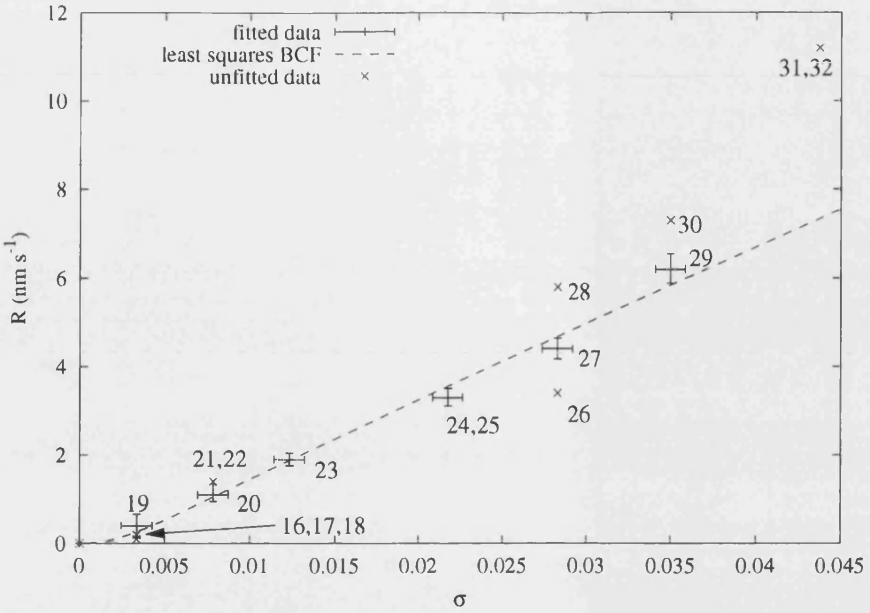

Figure 6.7: Normal growth rate vs supersaturation for KAP {010}, $T_{sat} = 29.26$ °C, with best fit BCF curve.

T/°C	σ
29.11 ± 0.02	0.0034 ± 0.0009
28.91 ± 0.02	0.0078 ± 0.0009
28.71 ± 0.02	0.0123 ± 0.0009
28.29 ± 0.02	0.0217 ± 0.0009
28.00 ± 0.02	0.0283 ± 0.0009
27.70 ± 0.02	0.0350 ± 0.0009
27.31 ± 0.02	0.0437 ± 0.0009

Table 6.5: Growth temperatures and relative supersaturation for solution saturated at 29.26 ± 0.02 °C

$\mathbf{T_{sat} = 29.26\ °C}$

The data obtained at a saturation temperature of 29.26 °C are shown in figure 6.7. In this case, a small but statistically significant value for σ_1 is obtained, though once again the standard error is large due to insufficient data at low supersaturation and hence the reliability of the numerical estimate is poor. The standard error in C is the largest obtained for any of the fitted curves though it is still sufficiently small (<5%) for reasonable statistical confidence in the estimate of C. With reference to figure 6.3 it appears that the slope, C, for this data set is low in comparison to the other data sets. Other data for which no reliable BCF fit can be obtained are also shown. Each point in figure 6.7 has been assigned a numeric label which corresponds to interferometry and AFM measurements and observations which will be dealt with later.

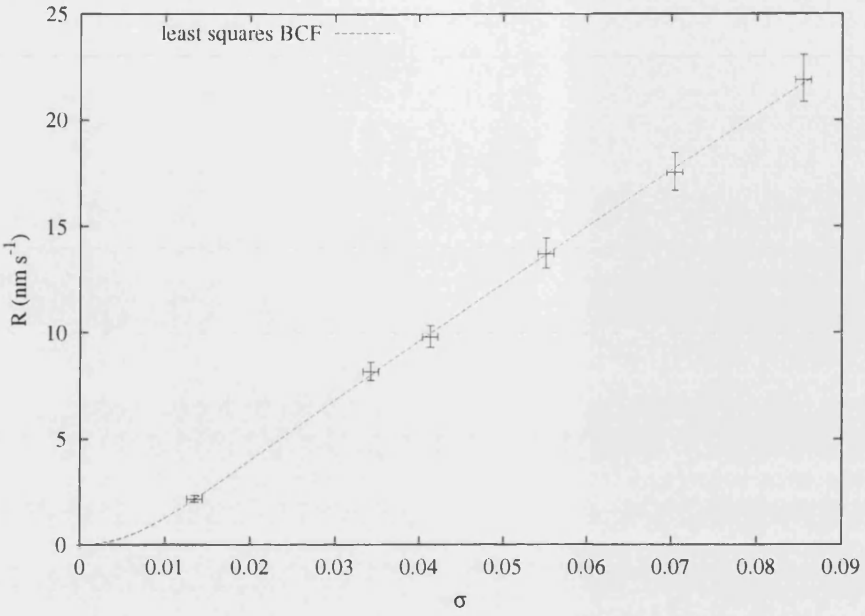

Figure 6.8: Normal growth rate vs supersaturation for KAP {010}, $T_{sat} = 30.12$ °C, with best fit BCF curve.

T/°C	σ
29.53 ± 0.02	0.0134 ± 0.0009
28.62 ± 0.02	0.0342 ± 0.0009
28.31 ± 0.02	0.0413 ± 0.0009
27.71 ± 0.02	0.0550 ± 0.0009
27.04 ± 0.02	0.0704 ± 0.0009
26.38 ± 0.02	0.0854 ± 0.0009

Table 6.6: Growth temperatures and relative supersaturation for solution saturated at 30.12 ± 0.02 °C

$T_{sat} = 30.12$ °C

For $T_{sat} = 30.12$ °C the data set available was limited[2]. A BCF curve has nonetheless been fitted to the data and good agreement is obtained. In fact the standard errors in both σ_1 and C are the smallest obtained in this study. However, in common with the data for $T_{sat} = 25.71$ °C, very few data were available at low supersaturations and the fitted curve at low supersaturation is effectively an extrapolation from higher supersaturations. Once again this makes it difficult to draw firm conclusions about the (R,σ) dependency. The comparatively small value of the standard error in σ_1 is potentially deceiving in this case. With so few data at the lower supersaturation, it is possible that

[2]This was a consequence of random and frequent activity changes of the dominant sources on the crystal and the fact that the growth solution cannot be maintained indefinitely.

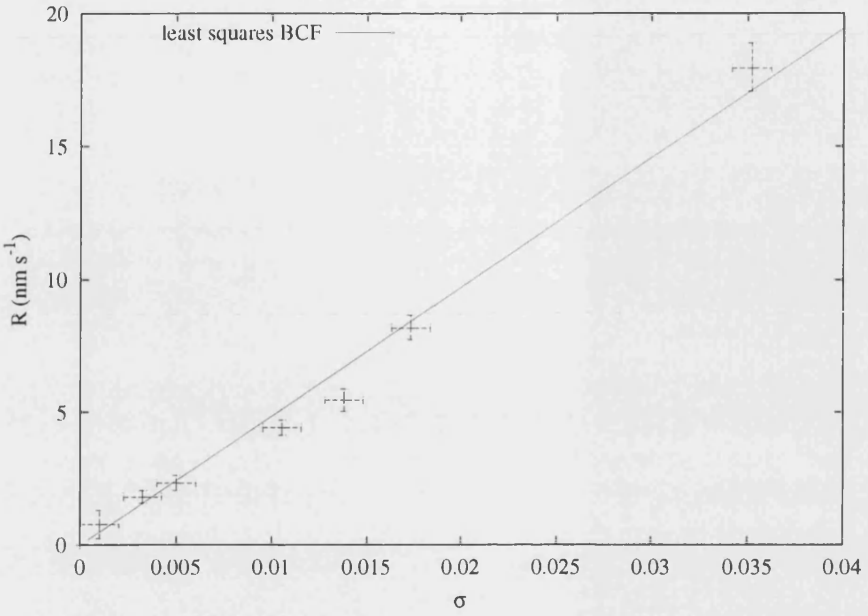

Figure 6.9: Normal growth rate vs supersaturation for KAP {010}, $T_{sat} = 39.66$ °C, with best fit BCF curve.

T/°C	σ
39.62 ± 0.02	0.0010 ± 0.001
39.53 ± 0.02	0.0032 ± 0.001
39.46 ± 0.02	0.0050 ± 0.001
39.24 ± 0.02	0.0105 ± 0.001
39.11 ± 0.02	0.0138 ± 0.001
38.97 ± 0.02	0.0173 ± 0.001
38.27 ± 0.02	0.0352 ± 0.001

Table 6.7: Growth temperatures and relative supersaturation for solution saturated at 39.66 ± 0.02 °C

the single data point near the parabolic region of the curve may have been apparently reliably fitted by chance. In common with $T_{sat} = 25.71$ °C is the value obtained for the critical supersaturation, σ_1, which with respect to the majority of the data sets is large. These data and those for $T_{sat} = 25.71$ °C appear then to be qualitatively different in character from the remainder. It is possible that these are artefacts of curve fitting with incomplete data sets or possibly due to the growth modifying effect of unintentional impurities.

$T_{sat} = 39.66$ °C

Finally, figure 6.9 illustrates the growth rate data measured for a solution saturated at 39.66 °C. In contrast to the data obtained at lower saturation temperatures, the data are more extensive at low supersaturation than high. This is because, as a result of the higher overall growth rates, it is easier to measure growth rates reliably at lower saturation temperatures. At high supersaturation however steady state growth was not maintained for long enough to obtain reliable growth rates due to the frequent occurrence of new sources. The overall growth rates are substantially higher than for lower saturation temperatures, as would be expected. The standard error in C is again comparatively small indicating a reliable estimate of C. The critical supersaturation, σ_1, obtained from the curve fit is vanishingly small in this case and the standard error estimate is comparatively enormous, indicating that σ_1 is statistically indistinguishable from zero.

6.3.3 Summary

Despite the large values for the standard error in σ_1, which are largely attributable to the absence of sufficient data at low supersaturation, those data for which curve fitting was performed were reasonably well fitted by the BCF model. The majority of the data were well fitted by the linear BCF model, giving small standard errors for the rate constant C. Furthermore, in general the temperature dependence of the values of the slope C of the BCF curves qualitatively exhibit behaviour typical of a thermally activated process. That is the values of the slope generally increase with increasing saturation and hence, growth temperature. Figure 6.10 shows the values of C obtained from the curve fitting with their standard errors. The obvious exceptional point is that of $T_{sat} = 26.71$ °C (B) where the source activity was apparently higher than typical. The constant, C, for $T_{sat} = 29.26$ °C also appears low in comparison to $T_{sat} = 26.71$ °C (A) and $T_{sat} = 30.12$ °C. This may also be a consequence of different source activity or may be attributable to another cause such as modification of the growth kinetics by unintentional impurities. With the present data it is difficult to be certain.

However, as has been clearly illustrated, particularly through the unfitted data sets; the BCF model alone cannot account for all of the observed growth rates without making the assumption that the scatter is simply a consequence of the random occurrence

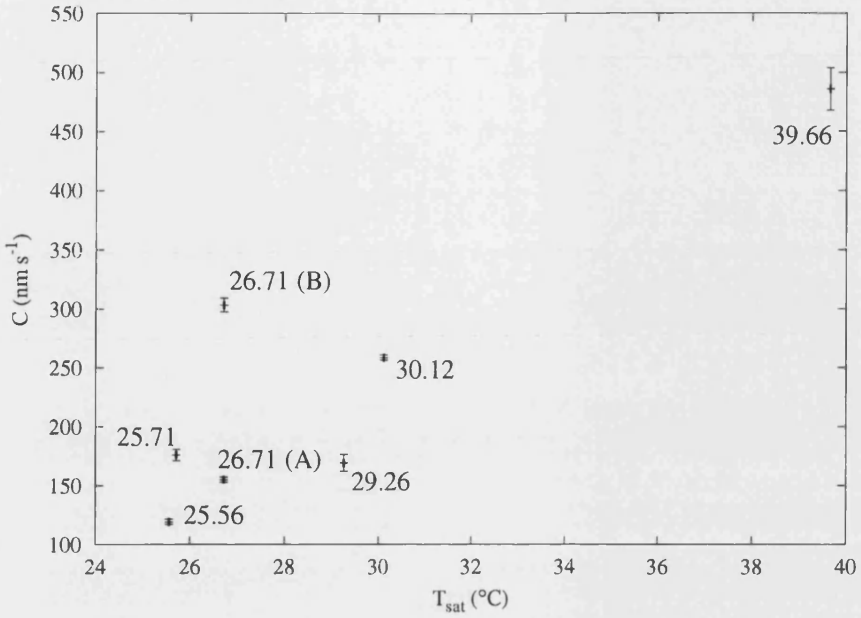

Figure 6.10: C vs T_{sat} obtained from the best fit BCF curves to the (R,σ) data. The numeric labels indicate the saturation temperature of the corresponding solutions.

of growth sources leading to sources of different activity. This presents a number of difficulties for the analysis of the data, especially at low supersaturation. A decision has to be made about which data to fit the model to and which to exclude on the basis of whether data points belong to sources of the same activity or not. Because the separation of growth rates, R, at low supersaturations is smaller, the choice is more ambiguous than for higher supersaturations. This is readily illustrated in the data for $T_{sat} = 26.71$ °C in figure 6.6; in which, at high supersaturation, the data sets are well separated and the data clearly belong to sources of different activity. However at low supersaturations the data are more closely spaced and the decision is much more difficult. Not least because error bounds may begin to overlap. This issue is compounded by the nature of the BCF model. In curve fitting it is normal to assume the measurement errors to be normally distributed. However, although apparently a continous variable, the constant σ_1 contains a discrete variable, the number of cooperating dislocations (c.f. equation 2.22). As a result of differences in the underlying number of dislocations responsible for growth the apparently random errors may in fact be systematic errors. Points apparently lying close together on a BCF curve may in fact belong to entirely separate BCF curves, the errors resulting from such differences are unlikely to be normally distributed due to the underlying discrete nature of the phenomenon. This is once again most clearly shown by figure 6.6 which clearly shows two distinct data sets for sources of differing activity. However the clarity in this case is a consequence

of the completeness of these data sets and for the more sparse data sets the ambiguity is much greater. Thus, distinguishing outlying points not belonging to a given BCF curve from points belonging to a curve but with relatively large measurement error is fraught with dangers, as are assumptions about source activity.

Clearly, growth rate data viewed in isolation are insufficient to explain the growth sources or mechanisms responsible for the observed growth rates. It is clearly invalid to dismiss that data which does not fit the particular model in question neatly. If better insights into the growth process are to be obtained then this data must be considered valid and taken into account. This leads inevitably to the central theme of the present thesis. That is, the need to image the surface at a resolution sufficient to resolve individual steps and dislocation outcrops so that the scatter in growth rate data may be rationalised through direct observation of the sources responsible[3].

6.4 *Ex-Situ* AFM Studies

In response to the limitations of examining (R,σ) curves in isolation, this section presents a more detailed examination of the growth rates and surface structure of the crystals from which two of the data sets presented in section 6.3.2 were obtained. Specifically these are the data sets obtained at saturation temperatures of 25.56 °C and 29.26 °C. *Ex-situ* AFM studies of the sources responsible for the growth rates plotted in figures 6.4 and 6.7 are shown where available along with the corresponding interference images. Extensive cross-referencing between the AFM, interference images and (R,σ) curves is given. In this way a more critical and thorough examination of the growth mechanisms can be made. In the AFM images which follow, all fundamental steps on the crystal surfaces were found to have step heights in the range 1.2 - 1.4 nm, in good agreement with the lattice translation vector of KAP in the direction normal to the surface (1.325_7 nm). All *ex-situ* AFM images in the following sections were obtained using the Digital Instruments Nanoscope III Multimode SPM in Tapping Mode (a trademark of Digital Instruments). All images are from the amplitude channel.

[3]Compare with the quotations in section 1.3.

6.4.1 $T_{sat} = 25.56$ °C

Equilibrium

Figure 6.11 shows a growth spiral on the face of a crystal which has been held at the saturation temperature of the solution for 18 hours, during which time no discernible growth or dissolution occurred. Some deposition on the surface has occurred due to inadequate protection during removal from solution, however the shape of the spiral is clear. The spiral shape is characteristic of growth spirals on KAP {010}, which have been described in detail in section 3.7 and elsewhere [119, 123, 124, 128, 148]. In this instance it is clearly polygonal, comprising largely straight steps oriented along the <101> directions, with other less clearly defined steps with a net orientation close to <001>, as shown schematically in figure 3.7. The characteristic mirror symmetry across the <001> direction is apparent. The non-centrosymmetric nature of KAP is also apparent in the lack of mirror symmetry about (001), resulting in two distinct sets of <101> steps, as discussed in section 3.6. It is instructive to measure the angles between the various sets of steps on this image. From the KAP unit cell, the acute angle between <101> directions is 112°. The angle measured between the equivalent sets of $<101>_s$ steps was 112°, in excellent agreement with the calculated value. The angle measured between the equivalent sets of $<101>_f$ steps was 100°, illustrating that the $<101>_f$ steps have a small misorientation from the <101> directions. A typical observation [148] on KAP {010} is that the $<101>_f$ steps are often more ragged and curved than the $<101>_s$ steps, suggesting that they are less constrained to the <101> direction and possibly that they may be more influenced by impurities which will have a significant effect at this supersaturation. It is probable that the spiral shape observed in these images is influenced by impurities. In fact the surface may not be exactly at equilibrium, the condition of zero growth may be due to the kinetic effects of impurities forming a *dead zone* as discussed in section 2.7.4. Despite the best experimental efforts to establish the saturation temperature, as described in section 4.4.4, absolute accuracy cannot be achieved. The role of impurities in affecting the growth behaviour is significant and will be returned to on several occasions throughout this chapter and the general discussion in chapter 8.

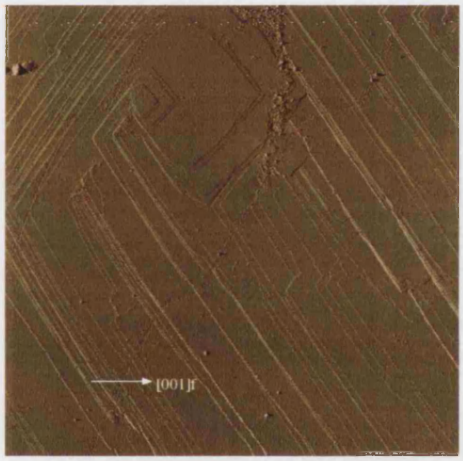

Figure 6.11: AFM image of equilibriated growth spiral. $T_{sat} = 25.56$ °C, $\sigma = 0$. Scan size 30 μm.

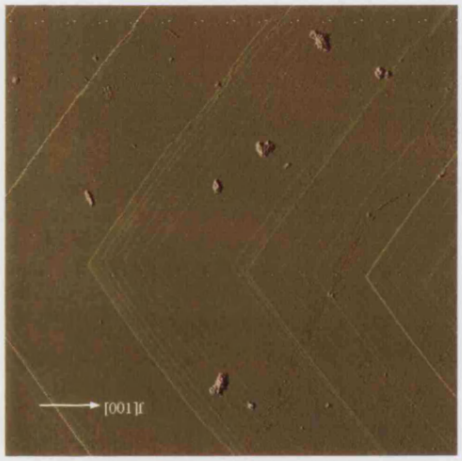

Figure 6.12: AFM image of $<101>_s$ steps of the equilibriated growth spiral shown in fig 6.11. Scan size 30 μm.

Hillocks 1, 2

Figure 6.13 shows the interference image for the crystal growing at a relative supersaturation of 0.0062 ± 0.0008. Several active sources are clearly visible on the crystal face, each giving rise to vicinal hillocks. The bright highlights apparent in the image are the result of light scattering from sub-surface inclusions formed during the crystal growth. There is a large central hillock which is growing with a normal growth rate corresponding to point 1 in figure 6.4. The growth rate of the large hillock at the bottom of the crystal was equivalent to that of the central hillock and is not shown separately. At the point in time at which this image was captured the crystal was in a state of rapid transition with the occurrence of a new very active hillock, labelled 2 in figures 6.13 and 6.4, on the $<101>_f$ steps of the large central hillock. This new hillock is significantly steeper and more rapidly growing than the other hillocks on the face, suggesting a high source strength relative to that of the other sources. Also, the interference fringes on this hillock are relatively uneven in width and spacing suggesting that the fundamental steps of which the hillock is formed are non-equidistant.

AFM of the $<101>_s$ steps of source 1 in figure 6.14 reveals steps which appear to be extensively pinned by impurities. Unfortunately imaging of the hillock source itself was unsuccessful in this instance. Figure 6.15 shows the source of hillock 2. The source is very complex, consisting of a large number of dislocations co-operating to form a spiral largely comprised of step bunches tens of fundamental steps high. Also, a large hollow pit has formed at the centre of the spiral. From the shape and size of the pit it appears that the source may be the result of a foreign particle alighting on the growing surface and inducing the formation of misfit dislocations and a new hillock. The turns of the macrospiral around the pit are clearly evident. In this image the depth of the pit was greater than the AFM tip height and consequently the pit appears to be shallow and flat bottomed, however this must be regarded as an artefact. It is consequently difficult to reach a definitive conclusion on the question of whether this source is the result of a foreign particle however subsequent observations on other sources will lend support to this hypothesis for this case. Also visible in this image is evidence of dislocation slip from the extensive slip steps which cross the surface. Whether slip was occurring during growth or only during removal is difficult to ascertain however the stresses which develop during the growth of such a complex source are likely to be considerable and sufficient to cause slip. A final observation from figure 6.15 is the fact that, in contrast to the $<101>_s$ steps on source 1 in figure 6.14, extensive pinning of the steps is not apparent. This applies to the <001> orientations also, which, as re-

ported by others [148] and will be shown in later sections, are most prone to pinning by impurities. Hillocks 1 and 2 are of the order of a millimetre apart at most and clearly growing under the same bulk conditions. Although local variations in supersaturation are possible on this scale these are likely to be small and fleeting, particularly since the growth has been shown to be insensitive to hydrodynamic conditions (see appendix B). Thus, the marked difference in the relative growth rates of hillocks 1 and 2 is best explained by the relative activities of the two sources.

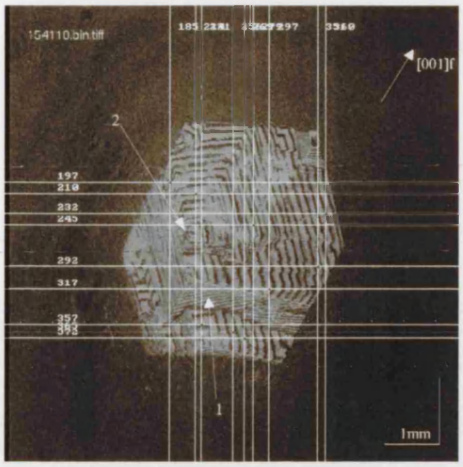

Figure 6.13: Interference image corresponding to sources 1 & 2 in Fig. 6.4. $T_{sat} = 25.56$ °C, $T_{growth} = 25.26$ °C, $\sigma = 0.0062 \pm 0.0008$.

Figure 6.14: AFM image corresponding to source 1 in Figs. 6.4 and 6.13. $<101>_s$ steps at low supersaturation, extensive blocking by impurities. $T_{sat} = 25.56$ °C, $T_{growth} = 25.26$ °C, $\sigma = 0.0062 \pm 0.0008$. Scan size 4.62 μm.

Figure 6.15: AFM image of high activity source corresponding to source 2 in Figs. 6.4 and 6.13. Macrostepped spiral with large hollow core and multiple dislocations. $T_{sat} = 25.56$ °C, $T_{growth} = 25.26$ °C, $\sigma = 0.0062 \pm 0.0008$. Scan size 16 μm.

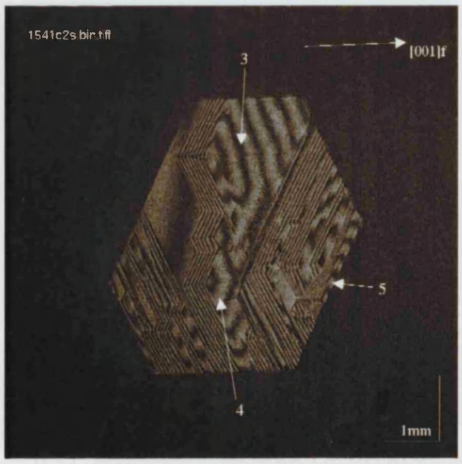

Figure 6.16: Interference image corresponding to sources 3, 4 & 5 in Fig. 6.4. $T_{sat} = 25.56$ °C, $T_{growth} = 24.86$ °C, $\sigma = 0.0143 \pm 0.0008$.

Hillocks 3, 4, 5

Figure 6.16 shows the crystal corresponding to points 3, 4 and 5 in figure 6.4, growing at a supersaturation of 0.0143 ± 0.0008. In comparison with the crystal in figure 6.13 the hillocks present are more shallow and uniform and, despite the higher supersaturation, are all growing at rates lower than the most active source on that crystal. This suggests that the sources present on this crystal are quite uniform and of low activity. Sources 3 and 4 have the same normal growth rate and appear to have similar slopes (see table 6.8), suggesting that they have the same activity. Source 5, although not easily visible on the edge of the crystal, grew faster and appears to be steeper than 3 and 4 indicating a greater activity. Numerous other small sources are visible on this face which have not yet developed into large hillocks. Such are the dynamics of a crystal face, any one of these hillocks may have grown to dominate the surface in time. Also notable in this image is the wide, flat region on the upper left hand side of the crystal. At the time of imaging, no steps from any of the hillocks had yet covered this region which is substantially the cleavage surface. This was quite an unusual observation in the context of this study. Typically, the faces were covered with very many new hillocks very soon after the start of new growth on the cleavage surface. Competition between these hillocks soon resulted in the dominance of a small number of hillocks. The persistence of this flat section is suggestive that the surface in this region was either very perfect, effectively containing no dislocations with screw character; or was otherwise very imperfect, containing so many dislocations with screw character that their separation was less than $2\rho_c$, preventing growth by the Gibbs-Thomson effect.

Unfortunately, AFM of this crystal was mostly unsuccessful and so these inferences could not be proven unequivocally. A single AFM image of the $<101>_f$ steps of hillock 3 is shown in figure 6.17 and reveals that the steps on this surface are not equidistant but bunched. They are also entirely straight suggesting that step pinning by impurities was unimportant at this supersaturation. The arrow indicates the direction of step advance and hence, the "downhill direction".

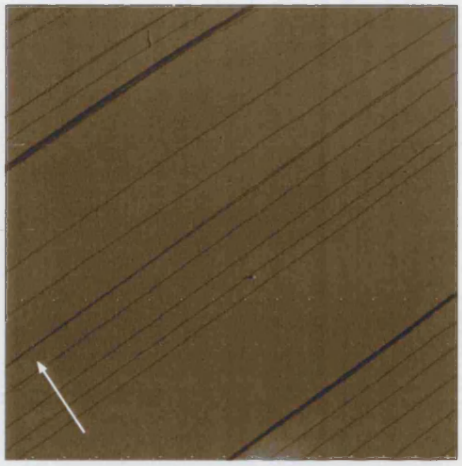

Figure 6.17: AFM image corresponding to source 3 in Figs. 6.4 and 6.16. Scan size 9.276 μm.

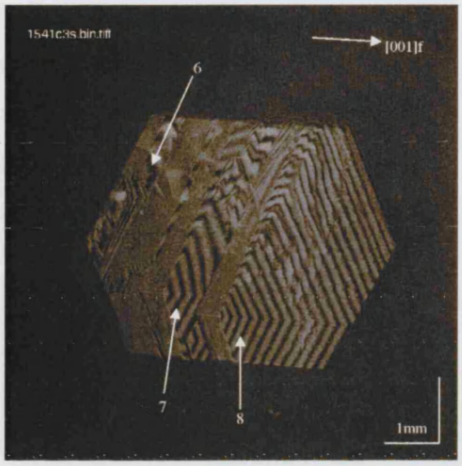

Figure 6.18: Interference image of crystal corresponding to sources 6, 7, 8 in Fig. 6.4. $T_{sat} = 25.56$ °C, $T_{growth} = 24.51$ °C, $\sigma = 0.0215 \pm 0.0008$.

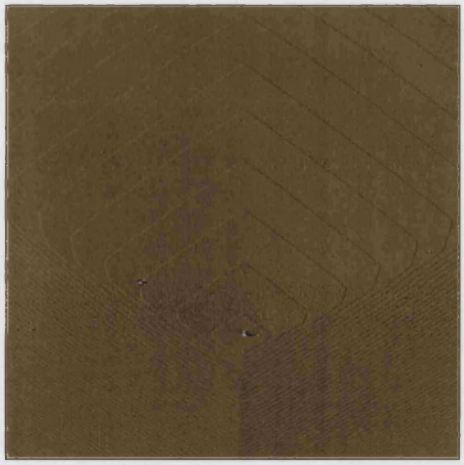

Figure 6.19: AFM image corresponding to source 6 in Figs. 6.4 and 6.18. Scan size 30 μm.

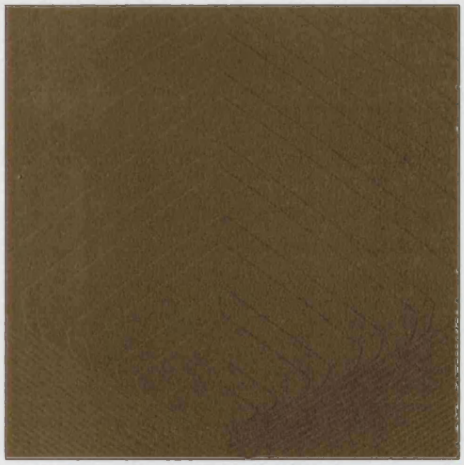

Figure 6.20: AFM image of dislocation outcrop corresponding to source 7 in Figs. 6.4 and 6.18. $T_{sat} = 25.56$ °C, $T_{growth} = 24.51$ °C, $\sigma = 0.0215 \pm 0.0008$. Scan size 30 μm.

Hillocks 6, 7, 8

Figure 6.18 shows a crystal growing at a relative supersaturation of 0.0215 ± 0.0008. This crystal is of particular interest due to the variety of source strengths which it exhibits. Also, the growth of this crystal was steady for the whole period of study with the exception that the small hillock at the bottom of the image between hillocks 7 and 8 was quickly engulfed by hillock 8. The most active hillock on this crystal is 8, which is also the steepest. Hillock 7 is more active and steeper than the row of small hillocks on the left hand edge of which hillock 6 is one. The difference in activity in terms of the normal growth rate of the respective hillocks is obvious in figure 6.4. Figure 6.19 shows the dislocation outcrop at the centre of hillock 6. A single dislocation is present giving rise to a polygonal spiral with essentially equidistant steps. The step spacing of the $<101>_f$ steps measured by AFM is 2.6 μm.

Figures 6.20 and 6.21 show the dislocation outcrop at the centre of hillock 7. A double spiral of non-equidistant step pairs is formed. In figure 6.21 it appears that the source is a single dislocation suggesting that the Burgers vector screw component is approximately equal to two lattice parameters normal to the surface, though the image resolution is insufficient to prove this beyond doubt. The hillock slope and step spacings on hillock 7 were measured by interferometry and AFM respecively. The step spacings of the $<101>_f$ steps of the spiral measured by AFM are 2.12 μm and 1.35 μm for the wide and narrow terraces respectively. The mean step separation y_0 and hillock slope p obtained from the step spacings are 1.74 μm and 0.00076 respectively. Direct interferometry measurement of the slope gave a value for p of 0.00115 from which a value of 1.15 μm for the mean step spacing y_0 was obtained. These values are tabulated in table 6.8. Differences between the results from interferometry and AFM are significant and will be considered further, both later in this chapter and in the general discussion of chapter 8. Step separations on the $<101>_s$ steps were measured directly by AFM as 0.21 μm and 0.13 μm respectively for the wide and narrow terraces, yielding 0.17 μm for y_0. It is notable that the relative widths of the wide and narrow terraces between the $<101>_f$ and $<101>_s$ steps are essentially the same, the wide terrace being 1.6 times the narrow terraces in both cases.

Figure 6.22 shows the dislocation outcrop at the centre of hillock 8. Multiple dislocations are present in this image. For the whole source at least 14 step generating dislocations were counted. Not all of these dislocations are cooperating however. Scrutiny of the image shows that only 4 dislocations are cooperating to produce a spiral consist-

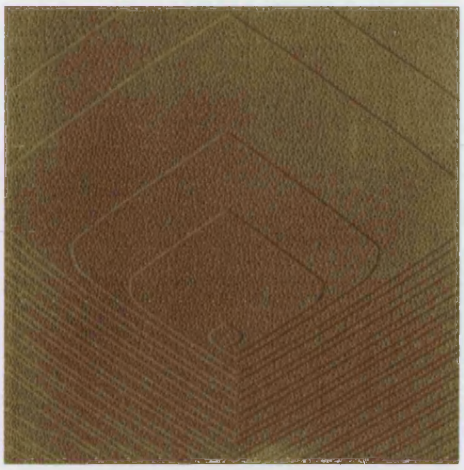

Figure 6.21: AFM image. 10 μm close up of double spiral from Fig. 6.20.

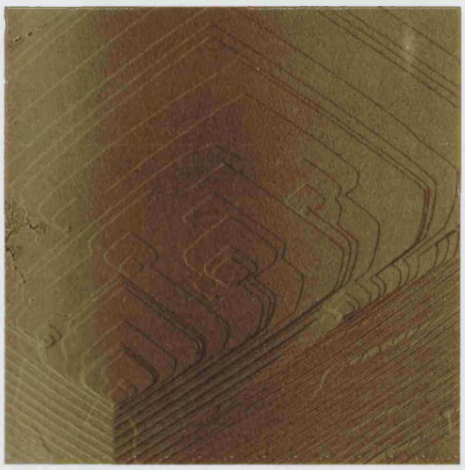

Figure 6.22: AFM image of dislocation outcrop corresponding to source 8 in Figs. 6.4 and 6.18. $T_{sat} = 25.56$ °C, $T_{growth} = 24.51$ °C, $\sigma = 0.0215 \pm 0.0008$. Scan size 30 μm.

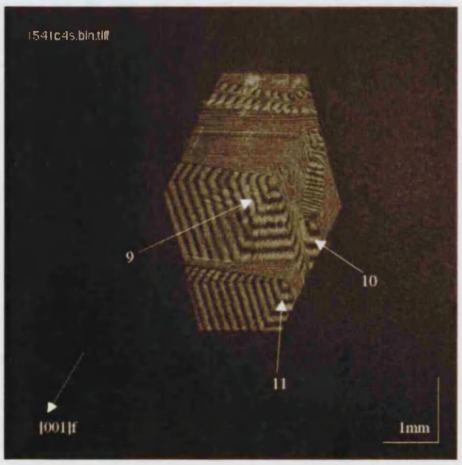

Figure 6.23: Interference image of crystal corresponding to sources 9, 10 & 11 from Fig. 6.4. $T_{sat} = 25.56$ °C, $T_{growth} = 23.96$ °C, $\sigma = 0.0326 \pm 0.0008$.

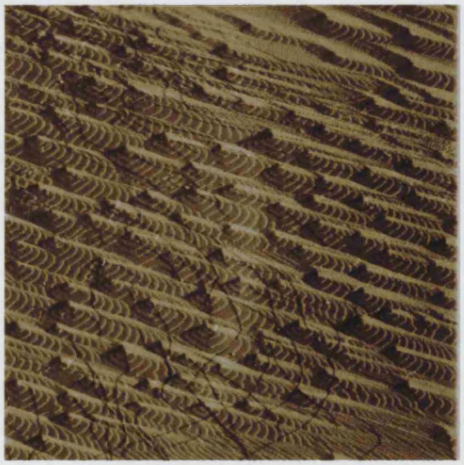

Figure 6.24: AFM image of multiple dislocation outcrop corresponding to source 9 in Fig.6.4 and 6.23. Scan size 45 μm.

ing of bunches of 4 steps separated by a wide terrace. Of these 4-step bunches, 3 are very close together, especially at the centre of the spiral; the other being more widely separated. Unfortunately it was not possible to resolve the spiral centre clearly enough to establish if the cooperating spirals were independent dislocations or if at least one was a single dislocation generating multiple steps. This was made more difficult by the dislocation slip from the centre of the spiral which is clearly visible. It is most likely in this case that dislocation slip has occurred during removal. The bunches of 4 steps appear to pass relatively unmodified through the region of dislocations on the right hand side of the spiral as can be seen from the step bunch farthest out from the spiral at the top right hand corner of the image, which has recovered from the distortions created by merging with the steps formed from the other dislocations.

It is now possible to see why growth rates and slopes of hillocks 6, 7 and 8 in figures 6.18 and 6.4 are different. They are formed from a single unit dislocation, a double dislocation and 4 cooperating dislocations respectively. It is notable that hillock 6 forms part of the fitted data in figure 6.4 and is in good agreement with the other data points in this data set. The implication is that these other data points also correspond to hillocks with a single dislocation source. However, the normal growth rates of hillocks 9 and 10 lie beneath this line, suggesting that sources of lower activity than those in the fitted data set are possible.

Hillocks 9, 10, 11

Figure 6.23 shows the crystal corresponding to hillocks 9, 10 and 11, growing with relative supersaturation of 0.0326 ± 0.0008. The surface is dominated by these three well developed hillocks with some smaller less well developed hillocks also present. Hillock 11 is most active and steepest, and yet lies in the fitted data set of figure 6.4 of which the single dislocation source 6 is a part. The activity of hillocks 9 and 10 then is apparently less than that of a singe dislocation. Figure 6.24 provides a clue to this result. The centre of hillock 9 contains an uncountable number of very small, apparently single, non-cooperating spirals. Extensive slip steps are also present. No true hillock centre could be established. These small spirals within the region of the centre of hillock 9 extend over an area greater than the AFM scan width for reliable imaging and apparently occupy an area of the order of 200 μm^2. No evidence of this appears in the interference image of hillock 9, which on this scale appears to be typical. The possibility that the spirals were formed during removal from solution cannot be

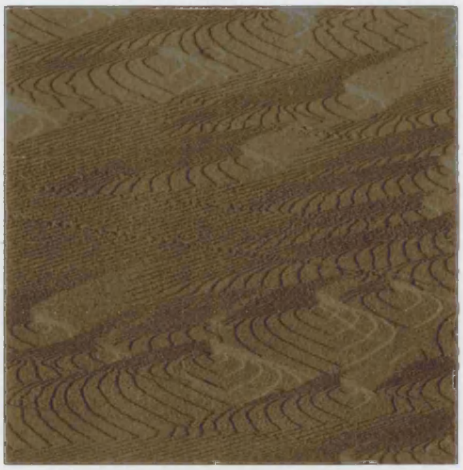

Figure 6.25: AFM image corresponding to source 9 from Fig. 6.4. Scan size 20 μm

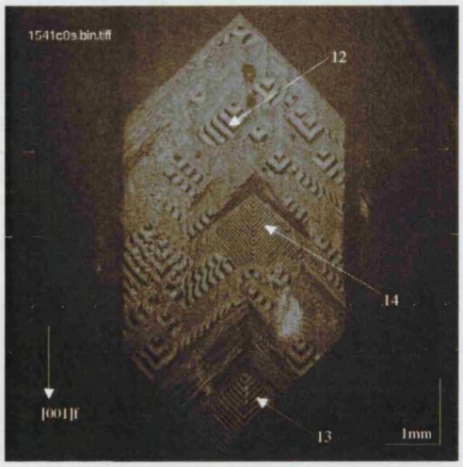

Figure 6.26: Interference image of crystal corresponding to sources 12, 13 & 14 in Fig. 6.4. $T_{sat} = 25.56$ °C, $T_{growth} = 23.46$ °C, $\sigma = 0.0427 \pm 0.0008$.

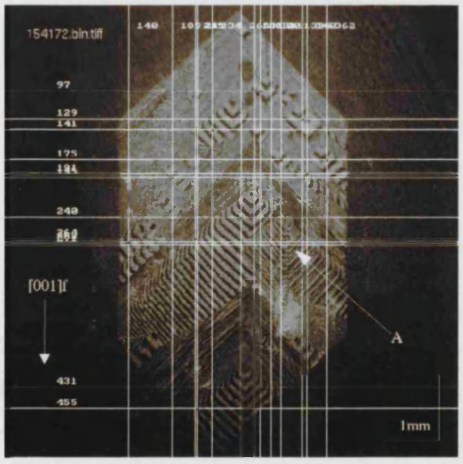

Figure 6.27: Interference image of crystal in Fig. 6.26 imaged 10 minutes later. Note the new very high activity source, labelled A. $T_{sat} = 25.56$ °C, $T_{growth} = 23.46$ °C, $\sigma = 0.0427 \pm 0.0008$.

Figure 6.28: AFM image of spiral centre corresponding to source 14 in Figs. 6.4 and 6.26. The complex source appears to be generated by an inclusion. Scan size 50 μm.

ruled out, however they have undergone sufficient growth to form several spiral turns. Had growth not been arrested by removal it is likely that the most active sources in the group would have eventually come to dominate the growth, leaving a single large and probably complex spiral. The measured normal growth rate of hillock 9 at least then may be regarded as a transient. What is surprising then is that this state has persisted for sufficient time for a reliable normal growth rate measurement to be made (15 minutes in this case).

Why its growth rate should be stable yet less than that expected for a single dislocation is not entirely clear. It is possible that the high step density and hence, kink density, formed by so many spirals has lead to local depletion of the solution so that the local supersaturation here is lower. However, the solution is well stirred and the growth was shown to be independent of solution flow rate (see appendix B) so any such concentration gradient should be restricted to the un-stirred boundary layer. Through the presence of so many dislocations the strain energy in this region of the crystal is likely to be greater than in the surrounding crystal. This will result in a raised free energy of the crystal with respect to an unstrained region, which may effectively reduce the local supersaturation, resulting in a lower growth rate. Although concentration gradients will not be allowed to grow large by virtue of stirring, the dislocations responsible for the heightened strain energy will persist, resulting in a consistently lower growth rate. In actuality, these effects are not so easily separated and both phenomena may contribute to the measured growth rate. To summarise, a hypothesis for the growth rate on this hillock is as follows. High dislocation density results in high kink density through the formation of many steps, leading to local depletion of solution. Mass transport to the kinks now becomes rate limiting (i.e. the growth makes a transition to a diffusion regime) and so growth is slowed. Simultaneously, the strain energy due to the high local dislocation density increases the local free energy of the crystal, reducing the local supersaturation and hence the growth rate.

It is also not certain that there is a dislocation for every spiral present in this region. There is clear evidence from the slip steps in figure 6.24 that dislocations have slipped from their positions at the centre of spirals, leaving closed step loops. Figure 6.25 shows the edge of the highly dislocated region of hillock 9 where the dislocation density is lower. For one of the spirals, the slip step formed by movement of the dislocation from the centre of the spiral is clearly visible. Since dislocation motion has clearly occurred, then it is possible that the very large numbers of growth spirals are actually a result of movement of a lesser number of dislocations. If the dislocation at the centre

of the spiral should move, the slip step produced may close the steps of the spiral into closed loops. These closed loops will continue to grow, however a new growth spiral will begin to form at the new location of the dislocation. If the dislocation moves again then this spiral will be closed and a new one formed elsewhere and so on. In this scenario, because new spirals are continually formed, provided that the dislocations keep moving then the multiple spirals may persist. This may explain why the multiple spirals are not rapidly eliminated. In the event that two dislocations come close enough to begin to cooperate then a stronger source will be formed and eventually dominate the surface. Note also in figure 6.25 that there exists what appears to be an isolated two-dimensional island between the terraces of the spiral at the top, middle of the image. This is probably a consequence of the higher supersaturation momentarily experienced during removal though such an island may be formed by slip of a dislocation from a spiral centre.

Unfortunately successful AFM imaging of hillocks 10 and 11 was not possible due to surface deposition during the solution removal procedure. It is therefore not possible to establish the structures of these hillocks. The apparent anomaly in the growth rate of hillock 10 may be a result of phenomena similar to that observed on hillock 9. For consistency with the measured growth rate of the single dislocation source 6 it should be expected that source 11 is also a single dislocation however this cannot be shown unequivocally in the absence of AFM images.

Hillocks 12, 13, 14

Figure 6.26 shows the crystal corresponding to points 12, 13 and 14 in figure 6.4, growing at a nominal relative supersaturation of 0.0427 ± 0.0008. This crystal is interesting in that it has a considerably greater number of macroscopic growth hillocks than is typically observed on KAP {010}. The majority of which all have the same slope and normal growth rate. Hillock 12 was selected as a representative example of these hillocks and the normal growth rates were all found to lie in good agreement with the BCF best fit line. Hillocks 13 and 14 are clearly steeper and have greater normal growth rates than those represented by hillock 12. Furthermore the activity of these hillocks appeared to slow during the experiment as witnessed by the change in slope and instantaneous normal growth rate (the growth rates shown in figure 6.4 are the mean growth rate during the growth period). Figure 6.27 shows the same crystal imaged 10 minutes later and comparison of this with figure 6.26 clearly shows that the

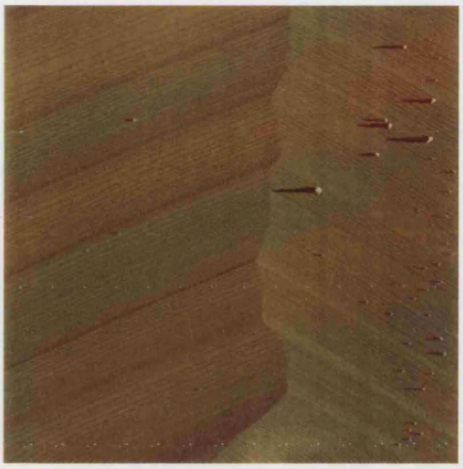

Figure 6.29: AFM image of a train of kinematic waves on the <101>$_f$ steps of source 14 in Figs. 6.26 and 6.4. Scan size 50 μm.

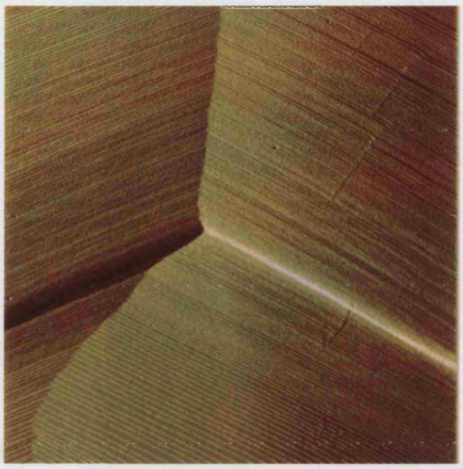

Figure 6.30: AFM image of a step shockwave on the <101>$_f$ steps of source 14 in Figs. 6.26 and 6.4. Scan size 40 μm.

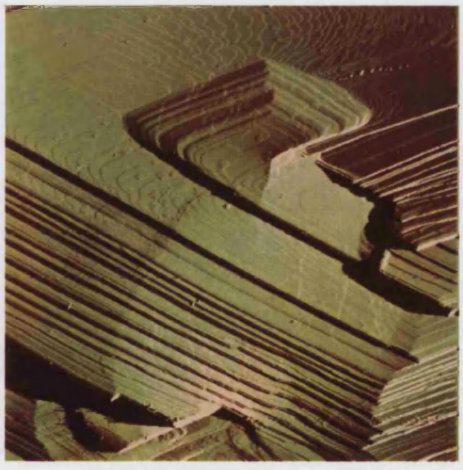

Figure 6.31: AFM image of spiral centre of new source (source A) in Fig. 6.27. Scan size 50 μm.

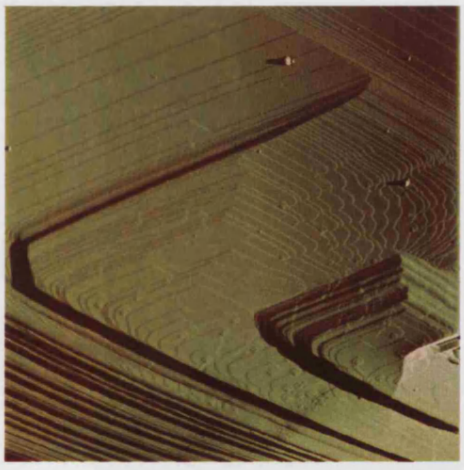

Figure 6.32: AFM image of source A in Fig. 6.27 showing second turn of macrospiral. Scan size 50 μm.

slopes of hillocks 13 and 14 have both become significantly shallower in this period. The slopes of the shallow hillocks have remained more or less constant. The reduction of activity of hillock 14 is clearly apparent since far from the source the slope becomes progressively steeper. The cause of such an apparently uniform reduction in activity is a matter for speculation. Local changes to source structure would appear to be ruled out by the simultaneous reduction in activity of the two separate sources. This also indicates that the local slope of the surface is preserved despite changes to the source activity (c.f. the assumptions of the Frank [50] and Cabrera-Vermilyea [51] kinematic models, section 2.7.3). Figure 6.27 also reveals that a new very high activity source, labelled A, has become active on the crystal. The interference fringes on this source are non-uniform suggesting that the surface has macroscopic features (of the order of the wavelength of light) present. The crystal was removed from solution shortly after the image of figure 6.27 was captured and imaged by AFM. It is again unfortunate that a shallow hillock could not be found and reliably imaged to establish if it comprised a single dislocation consistent with source 6 and the fitted BCF curve. Nor could the source of hillock 13 be found. However the sources of hillocks 14 and A were found and imaged. The source of hillock 14 is shown in figure 6.28. The growth spiral appears to have been formed around what appears to be a foreign inclusion which is acting as a source of steps. There are actually two spirals in this image, one formed by the inclusion, the other seems to be a native spiral. Substantial step bunching is evident on this spiral, as is dislocation slip which indicates significant stress. It is possible that the native spiral has formed as a result of the formation of dislocations due to the stress induced by the inclusion. The structure of this source appears to readily account for its heightened activity.

Figure 6.29 shows the $<101>_f$ steps of hillock 14 some distance from the source. A train of kinematic waves is clearly apparent. These bunches of steps have clearly been generated at the source shown in figure 6.28 and continue without dispersion in the manner described by Frank [50] (see also section 2.7.3). Figure 6.30 shows a step shockwave on the $<101>_f$ steps of source 14. The discontinuity in the slope of the surface here is readily apparent. Figures 6.31 and 6.32 show the source of hillock A in figure 6.27. A very large number of dislocations are cooperating to form a macrospiral which is sending out large, dense bunches of steps. The height of the macrosteps is sufficient to interfere with optical wavelengths, hence the non-uniformity of the interference fringes on hillock A in figure 6.27 is readily explained. The scale of some of the features in these images are approaching the upper limit for reliable imaging for the AFM and so some detail has been lost. Nonetheless these images give a striking

and graphic illustration of the structure of a source responsible for the generation of a macrospiral.

Hillocks B to F

Figures 6.33 to 6.46 correspond to another crystal which was growing under identical bulk conditions to those in figure 6.26 (relative supersaturation 0.0427 ± 0.0008). During growth the behaviour of this crystal appeared to be atypical. Due to the fleeting existence of many such transient phenomena, it was removed immediately for AFM study after only 3 minutes of growth at steady conditions so that the surface structure responsible for the atypical behaviour could be studied. Due to the very short duration of growth, reliable growth rates could not be obtained and so the growth of this crystal does not appear in figure 6.4. Regarding the atypical growth, in particular the slope of the dominant hillock B appeared to change abruptly and growth at the hillock centre appeared to cease, yet continued elsewhere on the hillock. The pixel intensity time series for the centre of hillock B is shown in figure 6.46. For the first 100 seconds of growth the passage of coherent interference fringes is obvious. Thereafter however the growth appears to change in character entirely, with the time-series becoming erratic and noisy. This had been witnessed previously on other crystals but no AFM observations had been made. A suggestion for the atypical behaviour became apparent with the AFM imaging. It was found that hillock B in figure 6.33 was covered by extensive two-dimensional islands over a wide area. The terraces of a dominant growth spiral were also apparent but the original source of the spiral could not be found. Figures 6.34 and 6.35 show a single two-dimensional island between the terraces of a growth spiral. The step height of the island was identical to that of the spiral and all other observations of fundamental steps on KAP {010}. The shape of the island is clearly seen to correspond to the first few turns of growth spirals on KAP {010} before they become completely polygonised, exhibiting mirror symmetry about the [001] direction. Figures 6.36, 6.37 and 6.38 each show multiple two-dimensional nuclei. Particularly notable in figure 6.36 is the occurrence of islands on top of islands which is characteristic of the multi-level or birth and spread model [5] described in section 2.7.1. The terraces of the original growth spiral and their interactions with the two-dimensional islands can also be clearly seen in figure 6.36, as can the characteristic shape of the islands. Figures 6.37 and 6.38 are large area scans of the same region of hillock B. The extent of two-dimensional nucleation is apparent here. A significant feature of both of these figures are the high ribbon like plateaus which have developed and appear to fol-

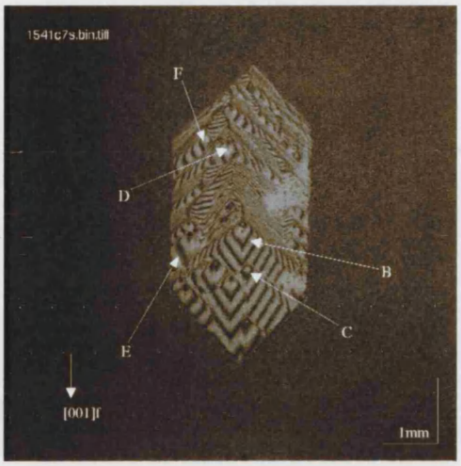

Figure 6.33: Interference image of a crystal growing under conditions identical to points 12, 13, 14 in Figs. 6.4 and 6.26. The crystal was removed after an abrupt change in activity. $T_{sat} = 25.56\ ^{\circ}C$, $T_{growth} = 23.46\ ^{\circ}C$, $\sigma = 0.0427 \pm 0.0008$.

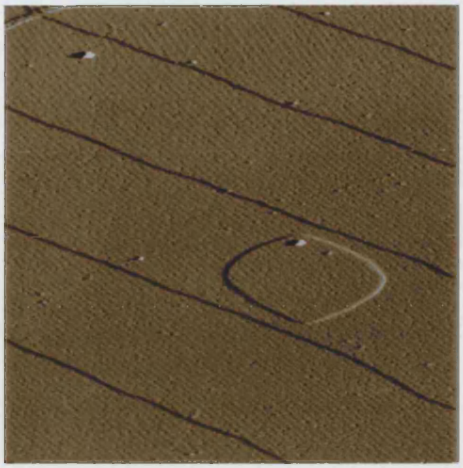

Figure 6.34: AFM image of region corresponding to point B in Fig. 6.33. 2-dimensional island between $<101>_f$ steps. Scan size 5.87 μm.

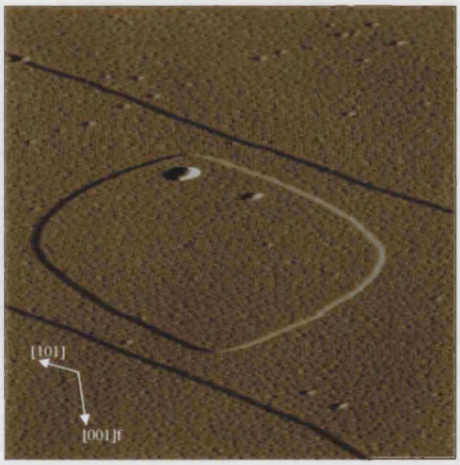

Figure 6.35: AFM image. Close up of 2-dimensional island shown in Fig. 6.34. Scan size 2.73 μm.

Figure 6.36: AFM image of extensive 2-dimensional islands. Region B of Fig. 6.33. Scan size 13.2 μm.

low the terraces of the original growth spiral. These "ribbons" appear to have formed by preferential two-dimensional nucleation on a single terrace and are typically tens of fundamental steps high. The steps of the two-dimensional islands are confined to this terrace and can grow along the terrace but are prevented from growing beyond it. Presumably, as the plateau grows higher it protudes further into the solution and preferentially receives more growth units from the solution, allowing it to grow higher still. In the lower edge of figure 6.38 a junction between two such "ribbons" appears to have formed, forming a plateau higher than the terrace itself. Also apparent in figure 6.38 are several small growth spirals co-existing with the two-dimensional islands. Their presence makes the orientation and symmetry of the islands clear. The origin of the islands is a matter for discussion. The discrete islands shown were almost certainly formed during removal of the crystal from solution, however the unusual behaviour of the hillock prior to imaging suggests that some unusual behaviour was occurring prior to removal. It is possible that the image represents an intrinsic but arrested two-dimensional nucleation process. This point will be returned to after examination of other hillocks on this crystal.

Another significant observation on hillock B was the occurrence of apparent microcrystal inclusions embedded in the surface, shown in figures 6.39 and 6.40. These microcrystals appear as microscopic analogues of KAP platelets embedded in the surface. The angle formed by the uppermost and lowermost edges on the microcrystal in figure 6.39 was measured as 102°. The corresponding angle on that in figure 6.40 was measured as 110°. For the angles between the top and side edges the values of 130° and 135° were obtained for figures 6.39 and 6.40 respectively. By reference to the "cusps" of the two-dimensional islands, which indicate the <001> direction, apparent in both images; their orientation on the main crystal face can be established. The upper right hand edge of the microcrystal of figure 6.39 was found to be misoriented from the <001> direction by approximately 3°. In figure 6.40, the upper right hand edge was found to lie precisely along the <001> direction. They also exhibit surface steps apparently independent of the surface in which they are embedded, however attempts to sharply resolve these steps failed, suggesting that they are qualitatively different from those on the surface at large. This is most readily seen in figure 6.39 in which the surface steps on the main surface are clearly resolved yet those on the microcrystal are diffuse and poorly resolved. The inclusions themselves were raised considerably above the underlying surface by tens of fundamental step heights so there was no scope for steps from the underlying crystal to migrate across the microcrystal surface. The final observation of these microcrystals is that no dislocations are apparent near

their interface with the bulk crystal suggesting that the interface is coherent. Crystallographically the microcrystals could be microscopic twin crystals which would have eventually grown to macroscopic dimensions or become a source of steps for the main crystal.

Figures 6.41 to 6.45 are AFM images of the hillocks C, D, E and F on the crystal shown in figure 6.33. Figure 6.41 shows the source of hillock C. The hillock is seen to be formed from a double growth spiral resulting from a dislocation with a multiple screw component Burgers vector. The step spacings are remarkably uniform until the steps meet a single dislocation in the bottom left hand corner of the image. The flux of steps from the main source are seen to interact with this dislocation creating a right angled corner in the step which must propagate normal to the main step direction. The most striking feature of this spiral however is the slip step which crosses it. The step is the same height as the steps of the spiral, approximately 1.3 nm, and has apparently formed by the slip of a dislocation with a screw component. The field of view is 30 μm and the dislocation has travelled at least that distance. The slip is most likely to have occurred after growth ceased because the step essentially remains straight. If it were present during growth then it would have been expected to grow and wind up into another spiral. Figure 6.42 reveals the source of hillock D. From inspection of figure 6.33 it appears that hillocks C and D have essentially the same slope. From the AFM image of hillock D it is clear that this hillock is also formed from a double growth spiral from a multiple dislocation. The step spacings of the narrow and wide terraces between the $<101>_f$ steps of hillock C were measured (in the AFM image) as 0.51 μm and 1.58 μm respectively. For hillock D the corresponding measurements were 0.51 μm and 1.45 μm respectively. The corresponding mean step spacings, y_0 for hillocks C and D then are 2.09 μm and 1.96 μm respectively. These hillocks are widely separated and yet are similar in shape and step spacing. It appears then that the growth conditions, i.e. local supersaturation and temperature, were similar for both sources despite the separation. Assuming that this is the case for all of the other crystals in this study, and this appears to be the case from the correlation in growth rate data from widely separated points, then this result serves to show that the stirring in the solution was adequate to minimise local supersaturation variations. It is abundantly clear from AFM of hillocks C and D however, that they do not exhibit any two-dimensional islands, despite the extensive two-dimensional nucleation on hillock B which lies between them. This result is somewhat puzzling. The absence of two-dimensional islands on C and D, the absence of any significant removal induced deposition, and the observed atypical growth of hillock B, all lend support to the argument that an intrinsic two-dimensional growth

Figure 6.37: AFM image of 2-dimensional islands. Region B of Fig. 6.33. Scan size 45 μm.

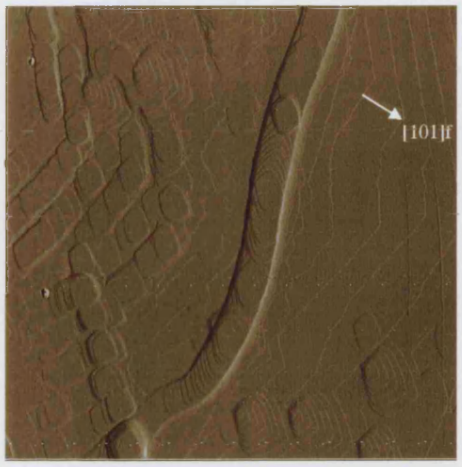

Figure 6.38: AFM image of extensive 2-dimensional islands with growth spirals. Region B of Fig. 6.33. Scan size 30 μm.

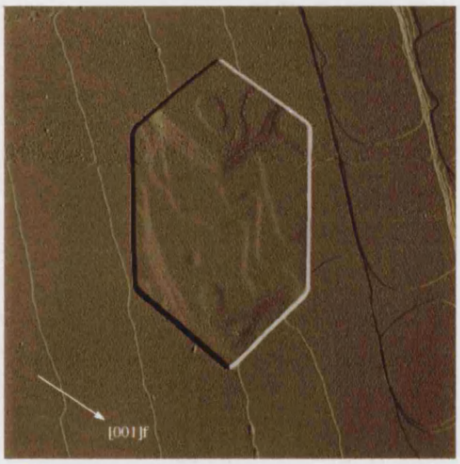

Figure 6.39: AFM image of an apparent micro-crystalline inclusion on region B of Fig. 6.33. Scan size 7.91 μm.

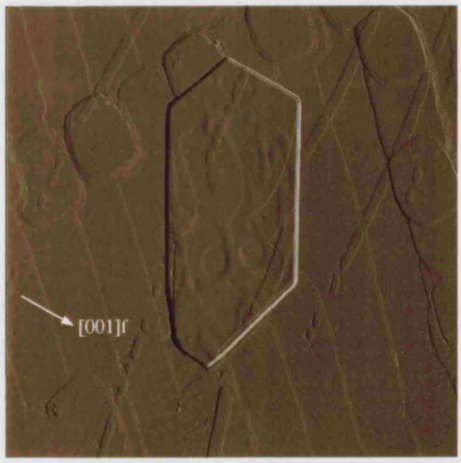

Figure 6.40: AFM image of an apparent micro-crystalline inclusion on region B of Fig. 6.33. Scan size 11.7 μm.

process was occurring on this hillock prior to removal from solution and that the islands are not merely artefacts of inadequate removal. A hypothesis to explain how such local and atypical two-dimensional nucleation may occur will be put forward in the general discussion in chapter 8.

Figure 6.41: AFM image of dislocation outcrop corresponding to point C in Fig. 6.33. Scan size 30 μm.

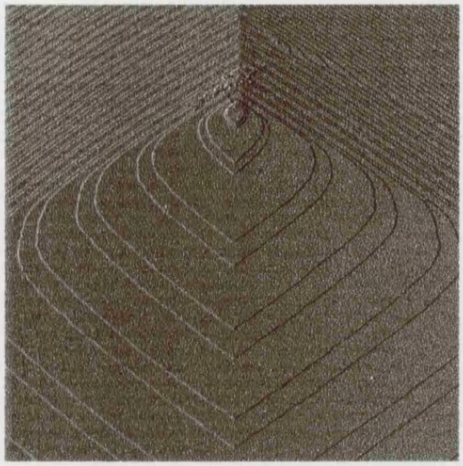

Figure 6.42: AFM image of dislocation source corresponding to point D in Fig. 6.33. Scan size 13 μm.

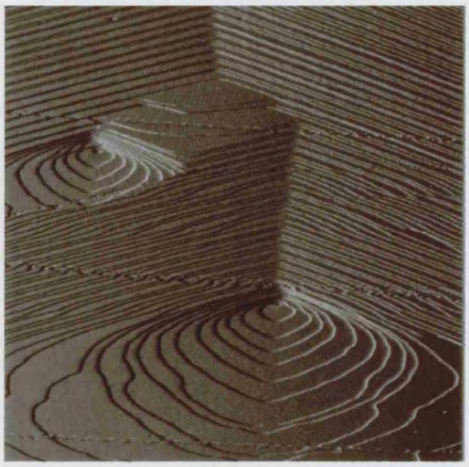

Figure 6.43: AFM image of dislocation outcrop corresponding to E in Fig. 6.33. Scan size 11.98 μm.

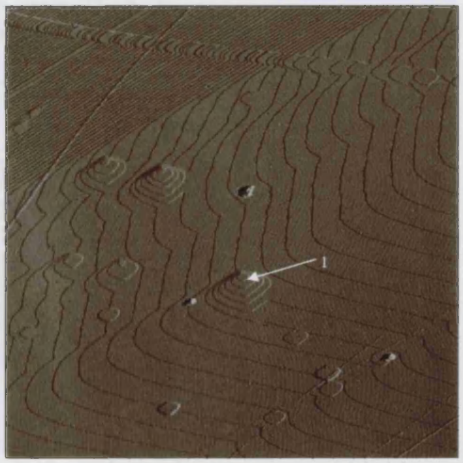

Figure 6.44: AFM image of left hand side of dislocation source corresponding to F in Fig. 6.33. Scan size 30 μm.

Figure 6.43 shows growth spirals at the centre of hillock E. The spirals are both formed from a single dislocation. It is notable that, in contrast to the double spirals of C and D, the steps are quite rounded and irregular, particularly for the main spiral. Why this should be so is not clear from this image. Unintentional impurities could be one explanation but why these should affect these spirals more than others is not clear. Also apparent in this image is the absence of two-dimensional islands. Figure 6.44 shows the left hand side of hillock F (the right hand side and hillock centre was engulfed). Hillock F has some limited two-dimensional islands present between the terraces of the main spirals along with some very small growth spirals. The interaction of the small spirals with the steps of the main spiral is apparent. Quite striking is the extended ribbon of apparent two-dimensional islands which have coalesced with the steps of the main hillock, stretching across the entire image field. Furthermore, in the lower half of the image is a row of two-dimensional islands which lie along a line formed by apparent cusps in the steps of the main spiral. It appears that the cusps and the islands are related. The islands are all similar in size and similar to the size of the second turns of the small growth spirals. A small area scan of one such growth spiral, that labelled 1 in figure 6.44, is shown in figure 6.45. A single dislocation is present and it can be clearly seen that it has slipped a very short distance from its original position at the centre of the spiral to the adjacent terrace of the main spiral. Its passage has closed the steps of the spiral into closed loops, leaving multi-level two-dimensional islands on the surface. It has also left distortions in its wake on the steps through which it has passed. If growth were not arrested the dislocation would have formed a new growth spiral at its new location and the two-dimensional islands formed by its passage would also continue to grow and merge with the steps of the main spiral. This image is striking proof that dislocation slip can cause the formation of two-dimensional islands. In this instance it seems that the slip must have occurred immediately before or during removal because there has been no time for the dislocation to form a new spiral at its final location. However this does not preclude slip from occurring during normal growth and there have been many other examples of dislocation slip presented in the previous figures. It appears then that dislocations, growth spirals and two-dimensional islands can all interact in complex ways. Further more detailed discussion of the occurrence of these apparently related phenomena will be given in the general discussion in chapter 8.

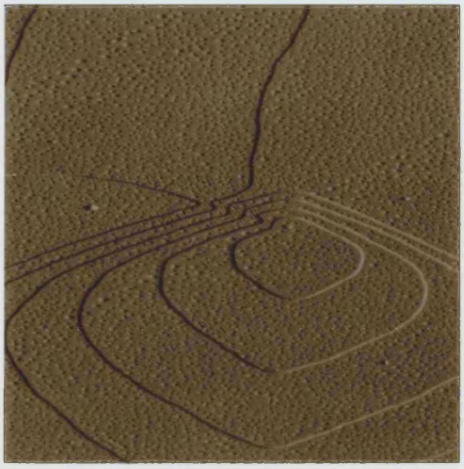

Figure 6.45: AFM image. Close up of growth spiral labelled 1 in Fig. 6.33. The dislocation has clearly slipped a short distance from the spiral centre leaving a step and islands enclosed by a closed loop. Scan size 3.0 μm.

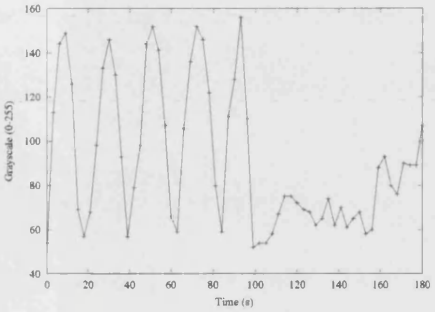

Figure 6.46: Intensity time series data for source B, Fig. 6.33.

Figure 6.47: Interference image of crystal corresponding to point 15 in Fig. 6.4. $T_{sat} = 25.56\,^{\circ}C$, $T_{growth} = 23.10\,^{\circ}C$, $\sigma = 0.0499 \pm 0.0008$.

Figure 6.48: AFM image. Close up of step source corresponding to point 15 in Fig. 6.4. The complex source appears to be generated by a twin crystal. Note the macrosteps. Scan size 15.0 μm.

Hillock 15

Finally, figure 6.47 (page 178) shows the crystal containing hillock 15, growing at a relative supersaturation of 0.0499 ± 0.0008. Hillock 15 dominates this crystal and from figure 6.4 it is clear that the activity of this hillock is considerably higher than that of the fitted data. The interference fringes are slightly irregular and suggest large features such as macroscopic steps or kinematic waves on the surface. AFM of the source of hillock 15 reveals that it is apparently generated at the boundary between the main crystal and a small KAP inclusion which may be a twin crystal. The edge of the inclusion being clearly visible jutting out from the main surface at a shallow angle. The growth spiral emanates from this edge resulting in the formation of a very steep spiral centre. So steep is the spiral centre that individual steps can only just be resolved. Away from the inclusion edge the hillock becomes shallower and eventually forms a macroscopic step. The inclusion appears to exhibit steps with the symmetry of KAP {010} growth spirals confirming that it is KAP and not some other foreign inclusion.

6.4.2 $T_{sat} = 29.26\ °C$

Hillocks 16, 17, 18, 19

Figure 6.49 shows the crystal on which growth rates 16, 17, 18 and 19 were measured. The crystal was growing at a low relative supersaturation of 0.0034 ± 0.0009. Multiple hillocks are present on the crystal. The hillocks are shallow as would be expected at this supersaturation. There are however clear differences in slope between hillocks. For example, hillock 16 appears to be approximately twice as steep as 19. According to figure 6.7 however, hillock 19 has the greatest normal growth rate, the others all having approximately the same normal growth rate. Due to the low supersaturation the normal growth rates of all of the hillocks are very low and according to the error bars on point 19 in figure 6.7, the differences between the various hillocks are hardly significant. Figures 6.50 and 6.51 show the dislocation outcrop at the centre of hillock 16. Immediately apparent in these figures is the roughness of the $<101>_f$ steps of the spiral. The steps appear to be extensively pinned by impurities. The $<101>_s$ steps appear to be hardly affected however, remaining essentially straight. Also apparent are numerous dislocations, their presence disclosed by the termination of surface steps.

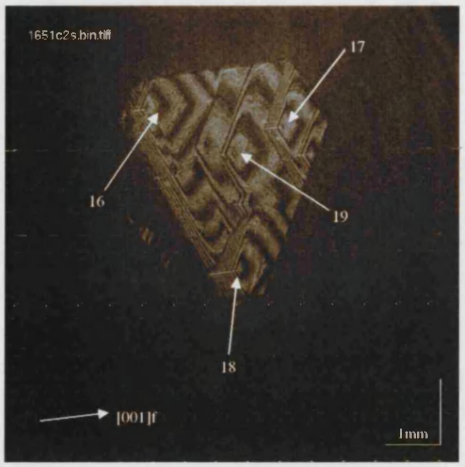

Figure 6.49: Interference image of crystal corresponding to points 16, 17, 18, 19 in Fig. 6.7. $T_{sat} = 29.26$ °C, $T_{growth} = 29.11$ °C, $\sigma = 0.0034 \pm 0.0009$.

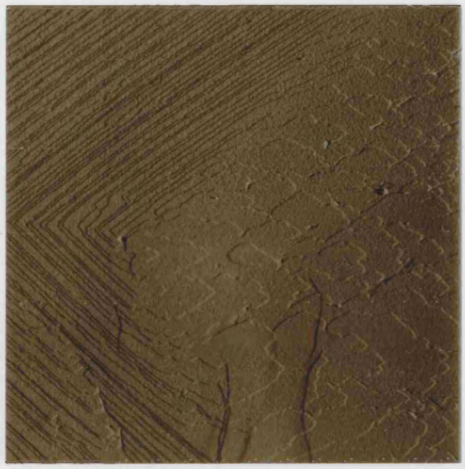

Figure 6.50: AFM image of dislocation outcrop from source 16 in Fig. 6.49. Scan size 40 μm.

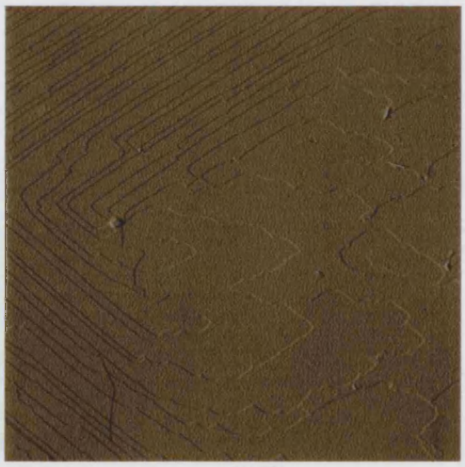

Figure 6.51: AFM image. Close-up of dislocation source 16 in Fig. 6.50. Scan size 20 μm

Figure 6.52: AFM image of dislocation outcrop from source 17 in Fig. 6.49. Scan size 38.98 μm.

Some of these dislocations have undergone slip and have left slip steps across the surface as evidence of this. As for the main source of the spiral, this appears to be due to a dislocation of high strength. At least five steps originate from what appears to be a single dislocation. The number could be greater because other adjacent steps could also originate from this dislocation however it was not possible to obtain sufficient resolution to prove this unequivocally. The other notable feature about this source is that a pit has formed at the dislocation centre. This is consistent with Frank's analysis of capillary equilibria of crystals and the formation of hollow dislocation cores [40] (see also section 2.7.2). The strain energy associated with a screw dislocation can be shown to be proportional to the square of the magnitude of the Burgers vector, which in this case appears to be at least 5 lattice parameters normal to the surface. The strain energy associated with such a dislocation then is large and the formation of a hollow core is favourable. It should be stressed that the image appears to show a shallow pit, however this is an artefact. The AFM tip cannot penetrate to the bottom of the pit and so a shallow flat bottomed pit appears in the image. In reality, the core could be very deep and extend a considerable distance into the crystal. Slightly above and to the right of the main dislocation is another dislocation outcrop, most clearly visible in figure 6.51. A small pit has developed here also and at least two steps appear to originate from it, suggesting a Burgers vector of magnitude approximately 2 surface normal lattice parameters. Assuming that these are indeed single dislocations then the strain energy will be many times less than that of the main dislocation and consequently the pit at this dislocation would be expected to be considerably smaller. The occurrence of surface pits, hollow cored dislocations and step pinning will be considered further in the general discussion.

Figures 6.52 and 6.53 show the dislocation outcrop at the centre of hillock 17. Some deposition of material during removal is apparent however the spiral is largely unaffected at the centre. For the first few turns of the spiral the steps remain separate. Beyond this however the fundamental steps coalesce to form macrosteps tens of fundamental steps high. These macrosteps then propagate outward from the spiral centre. After the first turn of the macrospiral no fundamental steps are visible outside of the macrosteps. Figure 6.54 shows a train of macrosteps on the $<101>_f$ steps of hillock 17. Very wide entirely flat terraces lie between the turns of the macrospiral. The width of the terrace at the point indicated was 16 μm. Why this source should produce a macrospiral is uncertain. The source itself appears to comprise multiple dislocations however extensive slip has occurred, most likely during removal, and the resultant slip steps make it difficult to establish the true nature of this source. It may be assumed that

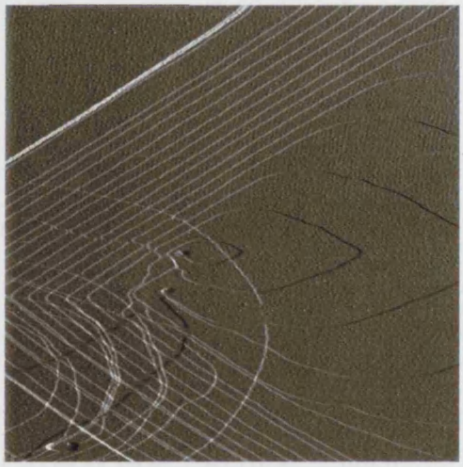

Figure 6.53: AFM image. Close-up of dislocation source 17 in Fig. 6.52. Scan size 5.34 μm

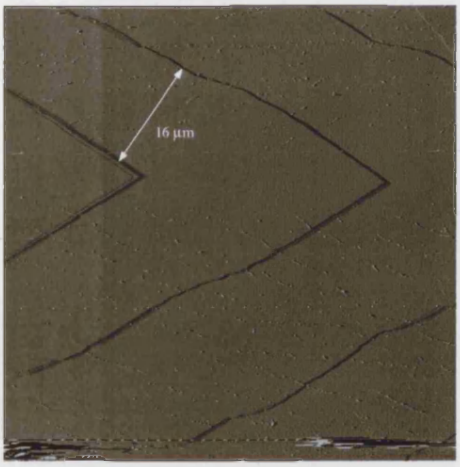

Figure 6.54: AFM image of step bunches oriented along $<101>_f$ emanating from source 17. Scan size 60 μm.

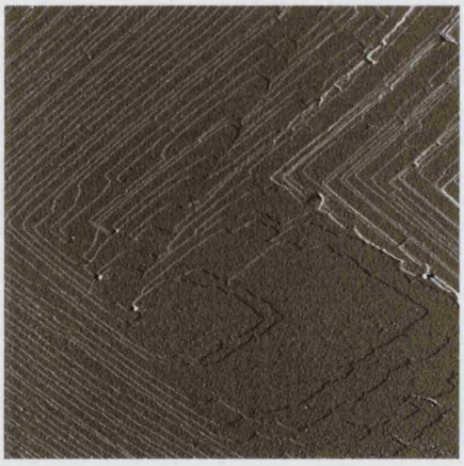

Figure 6.55: AFM image of dislocation source 18 in Fig. 6.49. Hollow cores are clearly visible. Another multiple source lies out of frame at the far right hand side and is shown in Fig. 6.57. Scan size 31 μm.

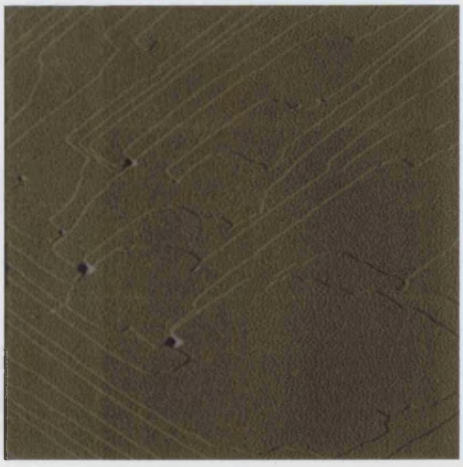

Figure 6.56: AFM image. Close-up of dislocation source 18 shown in Fig. 6.55. Scan size 13.22 μm.

the fundamental steps before the first turn of the macrospiral are moving faster than the macrostep and eventually catch it up and become part of it. If the macrosteps move with constant velocity and the source generates steps continuously then the macrostep would grow higher and higher as more fundamental steps joined it. This does not appear to happen however since after the first macrospiral turn the macrosteps appear to propagate with constant height and velocity. Certainly the growth rate data of this source showed it to be growing under steady state conditions. The macrosteps must either reach a constant height and break up or the source must undergo periodic activity variations, intermittently sending out steps and then ceasing. Each period of activity resulting in the formation of a new turn of the macrospiral. The absence of fundamental steps after the first turn of the macrospiral suggests that the macrospirals are stable and do not break up. Also remarkable about this hillock is that it does not appear to have been affected by the impurities which were so apparent on hillock 16, the steps having remained almost entirely straight. Furthermore, there is no evidence of a pit due to a hollow dislocation core, even though one of the dislocations appears to have a Burgers vector of at least two b lattice parameters due to the presence of two steps terminating at it. The double dislocation at source 16 had a pit. Why this hillock should be apparently unaffected by impurities and not form a pit at the dislocations is uncertain. The macrosteps themselves may be implicated in the apparent immunity to impurity pinning. One other significant observation on this hillock is that the straight step segments appear to deviate widely from the usual <101> directions. Some small misorientation from <101> is observed with reasonable frequency on the (nominal) $<101>_f$ step directions. However this is seldom observed for the nominal $<101>_s$ steps. In this case however the misorientation is large on both $<101>_f$ steps and $<101>_s$ steps. The measured angle between the equivalent sets of $<101>_s$ steps was 78°, and between the equivalent sets of $<101>_f$ steps was 70°. The angle between the <101> directions from the unit cell geometry is 112°. The spiral shape will be taken up in greater detail in the general discussion.

Figures 6.55 to 6.58 show the centre of hillock 18. The hillock actually comprises two very close together multiple spirals. The first of these spirals is shown in figures 6.55 and 6.56. The other spiral is shown in figures 6.57 and 6.58. Like hillock 16, the steps of this spiral exhibit extensive impurity pinning. Several multiple dislocation sources are also present with pits at their emergent points. Similarly to hillock 16, these appear to have Burgers vectors which are multiples of the surface normal lattice translation as revealed by multiple steps terminating at the emergency point. It is quite clear in these images that the size of the pit seems to depend on the number of steps terminating. For

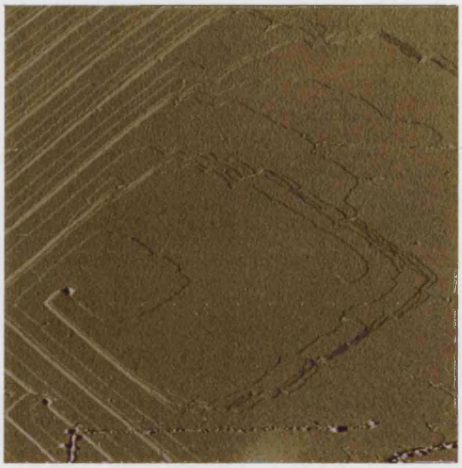

Figure 6.57: AFM image of rightmost part of dislocation source 18 in Fig. 6.49. This part of the source lies to the right of that shown in Fig. 6.55. Hollow cores are again clearly visible. Scan size 31 μm.

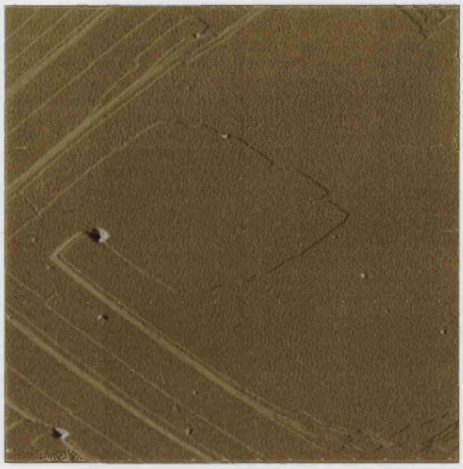

Figure 6.58: AFM image. Close-up of dislocation source 18 shown in Fig. 6.57. Scan size 16 μm.

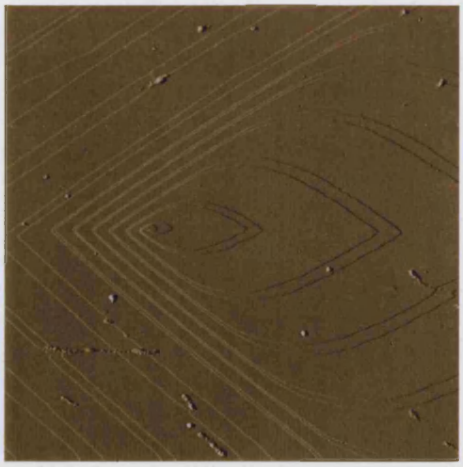

Figure 6.59: AFM image of dislocation source 19 from Fig. 6.7 and 6.49. Scan size 13.24 μm

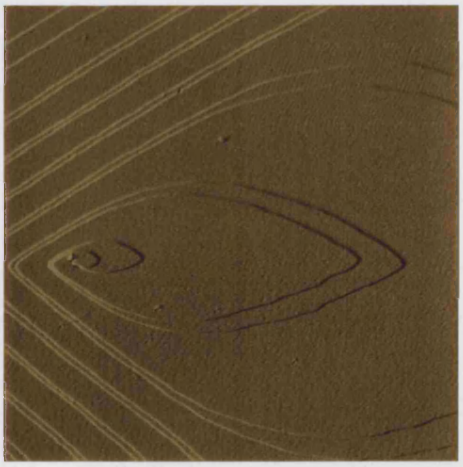

Figure 6.60: AFM image. Close-up of double spiral source 19. Scan size 4.71 μm.

example, the main source in figure 6.58 has a large pit and six steps terminate at it. At the top in the centre of the image a dislocation at which a single step terminates can be seen and the pit is only just visible. The score mark at the bottom of figure 6.57 is the result of an accidental crash of the AFM tip into the surface during an adjustment.

Figures 6.59 and 6.60 show the centre of hillock 19. Some debris due to inadequate protection is present on the surface here however it does not affect the interpretation of the image. The hillock is formed from a double spiral produced either from a single dislocation of strength 2 or two dislocations of like sign which are very close together (too close to be resolved). The first few turns of the spiral are very uniform after which the step separation begins to change. Like hillock 17 and in contrast to 16 and 18, the steps of this hillock are not pinned by impurities and there is no obvious pit at the centre of the source. Also, even more so than hillock 17, the steps are continuously curved from the $<101>_f$ to the $<101>_s$ steps with no sign of polygonisation except at the intersections of equivalent steps on [001]. The tangential angle at the intersections of the equivalent steps was 78° for the $<101>_f$ steps and 64° for the $<101>_s$ steps.

Hillocks 20, 21, 22

Figure 6.61 shows a crystal growing at a nominal relative supersaturation of 0.0078 ± 0.0009. Two dominant hillocks labelled 21 and 22 are present as are several other hillocks and the legacy steps of hillocks which have been, or are about to be, engulfed - such as the point labelled 20. Compared to the legacy hillocks left behind by inactive sources, which appear shallow, hillocks 21 and 22 appear to be steep, 22 being the steepest (see table 6.9 and figure 6.87). For example the $<101>_s$ steps of the dormant hillock on the right hand side of the crystal are very much more widely separated than those on 21 and 22 as can be seen from the spacing of the interference fringes. Figure 6.62 shows the dislocation source at the centre of hillock 21. Considerable deposition has occurred during solution removal though it is fortunate that the spiral centre is unaffected. Some of the larger debris particles have interrupted the imaging process creating artefacts in the images. The figure shows that the steps emitted from the source have a separation periodicity which repeats itself every four steps. That is, steps are emitted from the source in bunches of four. Figure 6.63 shows the centre of hillock 21. The bunches of four steps are apparent on the $<101>_s$ steps in this image. Furthermore, the four steps can all be seen terminating at a single dislocation at the centre of the spiral, indicating an apparently single dislocation of strength 4.

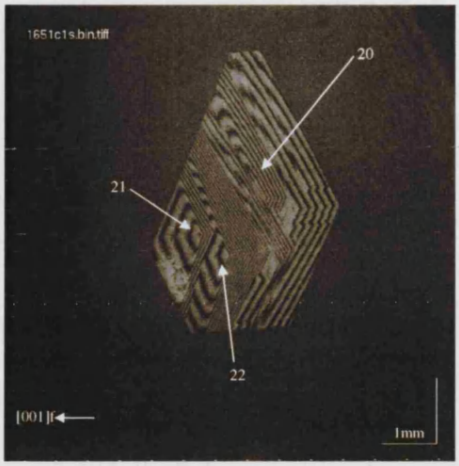

Figure 6.61: Interference image corresponding to points 20, 21, 22 in Fig. 6.7. $T_{sat} = 29.26$ °C, $T_{growth} = 28.91$ °C, $\sigma = 0.0078 \pm 0.0009$.

Figure 6.62: AFM image. Large area view of dislocation source corresponding to point 21 in Fig. 6.61. Scan size 50 μm.

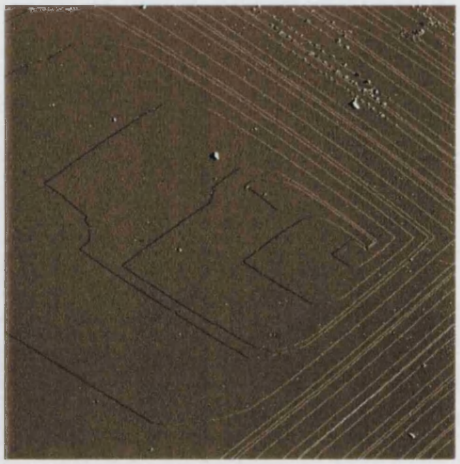

Figure 6.63: AFM image of centre of source 21 in Fig. 6.61. Scan size 17.33 μm.

Figure 6.64: AFM image. Close-up of dislocation source 21 from Fig. 6.63. Scan size 7.46 μm.

However, close inspection of figures 6.62 to 6.64 reveals a slip step from the centre of this dislocation, indicating that a single dislocation in the source has slipped away from the centre some time earlier. Although it is possible that a single dislocation of large Burgers vector has dissociated it appears to be more likely that the source is in fact made up of a group of very narrowly separated dislocations which are cooperating to form a multiple spiral. One of the spiral steps from the group appears to be terminated a short distance away by a single unit dislocation which must be of opposite sign. The separation between the main group and this dislocation was measured as 3.9 μm. The mean step separation on the $<101>_f$ steps of this source was measured by AFM as 2.47 μm. However the most narrowly spaced steps in the bunches of four had a separation of only 0.76 μm. The step emanating from the single dislocation encounters and coalesces with the steps from the other dislocation. The point of coalescence can be seen from the intersection that is introduced into the steps where they meet, which persists as they move away from the spiral centre (the trajectory followed by such an intersection is the *locus of intersection* defined by BCF [34]). Finally, a slight pit has developed at the centre of the strongest source but not at the unit dislocation which is consistent with the greater strain energy expected at the core of a dislocation of greater Burgers vector or a narrowly separated group of separate dislocations.

Figures 6.65 to 6.72 are of hillock 22. Figures 6.65 and 6.66 show the transition region between the $<101>_f$ and <001> steps. The <001> steps appear to be extensively pinned by impurities whilst the $<101>_s$ steps remain straight and unaffected. It is most clearly seen from the $<101>_s$ steps that steps are emitted from the source in bunches of five. Figure 6.67 shows the $<101>_f$ steps of hillock 22, periodic bunches of five steps are visible here also. Figures 6.68 and 6.69 reveal the source structure responsible for this hillock. There are actually three dislocations (or cooperating groups) at the hillock centre. Although the structure of the uppermost of these sources is masked somewhat by a slip step, it appears that there are five steps terminating at it. The middle dislocation clearly has four of the steps from the uppermost source terminating at it also (see figure 6.71), indicating that it is of opposite sign to the uppermost source. The remaining step from the uppermost source is terminated at the lowermost dislocation which must be a unit dislocation of the same sign as the middle dislocation. There are then effectively an equal number of right and left handed dislocations giving rise to closed loops of steps. The implication is that the hillock is not a spiral but a series of closed step loops. The sources lie almost on a straight line, the distance separating the uppermost and lowermost dislocations was measured as 9.41 μm. The mean step separation on the $<101>_f$ steps of this hillock was measured by AFM as 2.1 μm. The

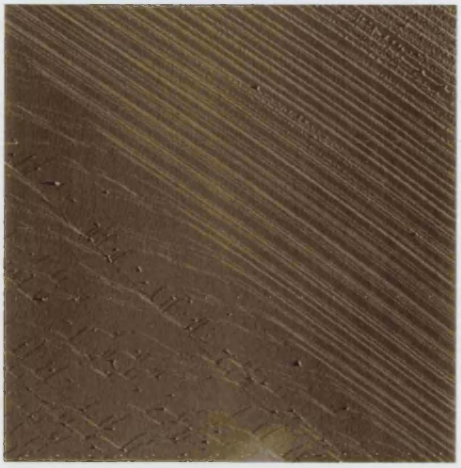

Figure 6.65: AFM image corresponding to point 22 in Figs. 6.7 and 6.61. Transition from $<101>_s$ to <001>. Scan size 40 μm.

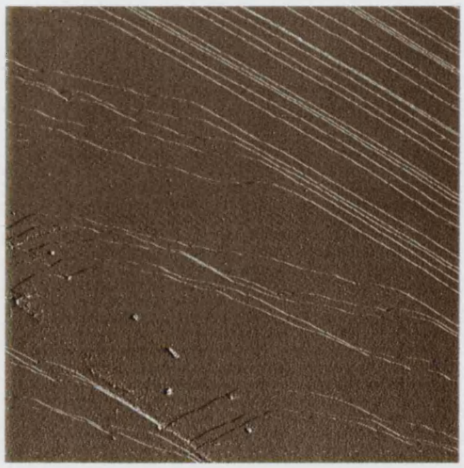

Figure 6.66: AFM image. Close-up of $<101>_s$ to <001> transition shown in Fig. 6.65. Scan size 14.56 μm.

Figure 6.67: AFM image of $<101>_f$ step trains emanating from the source corresponding to 22 in Figs. 6.7 and 6.61. Scan size 50 μm.

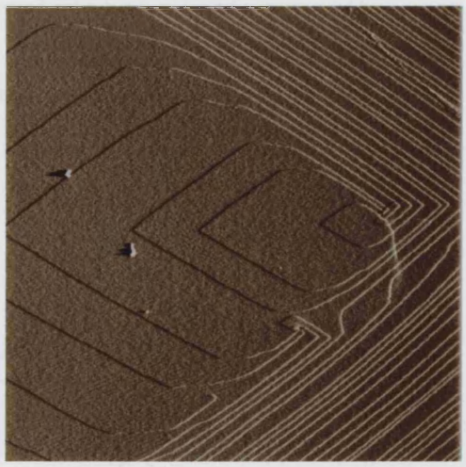

Figure 6.68: AFM image of centre of dislocation source corresponding to source 22 in Fig. 6.61. Scan size 16.46 μm.

intersections of steps from the upper and middle sources is clearly visible in figure 6.69. In this figure two almost touching steps are about to coalesce and the locus of intersections is clearly visible from steps which have coalesced earlier. Finally, figure 6.72 shows a wide area scan of hillock 22 from which the periodicity in the step spacing is apparent.

The strength, s, of a source was defined in section 2.6 as the excess of dislocations of one sign over dislocations of opposite sign [34]. As discussed in that section, the strength of a group of dislocations depends on whether they are cooperating, which depends in turn on their sign and separation. According to this, as far as can be established from the images of hillocks 21 and 22, the multiple dislocations or groups are producing cooperating spirals however the distinct groups are not themselves cooperating. Therefore in both cases the source activity is that due to the dislocation or group of highest strength. The respective strengths of hillocks 21 and 22 are potentially ambiguous due to the slip of dislocations from the centre of the main dislocations or groups. Fortunately however the step periodicity is clear in both cases. In the case of hillock 21 the step periodicity is clearly repeated every four steps, indicating a source of strength 4. For hillock 22, the step periodicity repeats itself every five steps, indicating a source of strength 5. From figure 6.7 it is evident that the normal growth rates of the two hillocks are virtually the same and that they agree very closely with the other data from the data set fitted with the BCF curve. This is apparently anomalous since sources of significantly higher strength would be expected to have a significantly greater normal growth rate. It was however found by reference to table 6.9 (page 204), figure 6.87 (page 205) and the step separations reported above, that source 22 is marginally steeper than source 21 and both are significantly steeper than other hillocks at similar supersaturations. This is consistent with the higher strength of source 22 and the overall strengths of these two hillocks respectively. The interactions of the dislocations on hillocks 21 and 22 are of considerable interest and will be discussed further in the general discussion.

Hillock 23

Figure 6.73 shows a crystal growing at relative supersaturation 0.0123 ± 0.0009. The crystal was unusual in that the surface was covered by a single growth hillock. Figure 6.74 shows the centre of the hillock. Unfortunately a piece of debris from removal of the crystal has deposited at the very centre of the spiral preventing examination of its

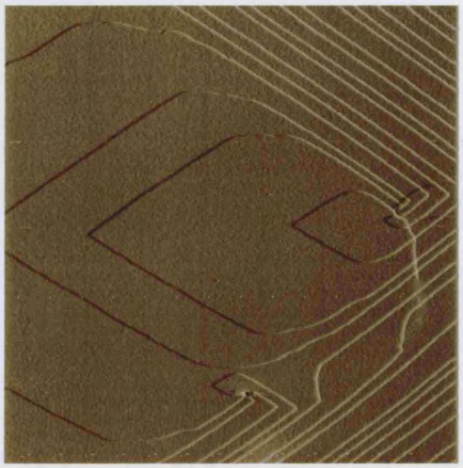

Figure 6.69: AFM image. Close up of source 22 shown in Fig. 6.68. Scan size 10 μm.

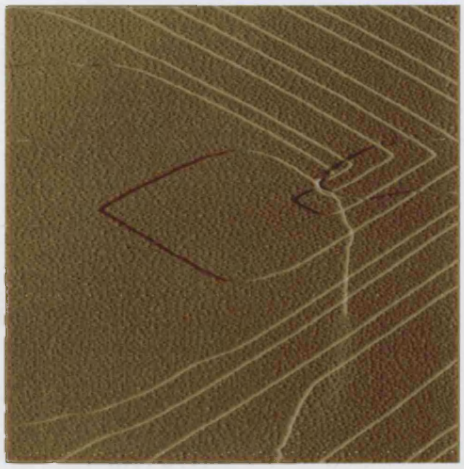

Figure 6.70: AFM image. Close-up of uppermost dislocation source in Fig. 6.69. Scan size 5 μm.

Figure 6.71: AFM image. Close-up of the middle dislocation source in Fig. 6.68. Scan size 2.6 μm.

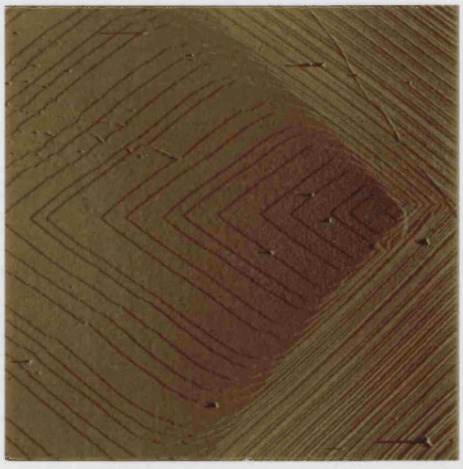

Figure 6.72: AFM image. Large area view of source 22 in . 6.61. Scan size 50 μm.

fine structure, however, the hillock is clearly formed from a double growth spiral. The source must then be either a single dislocation of strength 2, or two unit dislocations of equal sign. The unambiguity of a crystal with a single hillock provides a useful test of the quantitative agreement between interferometry and AFM. The mean step spacing of the $<101>_f$ steps on this hillock was measured as 2.7 μm by both techniques, providing a confirmation of the quantitative agreement between the two techniques. This also serves very well to illustrate the point that interferometry can provide a very accurate measurement of step spacing, but can only give a mean result. The AFM on the other hand can reveal the true step spacings. Perhaps even more important is the demonstration that the surface which is imaged *ex-situ* by AFM is substantially the same surface as when it was growing. On removal of the crystal from solution, the environment of the surface changes abruptly. In such a situation the question must always be asked, does the surface have sufficient time to relax to a new configuration? When this is the case, the surface observed *ex-situ* is not representative of the growing surface. This result of equal step spacing *in-situ* and *ex-situ* provides experimental verification that the surface imaged *ex-situ* by AFM is representative of the growing surface. Essentially, the surface is "frozen" in the state which it was in, in the final moments of growth.

Figure 6.73: Interference image of crystal corresponding to point 23 in Fig. 6.7. $T_{sat} = 29.26$ °C, $T_{growth} = 28.71$ °C, $\sigma = 0.0123 \pm 0.0009$.

Figure 6.74: AFM image of dislocation outcrop from source 23 in Figs. 6.7 and 6.73. Scan size 30 μm.

Hillocks 24, 25

Hillocks 24 and 25 are shown in figure 6.75. Hillock 24 is dominant, 25 being just visible. The crystal is growing at a relative supersaturation of 0.0217 ± 0.0009. Figure 6.76 shows the centre of hillock 24. The quality of preservation of the crystal surface during removal from the solution is poor in this case. Notable are the etch pits which have formed. The polygonal shape of these pits reflects the symmetry of the growth spirals and the underlying crystal. The AFM study of such pits on KAP has been discussed elsewhere [100]. Despite the inadequate preservation of the surface, the unambiguous presence of a uniform double spiral can be seen, indicating that the spiral is almost certainly formed by a cooperating source of strength 2. The case is very much the same for hillock 25, which is shown in figure 6.77. The surfaces have been poorly preserved. However unlike hillock 24, the steps and terraces are adequately preserved in places with local deposition elsewhere. Unfortunately, the spiral centre has been annihilated by debris however it may be clearly seen that the hillock is formed from a double spiral due either to two co-operating dislocations or one dislocation of double strength. From figure 6.7 it can be seen that the normal growth rates of hillocks 24 and 25 are identical within experimental error. This is entirely consistent with the two sources being generated by sources of the same strength. Although the normal growth rates were the same for both sources, the step spacings were found to differ slightly. The $<101>_f$ step separations for hillock 24 were measured as 0.9 μm and 4.1 μm for the narrow and wide terraces respectively, giving a mean step separation of 2.5 μm. For hillock 25 the corresponding step separations were 1.5 μm and 4.0 μm, giving a mean step separation of 2.8 μm. This indicates a slightly lower hillock slope for hillock 25 and implies a slightly different step velocity to maintain the same normal growth rate as hillock 24. Unfortunately, due to surface deposition on the crystal and the very restricted interferometry image of hillock 25, this point could not be addressed further. However it seems more likely that their respective growth rates were slightly different but insignificant experimentally.

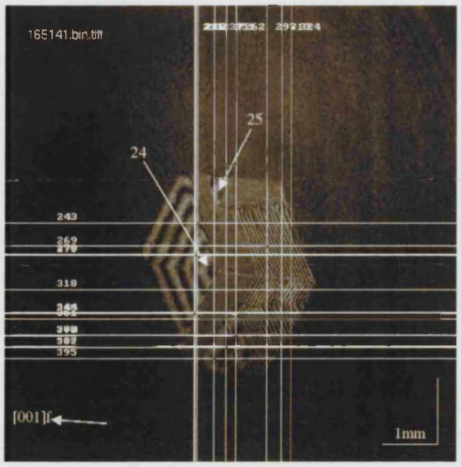

Figure 6.75: Interference image of crystal corresponding to sources 24, & 25 in Fig. 6.7. $T_{sat} = 29.26$ °C, $T_{growth} = 28.29$ °C, $\sigma = 0.0217 \pm 0.0009$.

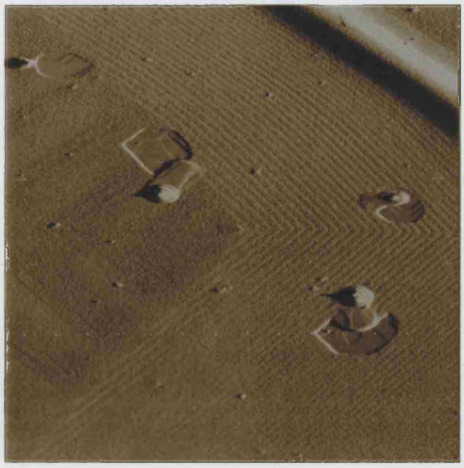

Figure 6.76: AFM image of dislocation outcrop from source 24 in Figs. 6.7 and 6.75. Inadequate removal from solution has resulted in surface degradation and etch pit formation. Nonetheless step pairs emanating from the source are visible. Scan size 40 μm.

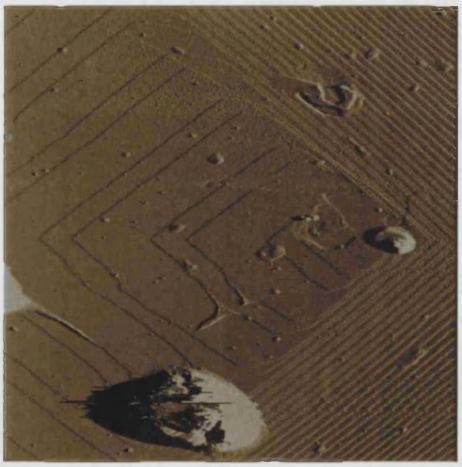

Figure 6.77: AFM image of dislocation outcrop corresponding to source 25 in Figs. 6.7 and 6.75. Inadequate solution removal has resulted in surface degradation. Step pairs are clearly visible. Scan size 36.63 μm.

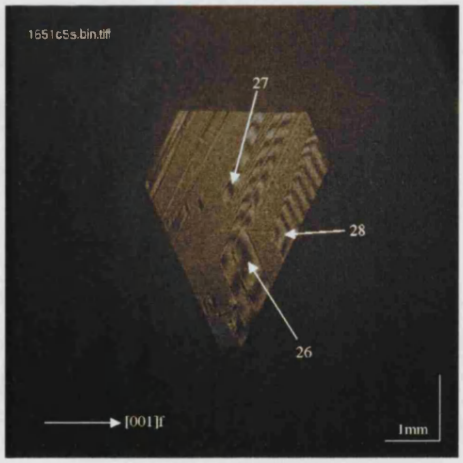

Figure 6.78: Interference image of crystal corresponding with points 26, 27, 28 in Figs. 6.7 and 6.79. $T_{sat} = 29.26$ °C, $T_{growth} = 28.00$ °C, $\sigma = 0.0283 \pm 0.0009$.

Hillocks 26, 27, 28

Figure 6.78 shows the crystal corresponding to hillocks 26, 27 and 28. A clear pattern between the slope and the normal growth rates of these hillocks can be seen by cross-reference to figures 6.7 (page 149) and 6.87 (page 205). Hillock 26 is the shallowest and has the lowest normal growth rate. Although only just visible, the slope of hillock 27 is intermediate of 26 and 28, as is the growth rate. The normal growth rate of 27 fits quite neatly with the BCF curve of the fitted data. Hillock 28 is the steepest and has the correspondingly highest normal growth rate. Unfortunately, the surfaces of this crystal were destroyed on removal, consequently no AFM images are available.

Hillocks 29, 30

Hillocks 29 and 30 are shown growing at a relative supersaturation of 0.0283 ± 0.0009 on figure 6.79. Inspection of this figure reveals that hillock 30 is steeper than 29. Reference to the normal growth rate in figure 6.7 shows that hillock 30 is growing faster than 29. Hillock 29 forms part of the data set which has been fitted with the BCF curve and its centre is shown in figure 6.80. Severe deposition has occurred on this crystal during removal from solution. However, underlying this the pattern of step pairs typical of a double co-operating spiral is just visible. Such deposition is unfortunate however this image and preceding images in which inadequate preservation was evident do serve to show that the *ex-situ* technique is quite robust, at least for obtaining specific information such as the number of co-operating spirals or the step spacing. This information may be reliably obtained from this image despite the deposition. Figure 6.81 shows the centre of hillock 30. Once again, debris has annihilated the spiral centre however the steps clearly show three co-operating spirals in this case. Note also the small growth spirals on the terraces of the main spiral. Their effect is to slightly impede the progress of steps of the main spiral which otherwise dominates them. It is now clear that the difference in slope and normal growth rate observed between hillocks 29 and 30 is a result of 29 consisting of two co-operating spirals and 30 consisting of three.

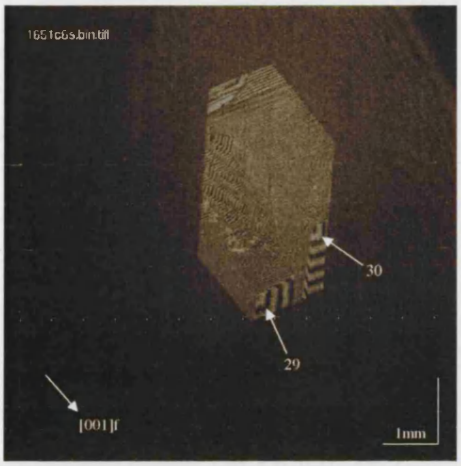

Figure 6.79: Interference image of crystal corresponding to points 29 & 30 in Fig. 6.7. $T_{sat} = 29.26$ °C, $T_{growth} = 28.00$ °C, $\sigma = 0.0283 \pm 0.0009$.

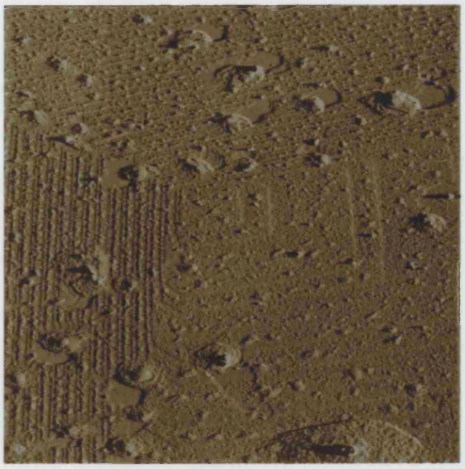

Figure 6.80: AFM image of source 29. Despite severe deposition from inadequate removal, step pairs are clearly visible. Scan size 19.9 μm

Figure 6.81: AFM image of source 30. Debris from the removal process has obliterated the spiral centre however step triplets are clearly evident indicating three cooperating dislocations. Scan size 30.1 μm

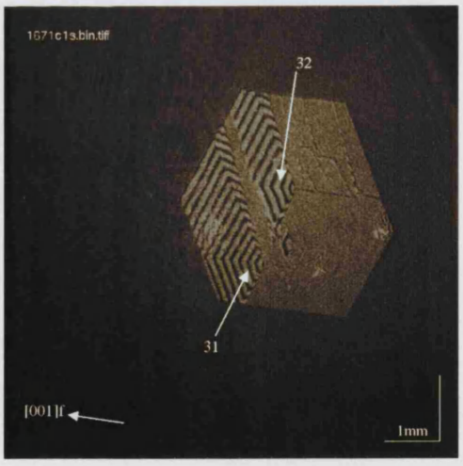

Figure 6.82: Interference image of crystal corresponding to sources 31 & 32 in Fig. 6.7. $T_{sat} = 29.26$ °C, $T_{growth} = 27.31$ °C, $\sigma = 0.0437 \pm 0.0009$.

Hillocks 31, 32

Finally, figure 6.82 shows a crystal growing at a relative supersaturation of 0.0437 ± 0.0009. The two main hillocks are labelled 31 and 32 respectively. Reference to figure 6.7 indicates that the normal growth rates of both hillocks were the same and that these were significantly higher than the data fitted with the BCF curve. The centre of hillock 32 could not be found and there is no AFM of this hillock as a consequence. The centre of hillock 31 is shown in figure 6.83 and is of considerable interest. The most immediately striking feature of the growth spiral is the extensive two-dimensional nucleation between the terraces of the spiral. The question whether these are true two-dimensional islands or an artefact must always be asked when considering such an image. Without exception, the step heights of these islands were found to be approximately unit cell height, the same as the fundamental steps of the growth spiral. Also, figure 6.83 illustrates the distinction between removal induced artefacts and genuine features of crystal growth well by virtue of the large deposit of debris in the lower part of the image. Previous images in which inadequate preservation of the surfaces is apparent also serve as a useful comparator between the artefacts and genuine features. Leaving aside the presence of the two-dimensional islands for a moment and considering the growth spiral itself, it can be seen that the hillock comprises three co-operating spirals. Tight bunches of three steps are clearly visible, especially on the $<101>_s$ steps. The source itself is quite complex and the debris nearby makes it difficult to interpret. The emergent point of one dislocation is apparent and labelled 1. This dislocation has clearly slipped from the centre of the spiral, leaving a pyramid of closed islands where the original spiral centre was. There appears to be another dislocation on the fourth terrace of this pyramid where the step seems to disappear. This appears to be an image artefact however caused by alignment of the step with the AFM scan direction, resulting in invisibility of the step at this orientation. The remaining dislocations responsible for the triple spiral are not in evidence however. Possibly they too have undergone slip away from the spiral centre, their passage masked by two-dimensional nucleation. Alternatively, they may have been covered up by debris. That there was a triple spiral during growth is beyond doubt from the pattern of steps however. Another notable feature of this spiral is the curvature. The first few turns of the spiral show almost no evidence of polygonisation and appear to be smooth elliptical curves. It is only further out that the polygonisation of the spiral becomes apparent. Figure 6.84 shows the intersection of the $<101>_f$ at some distance from the centre of the spiral. It is notable that the radius of curvature of the step at the intersection of the two sets of steps is very much greater than typically observed on KAP growth spirals. This figure

also serves to show that the two-dimensional islands on this spiral are not restricted to the spiral centre but are uniformly distributed across the terraces of the hillock. There are in this image also several instances of multi-level island formation where an island has formed on top of another.

One final observation which suggests that the presence of the two-dimensional islands is more than mere artefact is suggested by the measured normal growth rates. Hillock 30 was shown unambiguously to be formed from a triple co-operating spiral but with no evidence of two-dimensional islands. Hillock 31 is also unambiguously a triple spiral however its terraces are covered with two-dimensional islands. The growth rates of hillocks 30 and 31 are apparently inconsistent according to figure 6.7 however, a linear relationship between points 30 and 31 being unlikely. It may be argued that the activity of hillock 31 has changed during growth due to dislocation slip or some other cause and that the interferometric growth rate measurement has given the mean growth rate. A change of activity would be expected to cause a change in hillock slope and fringe frequency in the pixel intensity time series, neither of which was observed. Moreover, the growth rates of hillocks 31 and 32 were identical within experimental error. The chances of both hillocks undergoing a transition to a different activity as a consequence of a chance event such as dislocation slip must be vanishingly small. The implication then is that the measured growth rates of hillocks 31 and 32 are intrinsic to these hillocks. From the AFM image of hillock 31 it may be expected that the two-dimensional islands are the reason for the apparent anomaly in the normal growth rate, their effect being to accelerate the rate of advance of the steps of the spiral by coalescence with them as can be readily seen in figures 6.83 and 6.84. Further discussion of two-dimensional nucleation will follow in the general discussion.

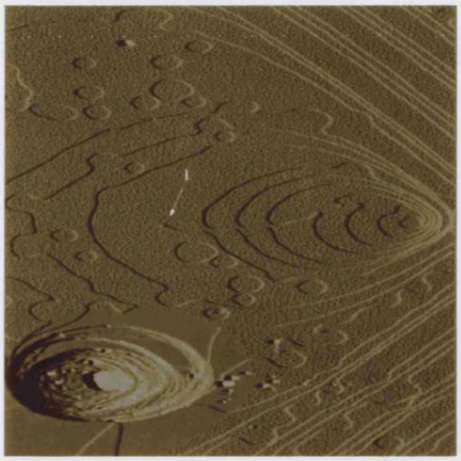

Figure 6.83: AFM image of dislocation outcrop of source 31 in Fig. 6.82. Scan size 6.19 μm

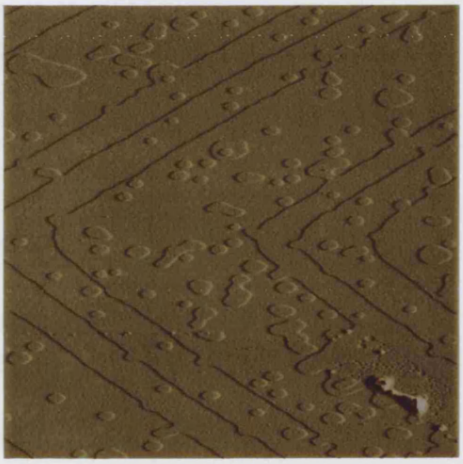

Figure 6.84: AFM image of <101>$_f$, <101>$_f$ step intersection of source 31 in Fig. 6.82. Scan size 10.57 μm.

6.5 Hillock Slopes and Step Velocities

Having considered normal growth rates and the structure of the corresponding sources for two of the saturation temperatures in the previous sections, this section briefly summarises the data and presents measured hillock slopes. Also presented are mean step separations and mean step velocities obtained from the measurements of hillock slope and normal growth rate. These measurements have been confined to the saturation temperatures for which AFM is available so that the results may be interpreted in context of the known structure of the sources responsible. To perform the same analysis for those data sets for which AFM is unavailable is prone with difficulties. As the preceding section has shown, apparently simple sources on the scale of interferometry can hide great complexity at the AFM scale. The dangers of drawing false conclusions in these cases are only too apparent.

Both AFM and interferometry are capable of the measurement of hillock slopes (and, by implication, step spacing); however their respective utility depends on the type of source under consideration. Interferometry measures the hillock slope directly, from which the mean step spacing can be obtained from knowledge of the height of a fundamental surface step. AFM on the other hand measures step spacing directly, from which the slope may be obtained. For simple sources which cover a large area of surface, either technique works well. See for example the result for hillock 23. If however the hillock is restricted to a very a small spatial region then it may be impossible to measure by interferometry due to the requirement that the hillock must be sufficiently spatially extended to allow a reliable measurement of fringe separation. This was the case for hillock 6. The hillocks' image by interferometry was too small for a reliable measurement so that AFM had to be used. On the other hand, for very complex sources, particularly those with macrosteps, it can be difficult to image a large enough area by AFM or measure macrostep heights with sufficient accuracy to obtain an accurate measurement of the slope. In these cases interferometry is more effective in providing a mean hillock slope. In the following most of the hillock slopes and measurements derived therefrom have been obtained by interferometry for the reason that the interferometry data are more complete, many of the hillocks having not been found unambiguously by AFM imaging. Where exceptions occur this has been made explicit. Also, the majority of the data are for the $<101>_f$ step vicinal facets. The $<101>_s$ steps are often either barely visible or too steep to be reliably resolved by interferometry (and in many cases by AFM). Often, discrepancies arise between the

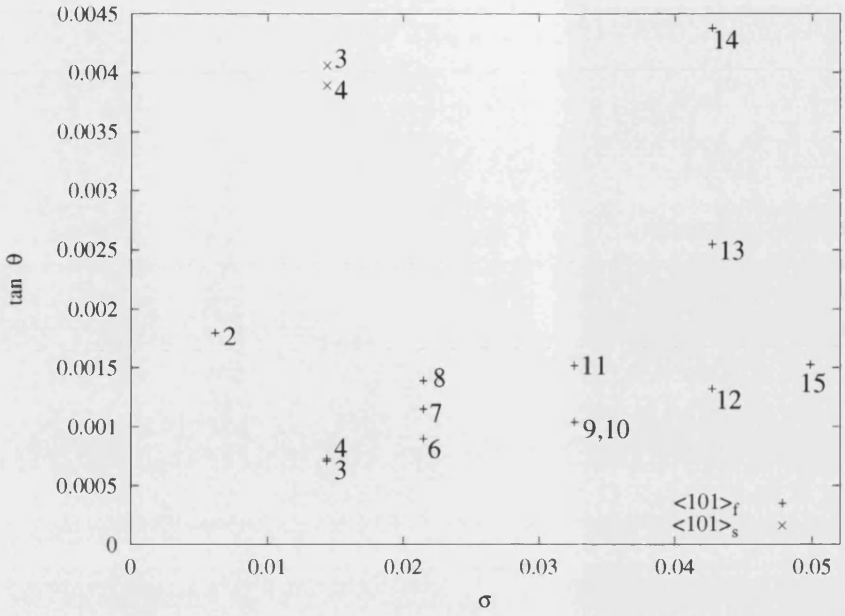

Figure 6.85: Vicinal hillock slope Vs supersaturation for sources 1 to 15, $T_{sat} = 25.56$ °C

hillock slopes measured by AFM and those measured by interferometry. Discussion of the agreement between AFM and interferometry will be taken up in the general discussion in chapter 8. However for the purposes of this section it should be stressed that the difference in scale of the two techniques is very large and the assumption that hillock slopes are always constant is not necessarily valid. With AFM for example, typically the step spacing of the first few turns of a spiral is measured over a typical distance of 10-20 μm or so, usually corresponding to a change in height of a few nanometres. For interferometry, the lateral distances involved are of the order of millimetres and the height changes are of the order of microns. It is inevitable then that some discrepancies will result, particularly where the region measured by AFM is not representative of the entire hillock. In ideal cases however, such as that of hillock 23, the techniques agree exactly.

6.5.1 Hillocks 1 to 15, $T_{sat} = 25.56$ °C

Table 6.8 summarises the data from hillocks 1 to 15 where σ is the relative supersaturation, R is the normal growth rate (as plotted in figure 6.4), p is the hillock slope, y_0 is the mean step spacing, $\bar{v}$ is the mean step velocity and ε is the source strength, as defined in section 2.6. Limited measurements of the values for the $<101>_s$ steps are included. The slope and velocity data are also shown in figures 6.85 and 6.86. The

Label	σ	Steps	R (nm s^{-1})	$p = \tan\theta$	y_0 (nm)	$\bar{v}$ (nm s^{-1})	s
1	0.0062	$<101>_f$	0.9	-	-	-	?
2	0.0062	$<101>_f$	4.1	0.00180	738	2277	*
3	0.0143	$<101>_f$	1.7	0.00071	1874	2394	?
3	0.0143	$<101>_s$	1.7	0.00406	326	419	?
4	0.0143	$<101>_f$	1.7	0.00073	1817	2329	?
4	0.0143	$<101>_s$	1.7	0.00389	341	437	?
5	0.0143	$<101>_f$	2.7	-	-	-	?
6	0.0215	$<101>_f$	2.5	0.00051†	2600†	4902	1
7	0.0215	$<101>_f$	4.0	0.00115	1154	3483	2
7	0.0215	$<101>_f$	4.0	0.00076†	1742†	5263	2
7	0.0215	$<101>_s$	4.0	0.0078†	170†	513	2
8	0.0215	$<101>_f$	5.2	0.00139	954	3741	4
9	0.0326	$<101>_f$	1.6	0.00104	1277	1503	‡
10	0.0326	$<101>_f$	2.5	0.00104	1277	2438	?
11	0.0326	$<101>_f$	3.9	0.00152	874	2572	?
12	0.0427	$<101>_f$	5.2	0.00132	1003	3934	?
13	0.0427	$<101>_f$	8.4	0.00255	520	3298	?
14	0.0427	$<101>_f$	11.3	0.00438	303	2581	*
15	0.0499	$<101>_f$	14.1	0.00152	871	9259	*

* Source formed by an inclusion

† Mean step spacing and hillock slope obtained by AFM.

‡ Very many dislocations however none apparently cooperating.

Table 6.8: Growth rate, slope and step velocity data at $T_{sat} = 25.56$ °C. R = normal growth rate, p = hillock slope, y_0 = mean step spacing, $\bar{v}$ = mean step velocity and s = number of cooperating dislocations.

trends in the data are reasonable given the complexity of some of the sources which generated them. There is a general rising trend in the hillock slope and step velocities with increasing supersaturation, as would be expected. The relationships between $p = \tan\theta$ and $\bar{v}$ for hillocks 12, 13 and 14 are interesting. The slopes increase in the order 12, 13, 14, with 14 being the steepest of all measured at this temperature. The mean step velocities $\bar{v}$ on the other hand show the opposite trend, with 14 having the lowest mean step velocity. Reference back to the AFM and interferometry of these hillocks assists in understanding these apparent trends. Source 12 was not imaged but is shallow and must therefore have a wide step spacing. Hillock 14 was shown to be due to an inclusion and is covered with macrosteps and generally has a very high step density. It would appear that these steps are sufficiently close to compete with each other and therefore impede each others progress, however there are so many steps that the normal growth rate is still considerably greater than that of the simple hillock 12, despite its apparently faster moving steps.

6.5.2 Hillocks 16 to 32, $T_{sat} = 29.26$ °C

The same information given for hillocks 1 to 15 is given for hillocks 16 to 32 in figures 6.87 6.88, and table 6.9. The trends in the slope and step velocity data for this solution are more uniform than that at $T_{sat} = 25.56$ °C. Notable however are the apparently anomalous slopes of hillocks 21 and 22. This is however entirely consistent with the examination of these sources by AFM which revealed them to be sources of high strength. Once again the point is stressed that individual data points are best understood by reference to the interferometry and AFM images, where available.

6.5.3 Summary

The discussion of results in this section has been deliberately brief. In principle, from knowledge of the normal growth rate, hillock slope and step height as a function of temperature, fundamental parameters such as the step kinetic coefficient and the rate limiting activation energy can be estimated [86]. However, this procedure involves several assumptions, including the nature of the source (i.e. its strength and activity) and in particular that the hillocks are formed from equidistant steps. The AFM study has shown that the sources can be of enormous complexity and are frequently formed

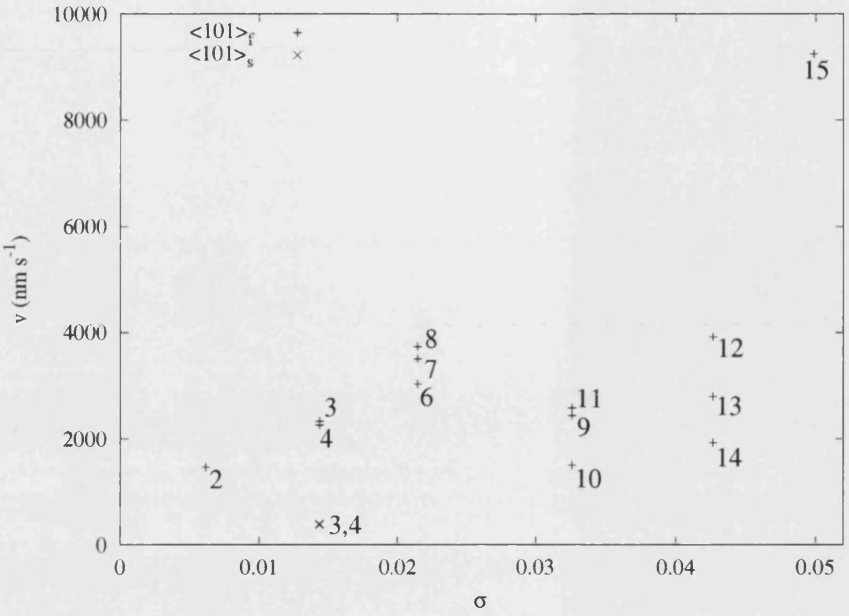

Figure 6.86: Effective step velocity Vs supersaturation for sources 1 to 15, $T_{sat} = 25.56$ °C

Label	σ	Steps	R (nm s^{-1})	$p = \tan\theta$	y_0 (nm)	$\bar{v}$ (nm s^{-1})	s
16	0.0034	<101>$_f$	0.1	0.00065	2044	150	5 (min)
17	0.0034	<101>$_f$	0.1	0.00058	2271	167	Multiple
18	0.0034	<101>$_f$	0.2	0.00061	2186	321	6
19	0.0034	<101>$_f$	0.4	0.00044	3009	908	2
20	0.0078	<101>$_s$	1.1	0.00359	369	306	?
21	0.0078	<101>$_f$	1.4	0.00099	2697	2848	4
22	0.0078	<101>$_f$	1.4	0.00123	1079	1139	5
22	0.0078	<101>$_s$	1.4	0.00377	352	504	5
23	0.0123	<101>$_f$	1.9	0.00049	2697 †	3865	2
23	0.0123	<101>$_s$	1.9	0.00377	352 *	504	2
24	0.0217	<101>$_f$	3.3	0.00097	1363	3392	2
25	0.0217	<101>$_f$	3.3	-	-	-	2
26	0.0283	<101>$_f$	3.4	0.00067	1987	5096	?
27	0.0283	<101>$_f$	4.4	-	-	-	?
28	0.0283	<101>$_f$	5.8	0.00121	1098	4802	?
29	0.0350	<101>$_f$	6.2	0.00093	1419	6638	2
30	0.0350	<101>$_f$	7.3	0.00117	1135	6253	3
31	0.0437	<101>$_f$	11.2	0.00153	868	7332	3
32	0.0437	<101>$_f$	11.2	0.00142	937	7914	?

* Result obtained by AFM

† Result obtained by interferometry and AFM

Table 6.9: Growth rate, slope and step velocity data at $T_{sat} = 29.26$ °C. R = normal growth rate, p = hillock slope, y_0 = mean step spacing, $\bar{v}$ = mean step velocity and s = number of cooperating dislocations.

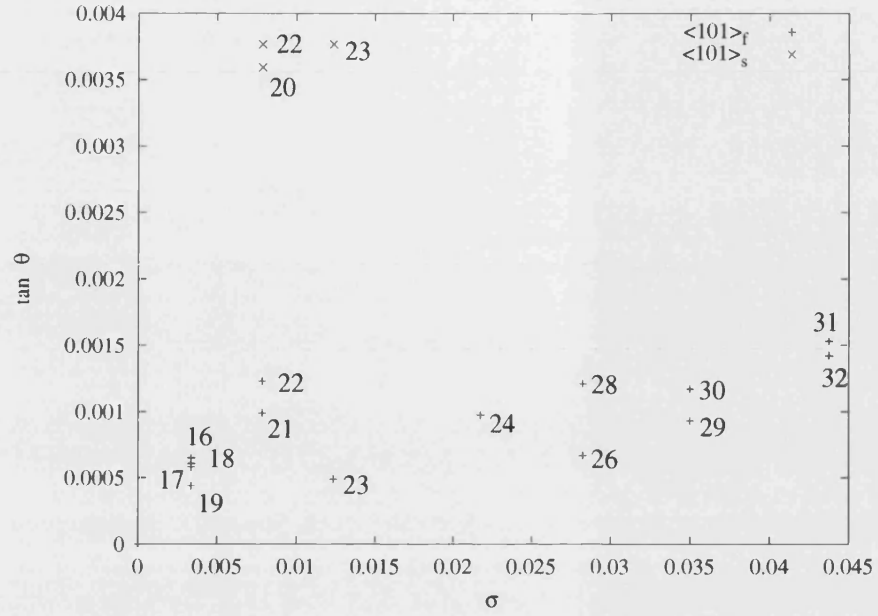

Figure 6.87: Vicinal hillock slope Vs supersaturation for sources 16 to 32, $T_{sat} = 29.26$ °C

from inclusions or twins. Also, equidistant step trains have been quite rare in this study, bunches or even macrosteps and kinematic waves being more typical. Finally, much of the growth behaviour, especially at low supersaturations, has been dominated by impurity effects which are not accounted for in most models. The AFM results have therefore served to undermine most of the assumptions made when estimating these parameters and there is consequently little purpose in a general attempt to estimate these parameters and draw conclusions therefrom. To do so would be misleading. There are however certain specific instances in the preceding data where a growth rate and hillock slope has been obtained for a simple source with a small known number of dislocations. Attempts at parameter estimation are of much greater value in these cases and this point will be taken up in the general discussion in chapter 8.

6.6 Dynamic Interferometric Observations

Crystal growth is by definition a dynamic phenomenon. In the results and discussion so far it has been more or less tacitly assumed that the growth rate measurements have taken place under steady state conditions; except where this condition has explicitly been shown not to be met, for example hillocks 13, 14 (page 168) and B (figs. 6.34 - 6.40; pages 171, 174). Although considerable measures were taken to ensure that the

crystals were growing under conditions as close to a steady state as could be achieved, inevitable fluctuations in source activity and growth rate occurred. Often the time-scale of such fluctuations was short. Frequently, growth would only remain in an apparently steady state for a matter of minutes before the activity of the sources on the surface completely changed. Since a reasonable period of steady growth was necessary to obtain reliable growth rates, such fluctuations were undesirable in this context and the scarcity of growth rate data at some saturation temperatures and supersaturations was largely a result of such fluctuations. This was especially true at low supersaturations where long periods of growth were necessary to obtain reliable growth rates. It would appear that the time-scale on which activity fluctuations occur becomes shorter with respect to the necessary duration of an experiment at low supersaturation. It is tempting to dismiss such fluctuations and concentrate on the steady state situation. However, experience shows that the steady state is very much the exception rather than the rule. Extended periods of steady state growth are rare, fluctuations being the norm. In this study, almost without exception a crystal left for more than 30-40 minutes under steady external conditions would undergo a change of activity. Phenomenological reasons for this, of which there are numerous, will be considered in chapter 8. It should be stressed that this does not invalidate the steady state measurements presented here, these are true representations of the growth of an individual hillock. The point is that an individual hillock appears to have a finite lifetime, sooner or later it will be overtaken by another source elsewhere.

For these reasons it is important that the fluctuations themselves receive some attention. Interferometry is the ideal technique with which to study growth rate fluctuations because it produces a continuous real time "movie" of the whole crystal face as it grows. The continuous time-series of pixel intensities obtained also allows instantaneous variations in source activity to be observed. In this way, the interactions of individual sources during growth is made apparent. Figure 6.89 shows a sequence of frames from an interferometry "movie" of a crystal growing at a supersaturation of $\sigma = 0.059 \pm 0.001$ from a solution saturated at 32.8 °C. The supersaturation and saturation temperature are both relatively high in the context of this study and so the activity of the sources may be expected to be high. This implies that the time-scale of fluctuations should be correspondingly short also. The images of the crystal have been cropped from their background and pseudo-coloured for clarity. The time elapsed between frames, arranged in successive rows, is 1 minute.

In the first frame several hillocks are apparent. At the top of the crystal are a group

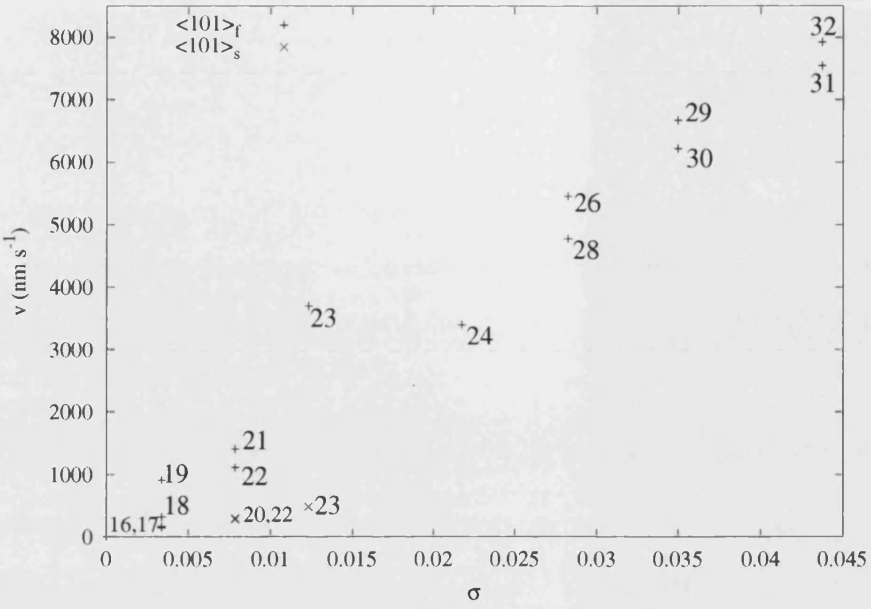

Figure 6.88: Effective step velocity Vs supersaturation for sources 16 to 32, $T_{sat} = 29.26$ °C

of hillocks, the $<101>_f$ steps of which are merging. Several other hillocks isolated from this group by the $<101>_s$ steps of the uppermost hillocks are also present. All of these hillocks have apparently the same activity, all having the same slope as far as can be ascertained from the image. On the right hand side at the top of the crystal is an isolated well developed hillock. At the very bottom corner of the crystal there is a source which has formed a hillock substantially steeper than the others. The fringe velocity over the surface was also greater than that of the other hillocks, indicating higher activity. Due to its location at the edge of the face, no $<101>_s$ step vicinal facets are apparent. It is notable that the hillock is steeper away from the source, suggesting that it has undergone an activity fluctuation.

In the second frame it is apparent that the lowermost hillocks of the top group and the well formed hillock on the right hand side of the image have been engulfed by the steps of the high activity hillock. In the third frame the engulfment by the active source continues. Just visible at the source of the active hillock now is a steepening of the hillock, disclosed by a reduction of the fringe spacing. The slope of the active hillock away from the source now appears shallower than in the preceding frames. In the fourth frame the engulfment of the low activity hillocks proceeds and the step change in slope and activity of the main hillock has propagated outwards away from the source. Immediately ahead of this "front"[4] of steps the slope appears to be shal-

[4]The analogy with wave phenomena is deliberate, the steps , and hence surface profile, generated by

lower than the rest of the hillock. In the fifth frame the low activity hillocks have completely disappeared from the crystal face. The steep region of the hillock continues to propagate, as does the shallow region ahead of it. Now however, the local slope at the hillock source has reduced, suggesting another change in activity.

In the sixth frame, the surface profile from the previous frames has radiated further out from the source. At the hillock centre now the interference fringes have developed non-uniformities. From the preceding sections, each time this was observed by interferometry, AFM revealed the surface to be covered with macrosteps, kinematic waves or shock-waves. For frames seven and eight the same situation prevails. By frame eight the shallower regions prior to the change in source activity have been completely eliminated by the steep region. Just visible in frames 7 and 8 in the middle of the crystal, long wavelength secondary modulations of the fundamental fringe spacings may be discerned. These modulations extend over several fringe spacings. Presumably they are formed by the modulated profile of the surface due to the kinematic waves or macrosteps which are almost certainly present. They are essentially Moiré fringes and if obtained with sufficient resolution could be used to study the dynamics of the macrosteps or kinematic waves responsible for them. To do this successfully however would probably require higher resolutions and magnifications than used in this study.

In frames 9, 10 and 11 the source appears to have reached a more or less steady state once more, the fringes due to the most recently emitted steps appear to be equidistant and show no evidence of long wave modulations of the type discussed above. By frame 12 the fringe separations on the whole crystal are almost completely uniform. However, very apparent here is that the source has once again abruptly undergone a large change in activity, a shallow plateau having developed at the source centre. By frame 13 the source activity has been restored to its previous state but the shallow plateau region has become a narrow band propagating away from the source. The spatio-temporal propagation of the shallow band away from the source is readily apparent in frames 14 and 15.

To summarise, the above sequence gives a clear picture of the time-scale on which activity fluctuations of a source can occur. Also notable is the wave-like behaviour of the surface profile emitted from the source. A characteristic of many kinds of wave motion is propagation without dispersion. In this context no-dispersion means that a local surface profile will change position but not shape with time. This is a premise of

the source appear to radiate outwards without dispersion, analogous to other types of wave.

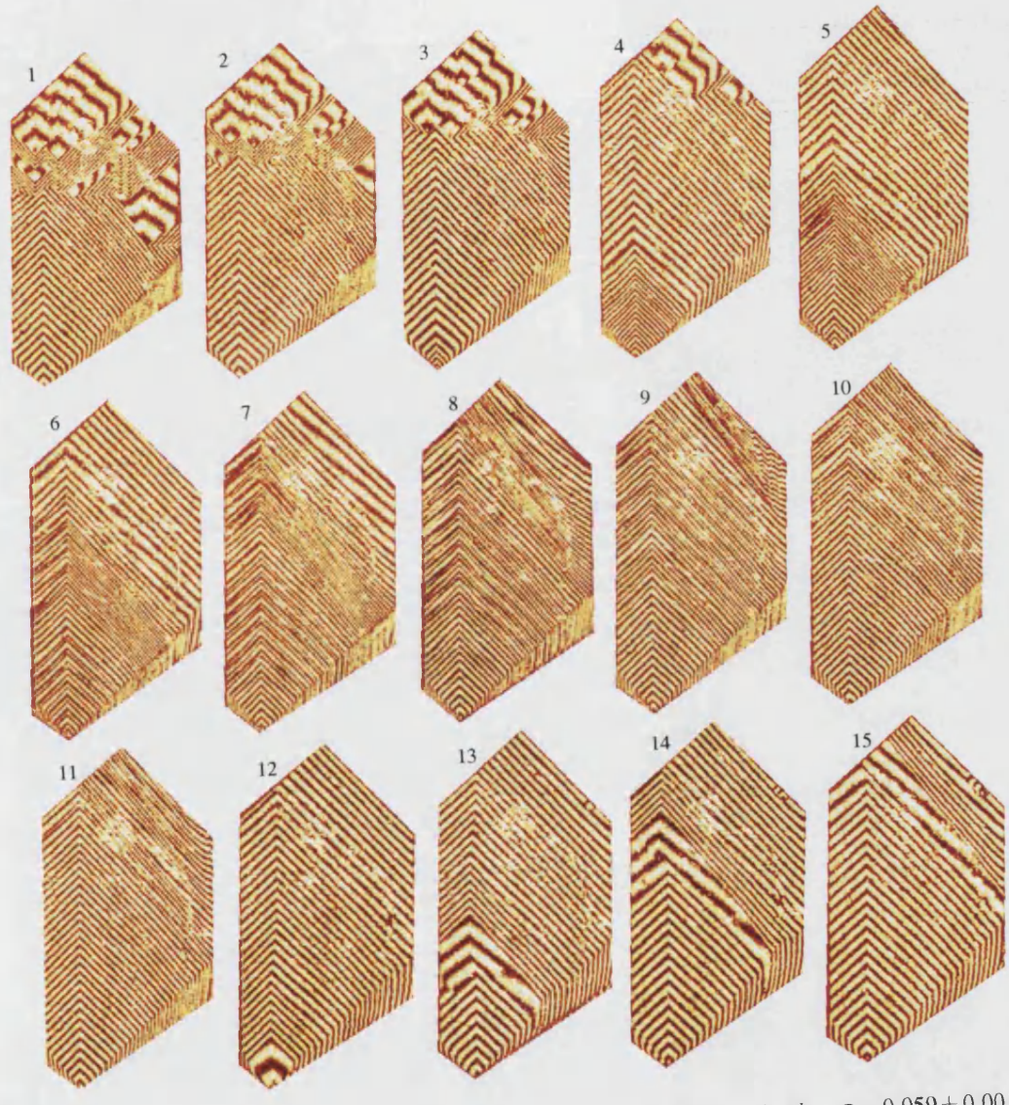

Figure 6.89: Interferometry sequence. Time between successive frames, 1 min. $\sigma = 0.059 \pm 0.001$, $T_{sat} = 32.8\ ^{\circ}C$.

the kinematic models of crystal growth and has been graphically demonstrated to hold in the case of KAP {010}, at least on the macroscopic scale.

Chapter 7

In-Situ AFM of KAP Crystal Growth from Impure Solutions

7.1 Introduction

This chapter presents the results of *in-situ* AFM studies of the growth of KAP {010} from impurity doped solutions as described in section 5.3. As in the previous chapter, some specific discussion will accompany the figures, with general discussion deferred to chapter 8 where the results from this chapter and the preceding chapter will be considered in the context of both.

7.2 *In-Situ* AFM Observations

KAP crystals were grown from $CrCl_3$ doped solutions by the techniques described in section 5.3. The saturation temperature of the solution was 24.8°C. To 50 ml of this solution, 5 μl of 3.75 molar aqueous $CrCl_3$ solution was added with a micro-pippette. From this the concentration of chromium ions in the solution was estimated at 670 parts per million parts KAP. Once suitable crystals had been selected for imaging they were imaged in single line scan contact mode while the solution temperature was adjusted by the PID controller. In this way the effect of changes in temperature on the velocity

of the steps could be used to judge when the crystal growth was sufficiently slow to prevent excessive distortion of the subsequent images.

Once a stable temperature had been achieved in the *in-situ* cell it was then possible to survey the crystal surface and seek regions of interest thereon. In particular, dislocation outcrops were sought. Due to the roughening effect of the impurity ions on the steps of the surface and the fact that the surface was continuously changing, locating dislocation outcrops on the surface is a considerably more difficult undertaking than in the *ex-situ* case in which the surface is static and the characteristic polygonal shape of the growth spirals assists in locating them. Previous work by Price *et al.* [148] has shown that the spiral anisotropy of KAP {010} is lost on the addition of $CrCl_3$. In the figures which follow, the temperature controller setpoint was 22°C. All images were captured in contact mode with a scanning frequency of 10 Hz. Each image contains 512 horizontal lines, therefore the time elapsed per frame is 51.2 seconds. All of the frames presented in the following sequence are consecutive scans of the same direction, therefore the time elapsed between successive scans of the same line in the frame is twice the time elapsed per frame, 102.4 seconds.

Figure 7.1 shows a consecutive sequence of contact mode AFM images of a KAP {010} surface growing at a temperature setpoint of 22.0°C. All of the fundamental steps were found to have heights in the range 1.2-1.4 nm. Generally speaking, the steps are quite rounded and appear to be pinned back, presumably by the deliberate impurities. The progress of steps on the surface can be clearly seen in this sequence. In the first frame the number of steps is relatively few. Notable features in this image are the pits, two of which are labelled 1 and 2, and the V shaped "trench" labelled 3. The AFM profile revealed all of these features to be deeper than the tip height. The pits have the appearance of hollow dislocation cores. The presence of a dislocation at pit 1 is disclosed by the termination of a step at it. The trench appears to have formed between two hollow cored dislocations. Hollow dislocation cores are impassable barriers for steps since there is no substrate on which to deposit new material and in any case, the strain energy of any material deposited here would be so great that it would rapidly re-dissolve. The core exists because deposition of solid is energetically unfavourable here [40]. The core therefore propagates as the crystal grows. It seems likely that steps encountering the hollow cores have been pinned back by them at the pits themselves but that they have bowed out between the cores. As described in section 2.7.3 when pinned at two points, a step will bow out until its curvature reaches a limiting curvature when it will cease to move. This hypothesis appears to readily account for the

existence of the trench.

In the remaining frames, a train of steps can be seen to approach the pits and trench from the top of the image. They are clearly pinned back by the pits, this being most apparent for pit 1 where the advance of the steps has been completely arrested. In the subsequent frames some small scale rearrangements of the steps are apparent, however, the progress of the step bunch appears to have been completely arrested by the pits and the trench. New steps bowing out around the ends of the trench may be observed. Most striking however is the build up of steps behind pit 1. In the whole sequence, no step has managed to pass pit one, the result being a dense pile up of steps behind it.

In figure 7.2, the emergent points of three screw dislocations are disclosed by the termination of surface steps at them. These are labelled 1, 2 and 3 in the first frame for clarity. A slight pit has formed at the core of the dislocations. In the sequence of images which follow, the rotation of the step around dislocation 1 can clearly be seen. It should be considered that there will be some distortion since the scan size was approaching the upper limit for reliable *in-situ* imaging at this growth rate. There is also some evidence of image drift due to the slight movement of positions of the dislocation outcrop from frame to frame. An alternative explanation for this apparent movement of the dislocation is that it as a real movement caused by slip induced by the effective tension of the step pulling on the dislocation line. This suggestion was first made by Cabrera and Levine [36] but has received little attention since that time. Although in this case the likelihood is that drift is responsible for the apparent movement, slip of dislocations in KAP was observed to occur readily in the observations of chapter 6. This observation is not unequivocal however, there is no way of establishing the true cause of the apparent movement.

A similar situation to that in figure 7.2 can be seen in figure 7.3 which once again shows consecutive frames of the same region of crystal surface. Two dislocations are present in this image. Once again hollow pits are just discernible at the centres of the dislocations. The rotation of the spiral step around the dislocations is apparent but concealed to some extent by the limited field area - only the first spiral turns are apparent. The consecutive frames of figure 7.4 graphically show the rotation of a spiral step around an emergent dislocation. More turns of the spiral are apparent in this image, allowing better visualisation of the spiral rotation.

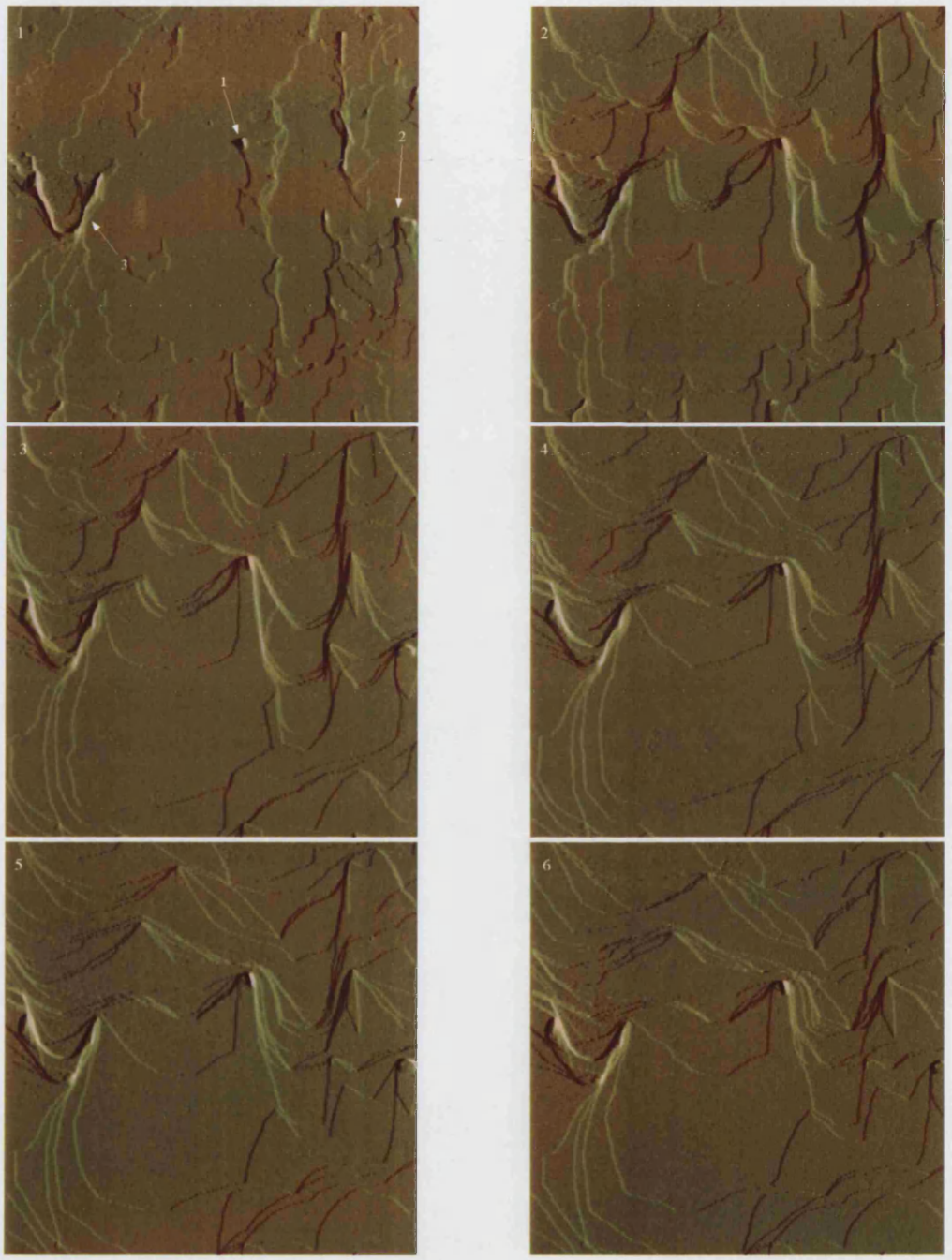

Figure 7.1: *In-situ* AFM sequence of KAP {010} growing from $CrCl_3$ doped solution. Consecutive "up" scans, scanning frequency 10 Hz, T_{sat} = 24.8 °C, temperature controller setpoint 22°C. Scan size 10 μm.

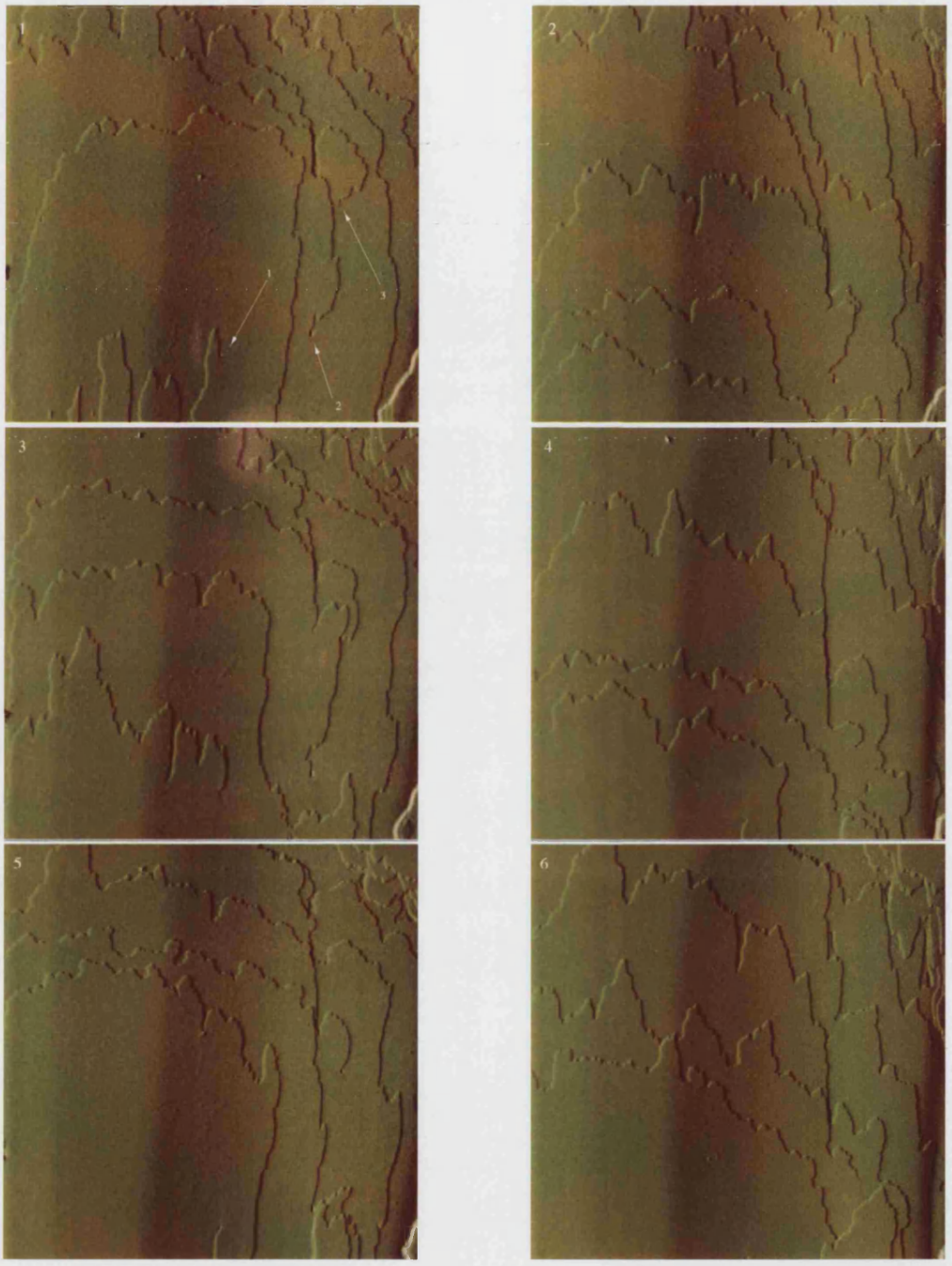

Figure 7.2: *In-situ* AFM sequence of growth spirals on KAP {010} growing from $CrCl_3$ doped solution. Consecutive scans, scanning frequency 10 Hz, Scan size 23.4 μm.

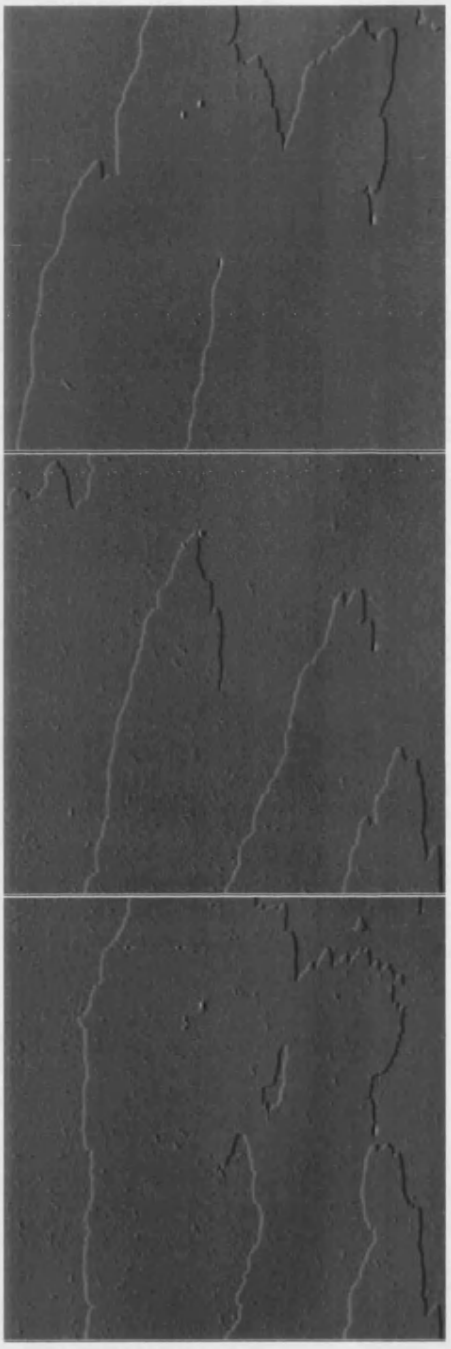

Figure 7.3: *In-situ* AFM sequence of rotating growth spirals. Consecutive images, scanning frequency 10 Hz, Scan size 14.2 μm.

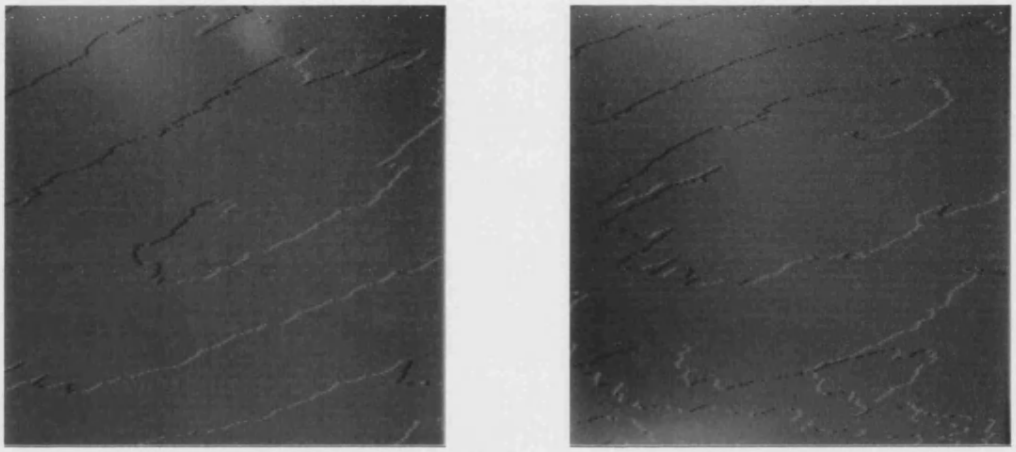

Figure 7.4: Consecutive *in-situ* AFM images of a screw dislocation growth spiral on a crystal growing from $CrCl_3$ doped solution. Scanning frequency 10Hz, Scan size 25 μm.

Chapter 8

General Discussion

8.1 Introduction

In this chapter the results of the preceding chapters will be considered more generally with particular reference to theory and other experimental results. The discussion is intended to complement the specific discussion which has accompanied individual results and figures. Crystal growth is a single dynamic phenomenon in the sense that every aspect of it is related to, and influenced by, every other. A reductionist view in which each aspect is treated in isolation is therefore difficult and of questionable value. Though the discussion is divided into sections for convenience, these are somewhat arbitrary and there will necessarily be considerable overlap.

8.2 Normal Growth Rates

It is instructive first to compare the normal growth rates of KAP {010} faces obtained in this study by interferometry with other measurements of the growth rate. As has been shown, the normal growth rates measured here are largely self consistent. A number of exceptional growth rates were measured, however several of these have been considered through the observation of their sources by AFM.

Another study of the growth rate of KAP crystals was made by Kuznetsov *et al.* [134]

as part of a study of the effect of organic impurities on the growth rates of KAP crystals. In their experiments seed crystals were grown in a stirred cell at constant supersaturation for 24-48 hours after which they were removed and the amount of new growth on top of the seed-crystal interface was measured with an optical microscope. The growth temperatures were considerably higher than in the present study, lying in the range 53-45 °C. Unfortunately these authors did not report saturation and growth temperatures of their solutions for the (R,σ) curves which they present for pure solutions, making comparison difficult. However, the growth rates were of the same order of magnitude as those obtained in the present study (10^{-8} m s^{-1}) though typically marginally greater, consistent with the higher saturation temperatures and supersaturations used. For example, they report a normal growth rate of approximately 40 nm s^{-1} at a supersaturation of 0.05, however the saturation temperature of the solution was undisclosed. These authors also measured the normal growth rates of the {110} and {111} faces, finding that the {010} was the slowest growing. The {111} being fastest growing, consistent with its lowest morphological importance of these three faces on the crystal form. To summarise, the results of the study by Kuznetsov *et al.* [134] appear consistent with those of this study, at least in terms of the order of magnitude of the normal growth rate. It should however be stressed that the methods used in their study were comparatively simple and cannot give such a clear insight to the dynamics of growth as is possible with interferometry. However, since fewer experimental difficulties are involved in their technique the fact that the normal growth rates measured appear to agree within order of magnitude with those of this study is reassuring.

Best fit BCF curves and their parameters were presented for a number of growth rates measured in this study. With some exceptions these were substantially linear and demonstrated a typical thermal activation type dependence on temperature. Although mostly consistent, some of the slopes of best fit BCF curves in this study appeared to not fit neatly with some others at different saturation temperatures. There are a number of explanations for this. Firstly, the strength and activity of the sources responsible may have been different from one curve to another. Since AFM studies were only performed on data from two of the saturation temperatures this could not be confirmed beyond doubt. Also, the amount of data obtained in some cases was inadequate for a reasonable statistical confidence in the BCF curves. This was particularly true for the fitted values of σ_1 for which the standard errors were in most cases very large. The temperature range spanned in the study was, for experimental ease, quite modest and it is possible as a result that the temperature differences from one saturation temperature to another (some of which were small) was insignificant experimentally. Finally, the

effect of impurities at very low levels can have a profound influence and may have distorted some of the curves. It is for these reasons that in depth analysis has been confined to the saturation temperatures for which AFM studies were conducted. For the same reasons, no attempts are made here to estimate activation energies for rate limiting processes by an Arrhenius method. For the accurate estimation of activation energies with this approach, data over a wide temperature range is necessary. Bennema [56] has cited this as a justification for only attempting an order of magnitude estimate of activation energies. Moreover, as the results have shown and as will be discussed subsequently, the apparent behaviour and structure of sources inferred from interferometry can be completely at odds with the actual sources when observed by atomic force microscopy. Thus, it is unsafe to assume that each measured data point has the same rate limiting process.

Recently, in the development of a self-consistent crystal growth model, Rubbo [45] has remarked with regard to the experimental measurement of (R,σ) curves, that they are often well fitted by a BCF curve but that the dispersion of growth rates is often very high and difficulties are reported. He noted that this applies even to individual growth hillocks and that for this reason growth measurements must be made on individual hillocks at the very least. These observations and this sentiment has been borne out exactly by the present study and is reflected in the present author's view. Those data sets to which BCF curves have been fitted but for which no AFM observations are available have been included principally to illustrate this point. That is, theoretical models may be easily fitted to growth rate data and interpreted within the context of the assumptions of that model with little justification of its applicability. In particular, the underlying discrete nature of spiral growth, due to the discrete occurrence of dislocations, must always be borne in mind. It is the present authors view that the wide dispersion of growth rates discussed by Rubbo [45] is in many cases a consequence of this and not merely a lack of experimental precision. For this reason, AFM resolution characterisation of sources is imperative if the pitfalls associated with this are to be avoided. It is worth noting in the context of the present study that Rubbo [45] has also remarked that many of the simplifying assumptions of BCF are often "taken for granted". In the present discussion, the validity of several of these assumptions will be questioned in light of the data of the previous chapters.

8.3 Agreement Between AFM and Interferometry

Since both interferometry and AFM give measurements of hillock slope and step separation, either directly or indirectly, a comparison between the two widely different techniques is important. This was already discussed briefly in section 6.4.2, where the excellent agreement between interferometry and AFM for the measurement of mean step separation of hillock 23 (fig. 6.73, 6.74; page 192) was discussed, and in section 6.5 where the differences of scale on which both techniques operate was discussed. Some of the slopes and step spacings measured by the two techniques were not in such good agreement. A possible reason for this is incorrect calibration of either the AFM, the interferometer or both. Both instruments were however calibrated periodically as described in the relevant experimental sections. Even the small deviations in refractive index of solutions described in appendix A are negligible. In any case, the fact that the agreement was so good in certain cases, such as hillock 23, serves as a confirmation of the calibration of both instruments. It appears then that the explanation of these discrepancies must lie elsewhere.

Provided that it is properly calibrated, the AFM gives a direct and definitive measurement of the spacing between steps on a growth hillock. The discrepancies are more likely then to lie with the interferometer, fine adjustment of which is imperative for reliable measurements. During the measurement of the normal growth rate, the intensity of an individual pixel is monitored. Slight misorientations therefore result in only a very small error in the normal growth rate. The normal growth rate measurement is therefore quite tolerant of small misalignments, making for reliable measurements. For slope measurements, the spatially extended measurement required along a line over a considerable length on the crystal surface makes it more sensitive to small misalignments. The misalignment being magnified in proportion to the length of the line measured. Unfortunately this conflicts with the requirement to obtain accurate measurements of fringe spacing by measuring a longer line. In this study, crystals were always grown from the cleaved surface of a seed crystal which was correctly aligned with the interferometer. Once the seed was aligned the interferometer was not adjusted. Only in this way could precise alignment of the interferometer with the underlying crystallographic (010) planes be ensured. However, it is possible that during growth of the crystal, in some cases the crystal may have developed a misorientation with the interferometer. Since growth was not restricted to the (010) face under observation it is possible that growth on other faces, such as the rear (010) face, may

have caused a rotation of the crystal with respect to the interferometer. Any effect was small, however the possibility that such misalignments may have occurred in this study cannot be eliminated. If a misalignment occurs then all hillocks on a crystal would be affected. Though this is unlikely to introduce significant error to the measurement of normal growth rate, the hillock slope measurement may be significantly affected.

In addition to instrumental errors there are other possible explanations for the noted discrepancies in the hillock slope. The first is due to a change in the hillock slope on removal of the crystal from the solution. As discussed in the context of hillock 23 in section 6.4.2, at least one observation showed this not to be the case and was taken as evidence that the crystal surface as imaged *ex-situ* by AFM was essentially unchanged from that which was studied *in-situ* by interferometry. Although some step motion is to be expected in the time period between the final stages of interferometry and complete removal from solution, this is expected to be insignificant. Van Der Hoek *et al.* [149] have described this as the "shut off" effect.

Another explanation was put forward in section 6.5 and concerned the very different length scale on which measurements are made by AFM and interferometry. It is quite possible that the particular region of the hillock measured by AFM is not representative of the entire spiral, or alternatively that the spiral does not have a uniform slope across it. That this may be the case is evident from several of the hillocks observed in chapter 6, hillock number 14 (fig. 6.28, page 165) for example. Since the main region of interest for AFM was typically confined to the spiral centre, step spacings were measured over the first few turns of the spiral. In contrast, interferometry typically measures slope over several hundred or even thousands of spiral turns. If the hillock slope is not constant, then disagreement between the two techniques will result.

Van Der Hoek *et al.* [149] state that the "shut off" effect is most pronounced at the spiral centre. However, for hillock 23 the slopes were in almost exact agreement between AFM and interferometry despite the AFM measurement having been made over the first few spiral turns. In this case at least then, any increase of step spacing at the spiral centre was very small and confined to the first turn only and no significant "shut off" effect was apparent. Despite the discrepancies discussed here, in general the measured hillock slopes increased with increase of supersaturation as predicted by theory. Apparent deviations from this general rule were generally explained by reference to AFM images of the source responsible.

8.4 Spiral Shape and Step Velocities

In this section the observed shapes of growth spirals and their calculated step velocities will be considered. The two are considered together as they are inextricably linked. The shape of the spiral is largely dictated by the velocities of the steps comprising it, and the anisotropy in velocities of the steps are determined by the symmetry of the crystal itself.

8.4.1 Observed Spiral Shapes

The majority of growth hillocks observed were found to be growth spirals formed by the outcrop of a modest number of dislocations, exceptions will be discussed later. The spirals formed therefrom were in general polygonal, exhibiting the now familiar shape of KAP growth spirals observed in other studies. Previous workers [122–124, 126, 128, 148] have discussed the shape of the KAP growth spiral in some detail. In particular these authors have discussed the non-equivalence of the $<101>_s$ and $<101>_f$ step directions in terms of the point group symmetry of KAP, which is non-centrosymmetric. Price *et al.* [148] introduced the fast and slow notation of Hottenhuis and Lucasius [124] to indicate the polarity of the polar axis. In the present study, typically the steps described here and previously as $<101>_f$ and $<101>_s$, were only approximately oriented along the indicated directions and there was some variability to this. Typically the nominal $<101>_s$ steps were more faithful to their designated direction than the $<101>_f$ steps. In some cases however, very large deviations from the <101> directions were observed and these have been discussed in the relevant sections. A notable result was that on the equilibriated spiral the $<101>_s$ steps were found to be exactly parallel to the <101> directions whilst the $<101>_f$ formed an angle of several degrees with these directions. So it would appear that although orientations close to <101> are favoured, that this is not a strict condition. Some of the large deviations from the nominal direction could not be easily explained, particularly in the case of hillocks 17 (figs. 6.52, 6.53; pages 180,182) and 19 (figs. 6.59, 6.60; page 184). Though impurities were clearly active on this crystal, these hillocks were qualitatively different to other hillocks simultaneously present on the same crystal. In DICM studies, Hottenhuis and Lucasius [124] considered deviations from the stated crystallographic directions to be misorientations and claimed that this was never observed on the $<101>_s$ step orientations of KAP, contrary to the AFM observation of

hillocks 17 and 19.

8.4.2 Step Velocities

The lateral velocity of steps is a composite result of a calculation of two measured quantities, the normal growth rate and the hillock slope. It is therefore prone to the errors associated with both of these measurements. As discussed in the preceding section, the normal growth rate is a rather reliable measurement, however the hillock slope is more prone to error. The latter is likely then to be the main source of error in step velocity calculations. Furthermore, the step velocity calculated is at best a mean step velocity. The AFM observations have shown that, with the exception of the very simplest sources, typically the steps on KAP {010} are non-equidistant. According to theory [49] the rate of advance of a bunch of steps may differ from that of a single isolated step. The step velocity measured indirectly then should be regarded as an effective velocity. In view of these potential sources of error in the mean step velocities, it is perhaps more reliable to consider specific cases where the source structure has been well characterised by AFM. Table 8.1 shows growth conditions, directly measured and derived parameters for hillocks 6, 7 and 23, the discussion of which is taken up in the following section.

Step Velocity of Specific Hillocks

Hillocks 6 (fig. 6.19, page 161) and 7 (figs. 6.20, 6.21; pages 161, 163) were definitively found to be growth spirals of strength 1 and 2 respectively. They are essentially adjacent hillocks growing on the same crystal at the same bulk supersaturation. Hillock 6 has equidistant steps generated by a single dislocation. Hillock 7 has non-equidistant steps due to the double spiral source. As reported in section 6.4.1, the wide terraces of hillock 7 were 1.6 times wider than the narrow terraces on both $<101>_f$ steps and $<101>_s$ steps. That both steps must move with equal velocity is obvious in this case from the uniformity of the step spacing.

The normal growth rate of hillock 6 was measured accurately as 2.5 nm s^{-1} at a relative supersaturation of $\sigma = 0.0215 \pm 0.0008$. The step spacing between fundamental $<101>_f$ steps (their height taken as the unit cell lattice parameter in the [010]

direction, 1.325_7 nm) was measured by AFM as 2600 nm, corresponding to a slope, $p = \tan\theta = h/y_0$, of 0.00051. Through the relationship $v = R/p$ the value 4902 nm s^{-1} is obtained for the step velocity. In this case the <101>$_s$ steps could not be resolved due to the very small area of this hillock on the crystal. However in every case of a steady state growth spiral encountered in this study, the same normal growth rate was measured for each vicinal facet (as must be the case if the spiral is to maintain a steady state). Assuming then that the normal growth rate was the same for the <101>$_s$ steps, and with the value of 266 nm measured by AFM for the <101>$_s$ step spacing, the corresponding velocity for these steps is 502 nm s^{-1}. The velocity of the <101>$_s$ steps is approximately one tenth that of the <101>$_f$ steps. It is notable that the ratio of the step spacing for <101>$_f$ steps to that of <101>$_s$ is numerically equal to the corresponding ratio of the step velocities. That this must be the case if the normal growth rates are to be equal and the spiral is to maintain a steady state is obvious. The number of steps passing a point on the surface in unit time must be equal. If steps of a certain orientation are advancing ten times more slowly than another orientation then they must be ten times more frequent to maintain the same normal growth rate.

For a comparison with hillock 6, hillock 7 must be approximated as an equidistant spiral of fundamental steps. Interferometry and AFM of hillock 7 yielded different results for the step spacing. In this case the geometry of the hillock made the interferometry measurement difficult and the AFM measurement is considered to be more reliable and will be used for comparison with hillock 6, the result from which was also obtained by AFM. As discussed in section 6.4.1, approximating the spiral as equidistant with the AFM measurements gives mean step spacings of 1742 nm and 170 nm for <101>$_f$ steps and <101>$_s$ steps respectively. Yielding values of 0.00076 and 0.0078 for the respective slopes. Immediately apparent here is that the ratio of step separations and slopes on the two distinct vicinal facets is essentially the same as on hillock 6, the <101>$_f$ step spacing and slope being approximately 10 times that of the <101>$_s$ steps. The normal growth rate of this hillock was reliably measured as 4.0 nm s^{-1}. The values 5263 nm s^{-1} and 513 nm s^{-1} are obtained for the respective step velocities of the <101>$_f$ and <101>$_s$ steps. Allowing for reasonable experimental and rounding errors, the agreement in step velocities for the two hillocks is good. Once again the same ratio is found for the step velocities on different vicinal facets.

This is an important result. It shows that the advance velocity of the step is a function of its local supersaturation only, and is independent of the source from which it is generated. Further, it suggests that the steps of the double spiral are not interacting

through overlapping diffusion fields for this would result in a lower velocity than that of the equidistant steps of hillock 6. The normal growth rates of the hillocks have been measured independently and yet the respective measured values are found to be exactly those which are required to ensure equal step velocities, within reasonable experimental error. Any other result would have implied an interaction between the steps of the double spiral through the overlap of diffusion fields. Locally, an element of step does not "know" which source it belongs to. Its rate of advance is determined entirely by its local supersaturation. If the supersaturation is uniform across the surface then the advance velocity of all steps of the same orientation and curvature should be the same. Strictly, according to BCF [34], for an isotropic spiral the advance velocity is actually a function of the local curvature according to formula 2.14, as a result of the Gibbs-Thomson effect. However, in the analysis of Budevski *et al.* [42] for a polygonal spiral the advance velocity for a finite straight segment greater in length than the critical length is considered to be equal to that for an infinite straight segment; that is, $v = v_\infty$.

The previous result prompts the question, is there anything special about the noted ratios of velocities and step separation for the distinct vicinal facets, or are they incidental? To investigate this the same analysis is performed for another unambiguous double spiral, that of hillock 23 (fig. 6.74, page 192), which must be regarded as the most accurately measured hillock in terms of slope. The normal growth rate measured for hillock 23 was 1.9 nm s^{-1}. The mean step velocities for $<101>_f$ and $<101>_s$ steps were given in table 6.9 as 3865 nm s^{-1} and 504 nm s^{-1} respectively, giving a ratio v_s/v_f of 0.13. The corresponding value for hillocks 6 and 7 was 0.1. Therefore for hillock 23 the relative step velocities were marginally less different than for hillocks 6 and 7. This may be a result of either temperature or supersaturation, or a combination of both. Unfortunately, such unambiguous spirals for which accurate growth rates and step spacings were available were quite scarce in this study, particularly at the same saturation temperature, making this a difficult point to answer. What is notable about this result is the similarity of the $<101>_s$ step velocity on hillock 23 with those of 6 and 7 which were growing at higher supersaturation but lower saturation temperature. The velocities are essentially the same. Though this may be a coincidence between the specific supersaturations at each temperature, alternatively it may indicate that the step velocity of this step orientation is particularly insensitive to changes of supersaturation and temperature.

Explanations for this could be that the density of kinks along the $<101>_s$ steps is low

and therefore rate limiting. If this were the case then the rate of advance of the step will be relatively insensitive to increases in supersaturation. However it would be expected to be more sensitive to increases in temperature since the step should become progressively rougher as the temperature increases, through the thermal creation of kinks. An analogous argument can be given for the energy barrier to incorporation of molecules at the kink site, which may be characterised by the activation free energy barrier at the kink (c.f. equations 2.21, 2.24). Even if the kink density were high, if the barrier to integration at the kink were rate limiting then the step velocity may be relatively insensitive to supersaturation. Increases in temperature would provide more energy for activation energy barriers to be overcome. Due to the aforementioned non-equivalence of the $<101>_f$ and $<101>_s$ steps they may be expected to differ chemically. Therefore it is quite possible that the step kinetic coefficient may be anisotropic, a greater energy barrier to incorporation existing for the $<101>_s$ steps. Similar arguments have been given by Price *et al.* [148] to account for the observed spiral shape of KAP. If either of these hypotheses were true then a decrease in the velocity difference between the $<101>_s$ and the $<101>_f$ with increasing temperature should be expected. This is what is observed in this study, albeit from limited data obtained over a restricted temperature range. The advance velocity of $<101>_s$ steps seems little affected by supersaturation, however it approaches more closely the velocity of the $<101>_f$ as the temperature increases. In part due to the restricted temperature range used in the present study, a definitive answer to the relative contributions of these two effects cannot be given. It would be instructive to examine growth spirals on crystals grown over a wide range of temperatures to investigate the effect of temperature on spiral shape and step advance velocity. The factors determining the orientation dependence of step velocity and hence, spiral shape, have been considered in detail by Frank [4] and Bennema [56].

Comparison With Other Studies

Hottenhuis and Lucasius [123] also made measurements of the velocity of steps on KAP {010} as part of a study of impurities by direct observation with differential interference contrast microscopy. Because the *in-situ* DICM technique could not unequivocally establish the step height, they could not establish if they always measured steps of the same height. They therefore presented data from a large number of experiments for which a relative error of 12% was estimated. It is probable that the steps that they observed were not fundamental. They also noted a significant change in growth

Hillock	σ	T_{sat}/°C	T_g/°C	y_{0f} nm	y_{0s} nm	$\bar{v}_f$ nm s^{-1}	$\bar{v}_s$ nm s^{-1}	β_s <101>$_f$ ms^{-1}	β_s <101>$_s$ ms^{-1}
6	0.0215±0.0008	25.56±0.02	24.51±0.02	2600	266	4902	502	3.2×10^{-3}	3.3×10^{-4}
7	0.0215±0.0008	25.56±0.02	24.51±0.02	1742	170	5263	513	3.5×10^{-3}	3.4×10^{-4}
23	0.0123±0.0009	29.26±0.02	28.71±0.02	2697	352	3865	504	4.13×10^{-3}	5.39×10^{-4}

Table 8.1: Comparison of growth parameters of steps on hillocks 6, 7 & 23 estimated from AFM and interferometry. $\bar{v}_f$, $\bar{v}_s$ and y_{0s}, y_{0f} refer to velocities and step separations of <101>$_f$ and <101>$_s$ steps respectively.

rate between stirred and un-stirred solutions indicating a transition from a diffusion to a kinetic regime. Measurements were made in the same saturation temperature and supersaturation range as the present study.

In terms of order of magnitude, their results were in good agreement with the present study, giving velocities of the order 10^{-6} m s^{-1}. For growth from a pure solution saturated at 25 °C at a relative supersaturation of 2%, a step velocity for the $<101>_f$ steps of 1.7 μm s^{-1} was measured. By way of comparison with the present study, for hillocks 6 and 7 a corresponding step velocity of approximately 5 μm s^{-1}, at similar saturation temperature and supersaturation was obtained. Given that the saturation temperature and supersaturation of hillocks 6 and 7 were both slightly greater and that the solution of the earlier workers was un-stirred, then the agreement must be considered to be good. Especially since they may not have been measuring fundamental step velocities as has been confirmed by AFM in the present study. The other results presented by Hottenhuis and Lucasius [123] are all in good agreement with this study given due allowance for the significant differences in experimental methods.

Step Kinetic Coefficients

It is worthwhile to estimate the constant of proportionality between step velocity and supersaturation in each of the above cases. The parameter in question is the step kinetic coefficient β_s. In a previous study by Chernov *et al.* [86] the step kinetic coefficients on the prismatic, {001}, face of ammonium dihydrogen phosphate (ADP) have been estimated from the results of extensive interferometry measurements. In their study Chernov *et al.* [86] identified two types of source which were referred to as weak and strong respectively. They measured the normal growth rates and slopes of these sources and obtained mean step velocities therefrom. The resultant (v,σ) curves were regression fitted to obtain an expression for each source. Then, by comparison with the equation for the step velocity as a function of supersaturation,

$$v = \Omega C_e \beta_s \sigma \tag{8.1}$$

and appropriate values for the constants, the values for β_s were obtained. In equation 8.1, Ω is the specific molecular volume of a growth unit and C_e is the equilibrium number concentration of growth units in the solution. Incidentally, as a result of this analysis these authors concluded that surface diffusion did not occur.

Chernov *et al.* [86] did however report a 20% discrepancy in the estimated value for β_s between the weak and strong sources. This was dealt with by a discussion of step bunching on the strong sources and the likelihood of the resulting overlap of diffusion fields. In the present study, the regression analysis approach of Chernov *et al.* could be readily applied to some of the more extensive data sets, particularly that at 26.71 °C, however the same difficulties are foreseen where AFM characterisation of the sources is not available. In the case of the sparse data sets, the assumptions would be unsafe. As AFM has revealed, for example in the cases of hillocks 21 and 22, sources which can be fitted well by a model relationship, in this case the BCF curve, do not necessarily have the same strength. For this reason, the approach of Chernov *et al.* [86] will not be applied here and instead the step kinetic coefficient β_s is estimated directly from the step velocities obtained before, with appropriate values for the parameters of equation 8.1.

From the dimensions of the KAP unit cell (see section 3.6), which contains four KAP residues, the value of 2.06 x 10^{-28} m^3 is obtained for Ω. From the relative molecular mass of KAP (204) and the solubility data of Solc *et al.* [117], the concentration is estimated[1] as 3.41 x 10^{26} m^{-3} and 3.69 x 10^{26} m^{-3} at 25.56 °C and 29.26 °C respectively. The relative supersaturations, σ, are as given in tables 6.8 and 6.9 respectively. The values obtained for β_s are tabulated in table 8.1.

For hillock 6, a value of 3.2 x 10^{-3} m s^{-1} for β_s for the $<101>_f$ steps is obtained. For the $<101>_s$ steps the corresponding value is 3.3 x 10^{-4} m s^{-1}. The results of hillock 7 are not significantly different from those of hillock 6. For hillock 23 the values 4.13 x 10^{-3} m s^{-1} and 5.39 x 10^{-4} m s^{-1} are obtained for the $<101>_f$ steps and $<101>_s$ steps respectively. Note that the ratios of the respective coefficients are necessarily the same as for the step spacings and velocities. The step kinetic coefficients for hillock 23 are larger than those of hillock 6, despite the lower growth rate. This result reflects the fact that the (v,σ) and consequently (R,σ) curves are functions of temperature. The value of β_s is related to the parameter C obtained from the best fit BCF curves. Sufficient data would allow an Arrhenius type estimation of activation energies from the step kinetic coefficient. The interrelationships between the various parameters discussed here have been considered at length by Bennema [56].

[1]This should be regarded as an underestimate since the density of solution was unknown. Consequently the volume is taken as that of pure water. Essentially this assumes that the partial molar volumes of the components are as for the pure components. In practice, aqueous solutions of electrolytes are typically denser than pure water. The resulting error is not expected to be large however.

It should be stressed that the above estimates of β_s are for illustrative order of magnitude purposes only. From the discussion in section 3.6.4 it was suggested that the actual growth unit of KAP may be a dimer. If this were the case then the value of Ω in the above calculations would need to be modified to account for this. This would effectively double the volume of the growth unit since the volume occupied by a dimer (of which there are two in the unit cell) is twice that of a single KAP residue, resulting in an additional factor of two in the right hand side of equation 8.1. Therefore to obtain the step kinetic coefficient for dimers, the result for an individual residue is simply divided by 2.

It is instructive to make a comparison with the results of Chernov *et al.* [86] for the prismatic face of ammonium dihydrogen phosphate (which has the highest morphological importance and is presumably slowest growing as a result). They obtained for growth of ADP {001} in the temperature interval 25-45 °C, values in the range 5.1-6.4 x 10^{-5} m s^{-1}. The comparison suggests that the step velocity on KAP {010} at the same supersaturation is 1 to 2 orders of magnitude greater, depending on the step orientation. Chernov and Malkin [87] performed similar studies on ADP {101} faces (they combined interferometry with x-ray topography also in this case, one result of which will be discussed later). They reported a value for the step kinetic coefficient of approximately 3.0 x 10^{-3} m s^{-1} which is very similar to that estimated for KAP {010} in the present study. As an aside, in the study of Chernov and Malkin [87], periodic oscillations of the normal growth rate were observed which was attributed to the passage of macrosteps. This was also a frequent observation of the present study, as was the occurrence of macrosteps.

8.4.3 The Origin of Near <001> Step Segments

All observations of polygonised growth spirals on KAP {010}, both in this study and in the published literature [122–124, 126, 128, 148], have consistently revealed the existence of finite segments of steps with orientations close to [001]. These have been described as <001> steps [128] however on fully polygonised spirals their orientation typically lies intermediate of <101> and <001>, they are rarely, if ever, parallel to <001> as may be seen in the AFM images of chapter 6. Hottenhuis and Lucasius [124] have subsequently reported that their orientation always lies between the <100> and the <102> directions. In the following discussion these steps will be referred to as

<001> steps for convenience though it is to be understood that this means steps with orientations close to <001>. To the best of the present author's knowledge no observation to date has shown a KAP {010} growth spiral from which these orientations are absent, which would result in a four sided spiral comprising only <101> step segments. Such a spiral has however been shown schematically by van Enckevort [127] and Hottenhuis *et al.* [128]. In the latter work, these authors regarded the <001> as "extra" steps. With reference to the PBC analysis due to Jetten [119], which concluded that the <101> was a PBC direction, these authors described the occurrence of these steps as "strange" because the <001> orientations were not found to be PBC directions by Jetten [119]. They argued that the occurrence of <001> could be a result of interactions with the solution which serve to stabilise the <001> step orientations. An obvious difficulty with this explanation is that it does not appear to account for the absence of steps close to [100] on the spiral form which, they argued, would be expected to appear from the PBC analysis. As discussed in section 3.6.4, in later publications by Hottenhuis *et al.* [120] and Hottenhuis and Lucasius [124] the PBC analysis of Jetten [119] was revisited and similar conclusions about the PBCs in the (010) slice were reached. In the remainder of this section the discussion of section 3.6.4 should be recollected with respect to the potential shortcomings of the available PBC analyses; that is the erroneous lattice parameter and the choice of dissociated ions as growth units.

The periodic bond chain model of Hartman and Perdok [22–25] and its extensions [39] are predictive tools for the morphology of crystals in terms of the singular faces present. It is a cornerstone of crystal growth theory that steps are non-singular and there are consequently theoretical difficulties with the application of PBCs to step shapes, with the exception of predicting the close packed orientations and hence the orientations of lowest kink density, as discussed in the preceding section. Hottenhuis and Lucasius [124] acknowledged these difficulties but used as their justification the fact that most of their observations were of macrosteps, the risers of which may be singular and amenable to a PBC analysis. Once again their PBC analysis concluded that the <100> step directions should be more stable than the <001> step directions and more likely to appear on the spiral form, in contradiction of experimental observations. They argued for an "extra stabilising factor" in the <001> step directions. Several hypotheses were submitted to account for this, once again the role of solvent and impurities were predominant amongst these[2]. They also introduced the idea of anisotropic kink integration as a result of the non-centrosymmetric nature of KAP and

[2]The influence of solvent on crystal growth has been discussed recently by Lahav and Leiserowitz [150].

re-entrant step junctions which they called "surface dendrites".

Price *et al.* [148] have discussed the occurrence of step segments with orientations close to <001> on the basis of AFM studies which have allowed far higher resolution studies of the spiral shape than was possible in the earlier DICM studies. Citing Hottenhuis and Lucasius [124], the occurrence of these orientations was described as anomalous since <001> is not a strong PBC direction according to the various PBC analyses. It was argued on this basis that segments with an orientation close to <001> will therefore have a greater kink density and would be expected to grow faster and hence be eliminated by "wedging out" from the spiral form. Thus leaving a four sided polygonised spiral. A number of arguments were presented by Price *et al.* [148] to explain the occurrence of step directions close to <001> and the overall supersaturation dependence of the curvature of the spiral. In particular the role of cationic impurities in preferentially adsorbing and hence retarding the net <001> step segments and consequently preventing their elimination was discussed. The absence of net <100> step segments at the intersections of the equivalent $<101>_f$ or $<101>_s$ segments was dealt with by the assumption that this must indicate anisotropic kink integration of impurities. Anisotropic integration of impurities on KAP {010} was found to be consistent with observations of the sectorial distribution of impurity striations by x-ray topography [138, 139]. Also, Price *et al.* [148] and the present study have shown that the <001> and $<101>_f$ step orientations are more affected by impurities than $<101>_s$ step orientations.

Reasonable though the anisotropic integration of impurities is, especially in view of the x-ray topographic and AFM evidence, the present author however offers an alternative hypothesis for the origin of the <001> steps which has the advantage that it automatically accounts for the absence of <100> steps. The hypothesis does not require any assumptions about the role of impurities, though in practice their role is likely to be significant. It is suggested that the net <001> steps appear on the spiral form for entropic reasons. Before proceeding to the argument a review of some results concerning the nature of steps is warranted. It is by now well established that the roughening temperature for a one dimensional step is absolute zero [34]. Physically, this amounts to the fact that steps cannot be facetted in the sense that a two-dimensional crystal face may be or, put differently, that a step cannot undergo a smooth to rough transition. The consequence of this, as described in chapter 2, is that whenever present on a crystal face, a step must contain kinks. Indeed this concept is a foundation of the theory of crystal growth. Therefore, even apparently straight step segments, such as the <101>

segments on the polygonal KAP {010} growth spiral, are in fact rough and will have a population of kinks along their length. For anisotropic spirals the actual kink density will vary with orientation as discussed by Frank [4] and Bennema [56], however kinks must nonetheless be present. The significance of this fact to the present situation is that the step must be regarded as continuous despite its apparent angular appearance. Even the apparent point intersections of the equivalent $<101>_f$ or $<101>_s$ step segments are necessarily curved and continuous, having essentially the same curvature as a critical nucleus [4].

The question of the occurrence of the <001> step segments is as much a question of explaining the absence of the predicted <100> steps between equivalent step orientations, given the reliable appearance of the <001> orientations. The clue to the present explanation is given by the point group symmetry of the crystal. The resulting non-equivalence of the <101> steps of opposite orientation on the polar [001] axis gives rise to the distinct step segments $<101>_f$ and $<101>_s$, as discussed by previous authors. In particular, the structure of kinks on the $<101>_s$ orientations is distinct from kinks on the $<101>_f$ orientations. If then it were possible to travel along a step from the $<101>_f$ orientation to the $<101>_s$ orientation, a change in chemical character of the kinks would be observed. In contrast, if it were possible to travel along the step from one $<101>_f$ segment to the other across the mirror plane, no change in chemical character to the kinks would be observed since the steps are equivalent. Similarly for the $<101>_s$ directions. It must be borne in mind that the transition from the different step segments is smooth and continuous, no discontinuity being permitted.

It is proposed then that at the (smooth) transition between $<101>_f$ and $<101>_s$ the configurational entropy of the step may be increased by adopting orientations which "mix" the two step configurations; that is, which contain kinks of both character. Essentially, the step edge may be regarded as a one-dimensional binary mixture of the two kink characters. It follows then that there will exist an entropy of mixing of these two kink characters on the step. The equilibrium shape of the step being that which minimises the step free energy, it is proposed that the intermediate step directions which are physically observed on KAP growth spirals are those which maximise the configurational entropy of the step and further, that this is governed by the configurational entropy of mixing of the two kink characters. The mixing of kinks of different characters on a step has been described by Chernov [37] and is also analogous to the reduction of step free energy by an increase in the configurational entropy of the step by the adsorption of impurities (see for example Chernov *et al.* [9]). The step configurational entropy has

been used in a proof of the impossibility of a point intersection between step segments by van Beijeren and Nolden [151] (see also Pimpinelli and Villain [19]). Recently, the step configurational entropy concept has been used by Giesen *et al.* [152] in a study of the equilibrium shape of two-dimensional islands on metal surfaces.

The process of mixing will be limited by the excess energy contribution from the increase in unsatisfied dangling bonds for intermediate orientations of the step as a consequence of deviating from a close packed or PBC direction. To illustrate this consider the following. If the fast and slow <101> step segments were to converge and "wedge out" the intermediate <001> segments, there would be only very limited mixing of kink characters at the corner, resulting in a low configurational entropy contribution to the step free energy. There would then be an effective line tension due to the Gibbs-Thomson effect tending to restore the step line to an orientation with higher configurational entropy. On the other hand, the excess step energy due to unsatisfied "dangling" bonds would be minimised due to the step direction being parallel to a PBC along its entire length and therefore minimising the number of dangling bonds. If now the intermediate direction step orientations were to increase in importance, the configurational entropy due to mixing of kink characters would increase. However this would serve to increase the number of unsatisfied dangling bonds. Therefore, at equilibrium, the step assumes the shape which minimises its free energy by maximising the configurational entropy of mixing whilst minimising the excess step energy due to dangling bonds.

In the case of the corners between equivalent step segments, for example from $<101>_f$ to $<101>_f$, the character of the step does not change. There is therefore no scope for minimising step free energy by mixing kinks of different character and so the steps remain parallel to the PBC direction <101> for as much of their length as possible to minimise the free energy by restricting the number of dangling bonds. Note that the energies of the unsatisfied dangling bonds on non-equivalent steps should be expected to be non-equivalent also and that this will play a role in determining the detailed shape of the growth spiral. These effects on the anisotropy of steps on KAP are apparent in the images of two-dimensional islands on hillock B (figures 6.34 - 6.40; pages 171, 174). They are "cusped" at the intersection of equivalent segments, and gently curved at the intersection of non-equivalent segments. The term cusp is used cautiously because, as was pointed out before, a step cannot be cusped in a strict sense.

Equilibrium arguments based on periodic bond chain directions serve only to minimise

the number of dangling strong bonds or the excess bond energy of the step, neglecting the role of entropy. From elementary chemical thermodynamics [153], thermodynamic equilibrium is achieved by maximising the entropy of the system and so ignoring entropic effects is clearly inadequate. In fact, entropy is fundamental to the condition that steps are necessarily always rough [34] for $T > 0$. Ignoring step entropy and minimising the number of dangling bonds of a step will result in straight steps in contradiction of theory. In the recent work by Hollander *et al.* [154] a two-dimensional Hartman-Perdok analysis has been developed to explain the step shapes observed by AFM on the surfaces of triacylglyceryl crystals. Although step roughness is acknowledged in their discussion, its implications in terms of step entropy are apparently ignored by their analysis. The entropy appears to be disposed of by the assumption that only kinetics determines the spiral shape. A quantity analogous to the attachment energy introduced by Hartman-Perdok [23–25, 27] is introduced and the postulate is made that the rate of advance of a step of the specified orientation is proportional to this quantity. It is also tacitly assumed by Hollander *et al.* [154] that steps always adopt PBC orientations. As has been shown, this is not necessarily the case. Configurational entropy of the step may also be implicated in the noted deviations from PBC directions. It would be instructive to apply the analysis of Hollander *et al.* [154] to the KAP growth spiral to find the shape predicted by this model, though it is beyond the scope of the present thesis.

Similar anisotropy in step shape to that noted for KAP has been observed with *in-situ* AFM by Pina *et al.* [155, 156] on the {001} faces of barite ($BaSO_4$). This work revealed remarkable images of the effect of a screw axis normal to a growing face and how this could affect the dynamics of growth. A main conclusion was that the results showed the inadequacies of the models which assume an isotropic structure. Almost a secondary feature of this work, two-dimensional nuclei were observed with a characteristic shape. This shape was interpreted in terms of the PBCs parallel to the {001} face. The crystal structure of barite is non-centrosymmetric and the same situation arises as for KAP where step orientations with non-equivalent kinks arises. Like KAP, the shape of the island is clearly dictated by the anisotropy. There is also clear scope for entropy of mixing of dissimilar kinks in the step edge. The islands were described as having a circle segment shape and were shown schematically as such, having very straight edges at one end of the polar axis and being essentially continuously curved at the opposite end. Though the resolution of some of the AFM images presented was limited, in several cases the actual shape appeared to deviate from the idealised shape of the schematic in that they possessed short step segments of intermediate orientation.

This is possibly indicative of an entropy of kink mixing effect similar to the hypothesis proposed for KAP. In some cases however this was absent and apparently sharp corners were present. The authors presented an argument invoking the PBCs to explain the shape. According to the present argument regarding the role of entropy of mixing of kinks, the islands would have been expected to have exhibited a more rounded transition across the opposite ends of the polar axis than was noted in many cases. However it should be stressed that the detailed shape will be dictated by both configurational entropy and the relative kink energies. Furthermore, this argument also holds strictly only at equilibrium. The study by Pina *et al.* [155, 156] was conducted *in-situ* at a high supersaturation. It is likely at such high supersaturations that the Gibbs-Thomson effect is overwhelmed by the supersaturation and the shape will be dictated by the kinetic factors alone. Also, the possibility that the island shapes were distorted as a result of the finite scanning rate must not be discounted, though the growth rate is reported to be very slow due to the sparing solubility of barite. In any case, it would appear that barite, with KAP, would be a suitable candidate for a test of the present hypothesis and also for the 2-D H-P analysis of Hollander *et al.* [154].

Of course, when growing the crystal is not at equilibrium and it may be justifiably argued that an equilibrium analysis, invoking the entropy, is invalid. In this case the shape of a step is determined entirely by its rate of advance as a function of orientation. However, although additional dynamic factors are present during growth as discussed by others, it is reasonable to expect that local equilibrium may in some cases be readily maintained, particularly at moderate supersaturations. This will be especially true if surface diffusion is easy as concluded by Price *et al.* [148]. The role of surface diffusion in polygonisation was discussed earlier [56]. Figure 6.11 (page 156) shows a growth spiral on an {010} face of a KAP crystal which has been allowed to equilibriate in solution at the solution saturation temperature for 24 hours. Despite some surface degradation and inevitable pinning of the steps due to impurities, it is clear that the spiral shape is substantially the same as for growing crystals. It may be supposed therefore that local equilibrium is easily maintained at low supersaturation and therefore that thermodynamic constraints may play as important a role as the advance velocities in governing the overall spiral shape. This will be particularly true where entropy of mixing of kinks of dissimilar character can lead to a greater entropic effect, leading to a more dominant role for thermodynamics. As for the role of impurities, the sectorial anisotropy of striations observed by Ester and Halfpenny [139] is quite conclusive in demonstrating anisotropic integration. This suggests a role for impurity adsorption at the step in dictating spiral shape, however their role need not only be kinetic, they

may also affect step entropy, thus modifying spiral shape thermodynamically rather than kinetically. This effect may account for some of the observed differences in spiral shape. The general hypothesis, neglecting the specific crystal structure of KAP or other crystals, is no doubt amenable to theoretical investigation, either analytically or by computer simulation. However either type of analysis is beyond the scope of the present thesis.

8.4.4 The KAP Growth Unit and Periodic Bond Chains

The foregoing discussion has drawn upon the PBC analyses of KAP performed by earlier workers and so it is useful now to revisit these analyses in view of the results of the present study. Earlier work on the PBC analysis of the KAP crystal structure in which the assumptions of the growth unit as separate K^+ and HP^- ions and the erroneous lattice parameter were used, was discussed in section 3.6.4. In the present study, all fundamental steps on KAP {010} including both growth steps and cleavage steps, whether imaged *in-situ* or *ex-situ*; were found to be of approximately unit cell height in agreement with earlier studies. This lends further support to the choice of a crystal slice of *b* lattice parameter thickness in the PBC analysis, consistent with Strom's [141] arguments for the PBC analysis of potassium dihydrogen phosphate, and the dimer as growth unit hypothesis. Also, the *in-situ* AFM measurements of KAP growth in $CrCl_3$ doped solutions revealed the strong interaction between KAP {010} and the chromium ion. This suggests that the surface is anion terminated and according to the argument put forward in section 3.6.4 and the results of Hottenhuis and Lucasius [128] is suggestive, though not sufficient proof, of the dimer as growth unit. It is therefore a priority that a new PBC analysis of KAP, with the correct lattice parameter and the assumption of a dimer as the growth unit, be performed. This is all the more timely in view of the enormous advances in computational power since the last published PBC analysis. For example, it would now be a much more realistic proposition to conduct a full second order PBC analysis.

Although the general method of Barber [157] has received little subsequent attention, greater knowledge of the state of aggregation of KAP in solution is also desirable in order to allow the results of this study and others to be interpreted correctly. In particular for understanding the steric and solvation energy barriers which conspire to form experimentally relevant quantities such as the step kinetic coefficient. In this regard the recently developed model of Liu *et al.* [59] which incorporates the role of steric

effects into a spiral growth model is of interest. More definitive understanding of the growth unit would also be of great utility in explaining the large number of observations concerning the role of impurities in KAP. A study of the surface termination and the energetics of relaxation and reconstruction for KAP {010} is also welcome. Surface x-ray diffraction and near molecular resolution AFM both have much to offer in this regard. By way of illustration, a recent study of the surface termination on potassium bichromate crystals utilising near molecular resolution AFM has been made by Plomp *et al.* [106].

8.5 Two-Dimensional Islands

Despite their rarity, the observations of two-dimensional islands on KAP {010} requires special attention. The observation is not unprecedented, having been reported on microcrystals by Ester and Halfpenny [139] in a combined AFM - x-ray topography study. However in that case, islands were only observed on crystals which had no active screw dislocation emergent on the {010} face under observation, being otherwise flat apart from the islands. The habit of these crystals was found to be quite distinct from that of crystals growing by a screw dislocation mechanism. In the present study however the two-dimensional islands were found co-existing with growth spirals, having formed on the terraces of the spiral. The question of whether these islands occurred as a result of removal from solution was discussed in chapter 6 where it was argued that there was evidence to suggest that islands were present during growth. In the case of hillock B (figs. 6.34 - 6.40; pages 171, 174), a distinct change in the character of growth was noted prior to removal, the affected region of which, on inspection by AFM, exhibited extensive multilayer two-dimensional nucleation and the observation of ribbon like features. Particularly notable about these islands was their obvious characteristic shape, analogous to the first or second turn of a growth spiral and with the same orientation. In the case of hillock 31 (figs. 6.83, 6.84; page 199), extensive two-dimensional islands were noted and the normal growth rate was found to be substantially greater than would have been expected from other hillocks of the same strength, the cause of which was cautiously attributed to simultaneous two-dimensional nucleation and spiral growth. The islands on hillock 31 were considerably smaller than those on hillock B and were less distinct in shape.

The very reason for Frank's [33] postulate of the role of screw dislocations in crystal

growth was to circumvent the impasse produced by the apparently enormous activation energy required for the formation of a two-dimensional nucleus, which when invoked to explain growth from the vapour phase predicted supersaturations of the order of 50% for any appreciable amount of growth. Assuming then that the islands of this study are not artefacts of removal from solution, should their presence come as a surprise?

Considering first the thin platelet crystals observed by Ester and Halfpenny [140], the approximate supersaturation here was 26% and their occurrence has been discussed in some depth by the authors with due consideration for the possibility of their occurrence during removal. In the work of Ester and Halfpenny [140] the most striking feature was that the two-dimensional nucleation was the only conceivable mechanism by which these crystals could be growing in the absence of dislocations, providing rather strong evidence in favour of their presence during growth since otherwise no growth could occur. The rather large supersaturation used does contrast with that of the present study however.

The maximum bulk supersaturation experienced by any crystal in the present study was approximately 8.5% and so the question of occurrence of the islands is rather more pointed. Moreover, extensive islands were observed on hillock B growing at a bulk supersaturation of only 4.3%. Is there any good reason to believe that two-dimensional nucleation should not occur at these supersaturations? Unfortunately much of the experimental evidence in the literature is indirect and comes primarily from growth rate measurements which are open to interpretation, as has been shown by the present study. For example, Bennema [85] attributed the positive deviation from linearity of growth rate data for potash alum at "high" supersaturation ($\sigma > 1\%$) to two-dimensional nucleation. A subsequent analysis with a "two-mechanism" model confirmed the validity of this assumption [55]. As an aside, it was found in this analysis that the two-mechanism model favoured surface diffusion as the dominant mass transport mechanism. The main reason for the absence of direct observations is that the only instrument reliably able to directly image two-dimensional islands is the AFM and this has only been available for approximately ten years, hence the sparsity of direct experimental observations. Recently Maiwa [107] *et al.* have observed two-dimensional islands between the terraces of growth spirals on barium nitrate crystals grown at a supersaturation of less than 4% though they were attributed to the higher supersaturation experienced on removal from solution. Land *et al.* [158] observed two-dimensional islands on the terraces of growth spirals on potassium dihydrogen phosphate. They observed that narrow terraces did not contain any islands however and interpreted this

in terms of the surface diffusion length. They concluded from this observation that surface diffusion was a dominant mass transport mechanism in this case. The observations of two-dimensional islands on barite by Pina *et al.* [155, 156] have been discussed already. In the latter work the supersaturation was large.

The original analyses of the early theorists discussed in chapter 2, which arrived at the conclusion that two-dimensional nucleation was insufficient to account for observed growth rates, were all concerned with growth from the vapour. For growth from solution the situation is rather more complex and is still imperfectly understood. The solution - crystal interface is still the subject of much investigation [150]. There is no general theory for the magnitudes of supersaturation required for two-dimensional nucleation to occur and this will almost certainly apply to every system individually. Furthermore, this will be a function of the purity of the system also since impurity adsorption at the step may reduce the step free energy through an increase in the configurational entropy of the step. Thus making two-dimensional nucleation possible at supersaturations for which it would be forbidden in a pure system. Frank [4] considered the supersaturation limits to two-dimensional nucleation in solution where he speculated that the critical supersaturation may be as low as a few per cent. This same conclusion has been re-stated by Sunagawa and Bennema [44]. Computer simulations have also been useful in this regard, having revealed that two-dimensional nucleation can occur in some circumstances at considerably lower supersaturations than anticipated [6] (Garside [159] has commented that simulations have given a new lease of life to nucleation models). This was in part attributed to the reduction of the step free energy by the configurational contribution to the entropy discussed previously.

The preceding argument about the role of entropy of mixing of dissimilar kinks in determining the spiral shape is of significance to the size and shape of a critical nucleus also. By the same argument the entropy of mixing of dissimilar kinks in the step edge would be expected to lower the step free energy of an island, resulting in a smaller critical nucleus for a given supersaturation than in the isotropic case where there is no scope for an additional entropy contribution by the mixing of dissimilar kinks. If the hypothesis were correct this would be a significant result since it would link the crystal symmetry to the radius of a critical nucleus and all that follows from it, such as the activation energy for growth by two-dimensional nucleation and the step spacing on vicinal hillocks *etc.* In the earlier discussion of the occurrence of the near <001> step orientations, the non-equilibrium nature of the spiral growth process was stressed as a caveat, though it was argued that local equilibrium may be maintained sufficiently

for thermodynamic factors to have a discernible effect. However in the case of establishing the shape and size of a critical nucleus, such as the analysis performed by BCF [34], no such caveat is necessary since the analysis is performed at thermodynamic equilibrium. Therefore the configurational entropy contribution from the mixing of dissimilar kinks is likely to be of even greater importance for the size and shape of a critical nucleus than for the case of the spiral shape, since the implications cannot be overwhelmed by kinetic factors. An analytical or computer simulation treatment of the subject is therefore an attractive proposition. The early work in the field of computer simulation has been the subject of numerous reviews, for example see Bennema and references cited therein [6, 60].

For the present case, the question of the critical supersaturation for two-dimensional nucleation must remain open in the absence of adequate data. That it will occur on KAP {010} under the right conditions appears to be without doubt and its occurrence should probably not come as a surprise. As for the co-existence of two-dimensional islands with growth spirals and the relative importance of each on the normal growth rate, Bennema [60] has argued that there will exist a small regime of supersaturation where both spiral growth and two-dimensional nucleation occurs, the islands forming between the steps of the spiral. Beyond which, he argues, two-dimensional nucleation will take over as the dominant mechanism. This appears consistent with the occurrence of two-dimensional islands on hillock 31 (figs. 6.83, 6.84; page 199) and its anomalous growth rate.

Following Ester and Halfpenny [140] the critical radius for a two-dimensional nucleus may be estimated from measured step separations with the expression of Cabrera and Levine [36], equation 2.20. For the mean step spacing of 1.75 μm (neglecting the bunching of steps) for the $<101>_f$ steps of hillock 31, the critical radius ρ_c is estimated at 92 nm. The smallest islands measured on hillock 31 were found to have diameters in the range 200 - 250 nm. For the step separation measured on hillock B (figs. 6.34 - 6.40; pages 171, 174) for the $<101>_f$ steps of the original growth hillock (1.37 μm) the value $\rho_c = 72$ nm is obtained. In common with Ester and Halfpenny [140], it must be stressed that the above relationship only holds strictly for an isotropic spiral and that by using the step separation of the $<101>_f$ step orientations that it is necessarily an overestimate. Furthermore, since the spacing of the spiral step may be modified by a number of causes such as the back stress effect [41] and elastic strain energy at the spiral centre [160], interpretation of the critical dimension from spiral spacing should be performed with caution. A demonstration of this caution is apparent in figure 6.38

(page 174). The widths of the terraces of the main spiral are estimated at 1.37 μm. However, the small new spirals which have formed at the bottom of the image have a step spacing for the $<101>_f$ steps of approximately 333 nm. Using this value gives for the two-dimensional nucleus a critical radius of only 17.5 nm. Based on this result, one interpretation of these images is that these dislocations have been dormant, having been dominated by the large spiral. However an abrupt change in local supersaturation has activated them, causing them to wind up into new more tightly wound spirals than the original. The increase in supersaturation has resulted in the extensive two-dimensional nucleation also. What may have caused this apparently very local increase in supersaturation is a matter for speculation though it seems likely that the hydrodynamics of solution flow may cause local changes in supersaturation. Where the solution impinges on the crystal, eddies and vortices may develop, causing local changes in the supersaturation at the surface. Moreover, as the crystal grows, the flow of solution around the crystal will be modified by its changing shape which may affect the local supersaturation. It is conceivable that where the flow of solution results in a high local supersaturation the threshold for two-dimensional nucleation may be surpassed.

Van Enckevort [127] made the remarkable observation that growth spirals on KAP occasionally ceased rotating despite exposure to supersaturated solution. As remarked in section 6.4.1 similar anomalous behaviour was observed on more than one occasion in the present study, for example in the case of hillock B, for which the apparent cessation of growth is evident in the intensity time-series shown in figure 6.46 (page 178). This behaviour was in this case found to be closely associated with the formation of two-dimensional islands, though why this should have resulted in the apparent cessation of normal growth is uncertain. One possible explanation is that the front of growth steps due to a spiral are all correlated and heading in essentially the same direction, giving rise to relatively steep vicinal facets and a relatively large normal growth rate. In growth by the polynuclear or birth and spread model [5], the growth fronts are random, approaching each other from all directions. The result is a macroscopic flattening of the face which may be interpreted by interferometry as a cessation of normal growth.

Clear evidence of a dislocation slip mechanism for the formation of two-dimensional islands was shown in section 6.4.1 (fig. 6.45, page 178). Frequently, observations of two-dimensional islands were made in regions of the crystal surface where dislocation slip was evident, disclosed by the presence of slip steps. That the slip of a dislocation from the centre of a growth spiral will form closed step loops is self evident, and its

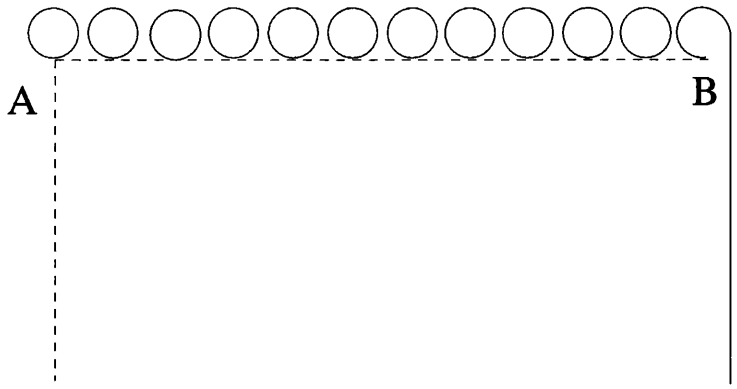

Figure 8.1: Schematic of island formation by dislocation slip

occurrence was shown unambiguously in figure 6.45. More specifically however, it was frequently observed that two-dimensional islands were distributed along straight lines associated with "cusps" in the terraces of the underlying growth spiral, which are observed to be formed by dislocation slip. A hypothesis for the occurrence of these features is as follows. If a dislocation with screw character, on the surface of a crystal exposed to supersaturated solution, undergoes slip motion; then it will create a slip step as it moves. The slip step will advance forward at a velocity dictated by its local supersaturation (including the effects of curvature). If now, the velocity of the step with respect to that of the dislocation exceeds a certain threshold, it will begin to wind up into a growth spiral, effectively winding back on itself. If the dislocation continues to move, it may cause the step to intersect itself, causing the formation of an island bounded by a closed step loop. As the dislocation continues the process will repeat itself until the dislocation comes to rest, where a new stationary growth spiral will begin to form. In its wake will be left a line of two-dimensional islands and, if this motion took place on the terraces of a growth spiral, a line of discontinuities in the steps of the terrace also. The process is illustrated schematically in figure 8.1. The initial position of the dislocation outcrop is A, as it moves towards B it leaves a row of islands in its wake. Obviously the diagram is not exact as the islands themselves will continue to grow and coalesce. The circles should be regarded as the outline of the original island formed at that position.

In any case, the existence of the islands will most likely be fleeting since they will rapidly merge with the steps of the new spiral formed at the dislocations' final resting place or the steps of the underlying spiral. Nonetheless they will form discontinuities in the steps of the spiral with which they merge, which will persist as long as the steps advance with constant velocity. If however the dislocation or dislocations continue to

move, then the continued formation of new islands will occur. The size of the islands and the number of layers will depend on the relative velocities of the dislocation slip and the advance velocity of the step. If the dislocation glide is very much slower than the step advance then several spiral turns may form before the dislocation cuts through and forms multilayer islands. This was put forward in section 6.4.1 as a hypothesis to explain the persistence of so many growth spirals, the apparent absence of dislocations from many of them and the extensive slip steps in figure 6.24 (page 163). If, on the other hand, the dislocation glide is very much faster than the advance velocity of the step then no spiral will form because the step advance will be unable to catch up with the dislocation. When the dislocation slips approximately the same distance as the radius of a first turn of a growth spiral in the time that it takes for such a turn to form, then monolayer islands should result, as is shown schematically in figure 8.1. The model should work equally well for intermittent glide of the dislocation also. A dislocation mechanism for the formation of two-dimensional islands obviously circumvents the nucleation barrier in the same way as it did in Frank's [33] original postulate. Thus providing a potential explanation for their existence at low supersaturations.

8.6 Dislocations and Other Step Sources

The defect structure of KAP crystals has been the subject of a number of studies discussed in section 3.6. The implications for the crystal growth of KAP have been extensively discussed by Ester and Halfpenny [138] and Ester *et al.* [139]. To summarise, these studies showed that several phenomena in the growth of KAP crystals could be explained from the defect structure. Of particular relevance was the observation that the {010} growth sector had a very low defect density and that in the case of small crystals this was consistent with the observation of dislocation free platelets discussed in the preceding section. Other notable observations were the nucleation of dislocation pairs from a common point at a growth sector boundary, the crossing of dislocations from the side and end growth sectors into the {010} growth sectors (disclosed by a change of dislocation line direction) and an anisotropic distribution of impurity striations in the {010} growth sector (consistent with the anisotropic integration of impurities discussed before.)

8.6.1 Source Strength and Activity

The number of dislocations observed in the sources of the present study ranged from one to sources apparently comprising possibly hundreds of dislocations, though these were usually associated with foreign particles. See for example hillocks 2 (fig. 6.15, page 159), 14 (fig. 6.28, page 165) and A (fig. 6.31, page 168). Hillock 6 (fig. 6.19, page 161) was found to be a single dislocation source and its normal growth rate was found to lie in good agreement with that of other hillocks studied at the same saturation temperature. It is unfortunate that, mainly due to inadequate preservation of the surface, most of these other sources were not imaged to confirm them as comprising single dislocations also. In general however, single sources appeared to be less common on the large crystals than in AFM studies of KAP microcrystals [139, 148], particularly in the case of the dominant sources. This is only to be expected and is a consequence of the competition between sources. The strongest sources will become dominant. In the case of microcrystals the duration of the competition has been short and the most dominant sources may not have had time to emerge. In the case of the larger crystals of the present study however, the duration of the competition has been much greater and a few complex sources have had time to become dominant. In much earlier work on the examination of etched KAP surfaces after crystal growth by Van Enckevort [127] the growth hillocks present were divided into two classes. These were shallow hillocks with small numbers of dislocations present (disclosed by their etch pits) and steep hillocks with a large number of dislocations present. These findings are borne out by the present study however now, with the resolution of AFM, it is possible to examine the dislocations and steps directly.

The interaction of dislocations on hillocks 21 (figs. 6.62 - 6.64, page 186) and 22 (figs. 6.65 - 6.72; pages 188, 190) was briefly discussed in section 6.4.2. It is worthwhile to analyse these sources in a little more detail. Fortunately, in matters of dislocation interaction, the detailed shape of the spirals may be neglected since only source topology is of interest. Source 21 comprised a source of strength 4, closely associated (but not cooperating) with another dislocation of strength 1 and of opposite sign, which emitted periodic bunches of four steps with constant separations. Figure 8.2 shows a schematic sequence of the topology of source 21. Part A shows the arms of the spiral with the terminated step interspersed between them. Part B illustrates the winding up of the isolated end of the terminated step into a growth spiral of opposite sign from the multiple spiral. Clearly the steps of the opposite spiral are about to coalesce with those of the adjacent turn of the multiple spiral. Part C shows the source after coalescence.

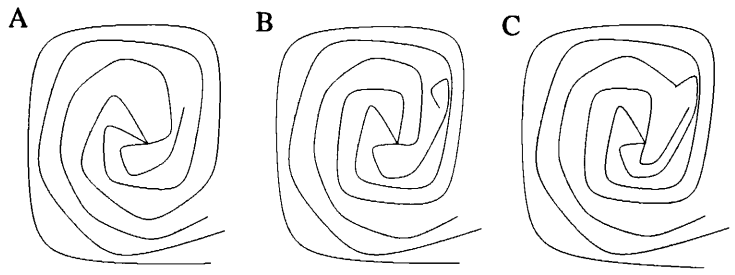

Figure 8.2: Schematic topology of source 21

The original configuration has been restored (topologically) and the cycle will repeat with the next step of the multiple spiral. Essentially each step of the multiple spiral is alternately exchanged with the isolated step. Note how this source structure can form a re-entrant intersection in the step. That this source will emit steps indefinitely with approximately the same activity of an isolated cooperating spiral of strength 4 and with a step separation periodicity repeated every four steps is readily apparent. In practice the activity of the source will be slightly less because of the impeding effect of the single dislocation [34, 37].

Figure 8.3 shows the topology of source 22. The source comprises one source of strength 5, a source of opposite sign of strength 4 and a single dislocation. These dislocations are arranged such that four of the steps are terminated at the multiple sources, with the extra step terminated at the single dislocation. Regarding the sources of like sign, in figure 6.68 these are clearly seen to be more widely separated than the most widely separated steps on the hillock and are therefore unambiguously non-cooperating. Hence the source is dominated by the source of greatest strength and activity. Part A shows an initial configuration. Note how all steps are terminated by a dislocation of opposite sign. Part B shows the configuration after the steps have all advanced a short distance, the first step of the multiple group and the isolated step are approaching each other at this point. In part C these two steps have coalesced to form a closed step loop and restored the isolated step and the step at the multiple source, which is in the process of restoring itself to the back of the group. Now the cycle can repeat, the next step of the multiple group coalescing with the isolated step. Once again it is obvious that this source can operate in this way perpetually and that for each complete cycle a group of five closed step loops with constant separation will be emitted. The source therefore has approximately the same activity as an isolated group of dislocations of strength 5.

In section 6.4.2 it was remarked that there was an apparent anomaly in the normal

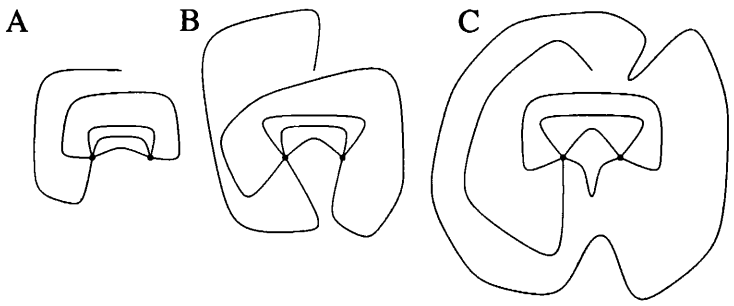

Figure 8.3: Schematic topology of source 22

growth rates of hillocks 21 and 22 with respect to the other hillocks measured at this saturation temperature and to each other, though their slopes were consistent. There are a number of potential explanations for the anomaly. Firstly, since the relative supersaturation was low in this case, it is to be expected that the absolute differences in measured growth rates between sources of different activity would also be small and may be within experimental error. Alternatively, it is possible that at this low supersaturation, the supply of growth units to the steps was insufficient for the maximum growth rate to be achieved. In effect this would mean that the high activity sources were growing in a diffusion regime since mass transport rather than integration at kinks had become the rate limiting step in the growth process. Since more active sources have higher step densities, it is possible that there may be insufficient growth units to supply all of these steps and as a consequence high activity sources may be diffusion limited when less active sources remain kinetically limited. Consequently the differences in growth rate between the sources of differing activity would be reduced. Transition to a diffusion regime was invoked in section 6.4.1 as a possible explanation of the apparently reduced growth rate of hillock 9 also. Similarly, step bunching may also be implicated in restricting the advance velocities of steps on these hillocks. The narrowest step separations observed on these hillocks may have been sufficient for diffusion fields to overlap, causing steps to compete for growth units and effectively reducing the advance velocities. In this case the activity of the spiral would be restricted by that of the slowest moving steps. On lower activity sources on which step bunching is less prevalent, the same restriction would be absent and so the difference in growth rate with source strength would again be narrowed.

The role of the elastic strain due to the dislocations themselves should not be overlooked when examining source activities. From BCF [34] the activity of a growth spiral is determined by the local curvature at its centre, which is assumed to be a function of the supersaturation of the growth medium. However, high elastic strain energy

at the centre of the spiral will effectively lower the supersaturation, resulting in reduced curvature and activity than would occur in the stress free case. Starting with Frank [40] and Cabrera and Levine [36], numerous authors have attempted to accommodate the effects of elastic strain on spiral growth [44]. More recently De Yoreo *et al.* [160, 161] have discussed the influence of hollow dislocation cores on the growth rate and the slope of vicinal hillocks on potassium dihydrogen phosphate. They found experimentally that for hollow cored dislocations, the terrace width (i.e. the hillock slope) was nearly independent of the supersaturation and the Burgers vector of the dislocation, in contradiction of the BCF model and by implication, equation 2.20. They developed a model based on the elastic strain energy with which to explain the observations and concluded that the elastic constants of the crystal played as great a role in determining the growth spiral as did the step free energy.

In the case of hillock 21, a hollow pit has clearly developed at the centre of the strongest source suggesting the possible presence of a dislocation of large Burgers vector with a hollow core. However the presence of a slip step away from this centre suggests that the source was in fact a group of narrowly separated dislocations, one of which has undergone slip during removal. In the case of hillock 22, the source of strength 4 has a well developed pit at its centre. However the source of strength 5 has no such pit and there is evidence of dislocation slip here also, again suggesting a group of dislocations. This may be an artefact of removal or it may be indicative that the group of strength 4 contained a dislocation of larger Burgers vector than the group of strength 5. This is of course entirely possible. A stronger source may nonetheless consist of separate cooperating dislocations of greater composite strength, yet lower overall strain energy due to the $|\mathbf{b}|^2$ dependence of the strain energy. Although the elastic properties of the dislocations themselves may be implicated in the activity of these hillocks, as suggested by the work of De Yoreo *et al.* [160, 161] the ambiguities in the nature of the sources makes a detailed analysis impossible. The detailed structure of the dislocation sources cannot be established from the AFM images alone. Finally, the possibility that the strength of these sources has changed due to dislocation slip during growth should not be overlooked. This is however considered unlikely since during growth the growth rate and hillock slopes were stable and the apparent slip on these sources has clearly occurred during removal.

In the present author's view, the significant anisotropy of the growth kinetics and step character should also be expected to play a role in determining the activity of such sources. Intuitively it seems that the orientation of the dislocations of the multiple

source, with respect to the polar axis and each other, should influence the activity of the source. The slowest growing orientations being expected to influence the overall growth rate. The positions of the dislocations with respect to each other and the polar axis will dictate the orientations where the step curvature is greatest and hence slowest growing. Conceivably, certain distributions of dislocations within a source, despite giving rise to the same source strength and separation, may result in lower activity. Due to the significant role played by the Gibbs-Thomson effect in dictating the rate of advance of a step; where the step free energy is anisotropic the activity of a source is likely to be anisotropic also.

8.6.2 Foreign Matter, Twins and Microcrystals

A frequent observation of this study was the occurrence of growth sources of very high activity which, on inspection by AFM, were found to be due to an inclusion or possibly a twin crystal. Notable examples are hillocks 2 (fig. 6.15, page 159), 14 (fig. 6.28, page 165), 15 (fig. 6.48, page 178) and A (fig. 6.31, page 168). The large increase in normal growth rate due to these hillocks is quite readily explained with reference to their sources. Large numbers of dislocations cooperate together to produce very dense spirals, usually resulting in the formation of macroscopic steps and kinematic waves which move across the surface apparently without dispersion. Any simple analytical expression for the growth as a function of the source structure breaks down in this case. That macrosteps and kinematic waves will likely result from such complex sources is entirely comprehensible. By interferometry, in several cases the appearance of these sources was quite orthodox and only distinguished from simple dislocation outcrop sources by their larger growth rates, though in some cases the fringe spacing was non-uniform, betraying the existence of large scale surface modulations such as macrosteps and kinematic waves. The frequent yet random occurrence of such sources posed experimental difficulties in obtaining (R,σ) curves and only lends further weight to the argument that interpretation of the step structure of the surface from the macroscopic growth rate should be performed cautiously, if at all.

The occurrence of macroscopic twins on KAP {010} is a frequent observation and it may be anticipated that a few apparent microscopic twins should be observed. In the case of foreign matter, given the precautions to eliminate "foreign matter" in the flow system, it must be assumed that the foreign matter in question is actually other very small particles of KAP which have formed in the reservoir. In terms of their mecha-

nism in promoting growth, it is likely that when a KAP particle alights on a growing face that it will be misoriented with respect to the lattice of the main crystal. As it is engulfed by the growing crystal, stresses will develop at the interface between the inclusion and the underlying crystal. These stresses will be relieved by the formation of misfit dislocations. The observation of apparent microcrystalline twins which appeared to promote no new growth, or form misfit dislocations, in figures 6.39 and 6.40 (page 174) is surprising as was discussed before. In general though, if the misfit dislocations have a screw component normal to the surface then they will form steps on which growth will occur. The resultant step change in normal growth rate will be marked. In the field of industrial mass crystallisation this may lead to the phenomenon of growth rate dispersion. Growth rate dispersion is a major factor in restricting product uniformity in industrial processes and as such is a major concern in chemical engineering [162].

The role of foreign matter, and the related subject of mechanical stress in influencing growth have long been recognised [4]. Increasing recognition of their importance in industrial processes has stimulated a growing number of recent publications [163–165]. The present study indicates that the combined AFM-interferometry approach could have valuable applications in this field, particularly if coupled with x-ray topographic studies to understand the defect formation as has been extensively studied recently by Sherwood and Ristic [166]. In the latter study, extensive studies of the role of mechanical stress on crystal growth rates was undertaken. These authors used interferometry and x-ray topography to study the effects of stress, including radiation damage, on a range of crystals. KAP itself has been used as a model compound in this regard in a recent study by Yokota *et al.* [83]. In this study the effect on growth rate by the deliberate adhesion of small crystals during growth in a flow cell was studied. The changes on growth rate were marked. The observations of the present study make the reasons for this clear. Unfortunately no simple comparison of the growth rates measured in the study of Yokota *et al.* [83] and the present study is possible since the former used an edge displacement technique with which to make comparative observations of relative changes in growth rate rather than the direct measurement of an absolute growth rate. Hottenhuis *et al.* [124] also observed growth rate enhancements due to inclusions in their *in-situ* DICM studies of KAP crystal growth. A more recent study on microcrystal adhesion to potash-alum crystals has also been made [167] in which a model to explain growth rate enhancement was proposed. Dislocation generation and propagation during crystal growth has been discussed recently by Klapper [168].

8.6.3 Dislocation Slip

A prominent feature of the latter publication by Klapper [168] is the role of post growth dislocation motion. The present study has revealed extensive dislocation motion which has been discussed in some length in other sections, particularly with respect to two-dimensional nucleation. Ester and Halfpenny [138, 139] in their x-ray topographic study found no evidence of significant post growth motion of dislocations in KAP. The distances slipped by dislocations in the present study were of the order of microns which, in heavily dislocated regions of crystal, may not be easily resolved by x-ray topography; the resolution of which is limited. Ester and Halfpenny [138, 139] reported that, due to the projection angle in the their x-ray topographs, dislocations in the {010} growth sectors appeared as short segments making them rather difficult to see by comparison with those in other growth sectors. It is therefore all the more unsurprising that any dislocation slip would not be apparent. That slip is occurring in the crystals of the present study is unequivocal, the only question is when it is occurring. It is most likely that the majority of observations of dislocation slip occurred during removal of the crystal from solution. In particular the force of the argon jet and the concomitant rapid cooling of the crystal due to the adiabatic expansion of the gas jet may have produced sufficient stresses to result in dislocation slip. It is nonetheless arguable that dislocation slip may occur during growth also. That this may occur is quite reasonable. During growth stresses develop in the crystal for a variety of reasons, for example, impurities and inclusions cause lattice strain. The crystal itself is confined since it is held in place by an adhesive, which may result in the development of stresses. These stresses may easily be sufficient to cause dislocation slip during growth and if the crystal is exposed to supersaturated solution then the slip step formed will necessarily begin to grow once its length exceeds $2\rho_c$. Possible resultant behaviour has been described at some length already in section 8.5.

These concepts have been known for as long as the concept of the screw dislocation as a source of steps itself. Frank [169] has discussed the role of dislocation motion on the growth of crystals. He argued that sudden changes in growth rates are only to be expected as a result of sudden rearrangements of dislocations which, in turn, are only to be expected since their ability to move under the influence of small stresses is one of their fundamental properties. In the same discussion, commenting on an apparent "transient extra growth", Frank [169] also remarks that "transient extra growth is to be explained / by completion of layers from the steps produced by slip." Cabrera and Levine [36] have discussed the effect of the line tension of the surface step on the emer-

gent point of a dislocation at which it terminates. They argued that the tension could be sufficient to cause slip of the dislocation near the surface. This was speculatively suggested as an explanation for the apparent drift of dislocation outcrops during *in-situ* imaging. Unfortunately this fascinating subject area has been largely incidental in the present study and it is the author's view that future experiments specifically designed to investigate dislocation slip could yield further insights.

To conclude the discussion of slip it is worthwhile to comment on the crystallography of slip in the KAP crystal. From Ester and Halfpenny's [138] x-ray topographic investigations of dislocations in KAP crystals, the dislocations in the {010} growth sector were found to have Burgers vectors [001] and <110>, the latter of which were commonly found to occur in pairs nucleating at a common point within the crystal which form a 'V' shape and lie in the (001) plane. Dislocations with Burgers vector [001] were however expected to be pure edge in character. The dislocations revealed by AFM clearly have a screw character, consistent with the mixed character of dislocations with Burgers vector <110>. As for the possible slip system, this is not easy to establish beyond doubt. Zhao [136] identified three slip systems in the KAP crystal, however none of these had a Burgers vector component normal to the {010} face and therefore cannot be that of the dislocations observed by AFM in the present study. As a general rule in simple non-directional crystal structures such as metals the most likely slip system will be the closest packed lattice direction in the closest packed lattice plane since in this way the work of dislocation slip is minimised. However in complex crystal structures such as KAP, matters are not so straightforward. The crystal structure consists of ions and therefore electrical effects may play a role in determining the favoured slip system. Also the bonding in KAP is a mixture of Coulombic and covalent giving rise to bond directionality. The resulting anisotropy will also influence the slip system. The slip trajectories traced out by the slip steps created in the surface in the present study appear to be arbitrary in direction. It is possible that this ability would be most easily achieved if a number of slip systems were available and that cross-slip from one slip system to another could occur readily.

8.6.4 Hollow Dislocation Cores

The occurrence of pits in the surface at the emergent points of dislocations has been quite prevalent in the present study, particularly at low supersaturations with multiple strength sources. They were also in evidence in the *in-situ* images at substantially

higher supersaturations (approximately 5.5%) and even for single dislocations. Bennema [60] has argued that for a given stress at the dislocation core, a large enough supersaturation will cause it to close. It is possible that during growth at modest supersaturations there is normally a hollow core however the momentarily increased supersaturation experienced during removal may act to close it. Alternatively, hollow cores observed *in-situ* may have formed as a result of impurity adsorption reducing the surface energy, making core formation more noticeable. The clearest *ex-situ* examples of surface pits at the centre of step sources were found on hillocks 16 (figs. 6.50, 6.51, page 180) and 18 (figs. 6.55, 6.56, 6.57, 6.58; pages 182, 184) where several were present in single images. There was a clear relationship between the pit diameter and the number of emergent steps, consistent with the $|\mathbf{b}|^2$ dependence of the elastic strain energy on Burgers vector magnitude. This same observation has been made on barium nitrate by Maiwa *et al.* [107], and is also apparent in the images of dislocation outcrops on calcite crystals by Teng *et al.* [104]. Unfortunately, in the present study the resolution of the cores was insufficient to quantify this or to study the core shape and depth profile. Another notable observation was that pits were absent from hillocks 17 (figs. 6.52, 6.53; pages 180, 182) and 19 (figs. 6.59, 6.60, page 184) on the same crystal. Possibly the sources of these hillocks were narrowly separated individual dislocations and consequently of lower strain energy than multiple dislocations. These spirals were also qualitatively different in shape and less pinned by impurities than those for which a pit had formed. The role of hollow cores in impeding step flow was graphically illustrated in the *in-situ* study (page 214). The advance of steps was halted by the hollow cores and lead to the formation of a "trench" which would presumably lead to the formation of an inclusion. The possible effects of the hollow cores on the hillock slope and normal growth rate was discussed in section 8.6.1.

The actual occurrence of dislocations with such apparently large Burgers vectors is remarkable in its own right. Due to the $|\mathbf{b}|^2$ dependence of the strain energy of a dislocation per unit length, it is energetically unfavourable for such dislocations to exist within the crystal. Consequently there should exist a thermodynamic driving force for the elimination of such dislocations. That they are present and apparently persist in KAP crystals therefore requires some consideration. It is notable that dislocations with such large Burgers vectors have not been characterised by x-ray topography [138]. The hollow cores themselves may stabilise dislocations of large Burgers vector. According to Frank [40], a hollow core forms to relieve the strain energy at the dislocation core. Therefore by formation of a hollow core the strain energy of a dislocation with a large Burgers vector may be reduced sufficiently to stabilise the dislocation, allowing it to

persist and participate in the spiral growth process. Indeed, hollow cored dislocations of very large Burgers vectors (up to approximately 0.5 μm) are frequently observed on silicon carbide crystals which would be expected to have very high core energies due to the magnitude of the elastic constants [170]. As a note of caution when interpreting images of surface pits at dislocation outcrops, the apparent single dislocations may in fact be several individual dislocations of like sign which are too narrowly separated to be resolved. The presence of a pit at the centre of such a dislocation source is not necessarily an indication of a true hollow core since a pit is expected to develop at the centre of a multiple dislocation source since steps are impeded from penetrating such a source [34]. In the present study, there was at least one clear example (hillock 21, fig. 6.64, page 186) of slip of a single dislocation from the centre of a multiple source, suggesting that the source was in fact a group of dislocations rather than a single dislocation. Such a group may nonetheless contain dislocations of large Burgers vector and so images of dislocation outcrops and hollow cores at the resolution used in the present study cannot be interpreted to unequivocally determine the source structure.

The detailed shape and size of the core is the result of a balance of surface energies and strain energies and therefore is likely to be complex in an anisotropic crystal such as KAP. Stability conditions for such hollow cores have been considered in depth by van der Hoek *et al.* [170]. The shape of hollow cores with respect to the polar diagram of surface energy and the anisotropy of elastic constants has been considered by Hirth and Srolovitz [171] and Srolovitz *et al.* [172]. The opening and closing of dislocation cores has also been the subject of Monte Carlo simulation studies [173]. The elastic constants of KAP and their anisotropy have been measured [174]. Given the apparent ready formation of hollow cores and their observation by AFM, KAP would make an ideal crystal with which to study the theoretical predictions, given suitably high resolution AFM. This would be especially valuable if a polar diagram of the surface free energy were available.

8.6.5 Kinematic Waves and Macrosteps

Numerous observations of kinematic waves and macrosteps were made in the present study. Typically, as was remarked earlier, their occurrence was coincident with the occurrence of a very complex source generated by an inclusion or similar. In some cases however comparatively simple sources formed macroscopic steps. The most striking example was hillock 17 (figs. 6.52, 6.53, 6.54; pages 180, 182) where true

macrosteps with a separation of approximately 16 μm were observed. It was remarked there that two of the other spirals on this crystal exhibited extensive step pinning by impurities however none was apparent on this spiral. The supersaturation was low in this case and, although a finite growth rate was measured, close to the dead zone where no finite growth rate could be measured. This is entirely consistent with the Cabrera-Vermilyea [51] model for impurity pinning resulting in a dead zone. The result of hillock 17 is apparently contrary to this however, with no pinning in evidence. Land *et al.* [175] have proposed a model, based on AFM observations of potassium dihydrogen phosphate crystal growth, in which macrosteps are implicated in the recovery of a layer-wise growing surface from a dead zone. They find that there are in fact two dead zone threshold supersaturations, one for fundamental steps and one for macrosteps; that for macrosteps being lower. In their model, macrosteps are unaffected by impurity pinning in the same way and so macroscopic spirals can grow when fundamental steps are immobile. Another observation of macrosteps on hillock 2 (fig. 6.15, page 159) was also made at low supersaturation. Notably, the $<101>_s$ steps of an adjacent hillock (hillock 1), which was not macrostepped, were extensively pinned in this case, whilst the steps of hillock 2 were not. The Cabrera-Vermilyea [51] model of impurity action is time dependent. The effectiveness of an impurity in retarding growth is dependent on the amount of time that the terrace is exposed to the fluid phase. When very tightly bunched, the amount of time for which a terrace is exposed is short and the impurity may be ineffective. This may explain some of the differences apparent between macrostepped and non-macrostepped hillocks in terms of impurity effects in the present study. In summary, it would appear from the present study that macrosteps play a significant role in the growth of KAP at low supersaturations close to the dead zone, and that the model of Land *et al.* [175] may apply in this case also.

Striking images of kinematic waves and step shock-waves were also obtained, particularly on hillock 14 (page 168). These were mostly associated with complex sources once again, however they appeared to suggest a periodic oscillation in the activity of the source. The kinematic theory of Frank [50] and Cabrera-Vermilyea [51] appears to be well supported by these observations. Bennema [56] has presented a model for periodic oscillations of source activity. One further notable observation on all of the spirals with macrosteps or kinematic waves was that <001> step orientations were present on these also. The role of impurities and the growth in general of such spirals, particularly macrostepped spirals where the step riser may be a singular face, may be quite different for that of simple spirals. Nonetheless the <001> step orientations appear, suggesting that their occurrence is quite independent of the integration of im-

purities and that they are the result of an intrinsic property of the steps themselves as was discussed in section 8.4.3.

8.7 Impurity Effects

The discussion of macrosteps and kinematic waves inevitably leads to consideration of impurities. The effects of deliberate impurities on the growth of KAP has been described at considerable length elsewhere [122, 123, 128]. In the present study their role has been largely incidental as a tool with which to allow *in-situ* imaging. Regarding the ever present unintentional impurities, their effects have been quite marked; especially at low supersaturations, with extensive step pinning being in evidence. The extent of step pinning was noticeably greater on the <001> steps and the $<101>_f$ steps in that order. The effect on the $<101>_s$ steps was by contrast quite restricted, with the exception of hillock 1 (fig. 6.14, page 159). This is in good agreement with the x-ray topographic evidence for anisotropic sectorial distribution of Ester and Halfpenny [138, 139]. That the unintentional impurities will inevitably play a role in dictating the spiral shape is obvious, though it is the author's view that they do not need to be invoked to explain the spiral shape (in particular, the occurrence of the near <001> orientations, as was discussed at length in section 8.4.3). In any case, their role is possibly thermodynamic in addition to kinetic. That impurities do have a kinetic effect also on the advance of KAP steps is vividly illustrated by the large number of observations of step pinning, the advance of steps clearly being retarded by the resulting curvature. This was most apparent on hillock 16 (figs. 6.50, 6.51, page 180), at low supersaturation, and in the *in-situ* images in the presence of $CrCl_3$. These observations were consistent with the Cabrera-Vermilyea [51] model. The critical supersaturation of some of the best fit BCF curves presented in chapter 6 were significantly greater than others. It is the authors view that, rather than being indicative of the fundamental growth mechanism, they owed more to insufficient data at low supersaturation and possibly the role of impurities in inhibiting growth in these instances. Despite precautions to maximise the purity of the growth solution and apparatus, inevitably some contamination will result and at times this will be greater than at other times.

8.8 Mass Transport

In every observation made in this study, evidence was sought for an answer to the question of the most likely route for mass transfer during growth of KAP. That is, does volume diffusion or surface diffusion dominate? This is actually a rather difficult question to answer. Many observations which at first sight appear to favour one mechanism of mass transport, on closer inspection can be equally well explained by either route. The mere fact that the growth rate was insensitive to solution flow rate above a certain threshold is of little value in this regard because, even if a surface diffusion mechanism dominates, a supply of growth units must diffuse through the stationary boundary layer of solution. The adequate stirring only serves to ensure that the growth was in the kinetic rather than the diffusive regime as a result of an adequate supply of growth units to the crystal surface. The actual route by which these units arrived at the kinks and became a part of the crystal is a separate question.

The relative merits of each mass transport mechanism has been much debated in the field of crystal growth for many years. Bennema [54, 56] has concluded from extensive studies that surface diffusion is essential to the understanding of growth rates and he has further argued that the occurrence of polygonal spirals can only result if surface diffusion occurs. For KAP specifically, Hottenhuis and Lucasius [124] concluded that surface diffusion was not significant for the growth of KAP, the direct integration of potassium ions from the solution being considered rate-limiting. The present author has questioned the assumption of the growth unit and so arguments based on the growth unit should be re-examined also. Similarly, Price *et al.* [148], in their study of spiral shape concluded that the dominant mechanism of mass transport was surface diffusion. The present author has offered an alternative hypothesis for the spiral shape on KAP {010} which does not rely on any particular mode of mass transport, consequently the conclusions of mass transport mechanism based on spiral shape must also be re-examined. A satisfactory resolution of the issue of the KAP growth unit may be helpful in addressing the dominant mode of mass transport. An electrically neutral KAP dimer may diffuse more easily over a KAP {010} terrace or it may experience even greater steric hindrance. In a similar study, Chernov *et al.* [86], reported that surface diffusion was negligible for the growth of ammonium dihydrogen phosphate.

The apparently easy occurrence of two-dimensional nuclei at modest supersaturation would appear to be favoured by surface diffusion, as has been suggested by numerous

Monte Carlo studies [39] and in the AFM studies of potassium dihydrogen phosphate by Land *et al.* [158]. Also, the apparent propensity for the formation of long ribbon like plateaus and multi-level islands appears to suggest a Schwoebel [57] barrier to step descent, which would also imply surface diffusion. The effect of a Schwoebel barrier on crystal growth has been considered by several authors [19, 35]. These suggestions are all speculative however and further work is required to settle the matter.

8.9 Dynamic Observations

To conclude the discussion, an interpretation of the dynamic sequence in figure 6.89 (page 209) will be given. The behaviour of the high activity source was described before. A clue to the intermittent activity of this source is given by the x-ray topographic study of Ester *et al.* [139]. They observed dislocations bending from the end and lateral growth sectors of the crystal into the {010} growth sectors. This was given as an explanation for the size dependence of growth by two-dimensional nucleation. Beyond a certain size, inevitably a dislocation with a screw component normal to {010} would emerge onto the {010} face from a neighbouring face. If the dislocation outcrop is less than $2\rho_c$ from the edge of the crystal then it will be dormant, its growth will be prevented by the Gibbs-Thomson effect. If, by slip or continued growth of the face from which it migrated, the dislocation exceeds this distance from the edge of the crystal then it will become active. The growth however will result in an increased growth rate of the {010} face, which will cause the {010} to shrink in morphological importance relative to the other faces. The result is that the edge will move relatively towards the dislocation. When the edge moves to within $2\rho_c$ of the dislocation it will cease growing once again. The {010} face will therefore increase in importance again, causing a relative movement of the dislocation away from the edge once more, where the cycle will repeat.

The result is an intermittent growth controlled by the distance to the crystal edge. This is effectively a self regulating feedback mechanism. The argument holds equally well for a group of dislocations, where individual dislocations within the group become active and dormant as their distance from the edge varies. In this way the number of cooperating dislocations may vary periodically with time, resulting in the kind of periodic activity variations witnessed experimentally. It was a common observation throughout this study that new high activity sources frequently appeared at the edge of

Figure 8.4: Interference image of KAP {110}

Figure 8.5: Interference image of KAP {111}

the {010} faces. It is the authors view that this is the basic mechanism occurring in the case of figure 6.89, the activity of the source on the very edge of the crystal varies periodically as would be expected from this mechanism. The interesting feature of this feedback mechanism is that it is dependent on the relative rate of advance of both faces, since both control the position of the edge. Unfortunately the removal technique for AFM studies was not perfected at the time when this observation was made and so the hypothesis could not be studied further. Moreover, successful AFM imaging at the very edge of the crystal is rather more difficult than on flat central regions. Some preliminary investigations of the {111} and {110} faces were made during this study by alignment of the crystal edge between these faces and the {010} face with the axis of the crystal stub in the growth cell. In this way the crystal could be rotated from one face to another and in some cases the occurrence of a new source on the {010} face edge coincided with the disappearance of a source from the side or end face. Both the side and end faces appeared to exhibit spiral growth as suggested by the x-ray topography. Examples of interferometry of {110} and {111} faces are shown in figures 8.4 and 8.5 respectively. A growth hillock with apparently square symmetry on the {110} face of KAP is apparent. Multiple hillocks are present on {111}, especially near the edges with {010}. The act of crystal rotation destroys the alignment of the interferometer and the work was not pursued for this reason, nonetheless this work correlates well with the other evidence for the suggested mechanism.

An almost identical argument has been promulgated and discussed in some detail for growth on ammonium dihydrogen phosphate by Chernov [37]. In this elegant experiment, x-ray topography was performed *in-situ* during growth. In this way the relative

position of the dislocation from the crystal edge could be studied. The schematic diagrams in Chernov's description apply also to the present case, given due regard for the labelling of the faces.

Part V

Concluding Remarks

Chapter 9

Conclusions and Future Work

9.1 General Conclusions

Having presented and discussed the results of the study in the preceding chapters it is now necessary to draw some conclusions from them. Before doing so it is worthwhile to reconsider the original objectives of the study. In section 1.3 several quotes were included. In particular a passage from a publication by Bennema [6] was quoted in which he called, amongst other things, for a network of experiments in which (R,σ) curves would be measured with subsequent observations of their step patterns after growth. At the time at which this and the other passages, which called for new instruments, were written; the atomic force microscope was not conceived. With the development of the atomic force microscope Bennema's appeal became feasible. This is what the present study set out to achieve, a study of the dependence of growth rate on the structure of the sources responsible for that growth rate. Bennema almost certainly conceived a more extensive network of experiments than was possible here, though it is doubtful that he, or anyone else for that matter, knew how successfully step patterns would be observed in the future at the time that he wrote the passage. This study has represented a small but hopefully significant fraction of the scheme which Bennema conceived. More recently Bennema [62] has written that after thirty years the interpretation of the measured (R,σ) curves is still not unambiguous. This study has supported that view to some extent, though the combination of AFM with measurement of (R,σ) curves goes a long way towards removing this ambiguity. In some cases the interpretation can be completely without ambiguity.

As is usual, this study has served to raise as many new questions as those which it has answered. Nonetheless, several conclusions can be drawn from the work contained herein and may be stated succinctly.

1. The dominant mechanism of crystal growth on KAP {010} is spiral growth induced by dislocations. However two-dimensional nucleation appears to occur with relative ease and may coexist with spiral growth.

2. Through slip, dislocations with a screw component can result in the formation of two-dimensional islands. A dislocation can therefore circumvent the activation energy required for the formation of a critical nucleus in more ways than one.

3. The shape of growth spirals on KAP {010}, in particular the occurrence and absence of <001> and <100> orientations respectively, may be explained through a combination of the non-centrosymmetric structure of KAP and the configurational entropy of the step due to mixing of kinks of different character. This concept is also implicated in determining the size of a critical nucleus.

4. The role of elastic strain energy, dislocation movement, foreign particles and growth rate fluctuations are of great significance and, in the case of large KAP crystals, may dominate growth. On such crystals simple, low activity, sources are the exception rather than the rule.

5. Hollow dislocation cores form at low supersaturations and are implicated in the formation of inclusions by inhibiting step advance.

6. The sectorial observations of dislocations by x-ray topography are consistent with a self regulating growth mechanism which is dependent on the relative rates of advance of more than one face which may be implicated in governing the overall habits of KAP crystals.

7. The postulates of the kinematic theory due to Frank and Cabrera-Vermilyea are consistent with the observations of the growth behaviour of KAP, which exhibits kinematic waves and shock waves.

9.2 Recommendations For Future Work

In making recommendations for future work, the stated objectives are revisited once again. Only a small part of the scheme proposed by Bennema has been addressed by the present study. It remains for others to complete. In addition a significant number of new questions have been raised and should be addressed. Also some new opportunities have arisen from the outcome of this study. Many of the suggestions for future work have been implied in preceding chapters where they have arisen, however they are now collected into one place.

Much of this study was less quantitative than was desired or originally intended. This owes much to the wide range of activity and complexity of many of the sources studied which prevented any meaningful quantitative comparison. It is in some ways unfortunate that more sources of the same activity were not found, though the chances of finding sources of equal activity on every crystal studied appears to be extremely small on the larger crystals since their growth is dominated by the high activity sources which are effectively unique. Also, the range of phenomena witnessed made focusing on any one small part in great detail difficult. The qualitative descriptions alone have been necessarily long in many cases. The result is a rather broad qualitative survey. A gesture to a quantitative study was made with the fitting of best fit BCF curves to the (R,σ) data produced at different temperatures. However as has been shown, simply lying on the same (R,σ) curve does not mean that two sources are comparable. It is the author's view that the data were too sparse to justify an in depth analysis and in any case the AFM images circumvented the need for interpretation of kinetic data to explain the source structure. A similar study with much greater regard for solution purity would be desirable, as would a study where many more data points are collected. A wider range of temperatures should also be studied to allow thermally activated events such as kink creation to be examined in greater detail. This would no doubt require the extension of the data for the solubility of KAP in aqueous solution to lower and higher temperatures. However the emphasis of the study would have to be on confronting the models themselves with the AFM images of the sources, rather than inferring the structure of the sources from the data, as has been done in the past before the advent of AFM. Such a study could be useful in addressing questions of mass transport mechanism. Alternative mass transport models [5] could be fitted to the data. However extreme precautions over purity and precisely defined hydrodynamics would be necessary to have a chance of providing unequivocal answers. The recent remarks of Rubbo [45]

are reiterated in this respect as a caution. Of particular interest also is the quantitative analysis of complex dislocation sources with interesting topology such as hillocks 21 and 22 of the present study. These kind of data where the growth rate, hillock slope, source strength and perimeter are all known; are clearly amenable to more detailed quantitative study to test the predictions of theory than has been possible here.

The emphasis on complementary techniques was here restricted to interferometry and AFM. However, the enormous value of x-ray topography in interpreting growth behaviour was made apparent by reference to other studies. It should be a simple matter to extend the techniques of the present study to include x-ray topographic investigation of the defect structure of the resulting crystals, with the caveat that the crystals will need to be handled with extreme care to prevent damage. In particular the occurrence of dislocation slip may be studied in greater depth by this approach. An early objective of this study was to combine interferometry studies with surface x-ray diffraction. To this end, an interferometer was designed and built for the surface x-ray diffraction station, station 16.2, at Daresbury Laboratory, Warrington, UK. Despite surmounting several technical hurdles, many remained, of which the most significant was inadequate source intensity at a wavelength appropriate for penetration of the solution layer. Consequently successful data was not available in the timescale of this study though this experiment remains as a very attractive proposition and will hopefully answer many questions, particularly about the termination of the {010} faces of KAP. These experiments are most likely to succeed with the x-ray intensities available from third generation synchrotron sources.

With respect to the termination of KAP {010}, its interaction with impurities and the question of the growth unit; a new PBC analysis, correcting for the erroneous lattice parameter and including the dimer as a growth unit, is clearly needed to address these questions. With the ever increasing computational power available this should be a relatively simple proposition. In a similar vein, the state of aggregation of KAP in solution is a fertile area for improved understanding. It is the authors opinion that the dimer hypothesis has merit. A better understanding of the structure of KAP solutions will be helpful in this regard. Conceivably the colligative and electrolytic properties of the solutions would be useful in addressing this question. In this regard, a preliminary study of the role of pH on the growth of KAP crystals was made. It was found that the addition of an arbitrary quantity of potassium hydroxide to KAP solutions caused a profound habit change, rhombs resulted. Excepting impurities, no new species are added to aqueous KAP solutions by the addition of KOH because both potassium and

hydroxide ions are already present. In this way the pH may be modified without introducing new species. It was found that, despite the distinct habit change, the spiral shape on the largest face was typical of KAP {010} however its axis was no longer parallel to the long edge of the crystal suggesting that the edge faces had become more important than the side faces of the orthodox habit. It appears then that the {010} face was unaffected by the pH change but other faces were greatly affected. Phthalic acid is a polyprotic acid and it was tentatively proposed that the pH change had modified its dissociation in solution in some way. Much interesting work is possible here.

There is now more than one hypothesis for the shape of the growth spiral, one having been promulgated here. This makes the KAP growth spiral an ideal testing ground for theories of spiral polygonisation, by both experimental and theoretical means. Analytical or computer simulation work on the configurational entropy of the step is attractive in terms of the hypothesis of the present author. Particularly attractive would be to apply the recent "two-dimensional Hartman-Perdok" analysis of Hollander *et al.* [154] to the KAP {010} growth spiral, drawing on the results of the new PBC analysis for which the present author has called. It is the present author's prediction that the method will fail to predict the occurrence of <001> directions due to the neglect of entropy. Instead, it will predict a four sided figure bounded entirely by <101> segments.

Related to this is the need for a better understanding of the critical supersaturation for two-dimensional nucleation on KAP {010}. The contribution of the entropy of mixing of dissimilar kinks to the step free energy and the expected concomitant decrease in the size of the critical nucleus is a significant finding of the present study and one which demands further analysis. Atomistic simulation would be of great value here. Also, experimental studies with the specific intent of studying two-dimensional nucleation are required. The techniques of this study could be used here also. If the seed crystal were replaced with dislocation free slices cut from larger crystals, then (R,σ) curves could be measured for dislocation free growth. Subsequent AFM analysis could be performed in exactly the same way. The predictions of the various two-dimensional models could then be confronted with experiment in an unambiguous manner.

Experimentally, there is still much scope for the AFM observation of impurities. In addition, measurement of the normal growth rates from quantitatively doped solutions by interferometry is an obvious addition. The techniques applied here to the nominally pure solution all apply equally well to growth from impure solution. This is actually one facet of Bennemas' scheme. For this reason some experiments were performed at

the time of the present study however these were very restricted.

The frequent observations of kinematic waves and macrosteps certainly warrant greater study and once again KAP appears to be an ideal candidate as a testing ground. The observations here have been entirely qualitative though quantitative measurements of the dynamics of these fluctuations is certainly reasonable with the techniques of this study. The analysis of the motion of the moiré fringes which betray the presence of kinematic waves and macrosteps in interferometry has already been suggested in section 6.6.

Finally, the frequent occurrence of elastic effects such as hollow dislocation cores merits extra attention. In addition to x-ray topography, transmission electron microscopy may assist in understanding the occurrence of hollow dislocation cores in KAP. Since the full elastic constants for KAP are available [174], it could be an ideal crystal with which to quantitatively test the predictions of theories of the role of elastic effects on crystal growth. Related to elastic effects is the slip of dislocations. A hypothesis was put forward to explain how dislocations could bring about polynuclear growth as a result of slip. The outline of this hypothesis could be developed into an analytical theory. Also, further evidence for this mechanism could be sought in AFM observations on other crystals. The techniques of this study would also, as has already been pointed out, be of great use in investigating industrially relevant phenomena such as collision breeding. Essentially the techniques would remain more or less unchanged.

Part VI

Appendices

Appendix A

Refractive Index Measurement of KAP Solutions

A.1 Introduction

In order to make accurate measurements of rates of growth and slopes of vicinal hillocks *in-situ* by laser interferometry it is essential that the refractive index of the solution be known so that the true path length can be obtained from the optical path length. The refractive index of solutions is normally sensitive to variations in concentration and temperature. Therefore aqueous KAP solutions saturated at different temperatures will have different refractive indices. For accurate work it is therefore necessary that refractive index data is obtained across the range of temperature and composition.

A.2 Experimental Method

A.2.1 Solution Preparation

KAP solutions were saturated at 20, 25, 30, 35 and 40°C respectively by stirring deionised, distilled water with excess KAP (BDH, Analar; recrystallised once) in sealed

vials immersed in a thermostatic water bath, for 72 hours. Upon removal from the bath, the solutions were immediately filtered from excess solid KAP by vacuum filtration (using Nalgene disposable filters) into a clean Buchner funnel (cleaned with a preparation of potassium permanganate in sulphuric acid). The solutions were sealed into vials and stored at a temperature slightly in excess of the saturation temperature in a laboratory incubator.

A.2.2 Refractive Index Determination

Refractive indices of the solutions were determined with an Abbé refractometer using the 589 nm line from a sodium vapour lamp for illumination[1]. The refractometer sample stage was regulated at constant temperature by recirculation of temperature regulated water from a large reservoir. Prior to refractive index measurements the reservoir temperature was set to the saturation temperature of the solutions and the solution vials were immersed in the reservoir to equilibriate for approximately 1 hour. Once equilibriated a sample of solution was dispensed onto the refractometer prism and sealed. Working quickly to avoid risking nucleation or evaporation, a reading of the position of the sodium lamp spot was taken from the refractometer graticule observed through the instrument eyepiece. Refractive indices relative to air were obtained from the sodium lamp spot position by reference to high precision tables supplied with the instrument.

A.3 Results

The values obtained for refractive index are shown in table A.3.

T_{sat}	n
20°C	1.348
25°C	1.351
30°C	1.355
35°C	1.358
40°C	1.361

Table A.1: Relative refractive indices of KAP solutions at various saturation temperatures. Sodium vapour illumination, 589 nm.

[1]The instrument and technical assistance was provided by the Dept. of Chemical Engineering, University of Bath.

A.4 Discussion

The refractive index values obtained were used as parameters in the program TRANSFORM to obtain normal growth rates and in subsequent calculation of hillock slopes. Although the refractive index of the solution will change by a small amount when supersaturated by cooling, the change is expected to be small at modest supersaturations and therefore the value obtained at the saturation temperature has been used in all calculations. There will also be a slight difference between the refractive index of the solution for the sodium vapour source at 589 nm and the helium:neon laser source at 632.8 nm due to the wavelength dependence of the refractive index. Once again the discrepancy is expected to be small and has been neglected in the crystal growth experiments. Verification of the results and justification of the assumptions is provided by the very close agreement obtained between mean step spacings obtained by interferometry and AFM. It has in fact been found that the refractive index change is only slight across the temperature and concentration range investigated and that for most measurements a value in the range of 1.35 - 1.36 is adequate. The change in optical path length per fringe, $d = \lambda/2n$, between the highest and lowest refractive indices measured is approximately 2 nm. This is approximately the height of two fundamental steps on KAP {010}. Over the height changes measured in growth rate and hillock slope determinations this error is insignificant.

Appendix B

Measurement of Growth Rate Dependence on Solution Flow Rate

B.1 Introduction

In any study of solution crystal growth it is important to know if growth proceeds in a kinetic or a diffusive regime. That is, is the rate of growth limited by the supply of matter to the crystal surface or by kinetic processes occurring at the crystal surface? If the kinetic processes at the surface are of primary interest rather than mass transport to the surface, then it is important to ensure that growth is kinetically limited by ensuring adequate mass transport into the adsorbed layer. In effect this amounts to ensuring adequate stirring or solution flow to ensure that the stagnant layer at the crystal surface does not become depleted. Because, in a kinetic regime, the growth is independent of mass transport from the bulk solution, it should be manifest as a regime of growth which is insensitive to solution flow. That is, changes in solution flow rate above a certain threshold should not perceptibly change the growth rate. The transition from a kinetic to a diffusion regime should be marked by the onset of dependence of growth rate on the flow rate as the flow rate is reduced.

For the flow-system used in the present study, the most practical way to check that this was the case was to conduct experiments in which the flow rate of solution in the growth cell was adjusted during steady state growth of a crystal whilst measuring the growth rate by interference fringe counting.

B.1.1 Experimental Method

The experimental method was essentially that for other growth rate measurements. A cleaved crystal was mounted in the growth cell as usual and dissolved and re-grown to present a growing face with a small number of vicinal hillocks. Once a stable steady state hillock was obtained the intensity time-series of selected pixels in the image of the hillock were continuously recorded whilst the solution flow rate was adjusted. The subsequent time series were clipped into intervals corresponding to each flow rate.

The solution flow rate was adjusted by means of a variable compression clamp on the cell bypass tubing of the flow-system. This arrangement was used because it was important that the flow rate of solution in the main flow system remained maximal. If the total flow rate in the main circuit was changed then the residence time in the battery of heat exchangers would also change with the result that flow rate adjustments resulted in small temperature changes also. In this case, measured changes in growth rate could not be unequivocally attributed to the solution flow. For this reason, the system was reconfigured such that the in-line flow-meter was in the cell bypass line. When the tubing of the bypass was fully clamped the flow in the cell was maximal at 800 ml/min. The flow rate was reduced in increments of 50 ml/min until the bypass circuit was fully open. The solution flow rate in the cell was obtained by continuity from the measured flow rate in the cell bypass. With the bypass open the flow rate in the bypass was 400 ml/min indicating a flow rate of 400 ml/min in the growth cell. Growth rate measurements were therefore made for flow-rates in the range 400-800 ml/min.

Measurements were made with solutions saturated at temperatures of 25.66 ± 0.02 °C and 35.42 ± 0.02 °C and at two relative supersaturations. The duration of the measurements was sufficient to obtain adequate confidence in the growth rates obtained. Attention was paid to the phenomenon of growth rate fluctuation which would invalidate the measurements. All data were recorded on hillocks which maintained a steady state during the measurement interval for all flow rates.

B.1.2 Results

Figures B.1 and B.2 show normal growth rates as functions of flow rate for solutions saturated at 25.66 ± 0.02 °C and 35.42 ± 0.02 °C respectively.

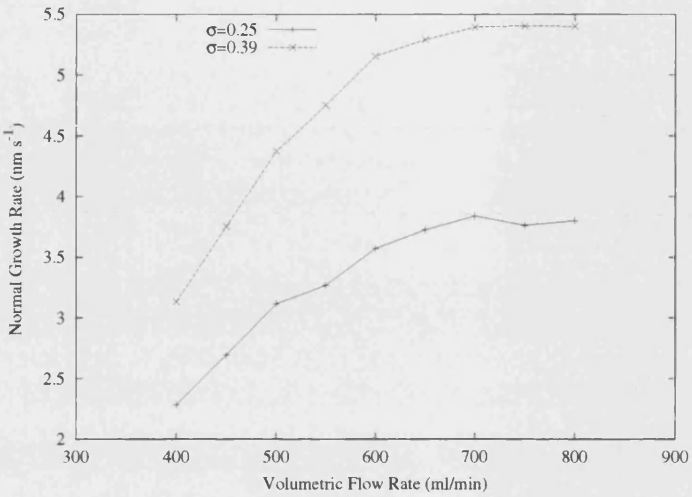

Figure B.1: Normal growth rate vs flow rate at 25.66 °C

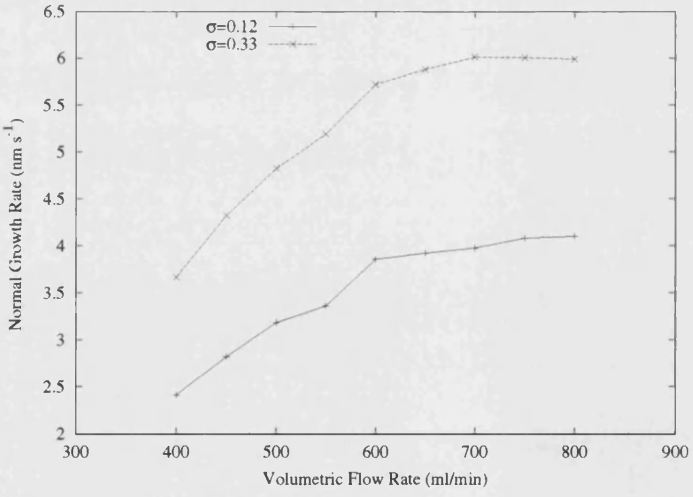

Figure B.2: Normal growth rate vs flow rate at 35.42 °C

B.1.3 Discussion

The data shown in the charts reveal a clear trend of increasing growth rate with increasing flow rate. As anticipated, the data exhibit a plateau in normal growth rate at the highest attainable flow rates. As the flow rate is increased the normal growth rate reaches a limiting value beyond which the further increase of flow rate does not increase growth rate. This is consistent with the transition to a kinetic regime where the growth rate is limited by kinetic processes at the surface rather than the supply of growth units from the bulk solution. The transition to the kinetic regime is not clearly defined in the data presented however beyond 700 ml/min the growth rate is insensitive to further increases in flow rate.

B.1.4 Conclusions

All growth rate measurements were conducted at the maximum attainable flow rate of 800 ml/min which is found to be within the kinetic regime. It may therefore be assumed that all of the measured growth rates were kinetically limited.

Appendix C

Data Acquisition/Analysis Software

C.1 PIXSEL

The C computer program PIXSEL allows the user to select up to 13 pixels in the video display of the crystal for digitisation. It presents the user with a cursor on the video display with which the selection may be made. It uses the CX100 frame-grabber library functions fg_moveto and fg_linerel to display the cursor. Once the desired pixel is located, F10 writes the data-file name and pixel coordinates to the parameter file which is read by analyse. Once 13 pixels have been entered the program exits. ESC quits the program at any time.

```
/*****************************************************************************
*  10/07/98      Martin McLoughlin                                             *
*  This program uses a cursor to select pixel coordinates and writes them to   *
*  a parameter file                                                            *
*                                                                              *
*****************************************************************************/

/*****************************************************************************
*       Preprocessor Directives
*****************************************************************************/

#include <string.h>
#include <stdio.h>
#include "c:\cx100\dos\cx100.h"
#define         UP_ARROW    0x48
#define         DN_ARROW    0x50
#define         RT_ARROW    0x4D
#define         LF_ARROW    0x4B
#define         PAGE_UP     0x49
```

```
#define         PAGE_DN     0x51
#define         INSERT      0x52
#define         BS          0x08
#define         HOME        0x47
#define         END         0x4F
#define         RET         0x0D
#define         ESC         0x1B
#define         DEL         0x53
#define         SPACE       0x20
#define         D_HATCH     0xB2
#define         L_HATCH     0xB0
#define         CHECK       0xFB

#define         F1          0x3B
#define         F2          0x3C
#define         F3          0x3D
#define         F4          0x3E
#define         F5          0x3F
#define         F6          0x40
#define         F7          0x41
#define         F8          0x42
#define         F9          0x43
#define         F10         0x44
#define         F11         0x85
#define         F12         0x86

/*
#define         UP_ARROW    0x48
#define         DN_ARROW    0x50
#define         RT_ARROW    0x4D
#define         LF_ARROW    0x4B
#define         ESC         0x001B
#define         CTRL_UP_ARROW     0x8D
#define         CTRL_DN_ARROW     0x91
#define         CTRL_RT_ARROW     0x74
#define         CTRL_LF_ARROW     0x73
*/
/*****************************************************************************
*       Structs, Unions and Typedefs
*****************************************************************************/
typedef struct {        int x;
                                        int y;
                                        int grey_scale;
                        }Pixel;

/*****************************************************************************
*       Global Variables
*****************************************************************************/
int xval;
int yval;
Pixel current_pixel;

/*****************************************************************************
*       Function Prototypes
*****************************************************************************/
//void get_coordinates(void);
```

```
void Cursor(FILE *fp, char *FileNameRoot);

/*****************************************************************************
*       Function: Main
*****************************************************************************/

void main (int argc, char *argv[3])
{
char *filename;
char *err;
FILE *fp;

if(argc>3){
                puts("Too Many Arguments.  Usage: pixsel filename.par");
                exit(1);
        }

if(argc>1){
        fp = fopen(argv[1],"w");
        filename = argv[1];
        printf("\n %s",filename);
        }
else
        fp = NULL;

        if(argc==2){
                puts("\nNo data filename root specified");
                exit(1);
                }

        err = init_library();  /*This section   */
        if(err != NULL)           /*initialises  */
                {                   /* the frame */
                        puts(err);       /* grabber */
                        exit(1);
                }
        clr(OVERLAY_ENABLE);
        clr(DISPLAY_OVERLAY);
        ft_setfont(1);
        grab();
        ft_gotoxy(80, 480);
        ft_print("Crystal Growth Interferometer");
        display;
        Cursor(fp,argv[2]);
}

/*****************************************************************************
*       Function: Cursor
*****************************************************************************
*       This function puts the pixel position crosshairs on the screen.     *
*****************************************************************************/

void Cursor(FILE *fp, char *FileNameRootConstant)
{
        int key, pixels;
        char *FileNumber;
```

```
char *FileNameRoot;
char *DatExtension;

DatExtension = ".dat";
strcpy(FileNameRoot, FileNameRootConstant);
current_pixel.x = 256;
current_pixel.y = 256;
fg_moveto(current_pixel.x , current_pixel.y);
fg_linerel(0,0);
pixels=0;


do
{
  key = getch();
  switch(key)
    {
    case UP_ARROW:
      {
        --current_pixel.y;
        printf("\n %d", key);
        printf("\n UP");
        printf("\n x = %d, y = %d", current_pixel.x, current_pixel.y);
        break;
      }
    case DN_ARROW:
      {
        ++current_pixel.y;
        printf("\n %d", key);
        printf("\n Down");
        printf("\n x = %d, y = %d", current_pixel.x, current_pixel.y);
        break;
      }
    case LF_ARROW:
      {
        --current_pixel.x;
        printf("\n %d", key);
        printf("\n LEFT");
        printf("\n x = %d, y = %d", current_pixel.x, current_pixel.y);
        break;
      }
    case RT_ARROW:
      {
        ++current_pixel.x;
        printf("\n %d", key);
        printf("\n RIGHT");
        printf("\n x = %d, y = %d", current_pixel.x, current_pixel.y);
        break;
      }
    case F10:
      {
        if(fp!=NULL){
          pixels++;
          itoa(pixels,FileNumber,10);
          strcat(FileNameRoot,FileNumber);
          strcat(FileNameRoot, DatExtension);
```

```
                fprintf(fp,"%s\n%d\n%d\n",FileNameRoot,current_pixel.x,
                        current_pixel.y);
                strcpy(FileNameRoot, FileNameRootConstant);
              }
              else
                break;
            }
          }
          fg_moveto(current_pixel.x , current_pixel.y);
          fg_linerel(0,0);
        }while(key!=ESC);
}
```

C.2 Example PIXSEL Parameter File

The following file listing illustrates the format of the parameter files created by PIXSEL and read by ANALYSE.

```
13
154131.dat
194
307
154132.dat
219
286
154133.dat
218
377
154134.dat
277
377
154135.dat
277
331
154136.dat
234
207
154137.dat
269
207
154138.dat
314
194
154139.dat
166
183
1541310.dat
195
340
1541311.dat
```

```
409
218
1541312.dat
331
165
1541313.dat
133
241
```

The first line contains the number of pixels to be sampled (13 in this case). Each set of three lines after the first contains the data file name to be created and the x and y pixel coordinates to be sampled.

C.3 ANALYSE

The C computer program `ANALYSE` reads the parameter file created by `pixsel` and command line options which include sampling rate, frame grabbing frequency and sampling duration and writes a data file of pixel intensity against time for up to 13 pixels simultaneously. It also superimposes a grid of pixel positions onto the grabbed frames to indicate the locations of sampled pixels. Some additional command line parameters include information which is included in the data file header.

```
/*****************************************************
18/07/97 Martin McLoughlin
Dept. of Materials Science, University of Bath
ANALYSE.C reads a parameter file in which the
coordinates of pixels for grayscale sampling and
their destination filenames are stored. The program
is designed for non-interactive use by means of
command line parameters which may be called from
MS-DOS batch files. Pixel elapsed time and pixel
grayscales are written to the data file in two column
space separated format.
Syntax, including command line arguments is as
follows:
analyse [parameter file name][tape description]
[frame grab rate][sampling rate][duration][Tsat]
[Tgrowth][Tres][T HE1][T HE2][image file root]
[tape counter start & finish]
Some of these arguments are used to control the
program execution, others simply provide header
information for the datafile.
*****************************************************/

/*****************************************************
        Preprocessor Directives
```

```
*****************************************************/
#include <dos.h>
#include <stdlib.h>
#include <stdio.h>
#include <time.h>
#include <string.h>
#include "c:\cx100\dos\cx100.h"

/*****************************************************
       Function Prototypes
*****************************************************/
int key_press (void);

/*****************************************************
        Type Definitions
*****************************************************/
typedef struct pixel
{
  int xval;
  int yval;
  int greyscale;
};

/*****************************************************
        Function: Main
*****************************************************/
void
main (int argc, char *argv[13])
{
  char *err;
  struct pixel PixelList[20];
  FILE * fpData[20];
  char *BinFileRoot;
  char *BinFileName;
  float Temps[5];
  char *BinExtension;
  int sampling_rate;
  int duration;
  int counter;
  int pixels;
  time_t now;
  time_t timer;
  time_t LoopStartTime;
  time_t * ptrCurrentTime;
  char *CurrentTime;
  int FilesGrabbed;
  int LoopCount;
  int FrameGrabRate;
  int pixelno;
  char *ptrColumnLabel;
  char *FileNumber;
  FILE * ParameterFile;
  char *FileName;
  char *TapeRef;
  char *StartFinish;
  if (argc != 14)
```

```
  {
    puts ("\nInsufficient Arguments");
    exit (1);
  }
err = init_library ();
if (err != NULL)
  {
    puts (err);
    exit (1);
  }
pixels = atoi (argv[1]);
BinExtension = ".bin";
printf ("Pixels = %d", pixels);
duration = atoi (argv[6]);
duration = duration * 60;
sampling_rate = atoi (argv[5]);
StartFinish = argv[13];
if (sampling_rate < 1)
  {
    puts ("\nSampling Period must be 1 second or greater" );
    exit (1);
  }
if (pixels > 13)
  {
    puts ("Too many pixels. Limit is 13");
    exit (1);
  }
ParameterFile = fopen (argv[2], "r");
for (counter = 1; counter <= pixels; counter++)
  {
    fscanf (ParameterFile, "%s", FileName);
    if (strlen (FileName) > 12)
      {
        puts ("Filename is invalid");
        exit (1);
      }
    fpData[counter - 1] = fopen (FileName, "w");
    fscanf (ParameterFile, "%d", &pixelno);
    PixelList[counter - 1].xval = pixelno;
    if (PixelList[counter - 1].xval > 512 || PixelList[counter - 1].xval < 0)
      {
        puts ("\nPixel coordinates must lie in the range 0 to 512");
        exit (1);
      }
    fscanf (ParameterFile, "%d", &pixelno);
    PixelList[counter - 1].yval = pixelno;
    if (PixelList[counter - 1].yval > 512 || PixelList[counter - 1].yval < 0)
      {
        puts ("Pixel coordinates must lie in the range 0 to 512");
        exit (1);
      }
  }
for (counter = 0; counter <= 4; counter++)
  Temps[counter] = atof (argv[7 + counter]);
FrameGrabRate = atoi (argv[4]);
strcpy (BinFileRoot, argv[12]);
```

```
  FrameGrabRate = FrameGrabRate * 60;
  TapeRef = argv[3];
  *ptrCurrentTime = time (NULL);
  CurrentTime = ctime (ptrCurrentTime);
  printf ("\nsampling period = %d \nduration = %d \ngrab period = %d",
          sampling_rate, duration, FrameGrabRate);
  for (counter = 1; counter <= pixels; counter++)
    fprintf (fpData[counter - 1],
             "%sxval = %d\nyval = %d\n%s\nDuration = %d seconds\nsampling
period =%d seconds\n
Tsat = %f\nTgrowth = %f\nTres = %f\nTHE1 = %f\nTHE2 = %f\n%s",
CurrentTime, PixelList[counter - 1].xval,
PixelList[counter - 1].yval, TapeRef, duration, sampling_rate,
Temps[0], Temps[1], Temps[2], Temps[3], Temps[4], StartFinish);
  ft_setfont (1);
  acquire ();
  now = time (NULL);
  timer = time (NULL);
  LoopStartTime = timer - now;
  LoopCount = 0;
  FilesGrabbed = 0;
  while (LoopStartTime < duration && !key_press ())
    {
      LoopCount++;
      timer = time (NULL);
      LoopStartTime = timer - now;
      for (counter = 1; counter <= pixels; counter++)
        PixelList[counter - 1].greyscale =
          get_pixel (PixelList[counter - 1].xval,
                     PixelList[counter - 1].yval);
      for (counter = 1;counter <= pixels;counter++)
        fprintf (fpData[counter - 1], "\n%ld %d ", LoopStartTime,
                 PixelList[counter - 1].greyscale);
      if (FrameGrabRate != 0)
        {
          if (LoopCount == FrameGrabRate / sampling_rate)
            {
              grab ();
              for (counter = 1; counter <= pixels; counter++)
                {
                  fill_column (PixelList[counter - 1].xval, 255);
                  fill_row (PixelList[counter - 1].yval, 255);
                  ft_gotoxy (60, PixelList[counter - 1].yval - 10);
                  itoa (PixelList[counter - 1].yval, ptrColumnLabel, 10);
                  ft_print (ptrColumnLabel);
                  ft_gotoxy (PixelList[counter - 1].xval + 10, 20);
                  itoa (PixelList[counter - 1].xval, ptrColumnLabel, 10);
                  ft_print (ptrColumnLabel);
                }
              write_ram_to_file (BinFileName, 0);
              acquire ();
              FilesGrabbed++;
              LoopCount = 0;
            }
          else
            {
```

```
            itoa (FilesGrabbed, FileNumber, 10);
            strcat (BinFileRoot, FileNumber);
            strcpy (BinFileName, strcat (BinFileRoot, BinExtension));
          }
        strcpy (BinFileRoot, argv[12]);
      }
    do
      {
        timer = time (NULL);
      }
    while (timer - now < LoopStartTime + sampling_rate);
  }
```

C.4 Example Raw Data File

An example of the pixel intensity raw data file produced by ANALYSE is listed below.

```
//Thu Feb 25 19:52:10 1999
//xval = 160
//yval = 247
//mjm1/38/tape1
//Duration = 300 seconds
//sampling period =3 seconds
//Tsat = 39.660000
//Tgrowth = 36.450001
//Tres = 37.799999
//THE1 = 36.500000
//THE2 = 0.000000
//85-90
0 137
3 185
6 239
9 232
12 227
15 222
18 204
21 150
24 144
27 49
30 47
33 149
36 212
39 232
42 234
45 225
48 222
```

C.5 Analysis Batch Files

ANALYSE was written to use command line arguments in order that it may be sequentially called from an MS-DOS batch file non-interactively. Once a batch file has been created for an entire videotape then it may be run continuously, making sequential calls to ANALYSE for each relevant section of tape. A typical batch file for digitisation of an entire videotape is shown below.

```
rem This file is a template for the analysis of videotapes
rem insert reference here when editing "reference"
rem It uses the analyse function to measure pixel intensity.
rem the syntax for the analyse function is as follows:
rem analyse [no. of pixels][parameter file name][tape descritption]
rem [frame grab rate][sampling rate][duration][Tsat][Tgrowth][Tres]
rem [T HE1][T HE2][image file root][tape counter start & finish]
rem  all arguments are mandatory.

rem This version uses command line parameters to enter the analyse command
rem line arguments.  It also uses command line arguments and the "creatdir"
rem program to sort the files into directories, ready for archiving as soon
rem as analysis is complete.

rem The command line parameters it uses are as follows:
rem %1 = the filename root, eg. "1361"  (1361)
rem %2 = the lab book reference eg. "mjm1" (mjm1)
rem %3 = the lab book page number (36)
rem %4 = the tape reference, eg. "tape1"
rem %5 = the number of separate parts to the file (20)


rem part 1
rem cxdemo  g w %1p1s.bin
rem analyse 9 %11.par %2/%3/%4 3 3 10 26.71 24.84  26  23.5 0  %11 0-10

rem part 2
rem cxdemo  g w %1p2s.bin
rem analyse 10  %12.par %2/%3/%4 3 3 10 26.71 26.01  26.5  25 0  %12 10-20

rem part 3
rem cxdemo  g w %1p3s.bin
rem analyse 12  %13.par %2/%3/%4 3 3 10 26.71 26.26  26.6  25.3 0  %13 20-30


rem part 4
rem cxdemo  g w %1p4s.bin
rem analyse 12  %14.par %2/%3/%4 3 3 12 26.71 26.46  26.7  25.5 0 %14 30-42

rem part 5
rem cxdemo  g w %1p5s.bin
rem analyse 12  %15.par %2/%3/%4 3 3 10 26.71 26.66  27  25.8 0 %15 42-52

rem wait 7
```

```
rem rem part 6
rem cxdemo  g w %1p6s.bin
rem analyse 11  %16.par %2/%3/%4 3 3 21 26.71 25.05  26  24  0 %16 59-80

rem part 7
rem cxdemo  g w %1p7s.bin
rem analyse 10  %17.par %2/%3/%4 3 3 10 26.71 25.31  26  24.3 0 %17 80-90

rem part 8
rem cxdemo  g w %1p8s.bin
rem analyse 10  %18.par %2/%3/%4 3 3 10 26.71 25.63  26.3  24.6 0 %18 90-100

rem part 9
rem cxdemo  g w %1p9s.bin
rem analyse 13  %19.par %2/%3/%4 3 3 10 26.71 25.86  26.6  24.9 0 %19 100-110

rem part  10
rem cxdemo  g w %1p10s.bin
rem analyse 13  %110.par %2/%3/%4 3 3 15 26.71 26.15  26.7  25.2 0 %110  110-125

echo part  11
cxdemo  g w %1p11s.bin
analyse 13  %111.par %2/%3/%4 3 3 15 26.71 26.34  27  25.5 0 %111  125-140

echo part  12
cxdemo  g w %1p12s.bin
analyse 10  %112.par %2/%3/%4 3 3 20 26.71 26.54  27  25.8 0 %112  140-160

echo part  13
cxdemo  g w %1p13s.bin
analyse 10  %113.par %2/%3/%4 3 3 25 26.71 26.81  27.2  26.1 0 %113  160-185

echo part  14
cxdemo  g w %1p14s.bin
analyse 10  %114.par %2/%3/%4 3 3 5 26.71 24.76  25.7  23.6 0 %114  185-190

echo part  15
cxdemo  g w %1p15s.bin
analyse 12  %115.par %2/%3/%4 3 3 5 26.71 24.56  26  23.2 0 %115  190-195

echo part  16
cxdemo  g w %1p16s.bin
analyse 12  %116.par %2/%3/%4 3 3 5 26.71 24.24  26  22.8 0 %116  195-200

echo part  17
cxdemo  g w %1p17s.bin
analyse 12  %117.par %2/%3/%4 3 3 5 26.71  23.9  26  22.4 0 %117  200-205

echo part  18
cxdemo  g w %1p18s.bin
analyse 7 %118.par %2/%3/%4 3 3 5 26.71  23.6  25.8  22 0 %118  205-210

echo part  19
cxdemo  g w %1p19s.bin
analyse 7 %119.par %2/%3/%4 3 3 5 26.71 23.32  25.8  21.6 0 %119  210-215
```

```
wait 5
echo part  20
cxdemo  g w %1p20s.bin
analyse 13  %120.par %2/%3/%4 3 3 24  37.5 36.81  38  37 0 %120  220-244
```

C.6 WAIT

Because occasional sections of videotape were blank or contained no relevant data then it was necessary to be able to make the system wait for the necessary number of minutes until a data containing section of videotape was reached. This was achieved by the program WAIT, the function of which was to do nothing for the number of minutes specified as an argument on the command line. The C code for WAIT is shown below.

```
/* 7/7/98        Martin McLoughlin wait.c
/* This program waits for a number of minutes specified in the arguments.*/

# include <stdlib.h>
# include <stdio.h>
# include <time.h>
# include <dos.h>
# include <conio.h>

void main(int argc,char *argv[2])
{
        int delay_value;
        time_t now;
        time_t timer;

        delay_value=atoi(argv[1]);
        printf("\n delay_value %d", delay_value);
        delay_value=delay_value*60;
        now=time(NULL);

        do{
                timer=time(NULL);
                timer= timer-now;
                delay(500);
                gotoxy(1,20);
                printf("\n Elapsed time = %d", timer);
        }while(timer <= delay_value);
        exit(0);
}
```

C.7 TRANSFORM

TRANSFORM performs off-line batch-wise spectral analysis of the pixel intensity data files created by ANALYSE by application of the FFT algorithm. Originally written in MATLAB, it has been ported to INRIA SCILAB. The version shown below is the SCILAB version.

```
[files]=unix_g("ls *.dat.sci")
A=9.2837
B=-0.0591
C=0.0058
Lambda=632.8
n=1.355
filecount=size(files,1);
filehandle=mopen("results.table","w");
mfprintf(filehandle,"%s,%s,%s,%s,%s,%s,%s,%s,%s,%s,%s\n","FILENAME",
"DURATION","XVAL","YVAL","Tsat","Tgrowth","Sigma","SAMPLE_PERIOD",
"FRINGE_FREQUENCY","FRINGE_PERIOD","R"); for counter=1:filecount,
        [rawdata]=read(files(counter),-1,2);
        //file("close",files(counter));
        rows=size(rawdata,1);
        [rawdata]=rawdata([13:rows],[1:2]);
        rows=rows-13;
        [time]=rawdata(:,1);
        sample_period=time(2);
        [intensity]=rawdata(:,2);
        //xbasc();
        xsetech([0,0,0.5,1]);
        plot2d(time,intensity);
        xtitle(files(1),"Time (s)","Grayscale (0-255)");
        [Y]=fft(intensity,-1);
        Y(1)=[];
        [power]=abs(Y(1:rows/2)).^2;
        [nyquist]=(1/sample_period)/2;
        [freq]=(1:rows/2)/(rows/2)*nyquist;
        [period]=[freq]^(-1);
        [period]=[period]';
        //xbasc();
        xsetech([0.5,0,0.5,1]);
        plot2d(period,power);
        xtitle("Periodogram of "+string(files(counter)),"Period (s)",
                "Power (Arbitrary)");
        xbasc();
        [m,k]=max(power);
        datfilehandle=mopen(files(counter));
        for fieldcount=1:1:10,
                field=mfscanf(datfilehandle,"%s");
                if fieldcount==7 then,
                        field=mfscanf(datfilehandle,"%d");
                        xval=field;
                end
                if fieldcount==9 then,
                        field=mfscanf(datfilehandle,"%d");
```

```
                        yval=field;
                end
        end
        for fieldcount=1:1:15,
                field=mfscanf(datfilehandle,"%s");
                if fieldcount==10 then,
                        field=mfscanf(datfilehandle,"%f");
                        Tsat=field;
                end
                if fieldcount==12 then,
                        field=mfscanf(datfilehandle,"%f");
                        Tgrowth=field;
                end
        end
        mclose(datfilehandle);

sigma=((A+(B*Tsat(1))+C*(Tsat(1)^2))/(A+(B*Tgrowth(1))+C*(Tgrowth(1)^2)))-1;
        R=(Lambda/n)*freq(k);
mfprintf(filehandle,"%s,%s,%s,%s,%s,%f,%f,%f,%s,%s,%s\n", files(counter),
string(time(rows)), string(sample_period), string(xval(1)), string(yval(1)),
Tsat(1), Tgrowth(1), sigma, string(freq(k)), string(period(k)), string(R));
end
```

References

[1] N Rodriguez-Hornedo and D Murphy. Significance of controlling crystallization mechanisms and kinetics in pharmaceutical systems. *Journal of Pharmaceutical Sciences*, 88(7):651–660, July 1999.

[2] A Ibanez, J P Levy, C Mouget, and E Prieur. Crystal growth of a promising nonlinear optical material: 2-amino-5-nitropyridinium chloride. *Journal of Solid State Chemistry*, 129:22–39, 1997.

[3] N P Zaitseva, L N Rashkovich, and S V Bogatyreva. Stability of KH_2PO_4 and $K(H,D)_2PO_4$ solutions at fast crystal growth rates. *Journal of Crystal Growth*, 148:276–282, 1995.

[4] F C Frank. The theory of crystal growth. *Advances in Physics*, 1:91–109, 1952.

[5] M Ohara and R C Reid. *Modelling Crystal Growth Rates From Solution.* Prentice-Hall International Series in The Physical and Chemical Engineering Sciences. Prentice-Hall, 1973.

[6] P Bennema. Crystal growth from solution - theory and experiment. *Journal of Crystal Growth*, 24/25:76–83, 1974.

[7] H J Scheel. *Handbook of Crystal Growth*, volume 1, chapter 1. Elsevier Science, 1993.

[8] J P Van Der Eerden. *Handbook of Crystal Growth*, volume 1, chapter 6. Elsevier Science, 1993.

[9] A A Chernov, E I Givagizov, K S Bagdasarov, V A Kuznetsov, L N Demyanets, and A N Lobachev. *Modern Crystallography III: Crystal Growth*, volume 36 of *Springer Series in Solid State Sciences*. Springer, 1984.

[10] R F Strickland-Constable. *Kinetics and Mechanism of Crystallization.* Academic Press, 1968.

[11] W A Tiller. *The Science of Crystallisation: Microscopic Interfacial Phenomena.* Cambridge University Press, 1991.

[12] J W Gibbs. *The Collected Works of J W Gibbs*, volume 2. Dover Reprints, 1951.

[13] I V Markov. *Crystal Growth for Beginners.* World Scientific, 1995.

[14] W L Bragg. *The Development of X-Ray Analysis.* Dover, 1992.

[15] D Hull and D J Bacon. *Introduction to Dislocations*, volume 37 of *International Series on Materials Science and Technology.* Pergamon, 3rd edition, 1984.

[16] C Barrett and T B Massalski. *Structure of Metals.* Volume 35 of International Series on Materials Science and Technology. Pergamon, 3rd revised edition, 1980.

[17] A H Cottrell. *Dislocations and Plastic Flow in Crystals.* Oxford University Press, 1953.

[18] A A Chernov. Crystal growth and crystallography. *Acta Crystallographica*, A54:859–872, 1998.

[19] A Pimpinelli and J Villain. *Physics of Crystal Growth.* Cambridge University Press, 1998.

[20] C Herring. Some theorems on the free energies of crystal surfaces. *Physical Review*, 82(1):87–93, 1951.

[21] R Gomer and C S Smith, editors. *Structure and Properties of Solid Surfaces*, chapter 1. University of Chicago Press, 1953.

[22] P Hartman, editor. *Crystal Growth: An Introduction*, chapter 14. North-Holland Publishing Co., 1973.

[23] P Hartman and W G Perdok. On the relations between structure and morphology of crystals. I. *Acta Crystallographica*, 8:49–52, 1955.

[24] P Hartman and W G Perdok. On the relations between structure and morphology of crystals. II. *Acta Crystallographica*, 8:521–524, 1955.

[25] P Hartman and W G Perdok. On the relations between structure and morphology of crystals. III. *Acta Crystallographica*, 8:525–529, 1955.

[26] W K Burton and N Cabrera. Crystal growth and surface structure. *Discussions of the Faraday Society*, pages 33–48, 1949. Parts I and II.

[27] P Hartman. *Crystal Growth: An Introduction*, chapter 13. North-Holland Publishing Co., 1973.

[28] R H Doremus, B W Roberts, and D Turnbull, editors. *Growth and Perfection of Crystals*, chapter 1, pages 3–10. John Wiley, 1958.

[29] F C Frank. An outline of nucleation theory. *Journal of Crystal Growth*, 13/14: 154–156, 1972.

[30] B R Pamplin, editor. *Crystal Growth*, chapter 2. Pergamon, 2 edition, 1979.

[31] W K Burton, N Cabrera, and F C Frank. Role of dislocations in crystal growth. *Nature*, 163:398–399, 1949.

[32] W K Burton. *Science News*, volume 21, chapter 3, pages 26–38. Penguin Books, 1951.

[33] F C Frank. The influence of dislocations on crystal growth. *Discussions of the Faraday Society*, 5:48–54, 1949.

[34] W K Burton, N Cabrera, and F C Frank. The growth of crystals and the equilibrium structure of their surfaces. *Philosophical Transactions of the Royal Society of London*, A243:299–358, 1951.

[35] P Hartman, editor. *Crystal Growth: An Introduction*, chapter 10. North-Holland Publishing Co., 1973.

[36] N Cabrera and M M Levine. On the dislocation theory of evaporation of crystals. *Philosophical Magazine*, 1:450–458, 1956.

[37] A A Chernov. Formation of crystals in solutions. *Contemporary Physics*, 30(4): 251–276, 1989.

[38] J Frenkel. On the surface motion of particles in crystals and the natural roughness of crystalline faces. *Journal of Physics, USSR*, 9(5):392–398, 1945.

[39] P Bennema. *Handbook of Crystal Growth*, volume 1, chapter 7. Elsevier Science, 1993.

[40] F C Frank. Capillary equilibria of dislocated crystals. *Acta Crystallographica*, 4:497–501, 1951.

[41] J J Gilman, editor. *The Art and Science of Growing Crystals*, chapter 1. John Wiley, 1963.

[42] E Budevski, G Staikov, and V Bostanov. Form and step distance of polygonised growth spirals. *Journal of Crystal Growth*, 29:316–320, 1975.

[43] H Müller-Krumbhaar, T W Burkhardt, and D M Kroll. A generalized kinetic equation for crystal growth. *Journal of Crystal Growth*, 38:13–22, 1977.

[44] W R Wilcox, editor. *Preparation and Properties of Solid State Materials*, volume 7, chapter 1. Marcel Dekker, 1982.

[45] M Rubbo. Spiral growth limited by surface kinetics a self-consistent model. *Journal of Crystal Growth*, 223:235–250, 2001.

[46] P Smereka. Spiral crystal growth. *Physica D*, 138:282–301, 2000.

[47] F C Frank. Note on the structure of a crystal surface. *Philosophical Magazine*, 41:200–205, 1950.

[48] R Gomer and C S Smith, editors. *Structure and Properties of Solid Surfaces*, chapter 8. University of Chicago Press, 1953.

[49] W W Mullins and J P Hirth. The microscopic kinetics of step motion in growth processes. *Journal of Physics and Chemistry of Solids*, 24:1391–1404, 1963.

[50] R H Doremus, B W Roberts, and D Turnbull, editors. *Growth and Perfection of Crystals*, chapter 10, pages 411–418. John Wiley, 1958.

[51] N Cabrera and D A Vermilyea. The growth of crystals from solution. In R H Doremus B W Roberts and D Turnbull, editors, *Growth and Perfection of Crystals*, pages 393–410. John Wiley and Sons, 1958.

[52] N Kubota and J W Mullin. A kinetic model for crystal growth from aqueous solution in the presence of impurity. *Journal of Crystal Growth*, 152:203–208, 1995.

[53] N Kubota, M Yokata, and J W Mullin. The combined influence of supersaturation and impurity concentration on crystal growth. *Journal of Crystal Growth*, 212:480–488, 2000.

[54] P Bennema. Analysis of crystal growth models for slightly supersaturated solutions. *Journal of Crystal Growth*, 1:278–286, 1967.

[55] P Bennema. Interpretation of the relation between the rate of crystal growth from solution and the relative supersaturation at low supersaturation. *Journal of Crystal Growth*, 1:287–292, 1967.

[56] P Bennema. The importance of surface diffusion for crystal growth from solution. *Journal of Crystal Growth*, 5:29–43, 1969.

[57] R L Schwoebel. Step motion on crystal surfaces II. *Journal of Applied Physics*, 40(2):614–618, 1969.

[58] M G Lagally and Zhenyu Zhang. Thin-film cliffhanger. *Nature*, 417:907–909, 2002.

[59] X Y Liu, E S Boek, W J Briels, and P Bennema. Prediction of crystal growth morphology based on structural analysis of the solid-fluid interface. *Nature*, 374:342–345, 1995.

[60] P Bennema. Spiral growth and surface roughening: Developments since burton, cabrera and frank. *Journal of Crystal Growth*, 69:182–197, 1984.

[61] P Bennema. Morphology of crystals determined by alpha factors, roughening temperature, f faces and connected nets. *Journal of Physics D: Condensed Matter*, 26:B1–B6, 1993.

[62] P Bennema. On the crystallographic and statistical mechanical foundations of the forty-year old hartman-perdok theory. *Journal of Crystal Growth*, 166:17–28, 1996.

[63] X Y Liu and P Bennema. Prediction of the growth morphology of crystals. *Journal of Crystal Growth*, 166:117–123, 1996.

[64] E S Boek, D Feil, W J Briels, and P Bennema. From wave function to crystal morphology: Application to urea and alpha glycine. *Journal of Crystal Growth*, 114:389–410, 1991.

[65] Z Berkovitch-Yellin. Toward an *ab-initio* derivation of crystal morphology. *Journal of The American Chemical Society*, 107:8239–8253, 1985.

[66] A L Rohl and D H Gay. Calculating the effects of surface relaxation on morphology. *Journal of Crystal Growth*, 166:84–90, 1996.

[67] E Vlieg. Understanding crystal growth in vacuum and beyond. *Surface Science*, 500:458–474, 2002.

[68] J P van der Eerden, P Bennema, and T A Cherepanova. Survery of Monte Carlo simulations of crystal surfaces and crystal growth. *Progress in Crystal Growth and Characterisation*, 1:219–254, 1978.

[69] H A Miers. An enquiry into the variation of angles observed in crystals, especially of potassium-alum and ammonium-alum. *Proceedings of the Royal Society*, 71:439–441, 1903.

[70] H A Miers. An enquiry into the variation of angles observed in crystals; especially of potassium-alum and ammonium-alum. *Philosophical Transactions of the Royal Society A*, 202:459–523, 1904.

[71] L J Griffin. Nucleation and normal growth: General discussion. *Discussions of the Faraday Society*, 5:192, 1949.

[72] N F Mott. Theory of crystal growth. *Nature*, 165(4191):295–297, 1950.

[73] L J Griffin. Observation of unimolecular growth steps on crystal surfaces. *Philosophical Magazine*, 41:196–199, 1950.

[74] L J Griffin. Microscopic studies on beryl crystals I. observation of uni-molecular steps. *Philosophical Magazine*, 42(330):775–786, 1951.

[75] S Tolansky. *Surface Microtopography*. Longmans, 1st edition, 1960.

[76] A R Verma. Spiral growth on carborundum crystal faces. *Nature*, 167(4258), 1951.

[77] A R Verma. Observations on carborundum of growth spirals originating from screw dislocations. *Philosophical Magazine*, 42(332):1005–1013, 1951.

[78] S Amelinckx. Letter. *Nature*, 167(4258):940, 1951.

[79] S Amelinckx. Growth features on crystals of long-chain compounds. *Acta Crystallographica*, 8:530–537, 1955.

[80] A J Forty. Observation of growth of cadmium iodine from aqueous solution. *Philosophical Magazine*, 42(330):670–672, 1951.

[81] A J Forty. The growth of cadmium iodide crystals: I - dislocations and spiral growth. *Philosophical Magazine*, 43(336):72–81, 1952.

[82] L J P Vogels, S J M Oosterbaan, P A van Koeven, P L M Pierrot, and J P van der Eerden. Real time digital video image processing of in situ crystal growth. *Journal of Crystal Growth*, 114(239–248), 1991.

[83] M Yokota, N Saito, J Hirai, A Sato, and N Kubota. Crystal growth rate enhancement caused by adhesion of small crystals. *AIChE Journal*, 43(12):3264–3270, 1997.

[84] P Bennema. Technique for measuring the rate of growth of crystals from solutions in dependence on the degree of supersaturation at low supersaturations. *Physica Status Solidi*, 17:555, 1966.

[85] P Bennema. Crystal growth measurements on potassium aluminium alum and sodium chlorate from slightly supersaturated solutions. *Physica Status Solidi*, 17:563, 1966.

[86] A A Chernov, L N Rashkovich, and A A Mkrtchan. Solution growth kinetics and mechanism: Prismatic face of ADP. *Journal of Crystal Growth*, 74:101–112, 1986.

[87] A A Chernov and A I Malkin. Regular and irregular growth and dissolution of (101) ADP faces under low supersaturations. *Journal of Crystal Growth*, 92: 432–444, 1988.

[88] L N Rashkovich and B Yu Shekunov. Morphology of growing vicinal surface: Prismatic faces of ADP and KDP crystals in solutions. *Journal of Crystal Growth*, 100:133–144, 1990.

[89] L N Rashkovich and G T Moldazhanova. Growth kinetics and morphology of potassium dihydrogen phosphate crystal faces in solutions of varying acidity. *Journal of Crystal Growth*, 151:145–152, 1995.

[90] K Maiwa, K Tsukamoto, and I Sunagawa. *Journal of Crystal Growth*, 102: 43–53, 1990.

[91] K Onuma, L Tsukamoto, and I Sunagawa. Growth kinetics of k-alum crystals in relation to the surface supersaturations. *Journal of Crystal Growth*, 100:125–132, 1990.

[92] P G Vekilov, L A Monaco, and F Rosenberger. High resolution interferometric technique for in-situ studies of crystal growth morphologies and kinetics. *Journal of Crystal Growth*, 148:289–296, 1995.

[93] K Tsukamoto. *In-situ* observation of crystal growth from solution. *Faraday Discussions*, 95:183–189, 1993.

[94] K Tsukamoto, E Yokoyama, S Maruyama, K Maiwa, K Shimuzu, R F Sekerka, T S Morita, and S Yoda. Transient crystal growth rate in microgravity: Report from TR-IA-4 rocket experiment. *J. Jpn Soc. Microgravity Appl.*, 15(1):2–9, 1998.

[95] Yong Kee Kim, B R Reddy, T G George, and R B Lal. Optical heterodyne interferometry for solution crystal growth rate measurement. *Optical Engineering*, 37(2):616–621, 1998.

[96] G Binnig and H Rohrer. Scanning tunneling microscopy. *IBM Journal of Research and Development*, 30(4):355–369, 1986.

[97] M G Lagally. Atom motion on surfaces. *Physics Today*, pages 24–31, November 1993.

[98] G Binnig, C F Quate, and Ch Gerber. The atomic force microscope. *Physical Review Letters*, 56:930, 1986.

[99] I Muševič, G Slak, and R Blinc. Temperature controlled microstage for an atomic force microscope. *Review of Scientific Instruments*, 67(7):2554–2556, July 1996.

[100] P A Campbell, G R Ester, and P J Halfpenny. In-situ studies of potassium hyrdrogen phthalate (KAP) crystal dissolution by scanning probe microscopy. *Journal of Vacuum Science and Technology*, 14(2):1373, 1996.

[101] D Gidalevitz, R Feidenhans'l, D M Smilgies, and L Leiserowitz. X-ray scattering from surfaces of organic crystals. *Surface Review and Letters*, 4(4):721–732, 1997.

[102] P E Hillner, S Mann, and P K Hansma A J Gratz. Atomic force microscope: A new tool for imaging crystal growth processes. *Faraday Discussions*, 95: 191–197, 1993.

[103] H H Teng, P M Dove, C A Orme, and J J de Yoreo. Thermodynamics of calcite growth: Baseline for understanding biomineral formation. *Science*, 282:724–727, 1998.

[104] H H Teng, P M Dove, and J J De Yoreo. Kinetics of calcite growth: Surface processes and relationships to macroscopic rate laws. *Geochimica et Cosmochimica Acta*, 64(13):2255–2266, 2000.

[105] Yu G Kuznetsov, A J Malkin, T A Land, J J De Yoreo, A P Barba, J Konnert, and A McPherson. Molecular resolution imaging of macromolecular crystals by atomic force microscopy. *Biophysical Journal*, 72:2357–2364, 1997.

[106] M Plomp, W J P van Enckevort, and E Vlieg. Etching and surface termination of $K_2Cr_2O_7$ {001} faces observed using in situ atomic force microscopy. *Journal of Crystal Growth*, 216:413–427, 2000.

[107] K Maiwa, M Plomp, W J P van Enckevort, and P Bennema. AFM observation of barium nitrate {111} and {100} faces: spiral growth and two-dimensional nucleation growth. *Journal of Crystal Growth*, 186:214–223, 1998.

[108] T A Land, T L Martin, S Potapenko, G Tayhas Palmore, and J J De Yoreo. Recovery of surfaces from impurity poisoning during crystal growth. *Nature*, 399:442–445, 1999.

[109] T A Land, J J De Yoreo, J D Lee, and J R Ferguson. Growth morphology of vicinal hillocks on the {101} face of KH_2PO_4: Evidence of surface diffusion. *Materials Research Society Symposia Proceedings*, 355:45–50, 1995.

[110] A R Lang. The early days of high resolution x-ray topography. *Journal of Physics D: Applied Physics*, 26:A1–A8, 1993.

[111] R P Chiarello and N C Sturchio. The calcite (1014) cleavage surface in water: Early results of a crystal truncation rod study. *Geochimica et Cosmochimica Acta*, 59(21):4557–4561, 1995.

[112] S A de vries, P Goedtkindt, S L Bennett, W J Huisman, M J Zwanenbuurg, D M Smilgies, J J de Yoreo, W J P van Enckevort, P Bennema, and E Vlieg. Surface atomic structure of KDP crystals in aqueous solution: An explanation of the growth shape. *Physical Review Letters*, 80(10):2229–2232, 1998.

[113] S A de Vries, P Goedkindt, W J Huisman, M J Zwanenburg, R Feidenhans'l, S L Bennett, D M Smilgies, A Stierle, J J De Yoreo, W J P van Enckevort, P Bennema, and E Vlieg. X-ray diffraction studies of potassium dihydrogen phosphate KDP crystal surfaces. *Journal of Crystal Growth*, 205:202–214, 1999.

[114] D Gidalevitz, R Feidenhans'l, S Matlis, D M Smilgies, M J Christiansen, and L Leiserowitz. Monitoring in-situ growth and dissolution of molecular crystals: Towards determination of the growth units. *Angwandte Chemie International Edition*, 36(9):955–959, 1997.

[115] R Feidenhans'l. Surface structure determination by x-ray diffraction. *Surface Science Reports*, 10:105–188, 1989.

[116] I K Robinson and D J Tweet. Surface x-ray diffraction. *Reports on Progress in Physics*, 55:599–651, 1992.

[117] Z Solc, J Kvapil, and J Vlček. Crystallization of potassium acid phthalate. *Kristall und Technik*, 8:59, 1973.

[118] Y Okaya. The crystal structure of potassium acid phthalate, $KC_6H_4COOH.COO$. *Acta Crystallographica*, 19:879–882, 1965.

[119] L A M J Jetten. Thesis, University of Nijmegen, 1983.

[120] M H J Hottenhuis, J G E Gardeniers, L A M J Jetten, and P Bennema. Potassium hydrogen phthalate: Relation between crystal structure and crystal morphology. *Journal of Crystal Growth*, 92:171–188, 1988.

[121] K Srinivasan, K Meera, and P Ramasamy. Enhancement of metastable zone width for solution growth of potassium acid phthalate. *Journal of Crystal Growth*, 205:457–459, 1999.

[122] M H J Hottenhuis and A Oudenampsen. Fe^{3+} and Ce^{3+} acting as competitive impurities in the crystallization process of potassium hydrogen phthalate from solutions. *Journal of Crystal Growth*, 92:513–529, 1988.

[123] M H J Hottenhuis and C B Lucasius. The role of impurities on the process of growing potassium hydrogen phthalate crystals from solution; a quantitative approach. *Journal of Crystal Growth*, 91:623–631, 1988.

[124] M H J Hottenhuis and C B Lucasius. The influence of internal crystal structure on surface morphology; in situ observations of potassium hydrogen phthalate {010}. *Journal of Crystal Growth*, 94:708–720, 1989.

[125] G R Ester, R Price, and P J Halfpenny. An atomic force microscopic investigation of surface degradation of potassium hydrogen phthalate (KAP) crystals caused by removal from solution. *Journal of Crystal Growth*, 182:95–102, 1997.

[126] L A M J Jetten, B van der Hoek, and W J P van Enckevort. In situ observation of the growth behaviour of the {010} face of potassium hydrogen phthalate. *Journal of Crystal Growth*, 62:603–611, 1983.

[127] B R Pamplin, editor. *Surface Microtopography of Aqueous Solution Grown Crystals*, volume 9 of *Progress in Crystal Growth and Characterization*, chapter 1. Pergamon Press, 1985.

[128] M H J Hottenhuis and C B Lucasius. The influence of impurities on crystal growth: In situ observation of the {010} face of potassium hydrogen phthalate. *Journal of Crystal Growth*, 78:379–388, 1986.

[129] K Sangwal and T Palcyńska. On the supersaturation and impurity concentration dependence of segregation coefficient in crystals growth from solutions. *Journal of Crystal Growth*, 212:522–531, 2000.

[130] G M van Rosmalen and Piet Bennema. Characterization of additive performance on crystallization habit modification. *Journal of Crystal Growth*, 99: 1053–1060, 1990.

[131] A E D M van der Heijden, M Elwenspoek, and J P van der Eerden. Size distribution of embryos produced by crystal-rod contacts. *Journal of Crystal Growth*, 98:398–410, 1989.

[132] A E D M van der Heijden and M Elwenspoek. Contact nucleation: in situ and ex situ observations of surface damaging. *Journal of Crystal Growth*, 99: 1087–1091, 1990.

[133] N Kubota, M Yamada, Y Fujisawa, and M Yokota. Impurity effect of chromium (III) on the growth rate of potassium hydrogen phthalate crystals. *Journal of Chemical Engineering of Japan*, 29(4):642–647, 1996.

[134] V A Kuznetsov, T M Okhrimenko, and M Rak. Growth promoting effect of organic impurities on growth kinetics of KAP and KDP crystals. *Journal of Crystal Growth*, 193:164–173, 1998.

[135] P Murugakoothan, R Mohan Kumar, P M Ushasree, R Jayavel, R Dhanasekaran, and R Ramasamy. Habit modification of potassium acid phthalate (KAP) single crystals by impurities. *Journal of Crystal Growth*, 207:325–329, 1999.

[136] Q L Zhao. Study of defects and structure in organic crystals of potassium hydrogen phthalate. *Journal of Applied Crystallography*, 26:243–250, 1993.

[137] Q L Zhao. An inclusion-probed method for studying the strained nature and inclusion contrast in potassium hydrogen phthalate crystals. *Journal of Materials Science Letters*, 13:1293–1295, 1994.

[138] G R Ester and P J Halfpenny. An investigation of growth-induced defects in crystals of potassium hydrogen phthalate (KAP). *Philosophical Magazine A*, 79:593, 1999.

[139] G R Ester, R Price, and P J Halfpenny. The relationship between crystal growth and defect structure: a study of potassium hydrogen phthalate using x-ray topography and atomic force microscopy. *Journal of Physics D: Applied Physics*, 32:A128–A132, 1999.

[140] G R Ester and P J Halfpenny. Observation of two-dimensional nucleation on the {0 1 0} face of potassium hydrogen phthalate (KAP) crystals using ex-situ atomic force microscopy. *Journal of Crystal Growth*, 187:111–118, 1998.

[141] C S Strom. Validity of Hartman-Perdok PBC theory in prediction of crystal morphology from solution and surface X-ray diffraction of potassium dihydrogen phosphate (KDP). *Journal of Crystal Growth*, 222(298–310), 2001.

[142] P G Barber and J T Petty. Use of moments of momentum to predict the crystal habit in potassium hydrogen phthalate. *Journal of Crystal Growth*, 100:185–188, 1990.

[143] S A de Vries. *Interface Structure of Growing Crystals*. PhD thesis, FOM Institute for Atomic and Molecular Physics, Amsterdam, 1999.

[144] D H Gay and A L Rohl. MARVIN: A new computer code for studying surfaces and interfaces and its application to calculating the crystal morphologies of corundum and zircon. *Chemical Society Faraday Transactions*, 91(5):925–936, 1995.

[145] E C Ifeachor and B W Jervis. *Digital Signal Processing: A Practical Approach.* Electronic Systems Engineering Series. Addison-Wesley, 1993.

[146] B Donohoe, R Price, and P J Halfpenny. Unpublished work. University of Bath, UK, 1998.

[147] William H Press, Saul A Teukolsky, William T Vetterling, and Brian P Flannery. *Numerical Recipes in C: The Art of Scientific Computing*, chapter 15. Cambridge University Press, 2nd edition, 1992.

[148] R Price, G R Ester, and P J Halfpenny. Supersaturation dependent polygonisation of growth spirals during crystallisation from solution. *Proceedings of the Royal Society A*, 455:4119, 1999.

[149] B Van Der Hoek, J P Van Der Eerden, and P Bennema. Some methods for the quantitative estimation of crystal growth parameters from observed step patterns. *Journal of Crystal Growth*, 56:108–124, 1982.

[150] M Lahav and L Leiserowitz. The effect of solvent on crystal growth and morphology. *Chemical Engineering Science*, 56:2245–2253, 2001.

[151] W Schommers and P von Blanckenhagen, editors. *Structure and Dynamics of Surfaces II*, chapter 1. Number 43 in Topics in Current Physics. Springer, 1987.

[152] M Giesen, C Steimer, and H Ibach. What does one learn from the equilibrium shapes of two-dimensional islands on surfaces? *Surface Science*, 471:80–100, 2001.

[153] M W Zemansky and R H Dittman. *Heat and Thermodynamics*. McGraw-Hill, 6th edition, 1981.

[154] F F A Hollander, M Plomp, J van de streek, and W J P van Enckevort. A two-dimensional Hartman-Perdok analysis of polymorphic fat surfaces observed with atomic force microscopy. *Surface Science*, 471:101–113, 2001.

[155] C M Pina, D Bosbach, M Prieto, and A Putnis. Microtopography of the barite (001) face during growth: AFM observations and PBC theory. *Journal of Crystal Growth*, 187:119–125, 1998.

[156] C M Pina, U Becker, P Risthaus, D Bosbach, and A Putnis. Molecular-scale mechanisms of crystal growth in barite. *Nature*, 395:483–486, 1998.

[157] P G Barber. Moments of momenta as predictors of "molecular" species in crystal growth solutions. *Journal of Crystal Growth*, 109(99–106), 1991.

[158] T A Land, J J De Yoreo, J D Lee, and J R Ferguson. Growth morphology of vicinal hillocks on the {101} face of KH_2PO_4: Evidence of surface diffusion. *Materials Research Society Symposia Proceedings*, 355:45–50, 1995.

[159] E Kaldis and H J Scheel, editors. *Crystal Growth and Materials*, chapter 10, pages 483–513. North-Holland, Amsterdam, 1977.

[160] J J De Yoreo, T A Land, and J D Lee. Limits on surface vicinality and growth rate due to hollow dislocation cores on KDP {101}. *Physical Review Letters*, 78(23):4462–4465, 1997.

[161] J J De Yoreo, T A Land, L N Rashkovich, T A Onischenko, J D Lee, O V Monovskii, and N P Zaitseva. The effect of dislocation cores on growth hillock vicinality and normal growth rates of KDP {101} surfaces. *Journal of Crystal Growth*, 182:442–460, 1997.

[162] D T J Hurle, editor. *Handbook of Crystal Growth*, volume 2, chapter 7, pages 315–412. Elsevier Science, 1994.

[163] U Tanneberger, R Lacmann, A Herden, H Klapper, D Schmiemann, R A Becker, A Mersmann, and U Zacher. The dispersion of growth rate as a result of different crystal perfection. *Journal of Crystal Growth*, 166:1074–1077, 1996.

[164] R I Ristic, J N Sherwood, and T Shripathi. The influence of tensile strain on the growth of crystals of potash alum and sodium nitrate. *Journal of Crystal Growth*, 179:194–204, 1997.

[165] M M Mitrovic, A A Zekic, and M M Napijalo. Correlation between the crystal size and crystal growth rate of KDP and Rochelle salt crystals. *Journal of Crystal Growth*, 216:437–442, 2001.

[166] J N Sherwood and R I Ristic. The influence of mechanical stress on the growth and dissolution of crystals. *Chemical Engineering Science*, 56:2267–2280, 2001.

[167] M Matsuoka, Y Abe, H Uchida, and H Takiyama. Mechanism of growth rate enhancement by micro-crystals for the potash alum-water system. *Chemical Engineering Science*, 56:2325–2334, 2001.

[168] H Klapper. Generation and propagation of dislocations during crystal growth. *Materials Chemistry and Physics*, 66:101–109, 2000.

[169] F C Frank. Nucleation and normal growth: General discussion. *Discussions of the Faraday Society*, 5:189, 1949.

[170] B van der Hoek, J P van der Eerden, and P Bennema. Thermodynamical stability conditions for the occurrence of hollow cores caused by stress of line and planar defects. *Journal of Crystal Growth*, 56:621–632, 1982.

[171] J P Hirth and D J Srolovitz. Shape of hollow dislocation cores. *Philosophical Magazine A*, 69(2):341–347, 1994.

[172] D J Srolovitz, N Sridhar, J P Hirth, and J W Cahn. Shape of hollow dislocation cores: Anisotropic surface energy and elastic effects. *Scripta Materialia*, 39 (4/5):379–387, 1998.

[173] G Zhao Liu, J P van der Eerden, and P Bennema. The opening and closing of a hollow dislocation core: A Monte Carlo simulation. *Journal of Crystal Growth*, 58:152–162, 1982.

[174] L M Belyaev, G S Belikova, A B Gil'varg, and I M Silvestrova. The growth of potassium hydrogen phthalate crystals and their optical, piezoelectric and elastic properties. *Soviet Physics - Crystallography*, 14(4):544–549, 1970.

[175] T A Land, T L Martin, S Potapenko, G Tayhas Palmore, and J J De Yoreo. Recovery of surfaces from impurity poisoning during crystal growth. *Nature*, 399:442–445, 1999.